

©Copyright 2012

Sean David Knecht

Comparison of Electrode Configurations on ZaP: Investigation of Heating Mechanisms in a Flow Z-Pinch

Sean David Knecht

A dissertation
submitted in partial fulfillment of the
requirements for the degree of

Doctor of Philosophy

University of Washington

2012

Reading Committee:

Uri Shumlak, Chair

Brian A. Nelson, Chair

Thomas R. Jarboe

Program Authorized to Offer Degree:
Aeronautics & Astronautics

University of Washington

Abstract

Comparison of Electrode Configurations on ZaP: Investigation of Heating Mechanisms in a Flow Z-Pinch

Sean David Knecht

Chair of the Supervisory Committee:

Professor Uri Shumlak

Aeronautics and Astronautics

Professor Brian A. Nelson

Electrical Engineering

The ZaP Flow Z-Pinch is a basic plasma physics experiment that investigates the effect of sheared axial flows Z-pinch stability. Two modifications are made: 1) Installation of a perforated conducting wall to evaluate the effect on Z-pinch stability; 2) The 10 cm diameter inner electrode is replaced with a 16 cm diameter version to evaluate the effects of adiabatic compression. It is determined that the conducting wall has no effect on the stability of the pinch. Expected effects of the inner electrode modification are increased temperature and density due to increased adiabatic compression and an increase in stable period length. Pinch density profile evolution is measured with a four-chord HeNe interferometer and temperature and magnetic field profiles are calculated with a radial heat conduction analysis. Pinch equilibrium comparison between the 10 cm and 16 cm inner electrode configurations shows that the 16 cm electrode is subject to greater non-adiabatic processes, such as shocks. Greater influence of shocks is attributed to a blunter nosecone and increased current in the accelerator for the 16 cm inner electrode. Pinch temperature for the 16 cm inner electrode is less than the 10 cm electrode due to higher linear density in the pinch and the increased size of the pinch is a result of the non-adiabatic formation process.

TABLE OF CONTENTS

	Page
List of Figures	iii
List of Tables	x
Chapter 1: Plasma and Nuclear Fusion	1
1.1 Plasma	1
1.2 Nuclear Fusion	3
1.3 Z-pinch	5
Chapter 2: Flow Shear Stabilization and the ZaP Flow Z-Pinch	12
2.1 Previous Z-Pinch Experimentation	12
2.2 The ZaP Flow Z-Pinch	12
2.3 Diagnostics on the ZaP Flow Z-Pinch	13
2.4 Shear Flow Stabilization and the Effects of Viscosity on the ZaP Flow Z-Pinch	28
2.5 Experimental Modifications on ZaP	36
Chapter 3: Optimum Operating Conditions for 16 cm Inner Electrode Configuration	38
3.1 Soft-Stop Operating Conditions	38
3.2 High Peak Magnetic Field Operating Conditions	41
Chapter 4: Effect of a Conducting Wall on Stability of the ZaP Flow Z-Pinch . . .	47
4.1 Experimental Evidence of No-Wall Stabilization on ZaP	47
4.2 Comparison to Computational Results	57
4.3 Conclusions	59
Chapter 5: Plasma Heating in the ZaP Flow Z-Pinch	61
5.1 Adiabatic Compression	61
5.2 Shock Heating	74

5.3	Advanced Compression Analysis	77
5.4	Ohmic Heating and Radiation	81
Chapter 6:	Equilibrium Evolution in the ZaP Flow Z-Pinch	83
6.1	Interferometry Analysis	83
6.2	Calculations of Magnetic Field and Temperature Profiles	89
6.3	Multiple Shooting Method	101
6.4	Generalized Thermal Conductivity	106
6.5	Solutions for Magnetic Field and Temperature Profiles	114
Chapter 7:	Comparison of Experimental Performance for 10 cm vs. 16 cm Inner Electrodes	119
7.1	10 cm Inner Electrode and Comparison with Thomson Scattering and Doppler Spectroscopy Measurements	119
7.2	Quiescent Period Behavior	123
7.3	Comparison of 10 cm and 16 cm Inner Electrode Configuration Performance .	133
Chapter 8:	Conclusions	143
Chapter 9:	Future Work	146
Appendix A:	Additional Pulse Data	147
A.1	10 cm Pulse Data	147
A.2	16 cm Pulse Data	159
Appendix B:	Computer Codes	183
B.1	Four Chord Equilibrium Calculations	183
B.2	Multiple Shooting Solver	210
B.3	ode15s Heat Conduction Equations	249
B.4	ode15s Heat Conduction Baseline Equations	251
B.5	ode15s Heat Conduction Events Equations	253
Bibliography	256

LIST OF FIGURES

Figure Number	Page
1.1 Schematic of a Hydrogen Atom with a Bound Electron	2
1.2 Schematic of an Ionized Hydrogen Atom	3
1.3 Schematic of Deuterium-Tritium Fusion Reaction	4
1.4 Simple Representation of a Z-Pinch	6
1.5 Static Z-Pinch Instabilities	8
1.6 Threshold of Z-Pinch Stability	10
1.7 Schematic of Destructive Interference of Instabilities	11
2.1 ZaP Flow Z-Pinch Geometry	14
2.2 Formation Sequence in a Flow Z-Pinch	15
2.3 Example of ZaP Stability Criterion	17
2.4 Schematic of ZaP HeNe Interferometry System	19
2.5 Intrinsic Mode Functions	20
2.6 Empirical-Mode Decomposition Filtered Interferometer Signal	21
2.7 Schematic of Bremsstrahlung Radiation Process	22
2.8 Schematic of Line Radiation Process	23
2.9 Schematic of Red Shift	24
2.10 Schematic of Blue Shift	24
2.11 Schematic of Thomson Scattering Effect	26
2.12 Schematic of Thomson-Scattering System	26
2.13 Intrinsic Mode Functions of Interferometry Data Related to an Imacon Image	29
2.14 Hilbert Transform of Intrinsic Mode Functions Produces Instantaneous Fre- quency and Amplitude	30
2.15 Visible Light Images from an Imacon 790 Fast-Framing Camera at $z = 0$ cm showing a Traveling Saturated Kink Instability	31
2.16 End of the Quiescent Period is Coincident with Drop in Current and Density in Acceleration Region	33
2.17 Axial Flow Profile is Correlated with Plasma Stability	34

2.18	Long Pinches and Sheared Flow Profiles are Consistent with Classical Viscosity	37
3.1	Current and Voltage Waveforms for Soft-Stop Operating Condition	39
3.2	Magnetic Data at $z = 0$ cm for Soft-Stop Operating Condition	40
3.3	Acceleration Region Data for Soft-Stop Operating Condition	40
3.4	Current and Voltage Waveforms for High Peak Magnetic Field Operating Condition	41
3.5	Magnetic data at $z = 0$ cm for High Peak Magnetic Field Operating Condition	42
3.6	Acceleration Region Data for High Peak Magnetic Field Operating Condition	43
3.7	Observation of Chord-Integrated Density Crash during High Peak Magnetic Field Operating Condition	44
3.8	Visible Light Images of Instability Onset related to Density Crash during High Peak Magnetic Field Operating Condition	45
3.9	Inset View of Chord-Integrated Density Crash during High Peak Magnetic Field Operating Condition	46
4.1	Schematic of ZaP Experimental Configuration with and without Perforated Electrode Section	49
4.2	Fourier Mode Data at $z = 0$ cm with and without Perforated Electrode Section	51
4.3	Fourier Mode Data with and without Perforated Electrode Section for 10 cm Electrode at $z = 35$ cm	52
4.4	Fourier Mode Data and Interferometer Data in Perforated Section for 10 cm Inner Electrode	53
4.5	Visible Light Images from an Imacon 790 Fast-Framing Camera in Perforated Electrode Section	54
4.6	Fourier Mode Data Upstream and Downstream of Perforated Electrode . . .	55
4.7	Fourier Mode Data and Interferometer Data in Perforated Section for 16 cm Inner Electrode	56
4.8	Visible Light Images from Fast-Framing Camera in Perforated Electrode Sec- tion with 16 cm Inner Electrode	57
4.9	Fourier Mode Data Upstream and Downstream of Perforated Electrode Sec- tion for 16 cm Inner Electrode	58
4.10	Cross-Sections of the Straight Cylinder and Cylinder with Extrusions Com- putational Geometries	58
4.11	Computational Results for Pressure Profiles at the Midpoint of the Axial Kink Wavelength for Multiple Plasma Size	59

5.1	Adiabatic Compression Geometry for Smaller and Larger Inner Electrode Configurations	67
5.2	Predicted Trends for Increasing Inner Electrode Size from Adiabatic Compression Analysis	71
5.3	Effect of Changing Annulus Density for Larger Inner Electrode	72
5.4	Effect of Changing Annulus Temperature for Larger Inner Electrode	73
5.5	Effect of Changing Pinch Current for Larger Inner Electrode	73
5.6	Schematic of Advanced Compression Analysis	78
6.1	Schematic of Four-Chord Interferometer Setup	84
6.2	Magnetic Mode Data for High Peak Magnetic Field Operating Conditions . .	84
6.3	Four-Chord Interferometry Data for High Peak Magnetic Field Operating Conditions	85
6.4	Inset View of Interferometry Data for High Peak Magnetic Field Operating Condition	85
6.5	Example Interferometry Data at a Temporal Point	86
6.6	Chord-Integrated Fits and Electron Density Profiles	88
6.7	Characteristic Pinch Radius and Peak Density as a Function of Time	90
6.8	Total Current and Linear Density as a Function of Time	91
6.9	Contour Plot of Electron Density for High Peak Field Operating Condition .	92
6.10	Diagram of the Multiple Shooting Technique	103
6.11	Multiple Shooting Method Iterations for Temperature	107
6.12	Multiple Shooting Method Iterations for dT/dr	107
6.13	Multiple Shooting Method Iterations for Magnetic Field	108
6.14	Synthetic Density Profile for Comparing Generalized and Magnetized Thermal Conductivity.	111
6.15	Temperature and Magnetic Field Profiles Comparing Generalized and Magnetized Thermal Conductivity	112
6.16	Current Density Profile for Generalized and Magnetized Thermal Conductivity.	113
6.17	Thermal Conductivity, Larmor Radii and Collisional Mean Free-Path for Ions	114
6.18	Magnetic Field and Temperature Profiles for High Peak Magnetic Field Operating Conditions	115
6.19	Peak Magnetic Field and Temperature as a Function of Time for High Peak Magnetic Field Operating Condition	116

6.20	Temperature Contours as a Function of Radius and Time for High Peak Magnetic Field Operating Condition	117
6.21	Magnetic Field Contours as a Function of Radius and Time for High Peak Magnetic Field Operating Condition	118
7.1	Magnetic Mode Data for 10 cm Diameter Inner Electrode Configuration	120
7.2	Four-Chord Interferometry Data for 10 cm Diameter Inner Electrode Configuration	120
7.3	Inset View of Interferometry Data for 10 cm Diameter Inner Electrode Configuration	121
7.4	Characteristic Pinch Radius and Peak Density as a Function of Time for 10 cm Diameter Inner Electrode	122
7.5	Total Current and Linear Density as a Function of Time for the 10 cm Diameter Inner Electrode	123
7.6	Peak Magnetic Field and Peak Temperature as a Function of Time for the 10 cm Diameter Inner Electrode	124
7.7	Electron and Ion Temperature Data for a 10 cm Diameter Inner Electrode Pulse	125
7.8	Volume-averaged Adiabatic Function as a Function of Time for 10 cm Diameter and 16 cm Diameter Electrode Configurations	126
7.9	Characteristic Pinch Radius as a Function of Time for the 10 cm and 16 cm diameter inner electrode configurations	127
7.10	Volume-averaged Ohmic Dissipation vs. Characteristic Pinch Radius for 10 cm and 16 cm Diameter Inner Electrode Configurations	128
7.11	Volume-averaged Ohmic Dissipation vs. Characteristic Pinch Radius for 10 cm and 16 cm Diameter Inner Electrode Configurations	130
7.12	Volume-averaged Ohmic Dissipation vs. Volume-averaged Adiabatic Function for 10 cm and 16 cm Diameter Inner Electrode Configurations	131
7.13	Volume-averaged Radiation as a Function of Time for Multiple Impurity Contents	132
7.14	Calculated and Predicted Characteristic Pinch Radius for 10 cm and 16 cm Diameter Inner Electrode Configurations	134
7.15	Calculated and Predicted Peak Electron Density for the 10 cm and 16 cm Diameter Inner Electrode Configurations	135
7.16	Calculated and Predicted Peak Temperature as a Function of Time for 10 cm and 16 cm Diameter Inner Electrode Configurations	136

7.17	Calculated and Predicted Peak Magnetic Field as a Function of Time for 10 cm and 16 cm Diameter Inner Electrode Configurations	137
7.18	Predicted Shock Mach Number to Account for Difference in Calculated and Predicted Equilibrium for 10 cm and 16 cm Diameter Inner Electrode Configurations	138
7.19	Predicted Compression Speed during Formation Process for 10 cm and 16 cm Diameter Inner Electrode Configurations	139
7.20	Plasma Arrival in the Acceleration Region for 10 cm and 16 cm Diameter Inner Electrode Configurations	140
7.21	Calculated Linear Density as a Function of Time for 10 cm and 16 cm Inner Electrode Configurations	141
7.22	Total Current as a Function of Time for 10 cm and 16 cm Diameter Inner Electrode Configurations	142
A.1	Magnetic Mode Data for 10 cm Diameter Inner Electrode Configuration, Pulse 100504014	148
A.2	Four-Chord Interferometry Data for 10 cm Diameter Inner Electrode Configuration, Pulse 100504014	148
A.3	Characteristic Pinch Radius and Peak Density as a Function of Time for 10 cm Diameter Inner Electrode, Pulse 100504014	149
A.4	Total Current and Linear Density as a Function of Time for the 10 cm Diameter Inner Electrode, Pulse 100504014	150
A.5	Peak Magnetic Field and Peak Temperature as a Function of Time for the 10 cm Diameter Inner Electrode, Pulse 100504014	151
A.6	Predicted Formation Compression Speed and Mach Number for the 10 cm Diameter Inner Electrode, Pulse 100504014	152
A.7	Magnetic Mode Data for 10 cm Diameter Inner Electrode Configuration, Pulse 100429022	153
A.8	Four-Chord Interferometry Data for 10 cm Diameter Inner Electrode Configuration, Pulse 100429022	153
A.9	Characteristic Pinch Radius and Peak Density as a Function of Time for 10 cm Diameter Inner Electrode, Pulse 100429022	154
A.10	Total Current and Linear Density as a Function of Time for the 10 cm Diameter Inner Electrode, Pulse 100429022	155
A.11	Peak Magnetic Field and Peak Temperature as a Function of Time for the 10 cm Diameter Inner Electrode, Pulse 100429022	155

A.12 Predicted Formation Compression Speed and Mach Number for the 10 cm Diameter Inner Electrode, Pulse 100429022	156
A.13 Magnetic Mode Data for 10 cm Diameter Inner Electrode Configuration, Pulse 100427017	157
A.14 Four-Chord Interferometry Data for 10 cm Diameter Inner Electrode Configuration, Pulse 100427017	157
A.15 Characteristic Pinch Radius and Peak Density as a Function of Time for 10 cm Diameter Inner Electrode, Pulse 100427017	158
A.16 Total Current and Linear Density as a Function of Time for the 10 cm Diameter Inner Electrode, Pulse 100427017	159
A.17 Peak Magnetic Field and Peak Temperature as a Function of Time for the 10 cm Diameter Inner Electrode, Pulse 100427017	160
A.18 Predicted Formation Compression Speed and Mach Number for the 10 cm Diameter Inner Electrode, Pulse 100427017	161
A.19 Magnetic Mode Data for 16 cm Diameter Inner Electrode Configuration, Pulse 90622010	162
A.20 Four-Chord Interferometry Data for 16 cm Diameter Inner Electrode Configuration, Pulse 90622010	163
A.21 Characteristic Pinch Radius and Peak Density as a Function of Time for 16 cm Diameter Inner Electrode, Pulse 90622010	164
A.22 Total Current and Linear Density as a Function of Time for the 16 cm Diameter Inner Electrode, Pulse 90622010	165
A.23 Peak Magnetic Field and Peak Temperature as a Function of Time for the 16 cm Diameter Inner Electrode, Pulse 90622010	165
A.24 Predicted Formation Compression Speed and Mach Number for the 60 cm Diameter Inner Electrode, Pulse 90622010	166
A.25 Magnetic Mode Data for 16 cm Diameter Inner Electrode Configuration, Pulse 90602008	167
A.26 Four-Chord Interferometry Data for 16 cm Diameter Inner Electrode Configuration, Pulse 90602008	168
A.27 Characteristic Pinch Radius and Peak Density as a Function of Time for 16 cm Diameter Inner Electrode, Pulse 90602008	169
A.28 Total Current and Linear Density as a Function of Time for the 16 cm Diameter Inner Electrode, Pulse 90602008	170
A.29 Peak Magnetic Field and Peak Temperature as a Function of Time for the 16 cm Diameter Inner Electrode, Pulse 90602008	171

A.30 Predicted Formation Compression Speed and Mach Number for the 60 cm Diameter Inner Electrode, Pulse 90602008	172
A.31 Magnetic Mode Data for 16 cm Diameter Inner Electrode Configuration, Pulse 81211023	173
A.32 Four-Chord Interferometry Data for 16 cm Diameter Inner Electrode Configuration, Pulse 81211023	173
A.33 Characteristic Pinch Radius and Peak Density as a Function of Time for 16 cm Diameter Inner Electrode, Pulse 81211023	174
A.34 Total Current and Linear Density as a Function of Time for the 16 cm Diameter Inner Electrode, Pulse 81211023	175
A.35 Peak Magnetic Field and Peak Temperature as a Function of Time for the 16 cm Diameter Inner Electrode, Pulse 81211023	176
A.36 Predicted Formation Compression Speed and Mach Number for the 60 cm Diameter Inner Electrode, Pulse 81211023	177
A.37 Magnetic Mode Data for 16 cm Diameter Inner Electrode Configuration, Pulse 90319026	178
A.38 Four-Chord Interferometry Data for 16 cm Diameter Inner Electrode Configuration, Pulse 90319026	178
A.39 Characteristic Pinch Radius and Peak Density as a Function of Time for 16 cm Diameter Inner Electrode, Pulse 90319026	179
A.40 Total Current and Linear Density as a Function of Time for the 16 cm Diameter Inner Electrode, Pulse 90319026	180
A.41 Peak Magnetic Field and Peak Temperature as a Function of Time for the 16 cm Diameter Inner Electrode, Pulse 90319026	181
A.42 Predicted Formation Compression Speed and Mach Number for the 60 cm Diameter Inner Electrode, Pulse 90319026	182

LIST OF TABLES

Table Number	Page
1.1 Partial List of Fusion Reactions	5
2.1 ZaP Operating Conditions with 10 cm Diameter Inner Electrode	14
5.1 Parameters for 10 cm and 16 cm Electrode Configurations undergoing Adiabatic Compression	71
5.2 Parameters for 10 cm and 16 cm Electrode Configurations undergoing Shock Heating	77

ACKNOWLEDGMENTS

Finishing this dissertation has been a long road and I could not have done it without a great deal of help. First and foremost I'd like to thank my advisors Professor Uri Shumlak and Professor Brian Nelson for all that they have taught me. Dr. Ray Golingo also deserves mention for training me on the experiment in the very beginning. Obviously I couldn't have done this without my friends. Whenever things got rough, I always knew that they had my back. So thanks to Bhuvana, Colin, Joe, Cesar, Katie, Josh and Allison amongst many others for being there for me. I'd like to thank my family for believing in me through it all. And, of course, Jenn for always being there for me.

Chapter 1

PLASMA AND NUCLEAR FUSION

Extracting energy from controlled nuclear fusion reactions is an important goal for plasma researchers around the world. The confinement and stability of plasma at thermonuclear temperatures is one of the many challenges that needs to be overcome to reach that goal. The majority of attention is presently being given to the tokamak magnetic confinement configuration [1]. However, other geometries in smaller-scale experiments can be used to perform basic research on confinement and stability mechanisms. The Z-pinch geometry is utilized in the ZaP Flow Z-Pinch Experiment at the University of Washington to investigate sheared-flow stabilization of a plasma. This dissertation will begin with an introduction to plasma, Z-pinches and nuclear fusion. The ZaP Flow Z-Pinch and its diagnostic systems and operations will be described. Recent experimental results including evidence of stability without the effects of a conducting wall and the results of equilibrium evolution measured by a four-chord interferometer will be discussed. An interpretation of these results will be made in order to identify the primary means of a heating in the ZaP Flow Z-Pinch.

1.1 Plasma

Plasma, often referred to as the fourth state of matter, is defined as a quasineutral fluid of charged and neutral particles which exhibits collective behavior. Plasma is the result of a neutral gas, such as hydrogen, undergoing the process of ionization. For example, a hydrogen atom consists of an electron orbiting a proton, shown in schematic form in Figure 1.1. This electron is bound to the proton through atomic forces. If the energy of the electron is increased, it will orbit further from the proton. When the electron has enough energy it can escape from the potential well produced by the proton. This process is called

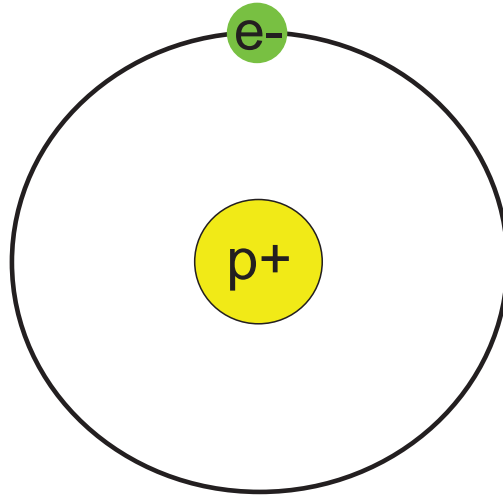


Figure 1.1: Schematic of a hydrogen atom with a bound electron. The negatively-charged electron orbits the positively-charged proton due to electrostatic forces.

ionization. A schematic of the resulting ionized atom is shown in Figure 1.2.

The formerly neutral gas now has the property of being electrically conductive. Current can flow in the plasma which gives rise to magnetic fields as described by Ampere's Law, shown in Equation 1.1 where \mathbf{B} is the magnetic field and \mathbf{j} is the current density. The charged particles in the plasma can also be manipulated with electric and magnetic fields which will produce a Lorentz force (Equation 1.2) on the charged particles. This is the basis of magnetic confinement fusion.

$$\nabla \times \mathbf{B} = \mu_0 \mathbf{j} \quad (1.1)$$

$$\mathbf{F} = q(\mathbf{E} + \mathbf{v} \times \mathbf{B}) \quad (1.2)$$

where $\mu_0 = 4\pi \times 10^{-7}$ H/m is the permeability of free space.

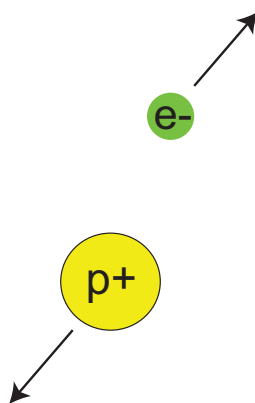


Figure 1.2: Schematic of an ionized hydrogen atom. When an electron gains enough energy, it escapes the potential well of the proton. This is the process of ionization.

1.2 Nuclear Fusion

Nuclear fusion is the process that powers the stars. Unlike nuclear fission, which consists of higher mass nuclei such as uranium and plutonium splitting into lighter nuclei, nuclear fusion is the process of combining lower mass nuclei such as deuterium and tritium into higher mass products. In a plasma, the two low mass fusion reactants have a positive charge and are subject to a Coulomb repulsion force. These nuclei need to get close enough to one another for the strong nuclear force to overcome the Coulomb repulsion force and allow fusion. The fusion reaction produces particles with a combined energy that is defined by Einstein's equation:

$$E = mc^2 \tag{1.3}$$

where m is the difference in mass between the reactants and the products and c is the speed of light. The resulting product of the deuterium-tritium fusion reaction, shown in Figure 1.3, is a helium nucleus, or α particle with an energy of 3.5 MeV and a neutron with an energy of 14.1 MeV. Additional fusion reactions are shown in Table 1.1.

The nuclei need to be raised to high temperature for this to occur (≈ 10 keV for D-T

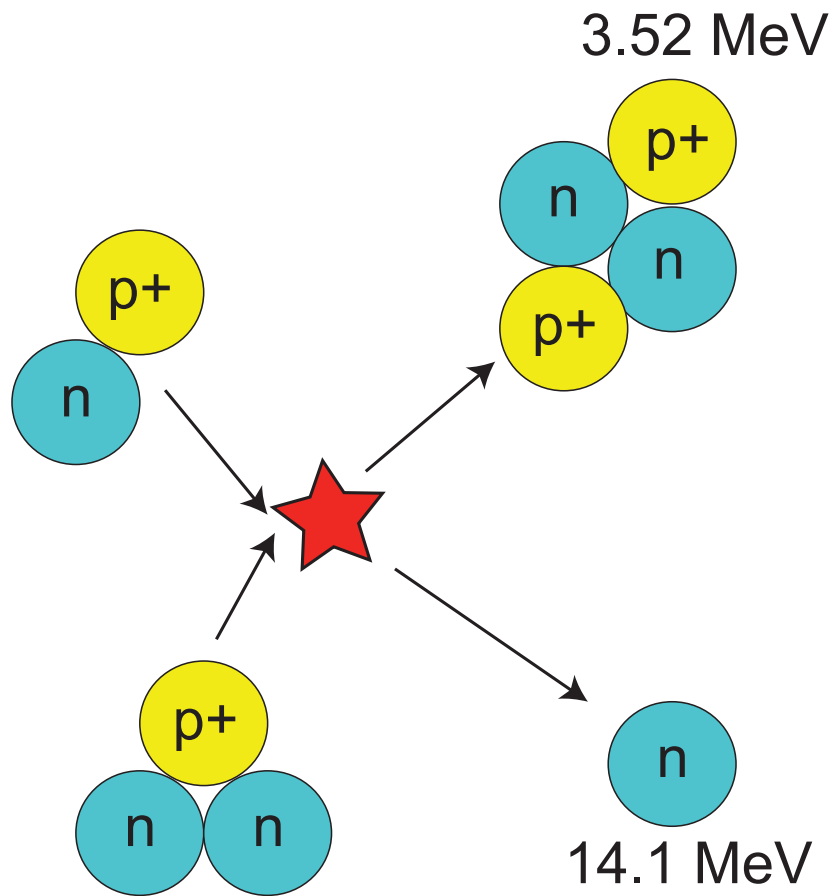


Figure 1.3: Schematic of deuterium-tritium fusion reaction. When the ion temperature becomes high enough that the deuterium and tritium approach each other close enough for the strong nuclear force to overcome the Coulomb repulsion force, a fusion reaction may occur. The resulting products are an α particle with an energy of 3.5 MeV and a neutron with an energy of 14.1 MeV.

Table 1.1: Partial List of Fusion Reactions .

Reactants	Products
D + T →	α (3.52 MeV) + n (14.1 MeV)
D + D →	T (1.01 MeV) + p (3.02 MeV) (50%)
	→ ${}^3\text{He}$ (0.82 MeV) + n (2.45 MeV) (50%)
p + ${}^6\text{Li}$ →	α (1.72 MeV) + ${}^3\text{He}$ (2.3 MeV)
p + ${}^{11}\text{B}$ →	3α (8.7 MeV)

fusion). In addition, for a fusion-grade plasma to reach ignition (energy input equal to energy loss), it must be maintained at this temperature for a sufficient energy confinement time, τ_E , and at a sufficient density, n , to produce enough fusion reactions. A figure of merit for this condition is the triple product, $n\tau_E T$. For D-T fusion, this value must exceed 10^{21} keV-s/m³.

Many magnetic confinement schemes exist to attempt to reach this triple product value. These include conventional geometries such as the tokamak and less common geometries such as spheromaks, field-reversed configurations and the Z-pinch configuration.

1.3 Z-pinch

The Z-pinch is a simple magnetic confinement configuration that consists of a column of plasma between two electrodes, as shown in Figure 1.4.

A Z-pinch is in equilibrium when radial force balance is satisfied; or when pressure gradient is balanced by magnetic force and magnetic tension.

$$\mathbf{j} \times \mathbf{B} = \nabla p \tag{1.4}$$

Using Ampere's Law,

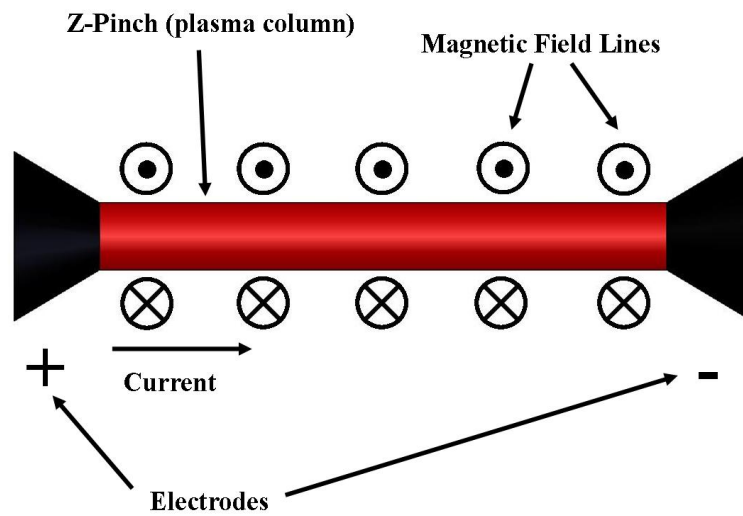


Figure 1.4: Simple representation of a standard Z-pinch. Red represents the plasma column in between the two electrodes with current flowing axially. The current generates an azimuthal magnetic field. The resulting inward $\mathbf{j} \times \mathbf{B}$ force is balanced by the plasma pressure.

$$\frac{1}{\mu_0}(\nabla \times \mathbf{B}) \times \mathbf{B} = \nabla p \quad (1.5)$$

Using the following vector identity, Equation 1.5 can be rewritten.

$$\nabla \left(\frac{1}{2} \mathbf{B} \cdot \mathbf{B} \right) = \mathbf{B} \times (\nabla \times \mathbf{B}) + (\mathbf{B} \cdot \nabla) \mathbf{B} \quad (1.6)$$

$$\frac{1}{\mu_0} (\mathbf{B} \cdot \nabla) \mathbf{B} - \nabla \left(\frac{B^2}{2\mu_0} \right) = \nabla p \quad (1.7)$$

The first term in Equation 1.7 represents tension parallel to \mathbf{B} due to curvature of the field lines. The second term represents an isotropic magnetic pressure.

A static Z-pinch suffers from two major magnetohydrodynamic (MHD) instabilities which have growth rates proportional to the Alfvén transit times which are often on the order of tens of nanoseconds, limiting the pinch from compressing and heating. These instabilities are the $m = 0$ “sausage” mode and the $m = 1$ “kink” mode, where m is the azimuthal mode number of the instability. Representations of these MHD modes are shown in Fig. 1.5.

The $m = 0$ mode occurs when the plasma column has a reduced radius at some point along its length, caused by turbulence or other phenomena. The regions of inward curvature are subjected to higher magnetic fields, resulting in a continual reduction in the column radius at that point, until the column eventually breaks and confinement is lost. The $m = 1$ mode occurs when the column bends or kinks at any point along its length. The inner side of the kink experiences greater magnetic field while the outer side of the kink experiences reduced magnetic field causing the bending of the column to increase until the plasma current is disrupted and confinement is lost. These instabilities prevent static Z-pinches from being a feasible fusion reactor geometry.

Several methods have been investigated to provide stability, however, there are problems associated with each of them. Using a conducting wall that is situated close to the edge of the plasma results in image currents being generated in the wall, these image currents

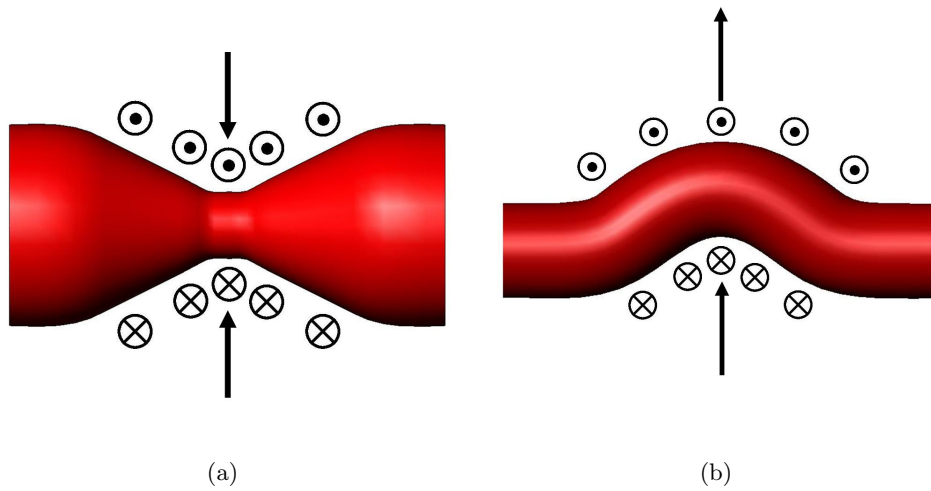


Figure 1.5: Static Z-pinch instabilities. (a) $m = 0$ sausage instability. Phenomena, such as turbulence, in the plasma result in the plasma column thinning at certain points, resulting in increased magnetic field which continues the pinching of the column until the plasma current is interrupted. (b) $m = 1$ kink instability. The plasma column bends along its length resulting in greater magnetic field in the regions of inward curvature and reduced field in regions of outward curvature, resulting in an increase to the bending until the plasma current is disrupted.

provide a stabilizing effect on both the $m = 0$ and $m = 1$ modes. The problem with this method is that the wall must be located very close to the plasma, $r_w/a = 1.2$, to provide stability [2], where r_w is the wall radius and a is the pinch radius. For fusion temperature plasmas, the heat flux would damage the wall and impurities would be introduced to the plasma that would cause cooling through enhanced radiation.

Controlling the radial pressure profile of the pinch is found to stabilize the $m = 0$ mode. Applying a functional minimization to the linear MHD equations results in a stability condition for the $m = 0$ mode [3].

$$-\frac{d \ln p}{d \ln r} \leq \frac{4\gamma}{2 + \gamma\beta} \quad (1.8)$$

where $\beta = 2\mu_0 p/B^2$ and γ is the ratio of specific heats, taken to be 5/3 for a plasma. Stability is possible if the pressure does not decrease too rapidly as a function of radius, but this method does not stabilize the $m = 1$ mode.

Applying an axial field can stabilize the $m = 1$ mode. Kinking of the column has the effect of stretching the axial field lines, the resulting tension force resists further kinking. However, this applied axial field limits the plasma current and pressure according to the Kruskal-Shafranov limit [4],

$$\frac{B_\theta}{B_z} < \frac{2\pi a}{L} \quad (1.9)$$

where a is the radius of the pinch and L is the length of the pinch. The resulting magnetic field lines also intersect the electrodes, resulting in particle and energy losses.

Another potential method of stabilizing the MHD modes of a pure Z-pinch that has been investigated is using a radially-varying axial velocity, dv_z/dr . Applying linear stability analysis of the MHD equations shows that a threshold exists, $dv_z/dr > 0.1kV_A$ [2], where the additional stabilizing effects of a conducting wall are unnecessary to maintain stability of the plasma column, as seen in Fig. 1.6. In this relation, k is the axial wavenumber of the instability and V_A is the Alfvén velocity. Another way to think about this mechanism is by imagining a plasma column consisting of two distinct regions, an inner cylinder of plasma

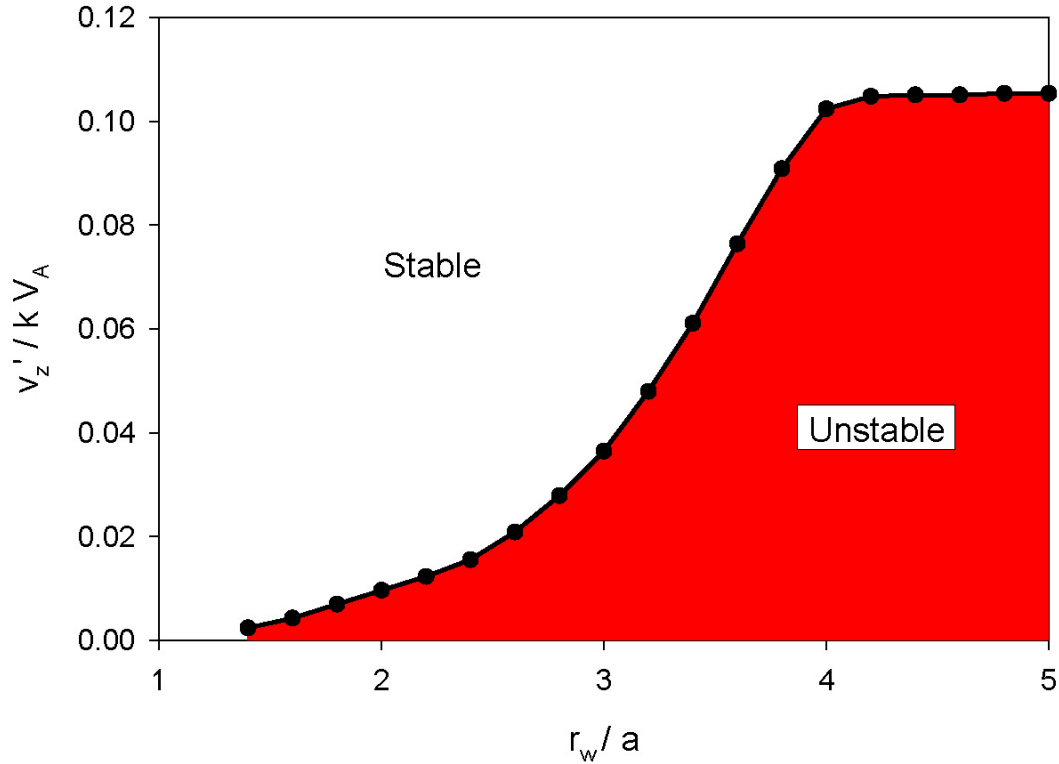


Figure 1.6: Threshold of Z-pinch stability. Without sheared flow, a conducting wall must be very close $r_w/a = 1.2$ to provide Z-pinch stability, where a is the characteristic radius of the pinch. As sheared flow is increased, the wall can be moved further away and stability can be maintained until the sheared flow can provide stabilization without a conducting wall. The limit for this is $v'_z > 0.1kV_A$.

flowing at some velocity, v_{inner} , and an outer annulus of plasma flowing at a different velocity, v_{outer} , relative to the inner cylinder. If both regions of the column are assumed to have the same initial instabilities as a function of axial location, the difference in flow velocities of the two regions will result in a mixing of the modes which destructively interfere with the mode's continued growth. A schematic of this concept is shown in Fig. 1.7.

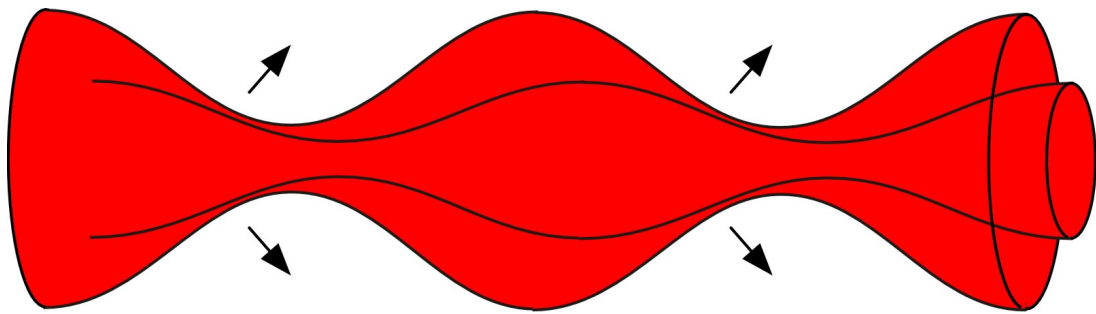


Figure 1.7: Schematic of destructive interference of instabilities. If the instability exists in both the interior column of plasma and in an annulus of plasma that is moving with a velocity relative to the interior column, the instabilities will interfere, negating them.

Chapter 2

FLOW SHEAR STABILIZATION AND THE ZAP FLOW Z-PINCH**2.1 Previous Z-Pinch Experimentation**

The origins of the ZaP Flow Z-pinch are found in the coaxial accelerator work performed in the 1950's and 1960's. In 1959, Marshall experimented with a coaxial acceleration geometry, referred to as a plasma gun, in which hydrogen plasma was injected into the plenum of the gun and allowed to expand. A 200 kA peak current was produced and the plasma had an axial flow velocity $v_z \approx 1.5 \times 10^5$ m/s. Spectroscopic evidence suggested that these conditions could be produced without detaching material from the electrodes [5]. D.Y. Cheng at Santa Clara also performed plasma acceleration studies on a coaxial gun experiment. That work was modelled as a deflagration process in which the deflagration wave front travels in the direction opposite the plasma with the result being an acceleration of the plasma in an expansion wave. Directed energies of 10-30 keV were produced [6].

2.2 The ZaP Flow Z-Pinch

The ZaP Flow Z-Pinch is a basic plasma physics experiment that investigates the use of sheared axial flows to maintain gross stability of a Z-pinch plasma. The geometry, shown in Figure 2.1, is a coaxial acceleration region coupled to a one meter pinch assembly region. Note the plane labeled $z = 0$ cm. This is the location of many of the diagnostic measurements that are presented. Locations upstream of this plane are identified as a negative z -location and locations downstream are identified as a positive z -location. The outer electrode is approximately twice the length of the inner electrode and terminates with an end-wall that has a 5 cm diameter hole to reduce flow stagnation. The outer electrode has an inner diameter of 19.36 cm with eight neutral-gas injection valves azimuthally-spaced at $z = -75$ cm (approximately half the length of the inner electrode) that inject gas radially

inward. The original inner electrode has a diameter of 10 cm with one neutral-gas injection valve with eight outlet holes aligned with the outer gas injection valves to inject gas radially outward.

Formation of a flowing Z-pinch is accomplished in the following manner. A capacitor bank is charged to a pre-determined voltage. Neutral gas is radially injected between the electrodes from the eight azimuthal locations and allowed to expand. The capacitor bank is discharged across the electrodes, ionizing the gas. The ionized gas can now conduct current and the current flows from the outer electrode to the inner electrode. The current creates a magnetic field and the two interact with one another, creating an axially-directed Lorentz force which pushes the plasma along the electrodes. The force is greater near the inner electrode resulting in a snowplow-type plasma acceleration. When the current sheet reaches the end of the inner electrode, the current connection on the inner electrode assembles onto the axis while the current connection on the outer electrode continues along the outer electrode until it reaches the end-wall. As the current sheet continues along the outer electrode, the length of the sheet continues to assemble onto the axis until a pinch with a one-meter length is formed that has an embedded radially-varying axial flow. Remaining gas in the acceleration region is continually ionized and accelerated into the pinch, replacing plasma that escapes through the end-wall. Table 2.1 shows typical ZaP operating parameters with the 10 cm inner electrode.

2.3 Diagnostics on the ZaP Flow Z-Pinch

2.3.1 Surface-Mounted Magnetic Probes

ZaP measures the magnetic fields throughout the experiment with arrays of surface-mounted magnetic probes. The probes consist of ten windings of copper wire around a Kel-F form. The probes observe a changing magnetic field which produces a voltage in the coil according to Faraday's Law [7],

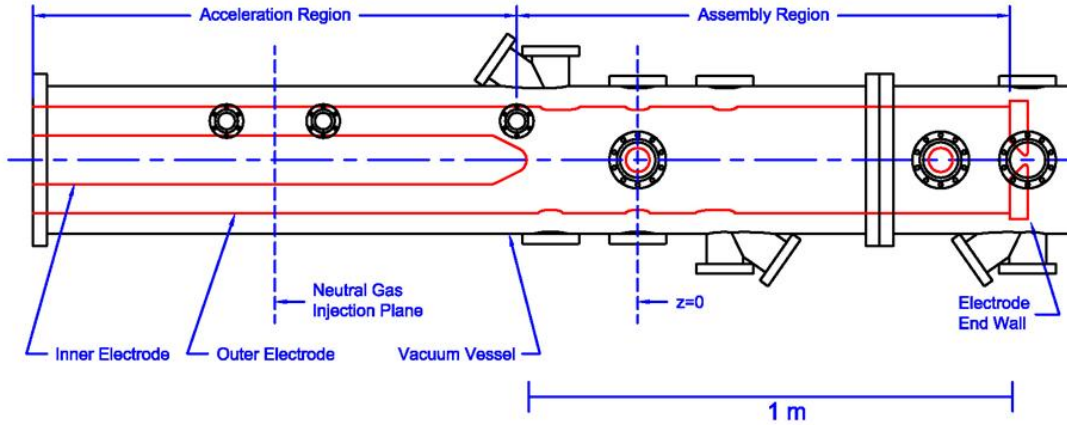


Figure 2.1: ZaP Flow Z-Pinch Geometry. ZaP consists of a one meter coaxial acceleration region coupled to a one meter pinch assembly region. Gas is injected radially at a location half the length of the acceleration region. The majority of measurements are made at the $z = 0$ cm plane. A one meter scale is included for reference.

Table 2.1: ZaP Operating Conditions with 10 cm Diameter Inner Electrode .

Parameter	Value
Pinch Radius, a (cm)	1
Pinch Length (cm)	100
Peak Current (kA)	200-250
Electron Density (m^{-3})	10^{22} - 10^{23}
T_e, T_i (eV)	75 - 125
Magnetic Field (T)	1-2
Pinch Duration (μs)	20-60

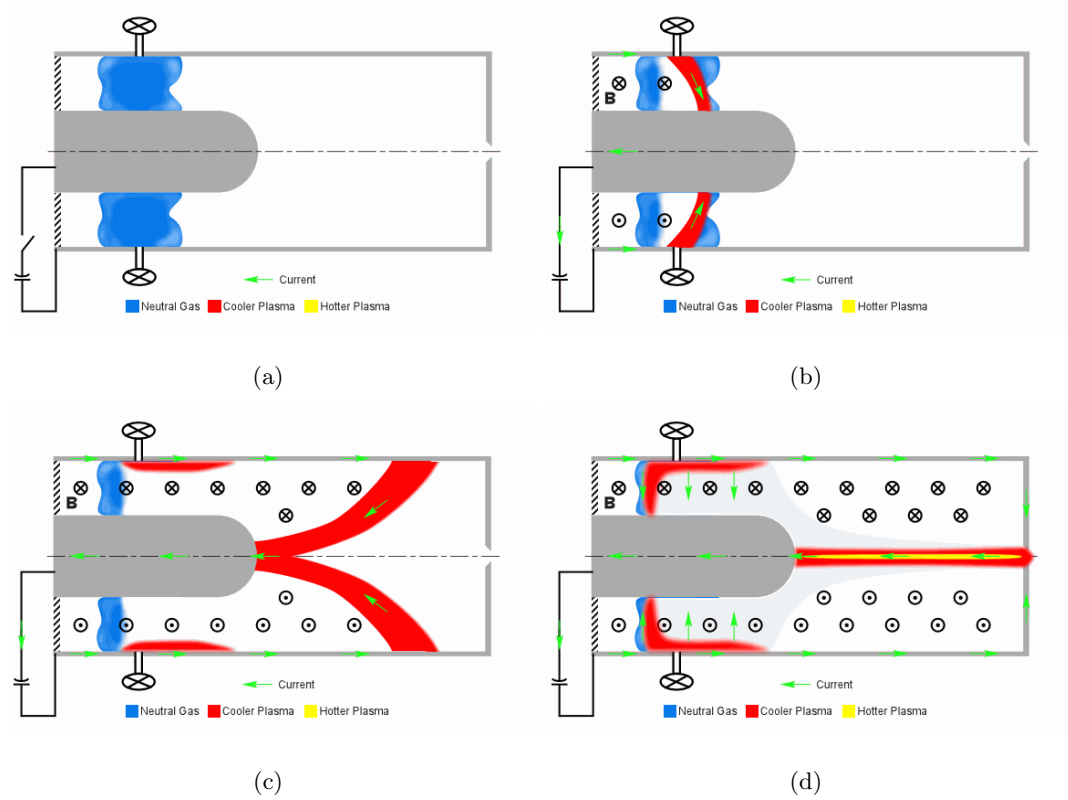


Figure 2.2: Formation sequence in a flow Z-pinch. (a) Neutral gas is injected radially between the electrodes and allowed to expand. (b) Voltage is applied across the electrodes, ionizing the gas. Current flows in the plasma from the outer to the inner electrode. $\mathbf{j} \times \mathbf{B}$ force accelerates plasma axially towards the assembly region. (c) Upon reaching the end of the inner electrode the Z-pinch begins to assemble on the axis. Current flowing in the Z-pinch generates an azimuthal magnetic field which pinches down on the plasma column until force balance is achieved. The current contact at the outer electrode continues to flow until it reaches the end-wall. (d) The plasma is fully assembled into a high-density, high-temperature Z-pinch with an embedded axial flow. Neutral gas remaining in the acceleration region continues to ionize and flows into the pinch, maintaining the flow shear.

$$\oint_c \mathbf{E} \cdot d\mathbf{l} = - \int_s \dot{\mathbf{B}} \cdot d\mathbf{s} \quad (2.1)$$

where \mathbf{E} is the electric field in the coil and $\dot{\mathbf{B}}$ is the time-varying magnetic field inside the coil. The voltage can be integrated with an analog integrator, producing a digitized voltage,

$$V_0 = \frac{NAB}{RC} \quad (2.2)$$

where V_0 is the measured voltage, N is the number of probe windings, A is the area of the probe, B is the average field over the area of the probe and R and C are the resistance and capacitance of the integrator.

An axial array of probes is located from $z = -120$ cm to $z = 109$ cm. Two of the probes are located at $z = -120$ cm and $z = -100$ cm and the probes from $z = -80$ cm to $z = 20$ cm are located every five cm. A probe array is located at $z = 31$ cm and probes are spaced every five cm from $z = 69$ cm to $z = 109$ cm. This axial array is used to determine the current distribution in the experiment.

Five azimuthal arrays of eight surface-mounted magnetic probes are located at $z = -25$, $z = 0$, $z = 31$, $z = 69$ and $z = 109$ cm. The azimuthal arrays are used to determine the stability characteristics of the pinch at those locations. Fourier decomposition of the data yields the azimuthal Fourier modes, (B_m) . The $m = 0$ mode is the average magnetic field measured by the probes. $m = 1$ indicates the radial offset of the current centroid from the axis of the machine. $m = 2$ is a measure of the ellipticity of the current distribution and $m = 3$ is the triangularity of the current distribution. $2m + 1$ probes are required to measure each Fourier mode, therefore eight probes limits the measurement to the $m = 3$ mode.

The azimuthal magnetic probe arrays are used to determine the stability criterion in ZaP. The stable (quiescent) period in ZaP is defined as the period of time for which the normalized $m = 1$ mode, (B_1/B_0) , is below 0.2. This value indicates a radial offset of the current centroid of 1 cm. An example of this criterion is shown in Figure 2.3 along with the average magnetic field, B_0 .

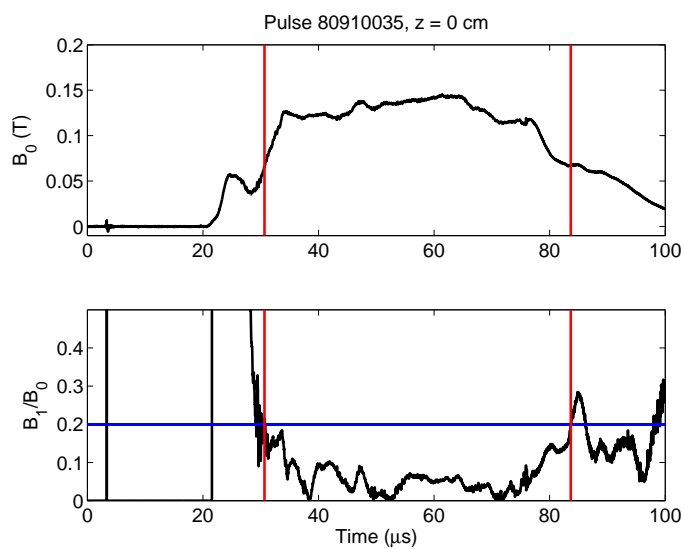


Figure 2.3: Example of the ZaP stability criterion. Top plot is the average magnetic field as a function of time at $z = 0$ cm. The bottom plot is the normalized $m = 1$ mode data as a function of time. This indicates the radial offset of the current centroid from the machine axis. The horizontal line at $B_1/B_0 = 0.2$ indicates a radial offset of 1 cm. When the data falls below this line, the pinch is considered stable or quiescent.

2.3.2 Interferometry

ZaP utilizes a four-chord Helium-Neon (HeNe) Mach-Zehnder heterodyne, quadrature interferometer for electron density measurements in the experiment. The HeNe laser (6328 Å) enters an acousto-optic modulator (Bragg cell) after which two beams are the result; one at the original laser frequency and one with a 40 MHz offset. For each individual chord, one of these beams passes through the experiment and the plasma (scene beam) and the other beam passes above the experiment (reference beam). The electric field of the electrons that the scene beam encounters in the beam has the effect of slowing the phase velocity of the light. The scene and reference beams are then combined and sent to a quadrature detector that measures the phase difference between the beams. This phase difference is directly proportional to the chord-integrated electron density, indicated by Equation 2.3.

$$\phi = \frac{\omega}{2cn_c} \int n_e dl \quad (2.3)$$

where c is the speed of light, ω is the frequency of the laser, n_e is the electron number density, $n_c = \frac{\omega^2 m_e \epsilon_0}{e^2}$ is the cut-off density of the laser, ϵ_0 is the permittivity of free space, e is the elementary electron charge and m_e is the rest mass of an electron.

The difference in the path length of the scene and reference beams must be less than the coherence length of the laser for proper interference. For off-the-shelf HeNe lasers, this coherence length is ≈ 20 cm.

Additional chords for the interferometer are produced by passing the beams through a beam splitter. ZaP has the capability to utilize four chords at various locations on the experiment. These multiple chords are used in a variety of configurations which include four chords at a single z -location at different impact parameters for measurements of the density profile as well as four chords at different axial locations to measure axial variations in the density profile.

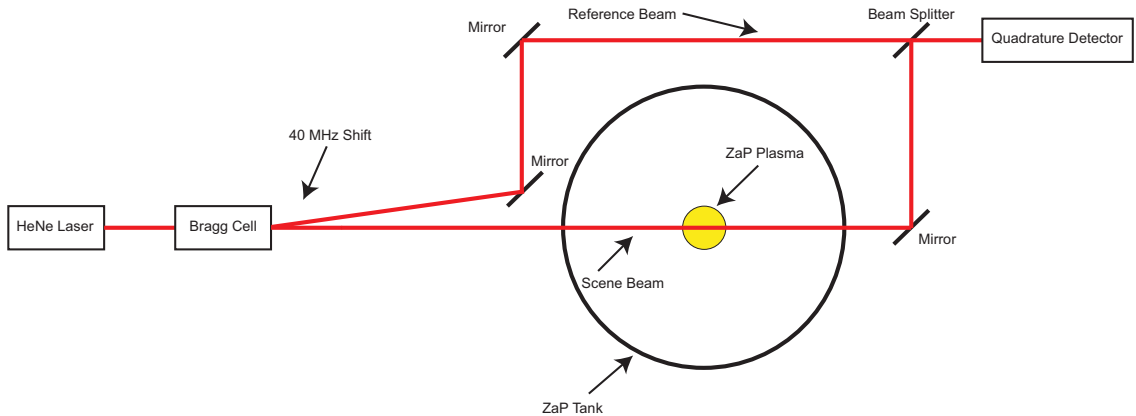


Figure 2.4: Schematic of ZaP HeNe interferometry system. A HeNe laser beam (6328 \AA) enters an acousto-optic modulator (Bragg cell) which produces a second beam with a 40 MHz offset. One beam passes through the experiment and the plasma (scene beam) and the other passes above the experiment (reference beam). The beams are combined and sent to a detector which measures the difference in phase shift.

2.3.3 Empirical Mode Decomposition

The resulting chord-integrated density as a function of time is often subject to high-frequency oscillations as a product of the passage of saturated instabilities in the pinch. For the determination of the density profile of the pinch, these oscillations are not of interest. The chord-integrated density as a function of time is filtered using a process called empirical mode decomposition (EMD) [8]. Interferometry data is assumed to consist of lower frequency “mean” behavior with high-frequency oscillations superimposed.

EMD operates by reducing a signal into a series of intrinsic mode functions (IMFs). An IMF is a function that satisfies the conditions that the mean value of the function defined by the local maxima and minima is zero and that the number of zero crossings and extrema are equal or differ by no more than one. EMD progresses in a process called sifting in which the IMFs are separated based on their characteristic time scales which are defined by the time lapse between successive extrema.

The first IMF identified is the highest frequency IMF. It is subtracted from the original

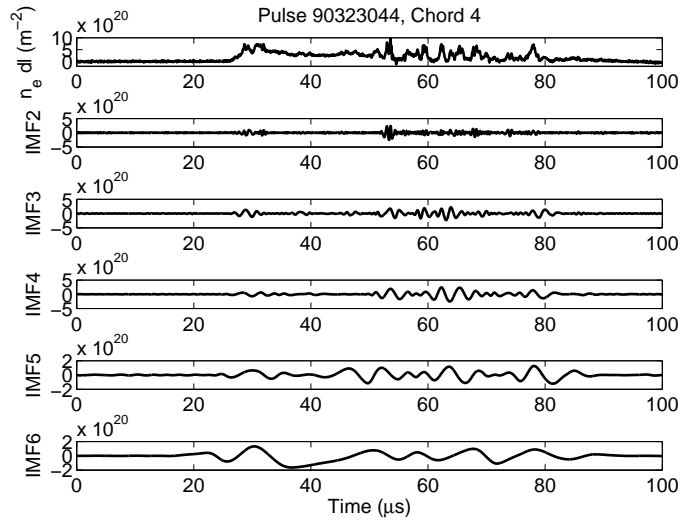


Figure 2.5: Intrinsic mode functions. Empirical mode decomposition breaks down the original signal (top plot) into a series of intrinsic mode functions by defining the highest frequency behavior in the signal as a function of time (first IMF) and subtracting it from the signal. This process continues until a monotonically increasing or decreasing function is the residual. It is observed that each IMF has a changing frequency and amplitude as a function of time.

signal after it is determined and then the sifting process continues on the residual (i.e. original signal without first IMF). This process continues until the remaining residual is either monotonically increasing or decreasing or a constant. Summing all of the resultant IMFs including the monotonic residual returns the original signal. An example of an IMF series from interferometry data is shown in Figure 2.5. Note that as the IMF number increases the frequency of the oscillations decreases.

EMD is used as a filter on ZaP interferometry data by summing all IMFs except for the highest frequencies (IMFs 1-3). The resulting signals retain the mean behavior of the chord-integrated density without high-frequency oscillations. An example of a filtered interferometer signal is shown in Figure 2.6

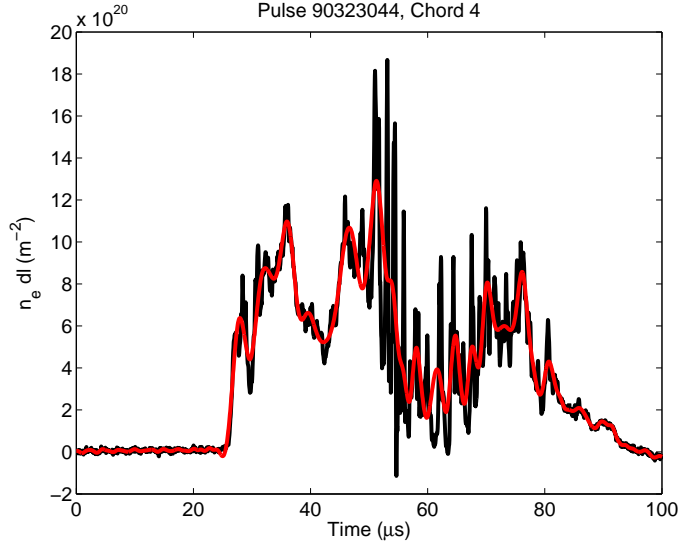


Figure 2.6: Empirical-mode decomposition filtered interferometer signal. Using EMD, the highest frequency oscillations in the interferometer data, which are correlated with short wavelength traveling saturated instabilities in the pinch, are removed from the signal. The black signal is the original signal and the red is the filtered signal.

2.3.4 Doppler Spectroscopy

The ZaP plasma emits radiation through a number of different processes including bremsstrahlung radiation and line radiation. Bremsstrahlung radiation is a result of free electron in the plasma undergoing Coulomb collisions with ions. These Coulomb collisions result in a changing trajectory and a deceleration of the electrons. The electrons emit radiation as a result of this deceleration, as shown in Figure 2.7. Bremsstrahlung radiation is broadband radiation that is dependent on the temperature and density of the plasma [9]

$$P_{\text{Brem}} = 1.69 \times 10^{-38} Z_{\text{eff}}^2 n_e^2 T_e^{1/2} \quad (2.4)$$

where Z_{eff} is the effective charge state, n_e is the electron number density and T_e is the electron temperature.

Line radiation is a result of bound electrons in the plasma moving from a higher energy

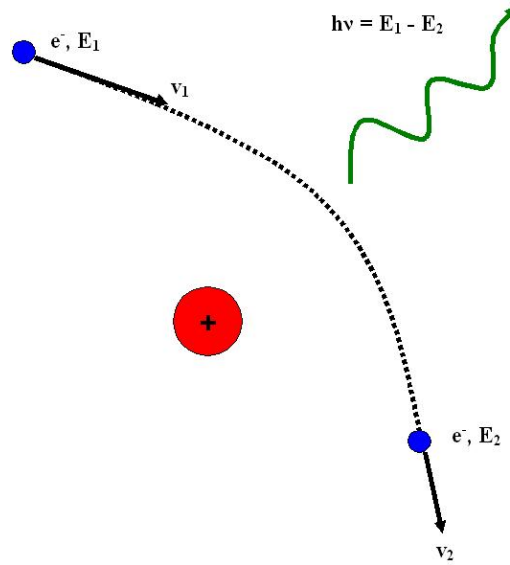


Figure 2.7: Schematic of bremsstrahlung radiation process. Free electrons undergo small-angle collisions with more massive ions. The collisions slow the electrons and change their trajectory. The deceleration of the electrons results in photon emission from the electron.

level in an atom to a lower energy level, as shown in Figure 2.8. The wavelength of the radiation is proportional to the difference in energy of the two levels and is well predicted by atomic physics,

$$\Delta E = h\nu \quad (2.5)$$

where ΔE is the difference in energy between the level from which the electron started and the level at which it ended, h is Planck's constant and ν is the frequency of the emitted radiation.

ZaP uses a 20-chord imaging spectrometer with an intensified charge-coupled device (ICCD) camera to evaluate the line radiation from impurity ions in the plasma. The fiber-optic collects light from $z = 0$ cm through either a radial-viewing telescope or a telescope on a 35° viewport. The radial-viewing port is used to measure the ion temperature profiles at a single time by measuring the Doppler broadening of the impurity radiation. Doppler

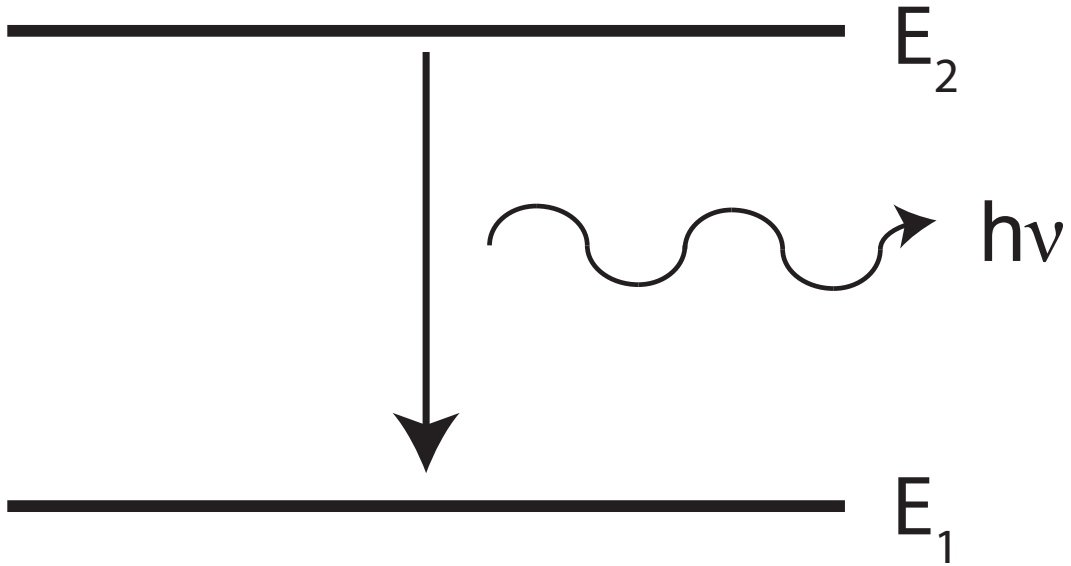


Figure 2.8: Schematic of line radiation process. Electrons bound to ions transition from a higher energy level to a lower energy level. A photon is emitted which has an energy equal to the difference in energy between the two levels.

broadening is a consequence of the random thermal motion of the ions. Ions moving away from the observer emit radiation that would appear to have a lower frequency, resulting in a red shift of the line, as shown in Figure 2.9. Ions moving toward the observer emit radiation that would appear to be blue shifted, as shown in Figure 2.10. The shift in the frequency of the radiation is proportional to the velocity,

$$\nu' = \nu_0 \left(\frac{1}{1 + \frac{v}{c}} \right) \quad (2.6)$$

where ν' is the Doppler-shifted frequency, v is the velocity of the ions and c is the speed of light. For small shifts, $\frac{\Delta\nu}{\nu} = \frac{\Delta\lambda}{\lambda}$ and Equation 2.6 becomes

$$\lambda' = \lambda_0 \left(1 + \frac{v}{c} \right) \quad (2.7)$$

where λ' is the Doppler-shifted wavelength.

Emitting Atom

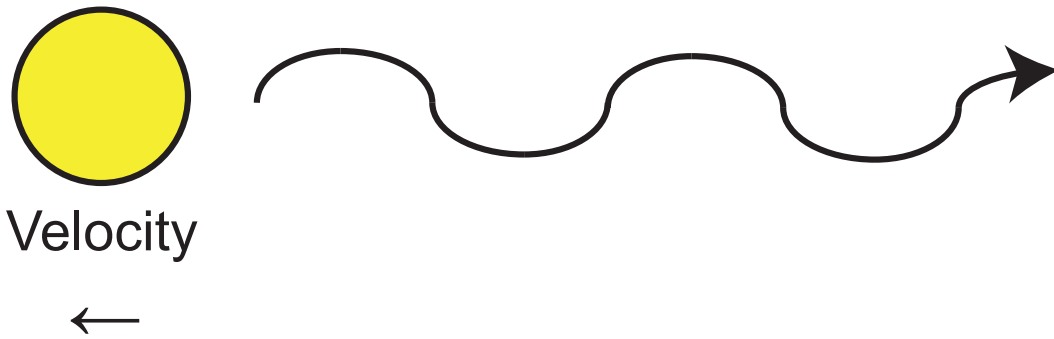


Figure 2.9: Schematic of red shift. A particle moves away from the observer and emits a photon. A lower frequency is observed at the detector, resulting in a red-shifted line.

Emitting Atom

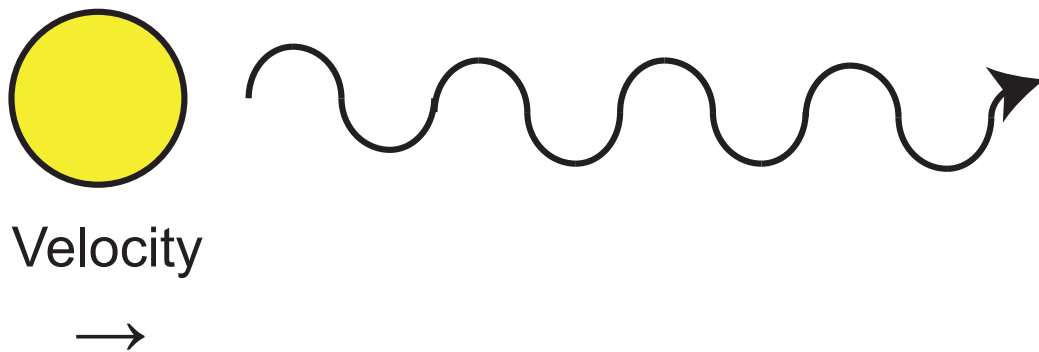


Figure 2.10: Schematic of blue shift. A particle moves toward the observer and emits a photon. A higher frequency is observed at the detector, resulting in a blue-shifted line.

The resulting shape of the emission in wavelength space as a result of this Doppler broadening is a Gaussian distribution and the full-width at half maximum (FWHM) of the distribution is proportional to the temperature

$$\Delta\lambda = \sqrt{\frac{8k_B T \ln 2}{m_i c^2}} \lambda_0 \quad (2.8)$$

where $\Delta\lambda$ is the FWHM of the distribution, $k_B = 1.6 \times 10^{-19}$ J/eV is Boltzmann's constant, T is the ion temperature in eV, m_i is the rest mass of the ion and λ_0 is the ideal wavelength of the emission.

The oblique-viewing port is used to measure the axial velocity profile at a single time. The bulk axial velocity of the ions in the plasma results in a Doppler-shifted emission line. The resulting axial velocity of the ions can be calculated by measuring the shifted centroid of the line emission and using Equation 2.7. The ICCD can be gated down to a collection time of 50 ns. The gate should be as short as possible in order to remove the effects of bulk motion or turbulence in the plasma, but long enough that sufficient intensity is measured.

2.3.5 Thomson Scattering

To measure the temperature of the free electrons in the plasma, Thomson scattering is used. The ZaP Thomson-scattering system utilizes a ruby laser (6943 Å) which is fired into the experiment at $z = 0$ cm. The electrons are influenced by the oscillating electric field of the laser. The effect of the magnetic field can be neglected if the electrons are non-relativistic. The oscillating electrons emit radiation at the same wavelength as the laser as shown in Figure 2.11. The ZaP Thomson-scattering system collects light through a vertical viewport at $z = 0$ cm as shown in Figure 2.12. Optical fibers send the collected light to a spectrometer which separates the light onto photomultiplier tubes (PMTs). These PMTs measure the intensity of the light as a function of wavelength. The random thermal motion of the electrons broadens the spectrum of the emitted radiation into a Gaussian shape in the case of ZaP and the width of this spectrum as a function of wavelength is proportional to the temperature of the electrons.

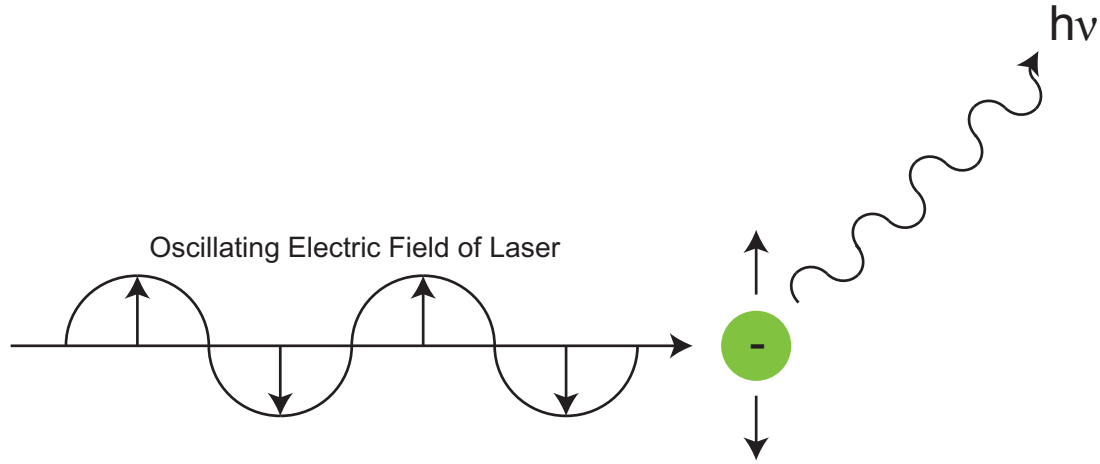


Figure 2.11: Schematic of Thomson scattering effect. A laser is sent into the plasma and the free electrons interact with the oscillating electric field. The resulting oscillations of the electrons reemit photons at the same wavelength as the laser.

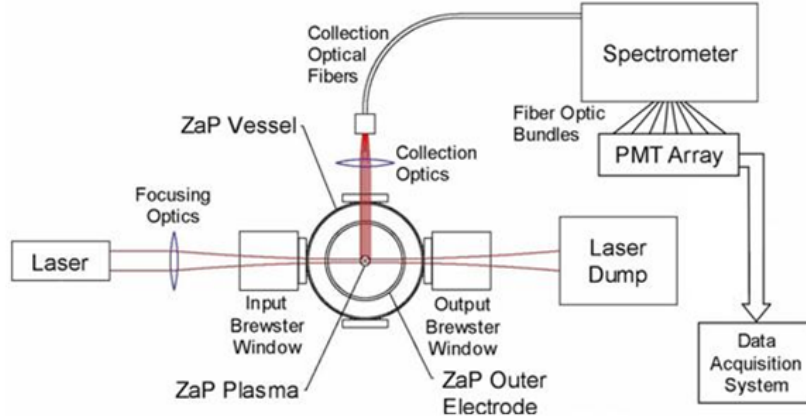


Figure 2.12: Schematic of Thomson-scattering system. The ZaP Thomson scattering system utilizes a ruby laser (6943 \AA) which is fired into the vacuum chamber at $z = 0 \text{ cm}$. The free electrons in the plasma are affected by the oscillating electric field of the laser and their resulting oscillations cause them to emit radiation at the laser frequency. The emitted radiation is collected through the vertical port and transmitted to a spectrometer through optical fibers. The spectrometer spreads the light onto an array of photomultiplier tubes as a function of wavelength. The width of the emitted radiation as a function of wavelength is proportional to the electron temperature.

ZaP Thomson scattering is capable of measuring the electron temperature at two locations (separated by 5 mm) at a single time during a pulse. These measurements can be made concurrently with Doppler spectroscopy measurements to provide a direct comparison of the electron and ion temperatures.

2.3.6 Fast-Framing Camera

Visible light emission from the plasma is imaged using an Imacon fast-framing camera. The camera uses Polaroid film and can produce one image every 200 ns. Another framing unit can be used that produces one image every 1 μ s. The images from the fast-framing camera are used to evaluate gross motion of the plasma, as well as the approximate size of the pinch. The images coupled with other diagnostics such as the interferometer or magnetic probe arrays can produce additional insight into the plasma behavior.

2.3.7 Application of EMD to Fast-Framing Camera Images and Interferometry

The optical images taken by the fast-framing camera in some cases indicate the existence of flowing, saturated instabilities in the plasma. The oscillations in the interferometry signals can be correlated with the observed instabilities using empirical mode decomposition.

Each of the IMFs from the interferometry signals has an instantaneous frequency and amplitude that can be determined by performing a Hilbert transform, $y(t) = H(x(t))$, on each IMF.

$$y(t) = \frac{1}{\pi} P \int_{-\infty}^{\infty} \frac{x(\tau)}{t - \tau} d\tau \quad (2.9)$$

where P signifies the Cauchy principal value of the integral. A complex analytic signal, $z(t)$, can now be written

$$z(t) = x(t) + iy(t) \quad (2.10)$$

which can be expressed as

$$z(t) = x(t) + iy(t) = A(t) \exp(i\psi(t)) \quad (2.11)$$

where $i = \sqrt{-1}$ and $A(t)$ is the instantaneous amplitude of $z(t)$

$$A(t) = |x(t) + iy(t)| \quad (2.12)$$

and $\psi(t)$, is the instantaneous phase

$$\psi(t) = \tan^{-1} \frac{y(t)}{x(t)} \quad (2.13)$$

The instantaneous frequency, $\omega(t)$, can then be defined as

$$\omega(t) = -\frac{d}{dt}\psi(t) \quad (2.14)$$

Instantaneous frequency is not a well-defined quantity for an arbitrary analytic signal, however, $\omega(t)$ is well-defined for an IMF by construction. The instantaneous amplitude and frequency are plotted as a function of time with a scatter plot as shown in Figure 2.14. These values are related to the observed saturated instabilities in the Imacon images.

Figure 2.15 presents Imacon images taken between $t = 75 \mu\text{s}$ and $t = 76.4 \mu\text{s}$ showing a traveling kink instability with an approximate wavelength of 3 cm, an axial flow velocity of $\approx 5 \text{ cm}/\mu\text{s}$. The expected frequency of density oscillations is $f \approx 1.67 \text{ MHz}$. The scatter plots for the interferometry chord in Figure 2.14 indicate strong oscillations at approximately $t = 76 \mu\text{s}$ in the range of 1-2 MHz. This is in reasonable agreement with the Imacon images.

2.4 Shear Flow Stabilization and the Effects of Viscosity on the ZaP Flow Z-Pinch

A quiescent period is observed in the ZaP Flow Z-Pinch that is coincident with a sheared axial flow profile and density and radial current in the acceleration region. Figure 2.16 shows normalized $m = 1$ data from the azimuthal magnetic probe array at $z = 0 \text{ cm}$, magnetic field data from the axial magnetic probe array in the acceleration region ($z = -120 \text{ cm}$

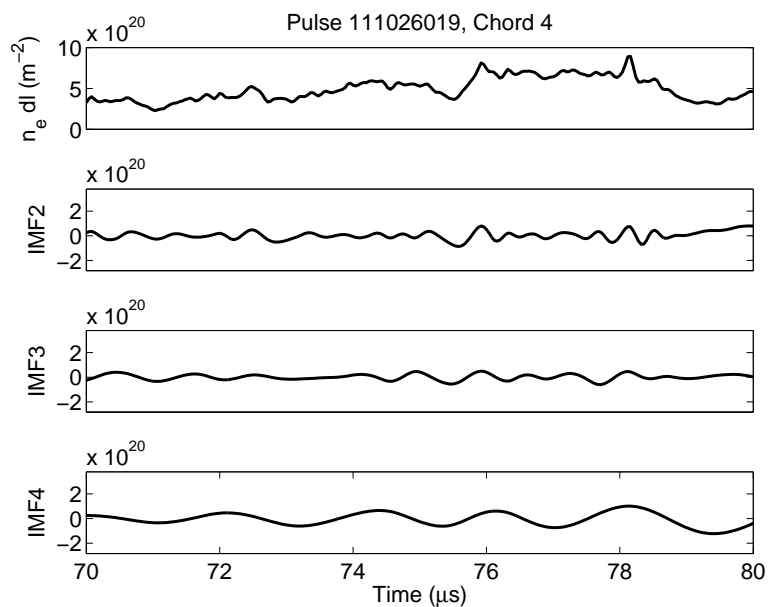


Figure 2.13: Intrinsic mode functions of interferometry data related to an Imacon image. For this plasma pulse, the interferometer and fast-framing camera are located at $z = 0$ cm. The Imacon image indicates a saturated kink mode that is traveling axially. Decomposing the interferometry data around this time leads to additional information after performing a Hilbert transform on the intrinsic mode functions.

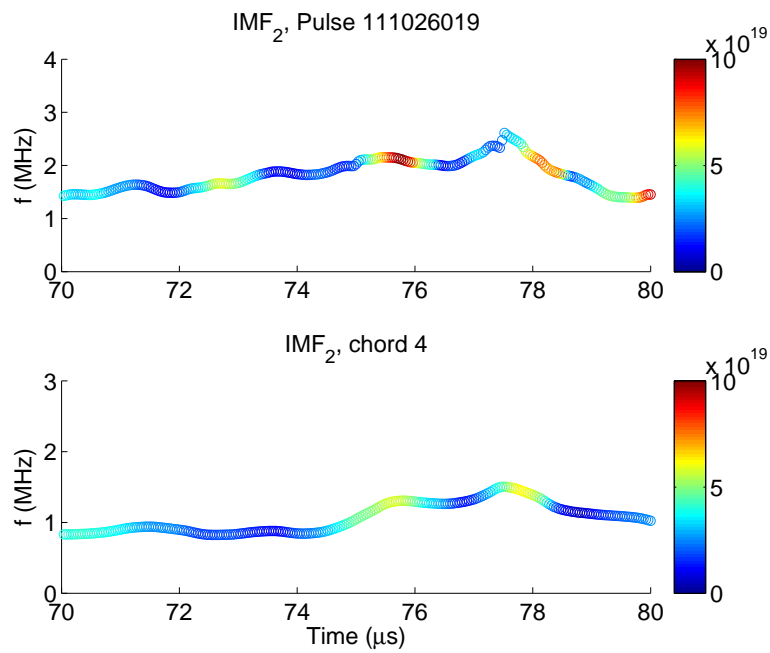


Figure 2.14: Hilbert transform of intrinsic mode functions produces instantaneous frequency and amplitude. The instantaneous frequencies of IMFs 2 and 3 for a single chord of interferometry (color indicates instantaneous amplitude) indicate that near $75 \mu\text{s}$ there are large amplitude oscillations in the signal between 1 and 2 MHz.

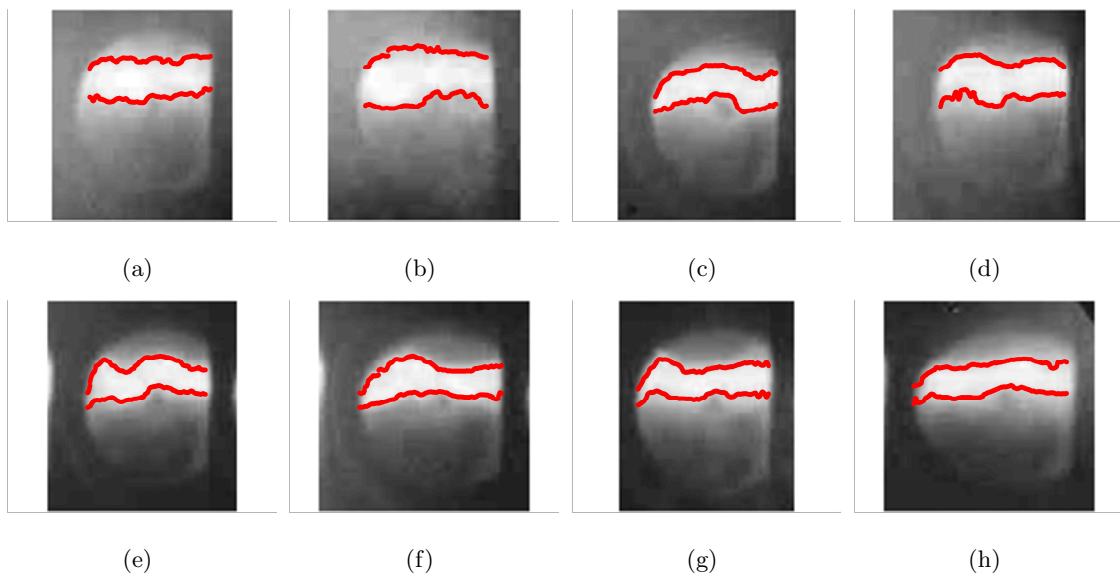


Figure 2.15: Visible light images from an Imacon 790 fast-framing camera showing a traveling saturated kink instability. The images begin at $75 \mu\text{s}$ and the time between images is 200 ns . The diameter of the hole in the electrode in the images is 5 cm . Estimating the wavelength of the kink as $\approx 3 \text{ cm}$ with a flow velocity of $\approx 5 \text{ cm}/\mu\text{s}$, the frequency of expected density oscillations is $f \approx 1.67 \text{ MHz}$. This estimated frequency is in reasonable agreement with the empirical mode decomposition of the density signal. Flow direction is from the right to the left. The red symbols indicate 75% of the maximum intensity.

to $z = -30$ cm) and electron density from interferometry at the exit of the acceleration region ($z = -25$ cm). A quiescent period is indicated in the normalized $m = 1$ data. The end of the quiescent period is marked by increased magnetic and frequency of the magnetic fluctuations in the $m = 1$ data. This quiescent period is coincident with a gradient in the magnetic field as function of axial location, $\partial B/\partial z$, which indicates a radial flow of current between the probe locations. The values of the magnetic field converge prior to the end of the quiescent period. Similarly, during the quiescent period, significant density is flowing out of the acceleration region which drops prior to the end of the quiescent period. The time difference between these phenomena and the end of the quiescent period is due to the flow velocity of the plasma.

Figure 2.17 shows a contour plot of the axial velocity measured with Doppler spectroscopy at $z = 0$ cm as a function of radius and a normalized time, τ . τ is defined such that $\tau = 0$ corresponds to the beginning of the quiescent period and $\tau = 1$ corresponds to the end of the quiescent period. The plot at the bottom is the normalized $m = 1$ mode data as a function of τ . The points in the plot are the values of the normalized $m = 1$ mode data during the gating time of the ICCD. The velocity profile prior to the beginning of the quiescent period is high and uniform as a function of radius. At the beginning of the quiescent period, the velocity near the axis is reduced and remains high near the edge. At $\tau \approx 0.5$, the flow profile reverses, coincident with a temporary increase in normalized $m = 1$ mode data, such that the velocity near the axis is higher than the edge. The velocity profile becomes low and uniform after the quiescent period. Flow velocities during the quiescent period are $v_z \approx 5 - 10$ cm/s. The direction of the flow shear is not important to the stability.

The flow profile is uniform near the axis of the pinch and the flow shear is localized near the edge. This flow profile and the observed length of the pinch (> 100 cm) is consistent with the predictions from classical viscosity calculations. Near the axis of the pinch, density is high and magnetic field is low resulting in high collisionality and correspondingly high cross-field viscosity. This high viscosity has the effect of flattening the velocity profile. Further from the axis, the density is reduced and the magnetic field is increased,

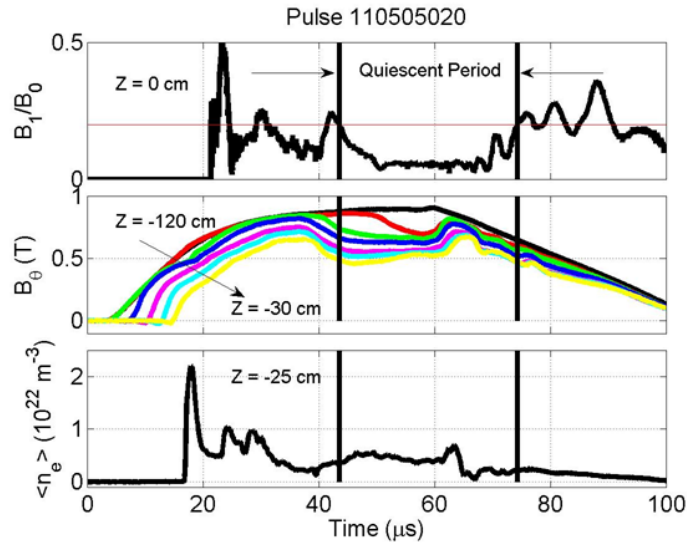


Figure 2.16: End of the quiescent period is coincident with drop in current and density in acceleration region. The quiescent period is defined as the period when the magnetic mode data drops to low magnitude with a reduction in the magnetic fluctuations. During the quiescent period, radial current persists in the acceleration region as defined by the gradient in the azimuthal magnetic field as a function of axial location. Prior to the end of the quiescent period at $z = 0$ cm, the radial current drops and the density flowing out of the acceleration region drops noticeably. The time lapse between the drop of current and density and the end of the quiescent period is a consequence of the flow velocity of the plasma.

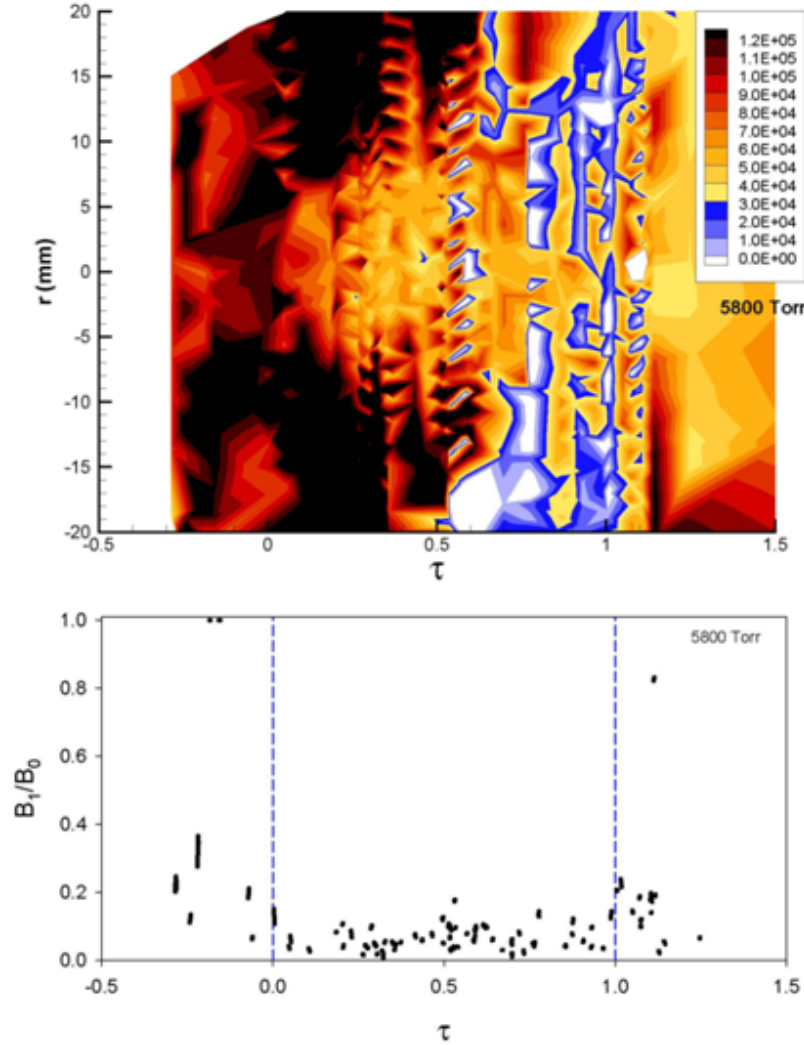


Figure 2.17: Flow profile is correlated with plasma stability. Top plot is contours of axial velocity as a function of radius and time normalized to the length of the quiescent period, τ . The beginning of the quiescent period is $\tau = 0$ and the end of the quiescent period is $\tau = 1$. The bottom plot is the normalized $m = 1$ data during the exposure time of the 20-chord imaging spectrometer. Prior to the quiescent period the flow velocity is high and uniform as a function of radius. When the quiescent period begins the flow velocity is higher near the edge of the pinch. Towards the end of the quiescent period, the flow profile reverses and the flow velocity becomes lower near the edge of the pinch. At the end of the quiescent period the flow velocity is low and uniform as a function of radius.

resulting in a magnetized plasma with a greatly reduced cross-field viscosity which allows a sheared flow profile to develop. The viscous damping time is underestimated if the effects of magnetization are ignored.

Figure 2.18 shows calculations of the unmagnetized and magnetized viscous damping times for a pinch with a Bennett equilibrium profile with a uniform temperature of $T = 100$ eV, $I_0 = 250$ kA and a characteristic radius, $a = 1$ cm. The Bennett equilibrium is

$$B_\theta = \frac{\mu_0 I_0}{2\pi} \frac{r}{r^2 + a^2} \quad (2.15)$$

$$j_z = \frac{I_0}{\pi} \frac{a^2}{(r^2 + a^2)^2} \quad (2.16)$$

$$p = \frac{\mu_0 I_0^2}{8\pi^2} \frac{a^2}{(r^2 + a^2)^2} \quad (2.17)$$

The top plot shows the profiles of density and magnetic field as a function of radius. The middle plot is the ratio of the ion cyclotron frequency, ω_{ci} , to the ion-ion collision frequency, ν_{ii} , which indicates the degree of magnetization of the particles. If the ratio is much less than 1, the particle behavior is dominated by collisions. If the ratio is much greater than 1, the particle behavior is dominated by their gyration about the magnetic field line. It is clear from this plot that the particles become magnetized close to the axis ($r \approx 0.3$ cm). The bottom plot is the unmagnetized and magnetized viscous damping times. The sheared-flow viscous damping time is approximated as

$$\tau \simeq \frac{\rho L_v^2}{\mu} \quad (2.18)$$

where ρ is the mass density, L_v is the velocity-shear scale length and μ is the plasma viscosity. μ is defined in Spitzer [10] for two regimes of the ratio, ω_{ci}/ν_{ii} . For $\omega_{ci}/\nu_{ii} \ll 1$

$$\mu = 2.21 \times 10^{-15} \frac{T^{\frac{5}{2}} A_i^{\frac{1}{2}}}{Z^4 \ln \Lambda} \quad (2.19)$$

and for $\omega_{ci}/\nu_{ii} \gg 1$

$$\mu_{\perp} = 2.68 \times 10^{-26} \frac{A_i^{\frac{3}{2}} Z^2 n_i^2 \ln \Lambda}{T_i^{\frac{1}{2}} B^2} \quad (2.20)$$

where A_i is the atomic weight and the units are defined in cgs-K. If the unmagnetized viscosity is used, viscous damping times are on the order of 100's of ns which would prevent the generation of a sheared-flow profile. In ZaP, the on-axis magnetic field is $B_{\theta} = 0$, but it increases as a function of radius and the density decreases significantly resulting in a magnetized plasma a short distance from the axis. At $r = a = 1$ cm, the viscous damping time is on the order of $5 \mu\text{s}$ and is greater than $10 \mu\text{s}$ at $r = 1.5$ cm for an experimentally observed sheared-flow scale length, $L_v \approx 0.3$ cm. These values for the viscous damping time are consistent with a long-lived stable pinch with a 1 meter length and a flow velocity of 2×10^5 m/s.

2.5 Experimental Modifications on ZaP

Experimental modifications have been conducted on the ZaP Flow Z-Pinch. The original inner electrode on the experiment has a diameter of 10 cm and a single neutral-gas injection valve with eight radial outlets. Another inner electrode is manufactured with a diameter of 16 cm and eight neutral-gas injection valves. This modification is to evaluate the effects of adiabatic compression on the temperature of the pinch by increasing the compression ratio from the acceleration region to pinch formation. Additionally, the increased number of gas injection valves allows greater control of the neutral-gas supply in the experiment. A modification to the outer electrode is performed to evaluate the effects of the conducting outer electrode on the stability of the pinch. A portion of the outer electrode is manufactured that has eight large openings in it, reducing the surface area of the conducting wall by $\approx 70\%$. Stability from a conducting wall is a result of the generation of azimuthal currents in the wall. By removing the conducting wall material, the azimuthal currents are unable to flow. The effects of both of these modifications are considered.

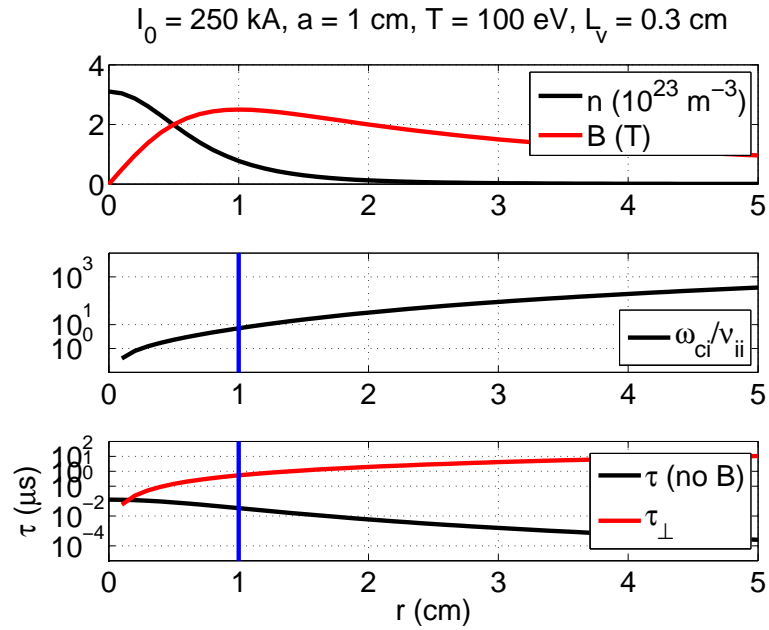


Figure 2.18: Long pinches and sheared flow profiles are consistent with classical viscosity. For a Bennett pinch equilibrium with a 1 cm characteristic radius, a uniform temperature of 100 eV, carrying a current of 250 kA, with a viscous length scale of 0.3 cm, profiles of density and magnetic field are shown in the top plot. The middle plot is the ratio of the ion cyclotron frequency, ω_{ci} , to the ion-ion collision time, τ_{ii} for these conditions. The bottom plot is the viscous damping time for these conditions with and without the consideration of the magnetization of the ions. The data indicate that when magnetization is taken into account the viscous damping time is $\tau_{\perp} \approx 6 \mu\text{s}$. This is consistent with a sheared flow Z-pinch with a 1 meter length with a flow velocity of $2 \times 10^5 \text{ m/s}$.

Chapter 3

OPTIMUM OPERATING CONDITIONS FOR 16 CM INNER ELECTRODE CONFIGURATION

Surveys of the experimental performance after the installation of the 16 cm inner electrode are conducted. Two distinct optimum operating conditions are determined through changes in capacitor bank energy, neutral-gas line pressure and neutral-gas injection time. One operating condition is characterized by a long quiescent period that typically terminates as result of plasma current dropping, referred to as a soft-stop operating condition. The other operating condition is characterized by a magnetic field profile as a function of time that reaches a plateau prior to increasing to a high peak magnetic field, referred to as a high peak magnetic field operating condition.

3.1 Soft-Stop Operating Conditions

The soft-stop operating condition is obtained with a capacitor bank voltage $V_{\text{mb}} = 9$ kV with 8 180 μF capacitors, a neutral-gas line pressure of 3500 torr and a neutral-gas injection time $t = -1.0$ ms relative to capacitor bank discharge. Peak total current in the experiment is $I_p \approx 350$ kA as seen in Figure 3.1 which shows the total current and electrode voltage differential as a function of time.

This condition is characterized by a magnetic field plateau that is coincident with a long quiescent period. The plateau magnetic field at $z = 0$ cm, as shown in Figure 3.2 approaches 0.15 T at the outer electrode wall ($I \approx 70$ kA). The normalized $m = 1$ mode data in the bottom plot of Figure 3.2 indicates that the quiescent period begins prior to the magnetic field plateau and ends after the end of the plateau. The red vertical lines indicate the beginning and end of the quiescent period. The end of the quiescent period is correlated with the end of the current waveform from the capacitor banks as opposed to a decay in the

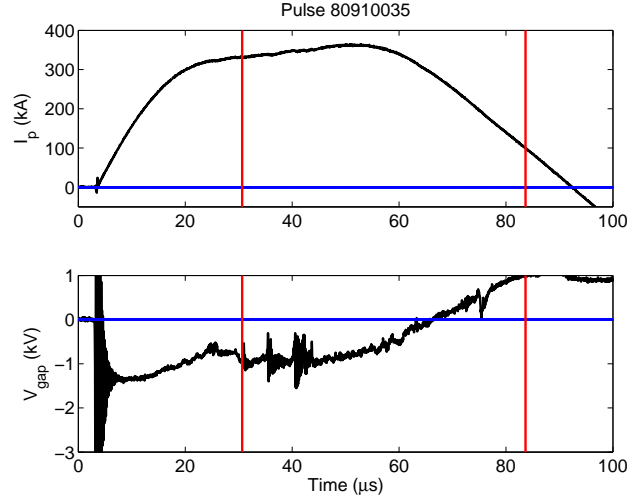


Figure 3.1: Current and voltage waveforms for soft-stop operating condition. Peak current in the experiment with $V_{mb} = 9$ kV on 8 $180 \mu\text{F}$ capacitors is $I \approx 350$ kA. The red vertical lines indicate the beginning and end of the quiescent period.

sheared flow profile. However, axial velocity profiles near the end of the quiescent period could not be obtained due to significantly reduced impurity emission intensity to the ICCD.

Figure 3.3 shows interferometry and magnetic field data in the acceleration region and the normalized $m = 1$ magnetic mode data at $z = 0$ cm. The top plot is the chord-integrated density as a function of time at the exit of the accelerator ($z = -25$ cm), the middle plot are magnetic data from the axial magnetic probe array from $z = -120$ cm to $z = -65$ cm and the bottom plot are the normalized $m = 1$ mode data at $z = 0$ cm. The red vertical lines indicate the beginning and end of the quiescent period. The data indicate that the electron density exiting the accelerator is gradually reduced as the quiescent period progresses. The radial current in the acceleration region also reduces slowly as a function of time during the quiescent period.

The soft-stop operating condition is a robust and repeatable operating condition. The operating condition could be retained in spite of a loss of operation neutral-gas puff valves on both the inner and outer electrodes.

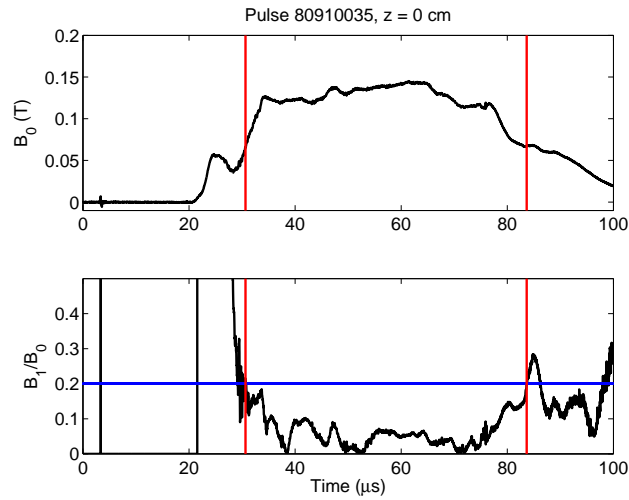


Figure 3.2: Magnetic data at $z = 0$ cm for soft-stop operating condition. Soft-stop operating condition is characterized by a long quiescent period coinciding with a magnetic field plateau at $z = 0$ cm. The end of the quiescent period is correlated with the drop in the current waveform from the capacitor bank. The red vertical lines indicate the beginning and end of the quiescent period.

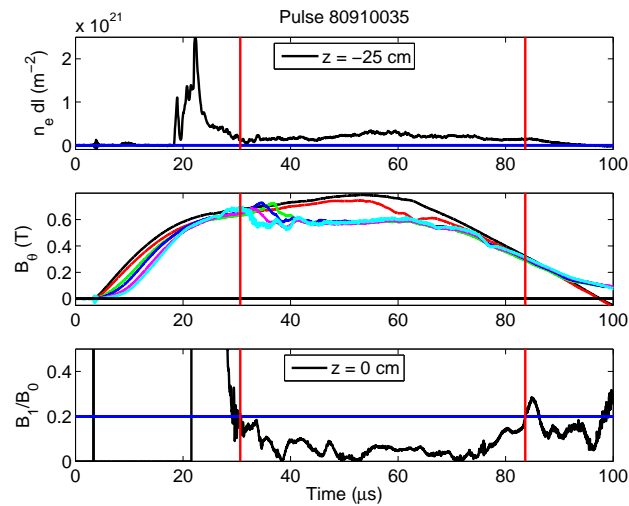


Figure 3.3: Acceleration region data for soft-stop operating condition. Interferometry at the exit of the accelerator indicates a gradual reduction of density as the quiescent period progresses. Similarly, the radial current in the accelerator, $\partial B_\theta / \partial z$ in the middle plot, is gradually reduced as a function of time. The red vertical lines indicate the beginning and end of the quiescent period.

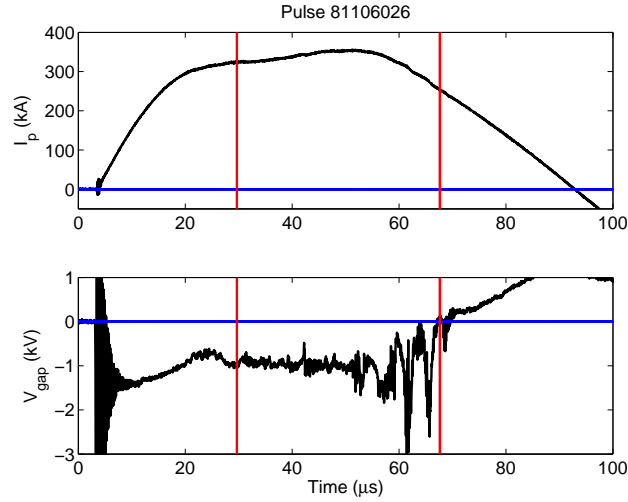


Figure 3.4: Current and voltage waveforms for high peak magnetic field operating condition. The current waveform is similar in magnitude and shape to the soft-stop operating condition, with a peak value of $I \approx 350$ kA. The voltage waveform exhibits a larger voltage differential for a longer period of time than the soft-stop operating condition, but suffers from major voltage fluctuations. The red vertical lines indicate the beginning and end of the quiescent period.

3.2 High Peak Magnetic Field Operating Conditions

The high peak magnetic field operating condition is obtained by reducing the neutral-gas line pressure from 3500 torr to 1500 torr. The capacitor bank voltage is $V_{\text{mb}} = 9$ kV on 8 $180 \mu\text{F}$ capacitors with a neutral-gas injection time of $t = -1.0$ ms relative to the capacitor bank discharge. The current waveform, as seen in Figure 3.4 is similar to the soft-stop operating condition with a peak total current in the experiment of $I_p \approx 350$ kA. The voltage differential on the electrodes stays larger for a longer period of time, but suffers from major voltage fluctuations at $t \approx 60 \mu\text{s}$.

These voltage fluctuations are correlated with a large magnetic field peak at $z = 0$ cm and an increase in the magnetic fluctuations in the normalized $m = 1$ mode data as shown in Figure 3.5. The behavior is characteristic of the high peak magnetic field operating condition as is the magnetic field plateau prior to the field peak. The field peak is often

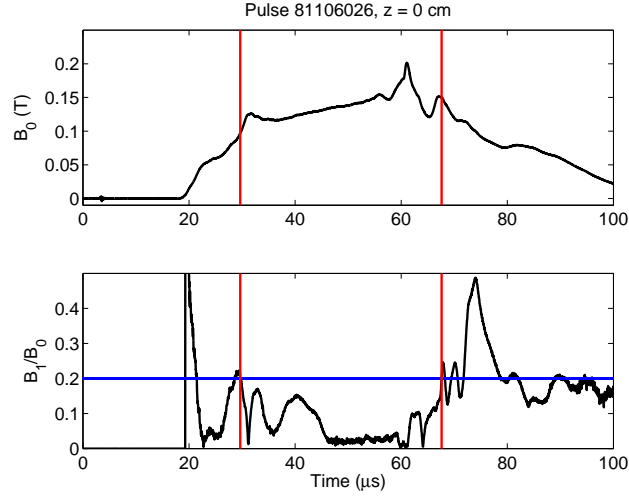


Figure 3.5: Magnetic data at $z = 0$ cm for high peak magnetic field operating condition. The high peak magnetic field operating condition is characterized by a magnetic field plateau preceding a peak in the magnetic field that is often in excess of twice the magnetic field value of the plateau. The field peak is correlated with the end of the quiescent period which typically occurs 1-6 μs afterwards. The red vertical lines indicate the beginning and end of the quiescent period.

in excess of twice the magnetic field value of the plateau. The field peak is also correlated with the onset of instability, which typically occurs 1 – 6 μs after the field peak.

Figure 3.6 shows interferometer and magnetic data in the acceleration region and normalized $m = 1$ magnetic fluctuations at $z = 0$ cm. Density leaving the accelerator is observed during the quiescent period along with radial currents in the accelerator. The density exhibits a prompt drop prior to the end of the quiescent period, as does the radial current.

Measurements of the chord-integrated density also show indications of the onset of instability in the pinch. Figure 3.7 shows chord-integrated density from four interferometry chords located at $z = 0$ cm with impact parameters of $y = -1.5$ cm, $y = -0.5$ cm, $y = 0.5$ cm and $y = 1.5$ cm and the y -location of the current centroid determined by the azimuthal magnetic probe array. Referring to Figure 2.4, the positive y -direction is up from

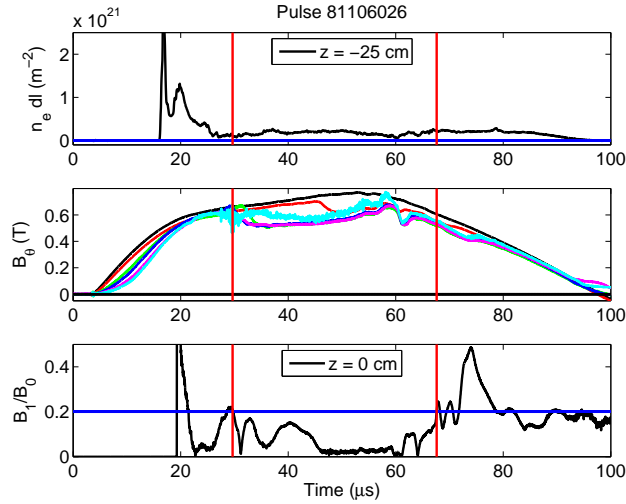


Figure 3.6: Acceleration region data for high peak magnetic field operating condition. The interferometer measures density flowing from the accelerator during the quiescent period with a sharp decline just prior to the end of the quiescent period. Radial current in the accelerator persists until the same time as the density reduction. The red vertical lines indicate the beginning and end of the quiescent period.

the machine axis and the positive x -direction is then specified by the right-hand rule (i.e. if the positive z -direction is out of the page, the positive x -direction is to the left). The magnetic data indicate a pinch elevated from the geometric axis of the machine during the quiescent period. The chord-integrated density data agree with this measurement. At the end of the quiescent period, the values of the chord-integrated data come together and begin to fluctuate significantly.

The fast-framing camera with a 200 ns frame rate is used during this pulse at time near the end of the quiescent period. Figure 3.8 shows the visible light emission from the plasma during the period of time from $t = 70 \mu\text{s}$ to $t = 71.4 \mu\text{s}$. A pinch structure is initially observed which quickly degrades due to the visible onset of instabilities in the pinch. These data are in reasonable agreement with the interferometry data shown in Figure 3.9 which shows the data from Figure 3.7 zoomed in to observe the time near the end of the quiescent period. The red vertical line indicates the end of the quiescent period and the blue vertical

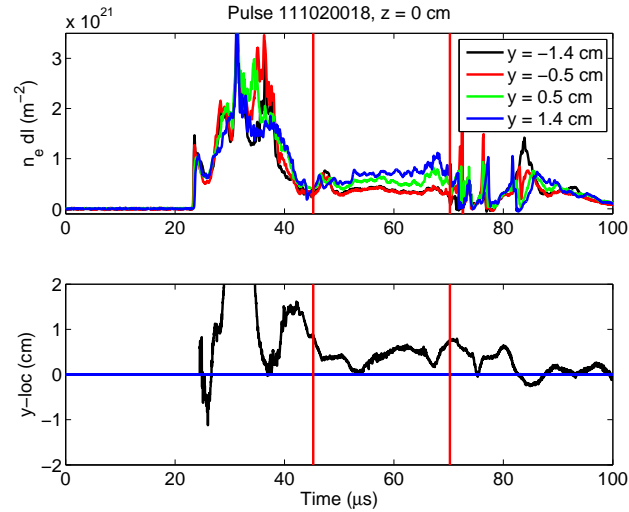


Figure 3.7: Observation of chord-integrated density crash during high peak magnetic field operating condition. During the quiescent period, a coherent pinch is observed with four chords of interferometry. At the end of the quiescent period, the values of the chord-integrated data come together and begin to fluctuate significantly. The red vertical lines indicate the beginning and end of the quiescent period.

lines indicate the times of the first and last fast-framing camera images. The initial images are prior to the end of the quiescent period with that later images after the end of the quiescent period. Both the fast-framing camera images and the interferometry data are in agreement with the end of the quiescent period.

The high peak magnetic field operating condition is also reasonably repeatable. The time at which the magnetic field peak occurs can be highly variable.

The soft-stop and high peak magnetic field operating conditions are further investigated for the equilibrium evolution and compared to the 10 cm inner electrode equilibrium. These data will be presented in Chapters 6 and 7.

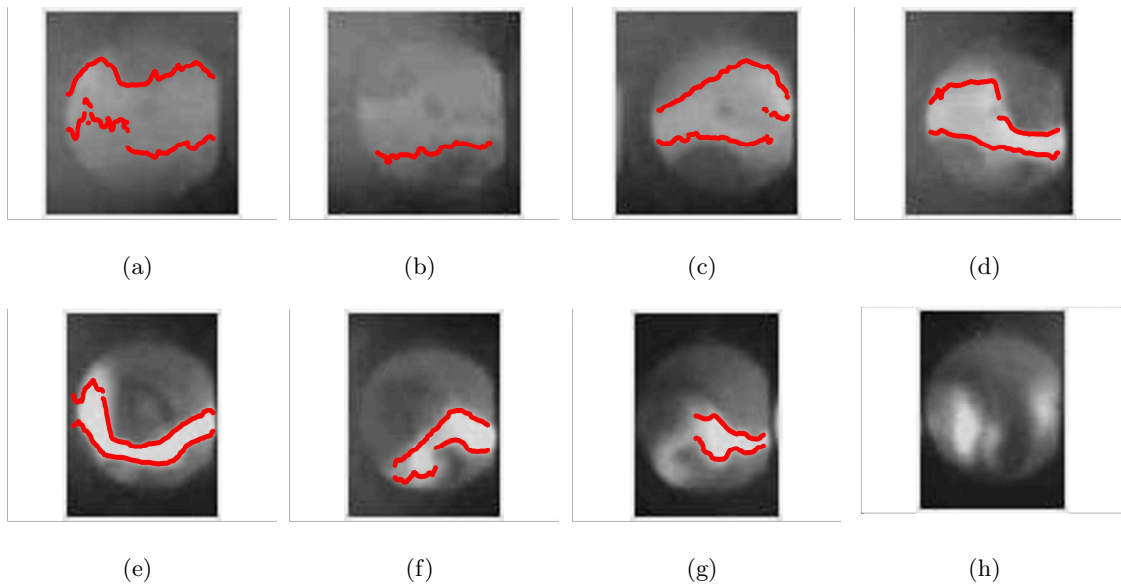


Figure 3.8: Visible light images of instability onset related to density crash in high peak magnetic field operating condition. Fast-framing camera with a 200 ns shutter is used. Initial image is at $t = 70 \mu\text{s}$ and the final image is at $t = 71.4 \mu\text{s}$. A coherent pinch structure is observed in the images (a)-(c) that degrades due to the observed onset of instabilities. Flow direction is from the right to the left. The red symbols indicate 75% of the maximum intensity

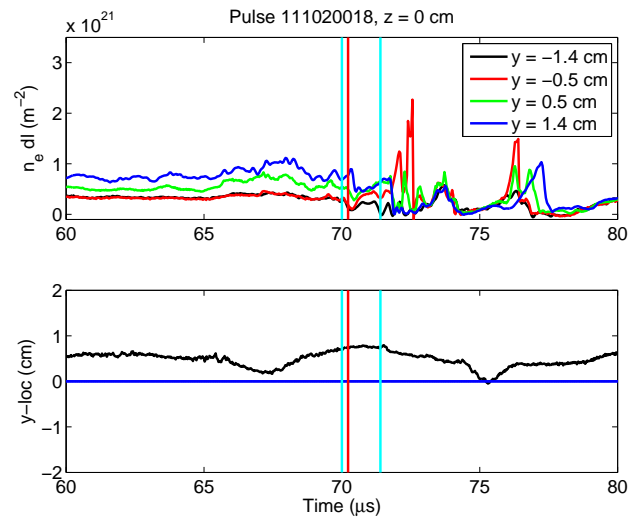


Figure 3.9: Inset view of chord-integrated density crash during high peak magnetic field operating condition. Red vertical line indicates the end of the quiescent period, blue vertical lines indicate the first and last fast-framing camera images. Interferometry data near the end of the quiescent period agree well with the fast-framing camera images with a coherent pinch structure just prior to the end of the quiescent period which is degraded due to instability onset.

Chapter 4

EFFECT OF A CONDUCTING WALL ON STABILITY OF THE ZAP FLOW Z-PINCH

4.1 Experimental Evidence of No-Wall Stabilization on ZaP

Close-fitting perfectly conducting walls have been observed to provide stability in many magnetic configurations, but the effect and the nature of the interaction with Z-pinches has not been thoroughly studied. Early experimental work with arc sources in high temperature gases found a close-fitting wall provides stability [11, 12]. Subsequently, early arcjet research in the 1960's established wall stabilization techniques empirically [13] and many early designs used a constrictor as a wall stabilization technique [14, 15, 16, 17, 18, 19, 20]. Much of this early work focused on finding optimal parameters to operate arcjets as rocket engines while changing the constrictor diameter, input power, breakdown voltage, gas flow, etc.

The wall stabilization techniques developed throughout the gas arc and arcjet research were extended in research directed towards fusion energy to Z-pinches and theta pinches [21, 22, 23, 24, 3, 25], and a more theoretical understanding of the phenomenon was established. Later research by Shumlak and Hartman [2] using a linear stability analysis found that a close-fitting conducting wall around a diffuse pinch provides a stabilizing effect up to a point. When the wall is moved beyond a threshold distance from the pinch, the wall no longer has a stabilizing effect.

Wall stabilization has also been observed in tokamaks, for example Refs. [26, 27], and can increase attainable values of β . Given a proper geometry, a close-fitting conducting wall stabilizes the tilt and shift modes in spheromaks [28, 29].

The effects of a conducting wall on Z-pinch stability are further investigated here with a modification of a Z-pinch experiment and nonlinear numerical simulations. An experimental modification is made on the ZaP Flow Z-Pinch [30, 31] to evaluate the effects of

the conducting wall on the stability of the pinch. A section of the surrounding conducting wall is manufactured that has approximately 70% of the material removed and the stabilization properties are experimentally investigated in this non-axisymmetric configuration. The HiFi [32] code is used to model the three-dimensional ZaP Flow Z-pinch configuration to better understand the stability properties of the pinch.

The Z-pinch $m = 1$ kink mode is explored as a verification of the HiFi code and the multi-block geometry framework that makes non-axisymmetric geometries possible. Experimental parameters are used in the simulations and compared to a linear stability analysis.

The experiment is modified to test the effects of the conducting wall on the pinch stability. A conducting wall produces a stabilizing effect on the kink mode by generating azimuthal currents. The outer electrode of ZaP consists of two sections: a solid cylindrical electrode section with a length of 150 cm that makes up the accelerator and a 50 cm section of the pinch assembly region; and a solid cylindrical 50 cm extension that increases the length of the assembly region. A third section with a length of 34 cm is manufactured that has eight large openings, reducing the surface area of the conducting wall by approximately 70%, as shown Figure 4.1. The effects of a conducting wall on the stability of ZaP are evaluated by removing a significant portion of the conducting wall area and preventing the generation of stabilizing azimuthal currents in the wall. The length of the perforated section is sufficient to evaluate its effect on instabilities as the optically-observed wavelength of instabilities in ZaP are on the order of the pinch radius (≈ 1 cm) [33]. The growth of instabilities should increase if the conducting wall contributes significantly to the stability of the plasma in ZaP.

The perforated section of the outer electrode is many wavelengths away from the end electrodes. In the measurement region, the pinch can effectively be considered to have infinite length.

ZaP is operated using similar accelerator and power source configurations with and without the perforated outer electrode section. An array of diagnostics is used to investigate the effects of the perforated electrode section on the stability characteristics of the pinch.

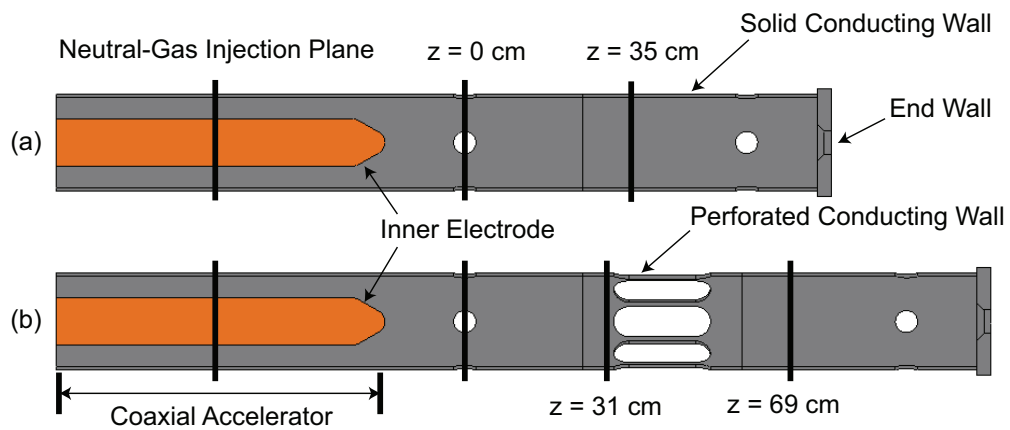


Figure 4.1: Schematic of ZaP experimental configurations used to evaluate effects of a conducting wall on plasma stability. (a) ZaP without the perforated electrode extension consists of an unmagnetized coaxial accelerator coupled to a pinch assembly region. (b) ZaP with the perforated electrode extension and 8 cm radius inner electrode. The perforated electrode section is 34 cm long with eight large openings, resulting in approximately 70% less conducting wall surface than the solid electrode section. Magnetic measurements are made at $z = 0$ cm, $z = 31$ cm and $z = 69$ cm. Optical and interferometry measurements are made in the perforated section.

It is seen from Table 2.1 that the ratio of the pinch radius to the conducting outer electrode radius for ZaP is in the range in which simulations indicate that the conducting wall should have no effect.

The effects of the conducting wall on stability are investigated by operating the experiment with the same bank energy, gas injection characteristics, and coaxial accelerator geometry with and without the perforated conducting wall section. For the data presented, the experimental conditions are a 5 cm outer radius inner electrode, a 10 cm inner radius conducting wall and a 7 kV capacitor bank voltage on eight 180 μF capacitors. The peak current in the experiment is $I \approx 200$ kA.

Figure 4.2 shows the magnetic data for two different pulses, one with the perforated conducting wall section and one without the perforated wall section at the axial location $z = 0$ cm. This is approximately 35 cm upstream of the perforated conducting wall section. The top plot is the average magnetic field and the bottom plot is the normalized $m = 1$ magnetic fluctuations. The horizontal green line in the bottom plot indicates the ZaP stability definition of $B_1/B_0 \leq 0.2$. The data indicate that for similar operating conditions the magnetic data at $z = 0$ cm is similar with and without the perforated conducting wall section. In both cases, the magnetic data indicate a well-centered pinch for an extended period of time and the average magnetic fields have similar magnitudes and waveforms. This suggests that the plasma characteristics are similar for both pulses.

Figure 4.3 shows the magnetic mode data at $z = 35$ cm for the solid conducting wall section and $z = 31$ cm for the perforated conducting wall section. These data indicate that for similar experimental operating conditions, the average magnetic field and the stability characteristics are similar in both the perforated conducting wall section and the solid cylindrical section. The average magnetic fields exhibit similar magnitudes and waveforms. Both pulses indicate a well-centered pinch for an extended period of time, from $t \approx 30$ μs to $t \approx 55$ μs . The difference in axial location of the probe array between the two configurations has little effect due to the observed axial uniformity of the plasma. The data indicate that the removal of conducting wall material does not have a discernible effect on the stability

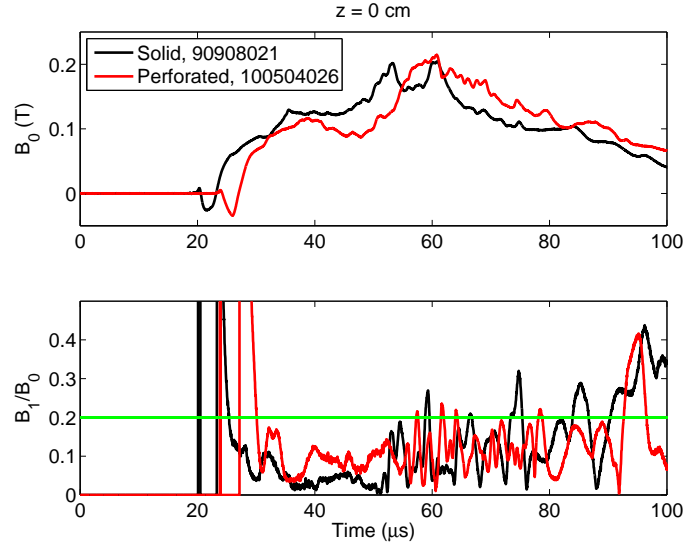


Figure 4.2: Fourier mode data from the azimuthal magnetic probe array at $z = 0$ cm with and without the perforated conducting wall section. Top plot is average magnetic field as a function of time, bottom plot is normalized $m = 1$ magnetic fluctuations as a function of time. Similar waveforms and stability characteristics suggest similar pinches.

of the pinch.

Figure 4.4 shows the magnetic mode data and interferometry data at two impact parameters at $z = 40$ cm in the perforated section. The operating conditions for this pulse are a 5 cm radius inner electrode with a 6 kV capacitor bank voltage on sixteen $180 \mu\text{F}$ capacitors. The peak current for this configuration is $I \approx 250$ kA. These data indicate that during periods of low magnetic fluctuations, a well-defined pinch is observed. When the normalized $m = 1$ data fall below the stability threshold, the central interferometry chord measures increased chord-integrated density while the off-center chord remains at the background level. The vertical green lines indicate the initial and final times for the fast-framing camera images shown in Figure 4.5.

Figure 4.5 shows images of visible light emission from a fast-framing camera in the perforated electrode section ($z = 40$ cm) for the pulse shown in Figure 4.4. The first image is taken at $35 \mu\text{s}$ and the last image is taken at $42 \mu\text{s}$ with $1 \mu\text{s}$ between images. The

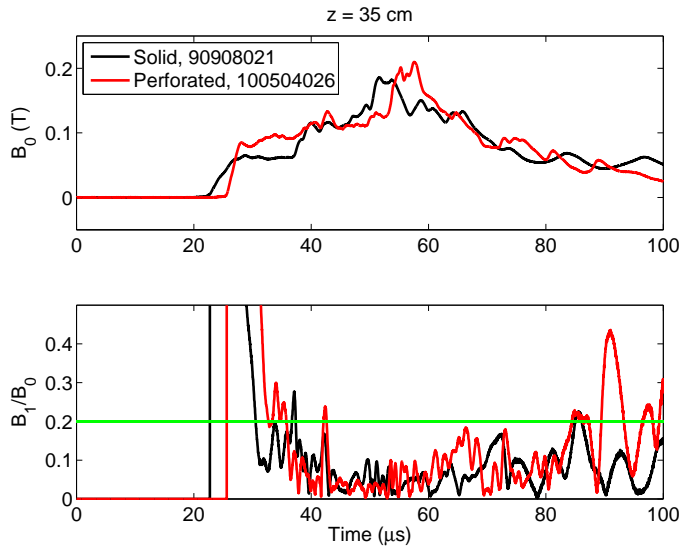


Figure 4.3: Fourier mode data from the azimuthal magnetic probe arrays at $z = 35$ cm and $z = 31$ cm with and without the perforated conducting wall section. Upstream of the perforated electrode section, the waveforms and stability characteristics are the same with and without the perforations.

images indicate a well-defined stable pinch. These data are in good agreement with the magnetic data and interferometry shown in Figure 4.4. During the periods in which magnetic fluctuations are low and a well-centered current centroid is observed with noticeably increased density measured by the central interferometer chord, the optical images show a well-defined pinch.

Measurements of the axial magnetic uniformity of the pinch indicate a confined, coherent structure within the perforated conducting wall section. These measurements are made by comparing the magnitude of the magnetic field and magnetic fluctuations at the probe arrays upstream and downstream of the perforated conducting wall section ($z = 31$ cm and $z = 69$ cm). These data are shown in Figure 4.6 and indicate that the magnetic field at these widely-spaced locations have similar magnitudes and waveforms indicating little current loss from the pinch in the perforated conducting wall section. Magnetic fluctuations are low at both locations during a similar time span. These data indicate a coherent axial

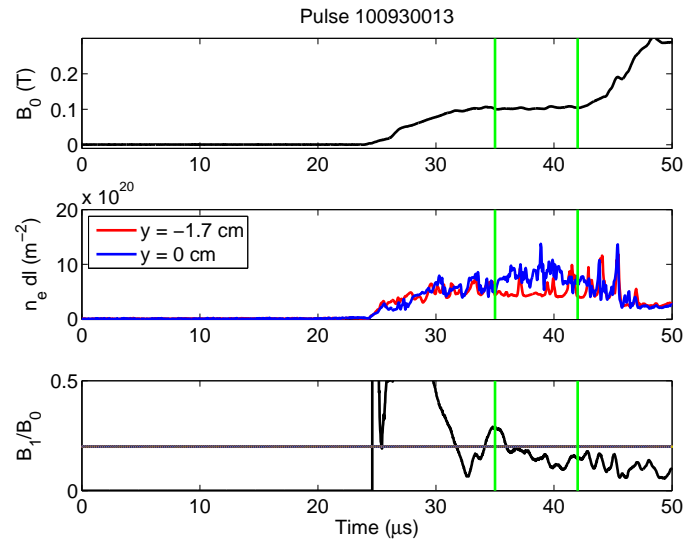


Figure 4.4: Fourier mode data from the azimuthal magnetic probe array at $z = 31$ cm and 2-chord interferometry at $z = 40$ cm, green vertical lines indicate the beginning and end of optical images seen in Figure 4.5. Top plot is average magnetic field as a function of time. Middle plot is chord-integrated data from two chords of interferometry located at $y = 0$ cm and $y = -1.7$ cm. Bottom plot is normalized $m = 1$ magnetic fluctuations. A gradient in chord-integrated density is observed at the beginning of the quiescent period.

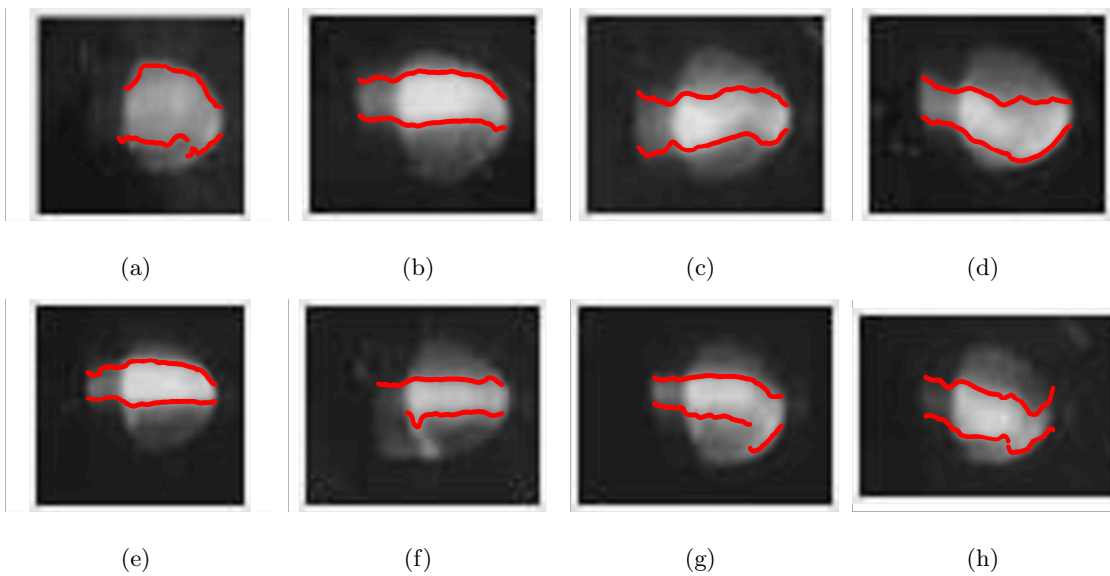


Figure 4.5: Visible light images from an Imacon 790 fast-framing camera with a $1 \mu\text{s}$ frame rate taken in the perforated conducting wall section for the pulse shown in Figure 4.4. The images begin at $35 \mu\text{s}$ and end at $42 \mu\text{s}$, flow direction is from right to left. The red symbols indicate the boundaries of the pinch as a function of axial extent, calculated as the point at which the intensity of the emission is 75% of the maximum value. A coherent pinch structure is observed that agrees with the interferometry measurements.

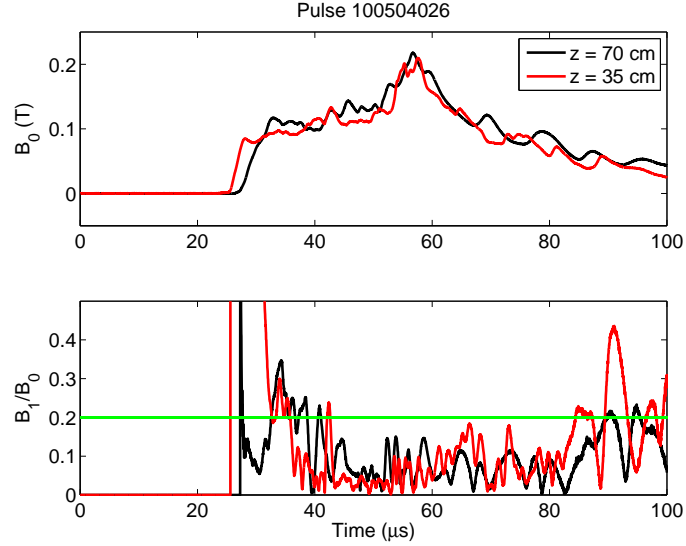


Figure 4.6: Fourier mode data from the azimuthal magnetic probe arrays at $z = 31$ cm and $z = 69$ cm (upstream and downstream of the perforated conducting wall section). Similar magnetic field waveforms indicate little radial current loss in the perforated section.

structure to the plasma in this region.

The evidence of stability without the effects of a conducting wall in ZaP is not limited to a single operating condition. ZaP uses a 8 cm radius inner electrode in addition to a 5 cm radius inner electrode. The difference in accelerator geometry makes the operating conditions for optimum performance different from those of the 5 cm radius inner electrode. The data presented for the 8 cm radius inner electrode are for a capacitor bank voltage of 6 kV on sixteen $180 \mu\text{F}$ capacitors. The peak current in the experiment for these configurations is $I \approx 400$ kA.

Diagnostics in the perforated conducting wall section indicate a well-defined pinch structure that persists for an extended quiescent period with these different operating conditions.

Figure 4.7 shows the magnetic data from the azimuthal magnetic probe array located at $z = 31$ cm and two chords of interferometry located in the perforated conducting wall section at $z = 40$ cm. The data indicate that at the beginning of the quiescent period, the

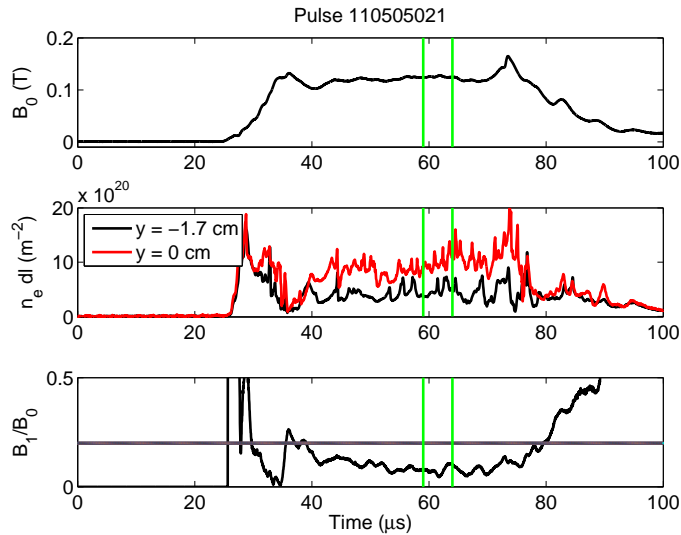


Figure 4.7: Fourier mode data and interferometer data in perforated section for 16 cm inner electrode. Green vertical lines indicate the beginning and end of optical images seen in Figure 4.8. A gradient in the chord-integrated density develops at the beginning of the quiescent period and persists throughout.

chord-integrated electron density from the central interferometry chord increases while the off-center chord remains at the background level. Similarly, as the quiescent period ends both interferometer chords exhibit background levels of chord-integrated density.

Figure 4.8 shows visible light images from the fast-framing camera in the perforated conducting wall section ($z = 40$ cm) for the pulse shown in Figure 4.7. The first image is taken at $59 \mu\text{s}$ and the last image is taken at $64 \mu\text{s}$ with $1 \mu\text{s}$ between images. The red symbols indicate the boundaries of the pinch. The images indicate a well-defined pinch structure that persists through the period of observation. Only one side of the pinch is observed due to the optical extent of the openings in the conducting wall in some images. This limited view still suggests an axial coherent structure. These images are in agreement with the magnetic and interferometric data shown in Figure 4.7.

This experimental configuration shows uniformity of the magnetic structure through the length of the perforated conducting wall section. Figure 4.9 shows data from the magnetic

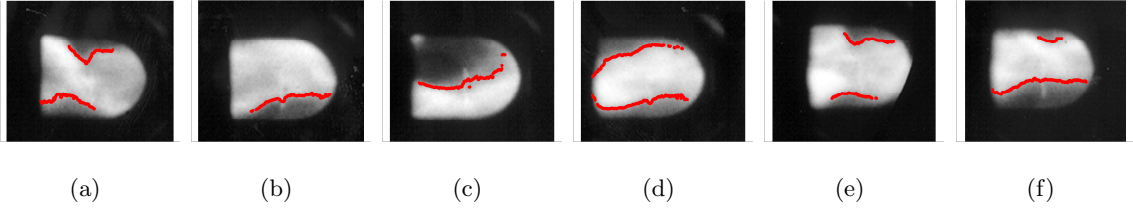


Figure 4.8: Visible light images from fast-framing camera in perforated section with 16 cm inner electrode. Images are taken with a $1 \mu\text{s}$ frame rate for the pulse shown in Figure 4.7. The images begin at $59 \mu\text{s}$ and end at $64 \mu\text{s}$, flow direction is from right to left. The red symbols indicate the boundaries of the pinch. Coherent pinch structure is in agreement with interferometry data.

probe arrays upstream and downstream of the perforated conducting wall section. The data indicate that the magnitude and waveform of the magnetic field are similar at these widely-spaced locations indicating little current loss from the pinch which is indicative of a coherent axial structure. Additionally, the stability characteristics indicate a stable pinch from $t \approx 40 \mu\text{s}$ to $t \approx 65 \mu\text{s}$ at $z = 69 \text{ cm}$ and from $t \approx 40 \mu\text{s}$ to $t \approx 80 \mu\text{s}$ at $z = 31 \text{ cm}$.

4.2 Comparison to Computational Results

The experimental results presented are compared to computational work conducted by Lowrie [34]. A periodic $m = 1$ kink mode is modeled using the HiFi code, developed by the PSI-Center [35], for two configurations: a straight cylindrical geometry and a geometry with extrusions which simulate the perforations in the experimental outer electrode. These geometries are shown in Figure 4.10.

Figure 4.11 shows axial slices of the computational domain at the midpoint of the kink axial wavelength for both computation geometries for pinch radii ranging from 1 to 8 cm. It is evident by comparing Figures 4.11(a), 4.11(e), 4.11(b) and 4.11(f) that for smaller pinch radii, the conducting wall is having little effect on the plasma. As the pinch size is increased the effects of the wall stabilization are observed. For the case of $a = 6 \text{ cm}$, the pinch is large enough to interact with both the wall and the perforated parts of the domain, but not large

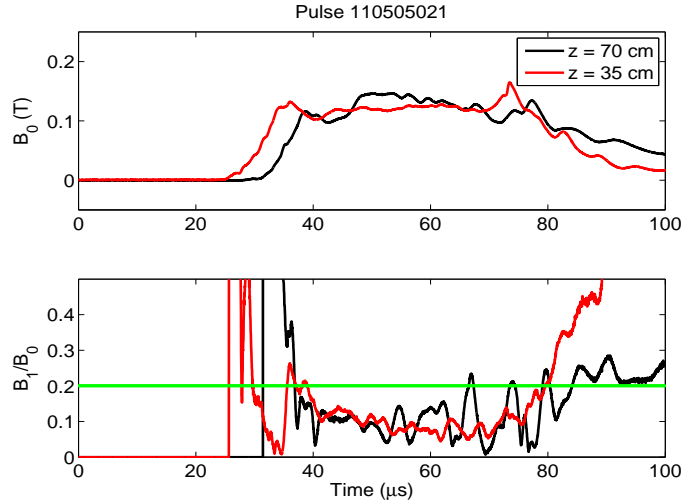


Figure 4.9: Fourier mode data upstream and downstream of perforated conducting wall for 16 cm inner electrode. Similar magnetic field waveforms indicate little radial current loss in the perforated section.

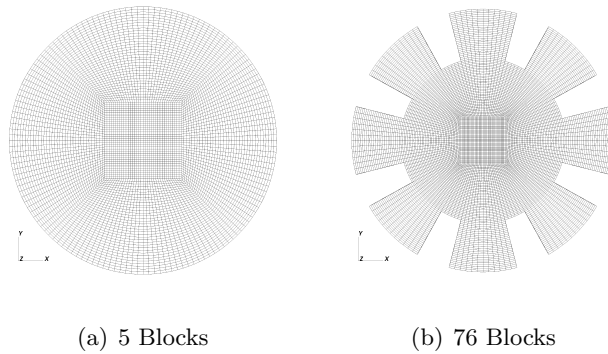


Figure 4.10: Cross-sections of the straight cylinder and cylinder with extrusions computational geometries. The computational geometries are used by the HiFi code to simulate the kink mode growth in the presence of a uniform cylindrical conducting wall (ZaP outer electrode without perforation) and in the presence of a cylindrical conducting wall with extrusions (ZaP outer electrode with perforations).

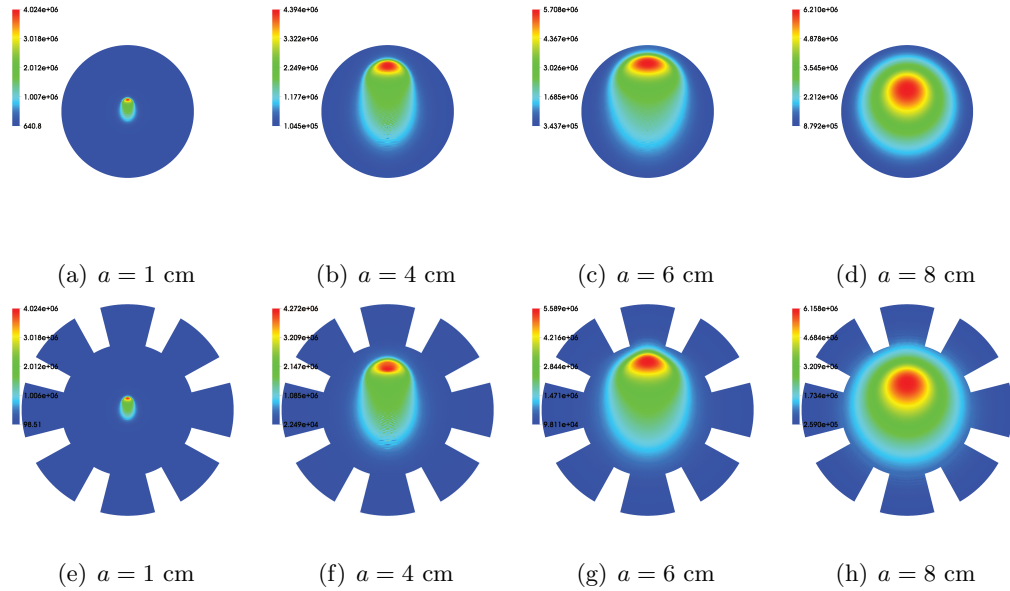


Figure 4.11: Pressure profiles at the midpoint of the axial kink wavelength for characteristic plasma sizes of $a = 1, 4, 6,$ and 8 cm while keeping $ka = \pi/2$ constant. Both a cylindrical cross section and cylindrical cross section with radial extrusions are shown. All figures are at time $\tau_A = 23.2$ normalized by the axial wavenumber times the Alfvén speed, kV_A .

enough to be affected by adjacent wall locations such as for the case of $a = 8$ cm.

4.3 Conclusions

An experimental modification to the ZaP Flow Z-Pinch to evaluate the effects of a conducting wall on pinch stability is performed. A perforated outer conducting wall section is manufactured that has approximately 70% of the conducting wall surface removed. The ratio of the pinch radius to the conducting wall radius is in the range in which simulations indicate the wall should have no effect. A coherent pinch structure is observed in the perforated conducting wall section that persists for lengths of time similar to that observed for a solid conducting wall section for multiple experimental configurations of accelerator geometry, capacitor bank characteristics and gas injection characteristics. Data from magnetic probe arrays indicate a stable, axially-uniform magnetic structure through the perforated

conducting wall section with little current loss from the pinch. Optical images and interferometry indicate a well-defined pinch structure in the perforated conducting wall section that persists for times much longer than the instability growth time. The data indicate that the removal of conducting wall material from the outer wall has no discernible effect on the stability of the Z-pinch. The experimental data is in agreement with simulations conducted with the HiFi code.

The engineering aspects of a Z-pinch configuration with a perforated outer conducting wall are substantial. Consider a Z-pinch configuration under which nuclear fusion is occurring. Reducing the surface area of the outer conducting wall reduces the amount of neutron-activated material that results. Another example is a Z-pinch space thruster. The cost of launching payload into space is significant. If the payload is a spacecraft with a Z-pinch thruster, reducing the outer conducting wall material substantially reduces the launch mass.

Chapter 5

PLASMA HEATING IN THE ZAP FLOW Z-PINCH

It is hypothesized that adiabatic compression during pinch formation is the primary form of heating on ZaP, but the effects of other heating mechanisms are being considered such as heating through shocks and the potential contributions of Ohmic heating.

5.1 Adiabatic Compression

Adiabatic compressional heating has been investigated in tokamaks [36, 37, 38], spheromaks [39] and field-reversed configurations (FRCs) [40, 41, 42].

Adiabatic compressional heating is used for auxiliary tokamak heating by compressing both the major and minor radius of the torus magnetically. Three types of compressional heating are typically investigated: minor radius compression with constant major radius accomplished by increasing the toroidal magnetic field; proportional compression of the major and minor radii; major radius compression with constant toroidal field.

Scaling laws for magnetic compression of tokamak discharges are described by Furth and Yoshikawa [36] with some results shown below.

$$n \propto a^{-2} R^{-1} \tag{5.1}$$

$$T \propto a^{-4/3} R^{-2/3} \tag{5.2}$$

$$I \propto R^{-1} \tag{5.3}$$

$$B \propto a^{-2} \tag{5.4}$$

These scaling laws are based on a number of assumptions [36]. The compression is assumed to occur from an initial low-temperature tokamak equilibrium. The compression occurs slowly compared with particle collision time, but rapidly compared to the energy confinement time. Perfect conductivity is assumed on the time scale of the compression. Three additional constraints exist:

$$a^2 B_t = \text{constant} \quad (5.5)$$

$$q = \text{constant} \quad (5.6)$$

$$T n^{-2/3} = \text{constant} \quad (5.7)$$

where q is the safety factor. The first condition suggests that flux through the toroidal cross-section is constant, meaning that as the minor radius, a , decreases the toroidal magnetic field increases. The second condition suggests that the current profile is self-similar during the compression. The third condition is the adiabatic condition and assumes particle conservation.

Minor radius compression at constant major radius by increasing B_t also requires that the vertical field, B_v , be raised in order to maintain equilibrium in major radius. This type of compression increases the aspect ratio of the tokamak and requires that total magnetic energy of the machine be increased which scales with the minor radius, a , ($W_m \propto B^2 \rightarrow a^{-4}$) with a smaller increase in plasma energy ($W_p \propto T \rightarrow a^{-4/3}$) [36].

Proportional increase of a and R is accomplished by increasing B_t and B_z such that a decreases and R is compressed by the vertical field. In this case, the magnetic and plasma energies scale equally, but still require very large pulsed magnetic energies [36].

Major radius compression at constant B_t is accomplished by increasing B_v . As the R is decreased, the plasma is forced into a region of increased B_t and a reduction in the minor radius results ($a \rightarrow R^{1/2}$). The required pulsed magnetic energy is now only due to the increase in vertical field [36].

The adiabatic toroidal compressor (ATC) experiment at Princeton showed a density increase of a factor of five and a temperature increase of a factor of three with an R -compression of a factor of 2.3 [37]. These values follow closely with the adiabatic relations shown above.

Minor radius compression of the Tuman-3 tokamak showed an increase in temperature of a factor of two and a 3-fold increase in density with an increase of a factor of three in B_t , consistent with adiabatic laws [38].

Adiabatic compression has also been investigated in FRCs. Two types of compression are considered: 1) wall compression via the radial collapse of a cylindrical flux-conserving liner, this collapse is assumed to occur rapidly compared the energy confinement time; 2) flux compression by increasing an externally-applied magnetic field.

For wall compression of an FRC where the separatrix location, x_s , is constant and an isothermal plasma within the separatrix of length l , scaling laws are shown below [40]

$$l \propto r_w^{(4-2\gamma)/\gamma} \quad (5.8)$$

$$T_m \propto r_w^{-4(\gamma-1)/\gamma} \quad (5.9)$$

$$n_m \propto r_w^{-4/\gamma} \quad (5.10)$$

$$B_w \propto r_w^{-2} \quad (5.11)$$

where T_m and n_m are midplane values of temperature and density, r_w is the wall radius, γ is the ratio of specific heats and B_w is the magnetic field at the wall. These scaling laws are based on the following assumptions [40]: 1) throughout the compression process, the FRC is in equilibrium that has the same entropy per unit flux with flux being conserved; 2) particles are conserved; 3) radial force balance is maintained.

For flux compression where r_w is constant and the separatrix location changes, scaling laws are [40],

$$l \propto x_s^{2(3-\epsilon-\gamma)/\gamma} < \beta >^{-(1+\epsilon-\gamma\epsilon)/\gamma} \quad (5.12)$$

$$T_m \propto x_s^{-2(3-\epsilon)(\gamma-1)/\gamma} < \beta >^{(1+\epsilon)(\gamma-1)/\gamma} \quad (5.13)$$

$$n_m \propto x_s^{-2(3-\epsilon)/\gamma} < \beta >^{-(1+\epsilon)(\gamma-1)\gamma} \quad (5.14)$$

$$B_w \propto x_s^{-3+\epsilon} \quad (5.15)$$

where $\epsilon = (x_s/f)(df/dx_s)$ and $f = x_s/\int_0^1(1-\beta)^{1/2}du$. These scaling laws are dependent on assumptions of particle conservation, magnetic flux conservation, radial force balance and an idealized geometry where the cylindrical volume inside the separatrix is, $V = x_s^2 l$.

These relationships for flux compression have been verified on the FRX-C/T experiment [41]. The use of imploding liners for FRC wall compression is planned on the Field Reversed Configuration and Heating Experiment (FRCHX) [42].

Adiabatic compression of a spheromak was investigated with the S-1 device at Princeton [39]. The compression factor of the spheromaks was $C = R_{\text{initial}}/R_{\text{final}} \approx 1.3 - 1.6$ with the predicted scaling relationships shown below.

$$B \propto C^2 \quad (5.16)$$

$$n_e \propto C^3 \quad (5.17)$$

$$T_e \propto C^2 \quad (5.18)$$

$$I \propto C \tag{5.19}$$

These scaling laws depend on particle conservation and the assumption that the compression time is less than the energy confinement time. Compression is assumed to occur from an initial Taylor state equilibrium to a final Taylor state equilibrium.

The relationships for density and temperature were not obeyed during compression of S-1. The density was found to increase only as $n_e \propto C$, while the temperature increased in excess of adiabatic predictions [39]. These deviations from adiabatic results are attributed to particle loss during the compression process.

5.1.1 Adiabatic Compression in ZaP

ZaP discharges are considered as two-stage operations. The first stage is the formation and compression of the pinch from a non-equilibrium annulus of plasma to a final equilibrium pinch state. The second stage consists of an evolving equilibrium pinch state subject to a time-varying current pulse. The formation stage is considered first.

Increasing the size of the inner electrode in ZaP is designed to increase the degree of heating of the pinch due to adiabatic compression from the acceleration region to the pinch region during the pinch formation process.

The following analysis results in a comparison of different electrode geometries, based on the following assumptions:

1. Compression occurs from an annulus of plasma matching the dimensions of the inner ($r_a = r_{\text{inner}}$) and outer electrodes ($r_b = r_{\text{outer}}$) to a cylinder of plasma with a radius calculated from radial force balance, as shown in Figure 5.1
2. The lengths of the annulus and resulting pinch are equal
3. Density and temperature in the annulus are uniform

4. Temperature and current density in the pinch are uniform, resulting in a parabolic density profile
5. Particle inventory is conserved
6. Density and temperature in the accelerator are the same for both electrode configurations, meaning for a larger inner electrode fewer particles are required
7. Current in the pinch is the same between the two electrode configurations
8. Compression occurs on a time scale faster than the energy confinement time.

The primary differing assumption between the ZaP analysis of initial compression and the previously-mentioned work is in the initial pre-compression state. Previous work has assumed compression from an initial equilibrium to a final equilibrium whereas ZaP assumes an initial non-equilibrium state which is intended to mimic the non-equilibrium plasma that exits the accelerator and compresses into the pinch. This initial state is an idealized cylindrical annulus geometry with uniform temperature and density and a length the same as the final pinch state. This idealized state is used to simplify calculations.

Other assumptions such as conservation of particles, compression on time scales faster than the energy confinement time and final equilibrium dictated by balance of forces are the same.

Z-pinch equilibrium is defined by radial force balance,

$$\frac{\partial p}{\partial r} = -j_z B_\theta \quad (5.20)$$

and the current density, j_z , and B_θ are related through Ampere's Law,

$$\frac{1}{r} \frac{\partial}{\partial r} (r B_\theta) = \mu_0 j_z \quad (5.21)$$

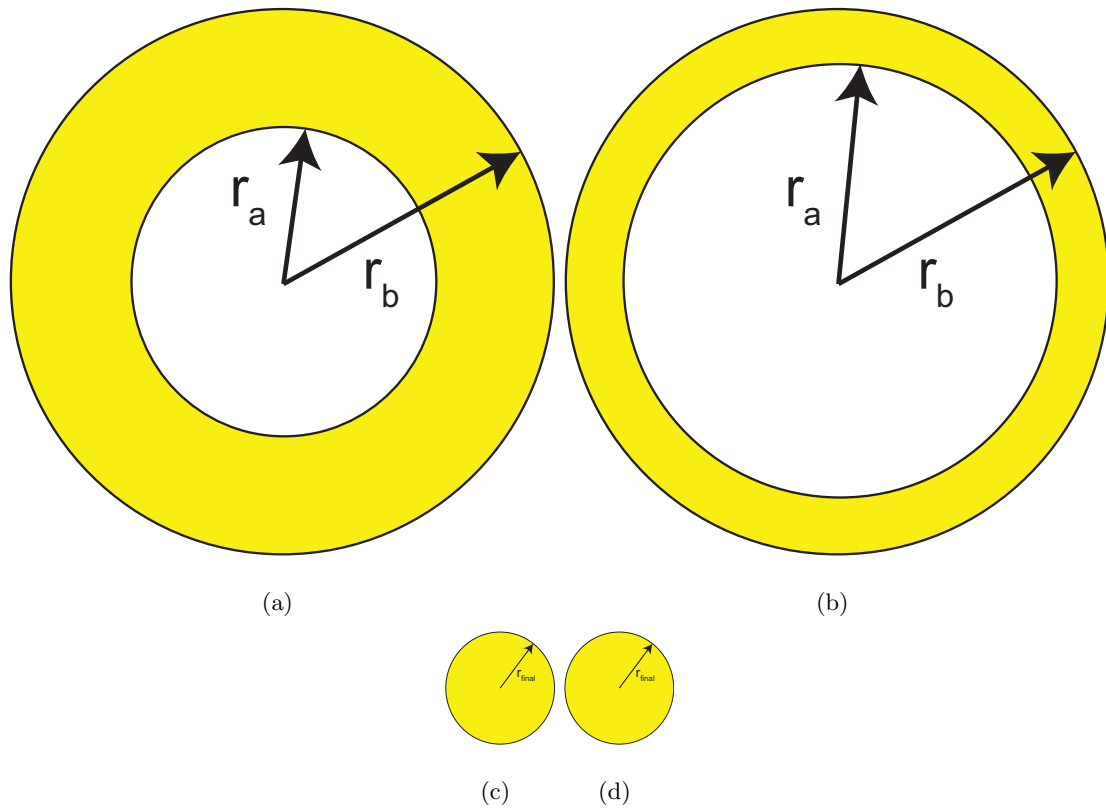


Figure 5.1: Adiabatic compression geometry for smaller and larger inner electrode configurations. (a) Annulus of plasma for smaller inner electrode, $r_a = r_{\text{inner}}, r_b = r_{\text{outer}}$. (b) Annulus of plasma for larger inner electrode, the density and temperature are the same between electrode configurations. (c) Annulus is compressed to a cylinder of plasma with a radius dictated by adiabatic compression analysis. (d) Given the same conditions of density and temperature in the accelerator and the same current in the pinch, a reduced pinch radius is expected.

Pressure is defined as $p = (Z_{\text{eff}} + 1)nk_B T$, where p is the total plasma pressure, the number density is $n = n_e/Z_{\text{eff}} = n_i$, $T = T_e = T_i$ is the temperature, k_B is Boltzmann's constant and μ_0 is the permeability of free space. n is related to the linear density, N , by

$$N = \int_0^a 2\pi n r dr \quad (5.22)$$

where a is the radius of the pinch. The axial current, I , is related to j_z by

$$I = \int_0^a 2\pi j_z r dr \quad (5.23)$$

Assuming a parabolic density profile with a uniform temperature in the pinch, the resulting current density profile is uniform producing a magnetic field profile that is linearly dependent on the radius.

$$n_{\text{pinch}}(r) = n_0 \left(1 - \frac{r^2}{a^2} \right) \quad (5.24)$$

$$j_z = \frac{I}{\pi a^2} \quad (5.25)$$

$$B_\theta(r) = \frac{\mu_0 I r}{2\pi a^2} \quad (5.26)$$

where a is the pinch radius. Using Equations 5.20, 5.22, and 5.24 - 5.26, the Bennett relation can be derived [43], which is a relationship between the pinch temperature, total current and linear density.

$$T_{\text{pinch}} = \frac{\mu_0 I^2}{8(Z_{\text{eff}} + 1)\pi k_B N} \quad (5.27)$$

The on-axis density is calculated as

$$n_0 = \frac{2N}{\pi a^2} \quad (5.28)$$

Compression from the initial annular state to the pinch conditions can now be considered. In an adiabatic process no heat is gained or lost by the system, $Q = 0$. When a system undergoes an adiabatic change of state, the relationship between the pressure and density in these states follows the adiabatic condition. This condition can be written in equation form as:

$$\left\langle \frac{p}{n^\gamma} \right\rangle = \text{constant} \quad (5.29)$$

where γ is the ratio of specific heats, typically taken to be 5/3 for plasmas. Equating the initial (annulus) and final (pinch) conditions Equation 5.29 can be written as,

$$\left\langle \frac{n_{\text{annulus}} k_B T_{\text{annulus}}}{n_{\text{annulus}}^\gamma} \right\rangle = \left\langle \frac{n_{\text{pinch}} k_B T_{\text{pinch}}}{n_{\text{pinch}}^\gamma} \right\rangle \quad (5.30)$$

In the annulus, the density, n_{annulus} , and temperature, T_{annulus} , are uniform and the density can be defined by the linear density and the dimensions of the accelerator

$$n_{\text{annulus}} = \frac{N}{\pi \left(r_{\text{outer}}^2 - r_{\text{inner}}^2 \right)} \quad (5.31)$$

The resulting volume-averaged adiabatic function in the annulus is

$$\left\langle \frac{p}{\rho^\gamma} \right\rangle_{\text{annulus}} = \frac{\left(Z_{\text{eff}} + 1 \right) k_B \pi^{\frac{2}{3}} T_{\text{annulus}} \left(r_{\text{outer}}^2 - r_{\text{inner}}^2 \right)^{\frac{2}{3}}}{m_i^{\frac{5}{3}} N^{\frac{2}{3}}} \quad (5.32)$$

Volume-averaging the adiabatic function for the pinch conditions produces the following expression

$$\left\langle \frac{p}{\rho^\gamma} \right\rangle_{\text{pinch}} = \frac{0.236 \mu_0 I^2 a^{\frac{4}{3}}}{m_i^{\frac{5}{3}} \pi^{\frac{1}{3}} N^{\frac{5}{3}}} \quad (5.33)$$

An equation for the pinch radius can now be determined,

$$a = 1.48 \times 10^{-9} \left[\frac{(Z_{\text{eff}} + 1)NT_{\text{annulus}}(r_{\text{outer}}^2 - r_{\text{inner}}^2)^{\frac{2}{3}}}{I^2} \right]^{\frac{3}{4}} \quad (5.34)$$

Equations 5.27, 5.28 and 5.34 give the pinch temperature, peak density and radius as a function of known values in the acceleration region and the current in the pinch.

These equations can also be directly compared between the previous electrode configuration and the modified configuration to yield the predicted changes in the pinch parameters due to the modification. Recall the assumption of equal density between configurations, $N_{\text{larger}} = N_{\text{smaller}} \frac{r_{\text{outer}}^2 - r_{\text{inner, larger}}^2}{r_{\text{outer}}^2 - r_{\text{inner, smaller}}^2}$.

$$\frac{a_{\text{larger}}}{a_{\text{smaller}}} = \left[\frac{r_{\text{outer}}^2 - r_{\text{inner, larger}}^2}{r_{\text{outer}}^2 - r_{\text{inner, smaller}}^2} \right]^{\frac{5}{4}} \quad (5.35)$$

$$\frac{n_{\text{larger}}}{n_{\text{smaller}}} = \left[\frac{r_{\text{outer}}^2 - r_{\text{inner, smaller}}^2}{r_{\text{outer}}^2 - r_{\text{inner, larger}}^2} \right]^{\frac{3}{2}} \quad (5.36)$$

$$\frac{T_{\text{larger}}}{T_{\text{smaller}}} = \frac{r_{\text{outer}}^2 - r_{\text{inner, smaller}}^2}{r_{\text{outer}}^2 - r_{\text{inner, larger}}^2} \quad (5.37)$$

Figure 5.2 shows the trends for these ratios with increasing larger inner electrode radius where $r_{\text{inner, smaller}} = 5$ cm. The trends for density and temperature increase with increasing electrode size and the pinch radius decreases. The green vertical line indicates the parameter values for the 16 cm inner electrode. The predicted values are $T_{16\text{cm}} = 2.16T_{10\text{cm}}$ for the temperature ratio, $n_{16\text{cm}} = 3.18n_{10\text{cm}}$ for the density ratio and $a_{16\text{cm}} = 0.38a_{10\text{cm}}$ for the characteristic radius ratio.

As an example, consider the 10 cm inner electrode configuration with a linear density, $N = 2 \times 10^{19} \text{ m}^{-1}$, a temperature in the annulus of 10 eV and a final current in the pinch of 75 kA. The final pinch temperature is 44 eV, the final radius is 1.68 cm and the final density is $4.5 \times 10^{22} \text{ m}^{-3}$. For the 16 cm inner electrode configuration with a pinch current of 150 kA, the linear density is $9.23 \times 10^{18} \text{ m}^{-1}$ resulting in a pinch temperature of 95.2 eV, a pinch radius of 0.64 cm and a final density of $1.44 \times 10^{23} \text{ m}^{-3}$. These parameters are summarized in Table 5.1.

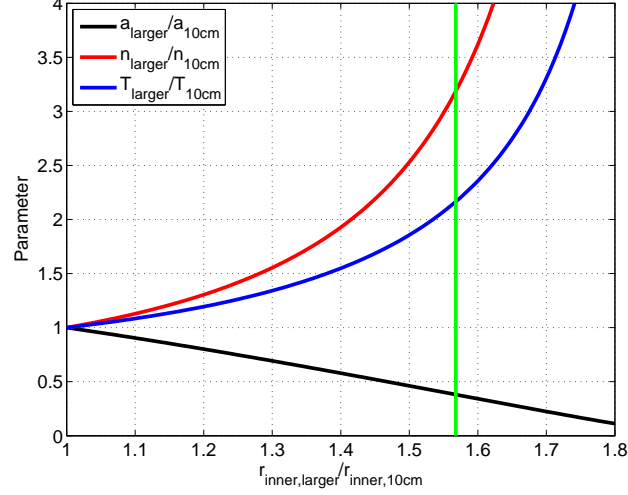


Figure 5.2: Predicted trends for increasing inner electrode size from adiabatic compression analysis. The trends for density and temperature increase with increasing electrode size and the pinch radius decreases. The green vertical line indicates the parameter values for the larger inner electrode $r_i = 7.84$ cm. The predicted values are $T_{16\text{cm}} = 2.16T_{10\text{cm}}$, $n_{16\text{cm}} = 3.18n_{10\text{cm}}$ and $a_{16\text{cm}} = 0.38a_{10\text{cm}}$.

Table 5.1: Parameters for 10 cm and 16 cm Electrode Configurations undergoing Adiabatic Compression .

parameter	10 cm	16 cm
N	$2 \times 10^{19} \text{ m}^{-1}$	$9.23 \times 10^{18} \text{ m}^{-1}$
T_{annulus}	10 eV	10 eV
I	75 kA	75 kA
$T = T_e = T_i$	44 eV	95.2 eV
$n = n_e/Z_{\text{eff}} = n_i$	$4.5 \times 10^{22} \text{ m}^{-3}$	$1.44 \times 10^{23} \text{ m}^{-3}$
a	1.68 cm	0.64 cm

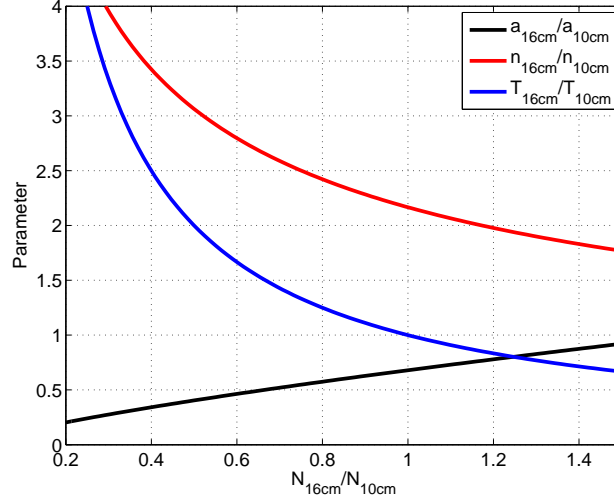


Figure 5.3: Effect of changing annulus density for larger inner electrode. Variations from the assumption of $N_{\text{larger}} = N_{\text{smaller}} \frac{r_{\text{outer}}^2 - r_{\text{inner, larger}}^2}{r_{\text{outer}}^2 - r_{\text{inner, smaller}}^2}$ affect the predictions of the model. If density in the annulus of the larger electrode configuration is increased compared to this assumption, the result is larger pinch radii, lower pinch densities and decreased pinch temperatures.

If the assumptions of the analysis regarding linear density and temperature in the annulus and current in the pinch are not met, the above predictions are not valid. If the linear density in the annulus is increased from the assumption of $N_{\text{larger}} = N_{\text{smaller}} \frac{r_{\text{outer}}^2 - r_{\text{inner, larger}}^2}{r_{\text{outer}}^2 - r_{\text{inner, smaller}}^2}$ for the larger inner electrode, the effect is larger pinch radii than predicted, lower pinch densities and decreased pinch temperatures, as shown in Figure 5.3. Increasing the temperature in the annulus for the larger inner electrode away from the assumption of equal temperatures between the two electrode configurations has no effect on the pinch temperature since it is based on current and linear density only, but pinch radii are increased with a decrease in pinch densities, as shown in Figure 5.4. Increasing the current in the pinch for the larger inner electrode away from the assumption of equal currents in the pinch results in reduced radii with increases in both temperature and density, as shown in Figure 5.5.

After pinch formation, additional heating can occur through adiabatic magnetic compression as current in the pinch increases as a function of time. This compression is similar

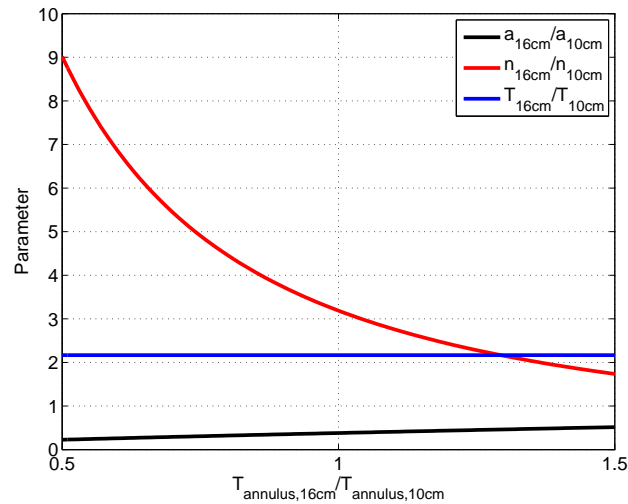


Figure 5.4: Effect of changing annulus temperature for larger inner electrode. If temperature in the annulus of the larger electrode configuration is increased compared to the assumption of equal temperatures between the two electrode configurations, the result is increased pinch radii and decreased pinch densities with no change in pinch temperature since it is dependent on current and linear density only.

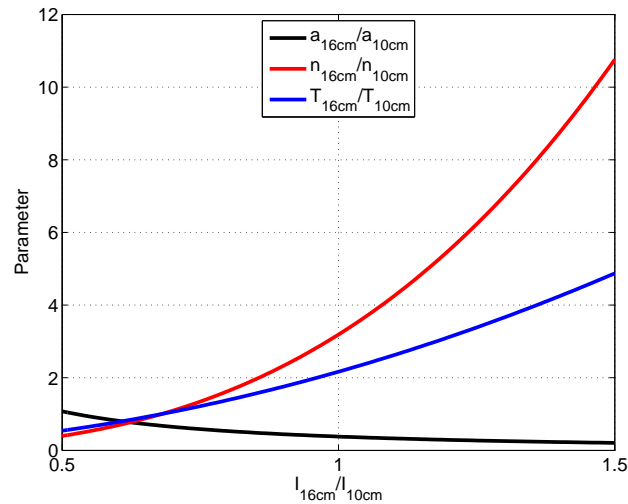


Figure 5.5: Effect of changing pinch current for larger inner electrode. If the current in the pinch for the larger electrode configuration is increased compared to the assumption of equal pinch currents between the two electrode configurations, the result is increases in pinch temperature and density with decreased pinch radii.

to adiabatic compression of tokamaks in that it is compression from one equilibrium state to another, unlike the compression during initial pinch formation.

Consider a pinch in an initial equilibrium state with radius a_1 , temperature T_1 and average density $\langle n_1 \rangle$ with total current I_1 that undergoes compression due to an increase in current to a final equilibrium state with radius a_2 , temperature T_2 and average density $\langle n_2 \rangle$ with total current $I_2 = \alpha I_1$. The pinch is assumed to maintain stability during this process and maintain a uniform temperature and current density. If linear density is assumed to remain constant during the compression, the final temperature can be determined using Equation 5.27 to be $T_2 = \alpha^2 T_1$. Using the adiabatic relation,

$$\left\langle \frac{n_1 k_B T_1}{n_1^\gamma} \right\rangle = \left\langle \frac{n_2 k_B T_2}{n_2^\gamma} \right\rangle \quad (5.38)$$

and Equation 5.28 the final radius is found to be $a_2 = a_1 \alpha^{-3/2}$ and the final peak density can then be calculated as $n_2 = \alpha^3 n_1$.

An increase in current results in increased temperature and density along with a reduced radius if the change is assumed to occur adiabatically.

5.2 Shock Heating

Heating plasmas to high transient temperatures with high-speed shocks has been considered in the past by de Hoffman and Teller [44], McLean [45] and Kolb [46] amongst others. Experiments have been conducted that combine shock heating with adiabatic compression after the shock in pinch discharges [47] [48]. These experiments successfully created thermonuclear neutrons, proving the capabilities of such methods.

5.2.1 Shock Heating in ZaP

ZaP is a slow discharge for a Z-pinch ($\approx 100 \mu s$) and is not designed to shock heat the plasma, but it may occur. For simplicity, a steady-state, one-dimensional shock is assumed viewed from the reference frame of the shock being stationary. In this way, the one-dimensional fluid equations describe the pre- and post-shock conditions of temperature and density.

Two limiting cases are considered for the investigation of shock heating in ZaP. The first is that of the plasma front moving at a slower velocity than upstream plasma layers. This results in a system of $M \approx 1$ shocks which are known to be infinitely weak, resulting in no compression or heating. This case reduces to the adiabatic compression case. The second limiting case considered is that the velocity of the plasma is equal throughout its volume. In this case, a shock occurs when the plasma front reaches the axis of ZaP. It is assumed that, at this point, the bulk velocity of the plasma is the Alfvén velocity, defined by the peak magnetic field

$$V_A = \frac{B}{(\mu_0 n_i m_i)^{\frac{1}{2}}} \quad (5.39)$$

where B is the magnitude of the magnetic field, n_i is the ion number density and m_i is the mass of the ion. Adiabatic processes are assumed prior to and after the shock and the initial bulk plasma velocity is assumed to be zero.

In the reference frame of the shock being stationary, the steady-state 1D fluid equations [49] reduce to the integrated forms of the conservation of mass, momentum and energy [50, 51]. η_0 in these equations is the isotropic viscosity coefficient for the ions or electrons, κ_e is the electron heat conduction coefficient and Z is the charge state of the ions.

$$nu = n_1 u_1 \quad (5.40)$$

$$nm_i u^2 + n(ZT_e + T_i) - \frac{4}{3}(\eta_0^e + \eta_0^i) \frac{du}{dx} = n_1 m_i u_1^2 + (1 + Z)n_1 T_1 \quad (5.41)$$

$$\frac{1}{2}nm_i u^3 + \frac{5}{2}nu(ZT_e + T_i) - \kappa_e \frac{dT_e}{dx} - \frac{4}{3}(\eta_0^e + \eta_0^i)u \frac{du}{dx} = \frac{1}{2}n_1 m_i u_1^3 + \frac{5}{2}(1 + Z)n_1 u_1 T_1 \quad (5.42)$$

Far upstream and downstream of the shock, all gradients vanish and the right-hand side of the equations become equal, yielding,

$$n_1 u_1 = n_2 u_2 \quad (5.43)$$

$$n_1 m_i u_1^2 + (1 + Z)n_1 T_1 = n_2 m_i u_2^2 + (1 + Z)n_2 T_2 \quad (5.44)$$

$$\frac{1}{2}n_1 m_i u_1^3 + \frac{5}{2}(1 + Z)n_1 u_1 T_1 = \frac{1}{2}n_2 m_i u_2^3 + \frac{5}{2}(1 + Z)n_2 u_2 T_2 \quad (5.45)$$

From this point, the pre- and post-shock state parameters can be derived [52],

$$\frac{u_2}{u_1} = \frac{n_1}{n_2} = \frac{M_1^2 + 3}{4M_1^2} \quad (5.46)$$

$$\frac{T_2}{T_1} = \frac{(M_1^2 + 3)(5M_1^2 - 1)}{16M_1^2} \quad (5.47)$$

where

$$M_1 = u_1 \sqrt{\frac{5(1 + Z)T_1}{3m_i}} \quad (5.48)$$

is the Mach number of the shock wave. These are conventional Rankine-Hugoniot conditions for an ideal gas with $\gamma = 5/3$.

Given the same initial annulus conditions as mentioned in the previous section and adiabatic processes before and after the shock, the result for the 10 cm electrode configuration is pre-shock conditions of $n_e = 2.97 \times 10^{21} \text{ m}^{-3}$, $T = 21.5 \text{ eV}$ and a $M = 2.2$ shock, resulting in post-shock conditions of $n_e = 7.36 \times 10^{21} \text{ m}^{-3}$, $T = 50.87 \text{ eV}$ and a radius of 2.94 cm. These conditions result in expansion to reach equilibrium with a temperature of 43 eV, a radius of 2.04 cm and a density of $3.07 \times 10^{22} \text{ m}^{-3}$. For the 16 cm electrode configuration, the pre-shock conditions are $n_e = 9.17 \times 10^{21} \text{ m}^{-3}$ and a temperature of 45.7 eV with a $M = 2.23$ shock, resulting in post-shock conditions of $n_e = 2.29 \times 10^{22} \text{ m}^{-3}$, a temperature of 109.42 eV and a radius of 1.13 cm. This results in expansion to reach equilibrium with a final temperature of 95.19 eV, a radius of 1.13 cm and a density of $9.66 \times 10^{22} \text{ m}^{-3}$. The final temperatures are the same regardless of shock occurrence since they must obey the Bennett relation. However, densities are reduced and pinch size is increased. The shock

Table 5.2: Parameters for 10 cm and 16 cm Electrode Configurations undergoing Shock Heating .

parameter	10 cm	16 cm
N	$2 \times 10^{19} \text{ m}^{-1}$	$8.5 \times 10^{18} \text{ m}^{-1}$
T_{annulus}	10 eV	10 eV
I	75 kA	75 kA
n_{pre}	$2.97 \times 10^{21} \text{ m}^{-3}$	$9.17 \times 10^{21} \text{ m}^{-3}$
T_{pre}	21.5 eV	45.7 eV
a_{pre}	4.63 cm	1.79 cm
V_A	$1.3 \times 10^5 \text{ m/s}$	$1.9 \times 10^5 \text{ m/s}$
C_s	$5.86 \times 10^4 \text{ m/s}$	$8.54 \times 10^4 \text{ m/s}$
M	2.2	2.23
n_{post}	$7.36 \times 10^{21} \text{ m}^{-3}$	$2.29 \times 10^{22} \text{ m}^{-3}$
T_{post}	50.87 eV	109.42 eV
a_{post}	2.94 cm	1.13 cm
T_{pinch}	43 eV	95.19 eV
n_{pinch}	$3.07 \times 10^{22} \text{ m}^{-3}$	$9.66 \times 10^{22} \text{ m}^{-3}$
a_{pinch}	2.04 cm	0.78 cm

heats the plasma and reduces its potential compression. These values are summarized in Table 5.2.

5.3 Advanced Compression Analysis

A more advanced method of calculating the effects of the pinch formation process is undertaken to account for the snowplow model of plasma acceleration in the acceleration region and realistic profiles of density and temperature in the pinch. The ZaP acceleration process is expected to produce a thin sheet of plasma near the exit of the accelerator prior

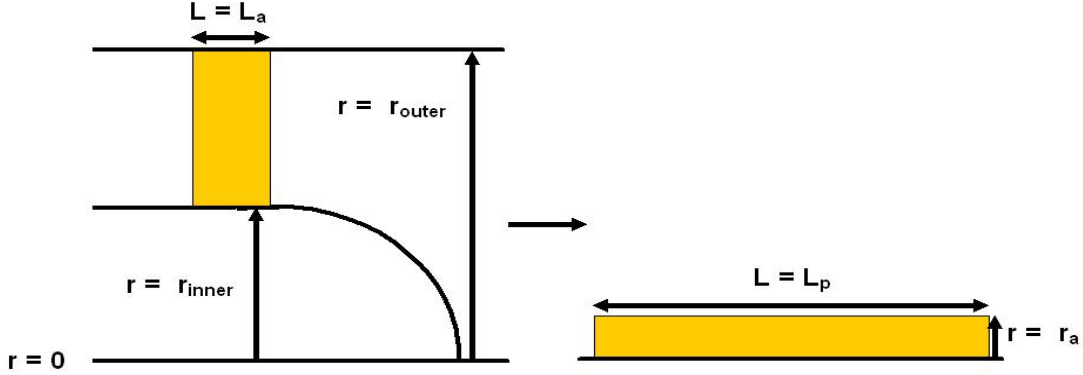


Figure 5.6: Schematic of advanced compression analysis. The snowplow formation process results in a thin sheet of plasma at the exit of the acceleration region. The mass of plasma is azimuthally symmetric with the radial dimensions of the ZaP acceleration region and a finite length, L_a . The mass is adiabatically compressed into a column of plasma with length, L_p , characteristic radius, a and a Lorentzian density and temperature distribution.

to the formation of the pinch. Consider the situation outlined in Figure 5.6, in which a azimuthally-symmetric mass of plasma exists with the radial dimensions of the ZaP plasma accelerator (r_{outer} and r_{inner}) and a finite width, L_a . This mass has a uniform density and temperature.

This mass is adiabatically compressed into a column of plasma with characteristic radius, a , length, L_p , and has axially and azimuthally-uniform Lorentzian density and temperature distributions.

$$n(r) = \frac{n_0 a^2}{r^2 + a^2} \quad (5.49)$$

$$T(r) = \frac{T_0 a^2}{r^2 + a^2} \quad (5.50)$$

where n_0 and T_0 are the peak (on-axis) electron density and temperature, respectively. The initial and final states are assumed to have an equal total number of particles, N_{tot} . The density and temperature profiles create a Bennett pressure profile which can be defined as

$$p = \frac{\mu_0 I^2 a^2}{8\pi^2 (r^2 + a^2)^2} \quad (5.51)$$

The volume-averaged adiabatic condition for the initial state is

$$\left\langle \frac{p}{\rho^\gamma} \right\rangle = \frac{(Z_{\text{eff}} + 1)k_B n_a T_a}{m_i^\gamma n_a^\gamma} \quad (5.52)$$

where T_a is the uniform temperature in the annular mass of plasma, n_a is the uniform density in the annular mass of plasma and $\gamma = 5/3$ is the ratio of specific heats.

$$n_a = \frac{N_{\text{tot}}}{\pi(r_{\text{outer}}^2 - r_{\text{inner}}^2)L_a} \quad (5.53)$$

The final form of Equation 5.52 is

$$\left\langle \frac{p}{\rho^\gamma} \right\rangle_{\text{annulus}} = \frac{(Z_{\text{eff}} + 1)k_B T_a \pi^{\frac{2}{3}} (r_{\text{outer}}^2 - r_{\text{inner}}^2)^{\frac{2}{3}} L_a^{\frac{2}{3}}}{m_i^{\frac{5}{3}} N_{\text{tot}}^{\frac{2}{3}}} \quad (5.54)$$

In this equation, L_a and T_a are free parameters.

The adiabatic condition for the the final state is

$$\left\langle \frac{p}{\rho^\gamma} \right\rangle_{\text{pinch}} = \frac{(Z_{\text{eff}} + 1)k_B n_0 T_0 a^4}{(r^2 + a^2)^2} \quad (5.55)$$

where n_0 can be replaced by

$$n_0 = \frac{N_{\text{tot}}}{\pi a^2 L_p \ln\left(\frac{r_{\text{outer}}^2 + a^2}{a^2}\right)} \quad (5.56)$$

Using Equation 5.51 and $p(r) = (Z_{\text{eff}} + 1)k_B n(r)T(r)$, T_0 can be replaced with

$$T_0 = \frac{\mu_0 I^2 L_p \ln\left(\frac{r_{\text{outer}}^2 + a^2}{a^2}\right)}{8\pi(Z_{\text{eff}} + 1)k_B N_{\text{tot}}} \quad (5.57)$$

and the final form of Equation 5.55 is obtained

$$\left\langle \frac{p}{\rho^\gamma} \right\rangle_{\text{pinch}} = \frac{3\mu_0 a^2 I^2 L_p^{\frac{5}{3}} \left(\ln \left(\frac{r_{\text{outer}}^2 + a^2}{a^2} \right) \right)^{\frac{5}{3}}}{16\pi^{\frac{1}{3}} m_i^{\frac{5}{3}} r_{\text{outer}}^2 N_{\text{tot}}^{\frac{5}{3}}} \left((r_{\text{outer}}^2 + a^2)^{\frac{2}{3}} - a^{\frac{4}{3}} \right) \quad (5.58)$$

The value of a must be solved for by setting Equations 5.54 and 5.58 equal to each other for known values of I and N_{tot} . A closed-form solution to a does not exist for this problem, so it must be solved for iteratively. Once a is known, the temperature profiles are known through Equations 5.50 and 5.57 and the density profiles are known through Equations 5.49 and 5.56.

The equation set must be modified if non-adiabatic effects such as shocks are considered. Assume a process in which adiabatic compression is the case until the mass of plasma reaches the axis ($r = 0$) at which point a shock occurs, followed by adiabatic expansion to the final state. In this scenario, the equation for the final state remains the same, Equation 5.58. The initial state of the plasma mass is still Equation 5.54. A new state immediately prior to the shock must be computed. This state exists under the assumption that the compression process occurs without a change in the radial thickness of the plasma mass, the length is the same as the length of the final state, L_p , and that the density and temperature are uniform. Therefore the pre-shock radius of the plasma column is $r_{\text{outer}} - r_{\text{inner}}$ and the pre-shock density is

$$n_{\text{pre}} = \frac{N_{\text{tot}}}{\pi (r_{\text{outer}} - r_{\text{inner}})^2 L_p} \quad (5.59)$$

The pre-shock adiabatic condition is

$$\left\langle \frac{p}{\rho^\gamma} \right\rangle_{\text{pre}} = \frac{(Z_{\text{eff}} + 1) k_B L_p^{\frac{2}{3}} T_{\text{pre}} \pi^{\frac{2}{3}} (r_{\text{outer}} - r_{\text{inner}})^{\frac{4}{3}}}{m_i^{\frac{5}{3}} N_{\text{tot}}^{\frac{2}{3}}} \quad (5.60)$$

The pre-shock temperature can now be computed

$$T_{\text{pre}} = \frac{T_a (r_{\text{outer}}^2 - r_{\text{inner}}^2)^{\frac{2}{3}} L_a^{\frac{2}{3}}}{(r_{\text{outer}} - r_{\text{inner}})^{\frac{4}{3}} L_p^{\frac{2}{3}}} \quad (5.61)$$

The planar, isentropic shock relations, Equations 5.46 and 5.47, are used to calculate the temperature and density after the shock jump. Cylindrical shock solutions are not used due to their complexity. This scenario presently consists of several arbitrary assumptions for which calculating more exact shock solutions won't produce a more accurate result. The post-shock conditions, assuming uniform temperature and density, are

$$n_{\text{post}} = \frac{4M^2}{M^2 + 3} \frac{N_{\text{tot}}}{\pi(r_{\text{outer}} - r_{\text{inner}})^2 L_p} \quad (5.62)$$

$$a_{\text{post}} = (r_{\text{outer}} - r_{\text{inner}}) \sqrt{\frac{M^2 + 3}{4M^2}} \quad (5.63)$$

$$T_{\text{post}} = \frac{(M^2 + 3)(5M^2 - 1)}{16M^2} \left(\frac{T_a(r_{\text{outer}}^2 - r_{\text{inner}}^2)L_a^{\frac{2}{3}}}{(r_{\text{outer}} - r_{\text{inner}})^{\frac{4}{3}}L_p^{\frac{2}{3}}} \right) \quad (5.64)$$

where M is the Mach number of the shock. The final form for the adiabatic condition after the shock is

$$\left\langle \frac{p}{\rho^\gamma} \right\rangle_{\text{post}} = \frac{(Z_{\text{eff}} + 1)k_B T_a L_a^{\frac{2}{3}} (r_{\text{outer}}^2 - r_{\text{inner}}^2)^{\frac{2}{3}} \pi^{\frac{2}{3}} (M^2 + 3)^{\frac{5}{3}} (5M^2 - 1)}{N_{\text{tot}}^{\frac{2}{3}} L_p^{\frac{2}{3}} (4M^2)^{\frac{2}{3}} m_i^{\frac{5}{3}} 16M^2} \quad (5.65)$$

Equation 5.65 is set equal to Equation 5.58 with a known Mach number to solve for a iteratively. Once a is known, the temperature profiles are known through Equations 5.50 and 5.57 and the density profiles are known through Equations 5.49 and 5.56.

5.4 Ohmic Heating and Radiation

Plasma heating through current flowing through the resistive medium of the plasma, known as Ohmic heating, is used as a primary heating mechanism on most plasma devices. However, Ohmic heating becomes less efficient as the plasma heats up. Ohmic power density to the plasma is defined by $P_{\text{ohmic}} = \eta_{\perp} j^2$ where j is the current density and η_{\perp} is the resistivity of the plasma. Assuming Spitzer resistivity, η_{\perp} is proportional to $T^{-3/2}$ meaning that as temperature increases, resistivity decreases, reducing the Ohmic power contribution.

For this reason, Ohmically heating a plasma to ignition is very unlikely and auxiliary heating systems are often used for plasma heating. In the case of a Z-pinch undergoing Ohmic heating and losing energy through bremsstrahlung radiation a current threshold exists at which the contributions from Ohmic heating are balanced by the losses from bremsstrahlung radiation. This is known as the Pease-Braginskii current [53] [54] and has a value of approximately 1.2 MA. Increasing the current beyond this threshold results in radiative collapse of the pinch [55]. Radiation losses require a contraction of the pinch, increasing the density and the associated radiation until a runaway situation occurs.

5.4.1 Ohmic Heating and Radiation in ZaP

Ohmic heating and radiation effects can occur in both the compression phase and the equilibrium phase of the discharge. Ohmic heating during the compression phase has an effect similar to heating through shocks: potential compression is reduced by the non-reversible increase in energy.

During the equilibrium phase, consider a pinch in some initial equilibrium state that is undergoing Ohmic heating and dissipating energy through bremsstrahlung radiation simultaneously. A radial force balance is assumed that prevents a change in pinch dimensions [56]. For a time-varying current, $I(t)$ well below the Pease-Braginskii limit, the temperature of the pinch is dictated by the Bennett relation. As temperature increases due to Ohmic heating, the current must increase to maintain the pinch dimensions. Additional loss mechanisms such as line radiation, radial heat conduction and convection are possible on ZaP and could result in a reduction of temperature and, by extension, current.

Alternately, with a radial force balance that allows changes in the pinch dimensions, if Ohmic contributions from a constant current pinch are greater than potential loss mechanisms such as radiation, heat conduction and convective losses, the result is an increase in pinch radius and a reduction in density. For an Ohmic contribution that is less than these potential losses, a constant current pinch would contract, increasing the density.

Chapter 6

EQUILIBRIUM EVOLUTION IN THE ZAP FLOW Z-PINCH

6.1 Interferometry Analysis

The equilibrium evolution in the ZaP Flow Z-Pinch is calculated using a four-chord interferometer. The four chords are placed at $z = 0$ cm at different impact parameters. Figure 6.1 shows a schematic example of the four-chord interferometry setup. The yellow circle is an axial view of the Z-pinch plasma column. The black dot indicates the location of the current centroid. The four colored horizontal lines indicate an example of the locations of the four interferometry chords. Figure 6.2 are the magnetic data at $z = 0$ cm for a representative high peak magnetic field pulse. The resulting chord-integrated density data as a function of time and the y -location of the current centroid for this pulse are shown in Figure 6.3. The colors in Figure 6.3 are representative of the colors in Figure 6.1 and their relationship to the location of the current centroid. Figure 6.4 are the same data during the quiescent period of the pulse. The data indicate a well-defined pinch with a noticeable density gradient. The interferometry chord closest to the current centroid has the highest chord-integrated density. As the chords move away from the current centroid, the chord-integrated density decreases.

As mentioned previously, the fast oscillations in the chord-integrated density data are likely related to saturated instabilities traveling along the length of the pinch and are not of interest to the calculation of the equilibrium. The chord-integrated data are filtered with EMD and a smoother signal is the result, see Section 2.3.3.

At each temporal point during a pulse, the four chord-integrated data points and the location of the current centroid are analyzed with respect to one another. Figure 6.5 shows an example of the data as a function of impact parameter relative to the machine axis with

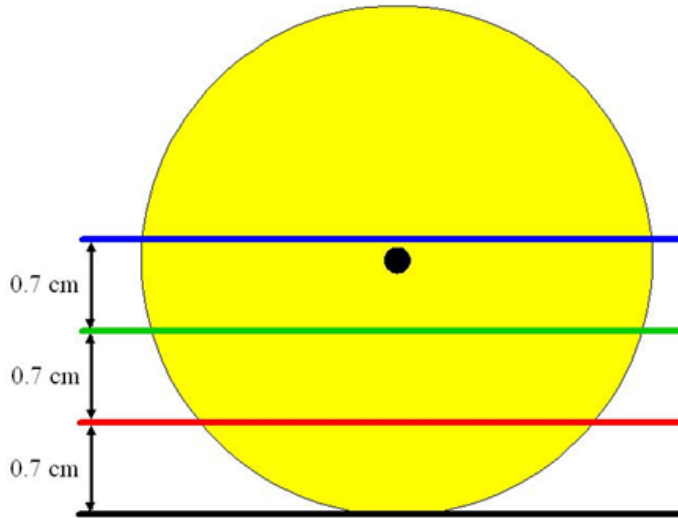


Figure 6.1: Schematic of four-chord interferometer setup. The yellow circle signifies an end-on view of the pinch with the four interferometer scene beams passing through at impact parameters that are spaced 7 mm apart. The colors of the scene beams are consistent with the colors of the data in Figure 6.4.

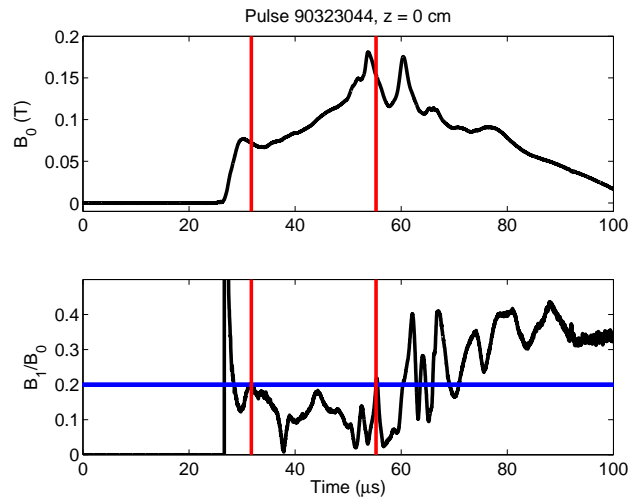


Figure 6.2: Magnetic mode data for high peak magnetic field operating conditions. Pulses are characterized by a magnetic field plateau during the quiescent period preceding a steep rise in the magnetic field. The peak of the magnetic field typically precedes the end of the quiescent period. Vertical red lines indicate the beginning and end of the quiescent period.

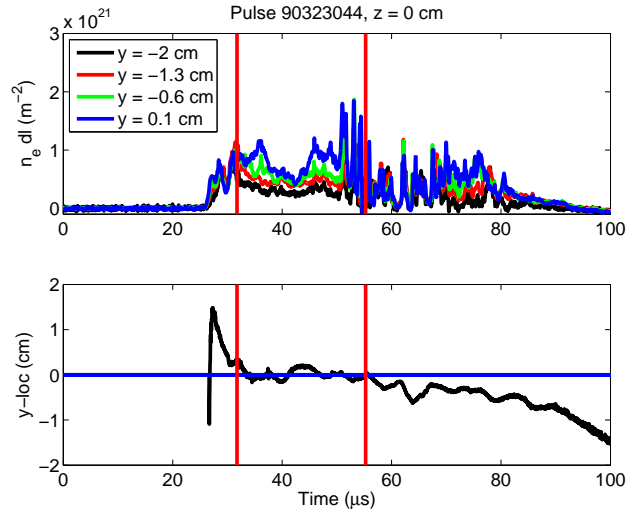


Figure 6.3: Four-chord interferometry data for high peak magnetic field operating conditions. A gradient in chord-integrated density is observed during the quiescent period. Bottom plot is the y -location of the current centroid. Vertical red lines indicate the beginning and end of the quiescent period.

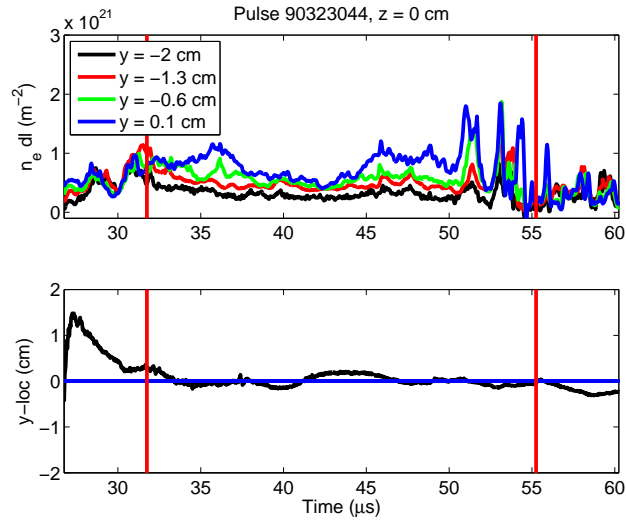


Figure 6.4: Inset view of interferometry data for high peak magnetic field operating condition. Interferometry data during the quiescent period for the high peak magnetic field operating condition shows a well-defined pinch with a noticeable density gradient. This is shown by noting that the chord located closest to the machine axis has the highest magnitude and as the chords move away from the machine axis, the magnitudes decrease.

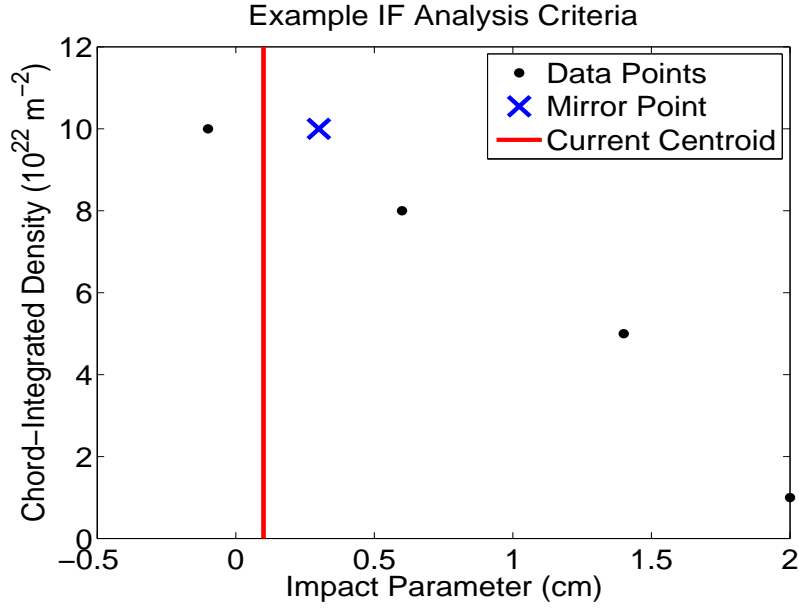


Figure 6.5: Example interferometry data at a temporal point. Values of the chord-integrated density must be monotonically decreasing with increasing distance from the current centroid. Impact parameter is with respect to the machine axis.

the four points indicating magnitudes of the chord-integrated data and the vertical line indicating the location of the current centroid. The following analysis assumes a diffuse density profile that extends to the outer electrode and that the location of the current centroid is coincident with the pinch axis. Azimuthal symmetry about the current centroid is assumed. The values of the chord-integrated density must be monotonically decreasing with increasing distance from the current centroid. If this condition is not met, the temporal point is skipped and the next temporal point is investigated.

A density profile is assumed that is based on a Bennett equilibrium pressure profile. The Bennett equilibrium is chosen because it is an analytic solution that is well-studied,

$$p = \frac{\mu_0 I_0^2}{8\pi^2} \frac{a^2}{(r^2 + a^2)^2} \quad (6.1)$$

The resulting temperature is expected to have a profile as a function of radius, not a

uniform temperature profile, so the initial assumption is that the density and temperature profiles are proportional to each other. This produces a Lorentzian density profile

$$n(r) = \frac{n_0 a^2}{r^2 + a^2} \quad (6.2)$$

where n_0 is the density at $r = 0$ and a is the characteristic radius of the pinch. An assumed profile for the chord-integrated density profile can be calculated given a Lorentzian density profile assumption.

$$n_{\text{chord-int}} = \int_{-x'}^{x'} n_e(r) dl \quad (6.3)$$

where $dl = dx$ and x' is the horizontal extent of the outer electrode at a given impact parameter. The resulting equation for the chord-integrated density profile becomes

$$(n_{\text{chord-int}})_i = 2n_0 a^2 \left(\frac{\tan^{-1} \left(\frac{x'}{\sqrt{y_i^2 + a^2}} \right)}{\sqrt{y_i^2 + a^2}} \right) \quad (6.4)$$

where y_i is the impact parameter and $x = \sqrt{r_w^2 - y_i^2}$ is the chord length within the outer electrode. The four chord-integrated points are fit to this chord-integrated profile with a nonlinear least-squares solver that has two parameters for which to solve, a and n_0 . The least-squares solver uses a Newton iterative method to determine the values of these parameters. An initial profile is guessed and the difference between the measured chord-integrated values and the assumed profile is assessed

$$d\beta = |n_{\text{chord-int}}(\text{measured}) - n_{\text{chord-int}}(\text{guess})| \quad (6.5)$$

which produces a column vector of length 4. An 4×2 Jacobian matrix is produced with the assumed profile.

$$A_i = \left(\frac{d(n_{\text{chord-int}})_i}{da} \quad \frac{d(n_{\text{chord-int}})_i}{dn_0} \right) \quad (6.6)$$

A and $d\beta$ are then solved as the system of equations

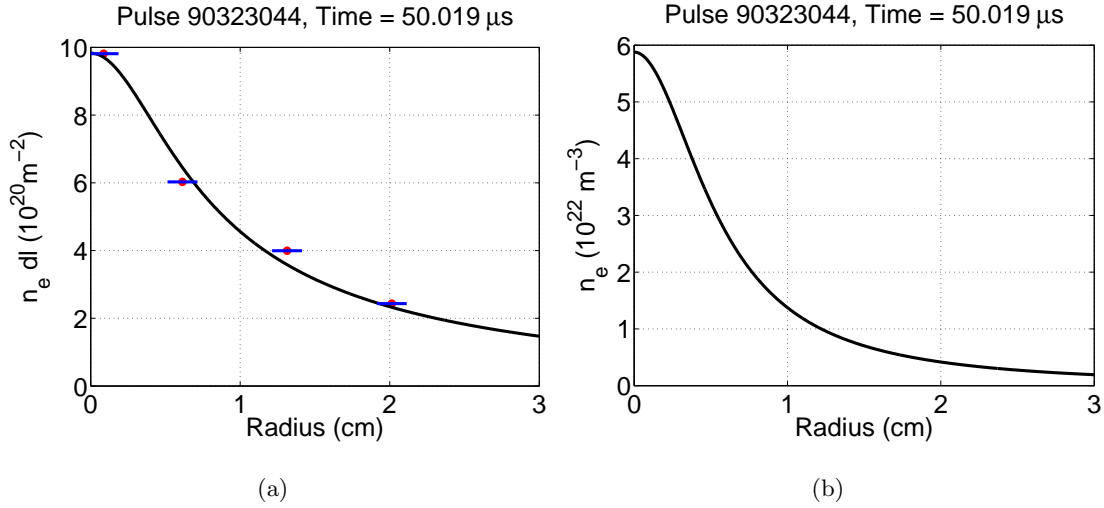


Figure 6.6: Chord-integrated fits and electron density profiles. (a) Chord-integrated data points are with a nonlinear least-squares approach. Impact parameter is with respect to the current centroid. Red points are experimentally-measured; blue horizontal lines are the estimated measurement uncertainty of chord locations. (b) A Lorentzian electron density profile is calculated with the known values of a and n_0 .

$$A \begin{pmatrix} a \\ n_0 \end{pmatrix} = d\beta \quad (6.7)$$

to produce a new guess for the values of a and n_0 . This process is iterated until a converged solution is determined.

Figure 6.6 shows the chord-integrated points and the converged chord-integrated fit at a single time for the given pulse, and the resulting electron density profile. The red points are the experimentally-measured chord integrated values as a function of impact parameter relative to the current centroid. The horizontal blue lines indicate the estimated measurement uncertainty of the chord locations which is ± 1 mm. The vertical error bars are smaller than the symbol size.

The evolution of the density profile can be evaluated due to the time-resolved nature of the interferometer. Figure 6.7 shows the evolution of the values of the characteristic radius

and the on-axis density as a function of time. The gaps in the data are due to failure to meet the condition of monotonically decreasing values of chord-integrated with increasing distance from the current centroid. The overall behavior of this pulse suggests that the pinch is being compressed as a function of time with the characteristic radius of the pinch decreasing by up to a factor of 3 and the resulting peak electron density increasing similarly to a peak of $7.5 \times 10^{22} \text{ m}^{-3}$. The red lines are analytic linear trendlines that are fit to the data, with R^2 values of the fit specified. This is expected from Figure 6.8 which shows the total current at $z = 0 \text{ cm}$ and the linear density as a function of time. The total current is calculated using Ampere's law with the measured magnetic field at $z = 0 \text{ cm}$. The total current is increasing by a factor of 2 and the linear density is staying approximately constant as a function of time which results in a compression of the pinch. The data also indicates that there are irregular oscillations in the size of the pinch, the cause of which will be investigated later. These oscillations can be as much as a factor of two for the high peak magnetic field operating condition.

The overall evolution of the density profile can more readily be investigated using a contour plot of electron density as a function of radius and time as shown in Figure 6.9. The oscillations in the characteristic radius of the pinch are more readily apparent, as is the overall trend of compression.

6.2 Calculations of Magnetic Field and Temperature Profiles

Using the calculated density profiles at a given time, the equations of conservation of energy and radial force balance can be used to calculate profiles for the magnetic field and temperature of the pinch. The conservation of energy equation is

$$\frac{3}{2} \frac{\partial p}{\partial t} + \frac{3}{2} \nabla \cdot p\mathbf{v} + p\nabla \cdot \mathbf{v} + \nabla \cdot \mathbf{q} = S \quad (6.8)$$

where the first term in Equation 6.8 represents the time rate of change of the internal energy density, the second term represents the convection losses, the third term is energy loss due to fluid expansion, the fourth term is losses due to diffusive processes and S represents

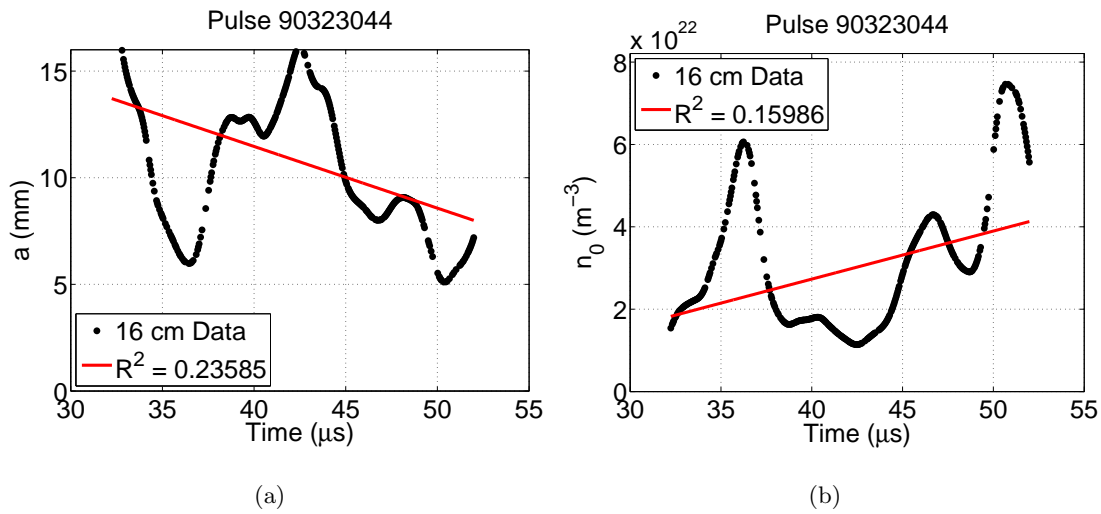


Figure 6.7: Characteristic pinch radius and peak density as a function of time. (a) Overall trend is a decrease in the size of the pinch with increasing time. Irregular oscillations can be as much as a factor of two for high peak magnetic field operation. (b) On-axis density is anti-correlated with the pinch size, as expected. Overall trend is increasing peak density to a maximum of $7.5 \times 10^{22} \text{ m}^{-3}$. The pinch is compressing as a function of time. The red lines are linear trendlines to the data.

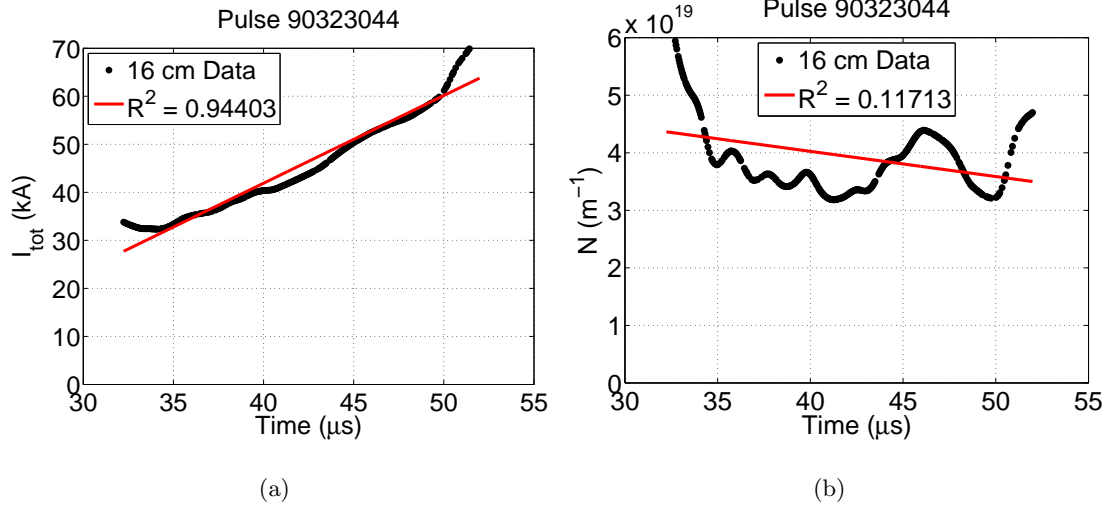


Figure 6.8: Total current and linear density as a function of time. (a) Total current is increasing as a function of time, consistent with the compression of the pinch. (b) The linear density is approximately constant as a function of time, resulting in an increase in peak electron density due to compression of the pinch. The red lines are linear trendlines.

sources and sinks of energy in the system [57].

The equation for radial force balance is

$$\frac{B_\theta}{r} \frac{d(rB_\theta)}{dr} = -\mu_0 k_B \frac{d}{dr} (n_e T_e + n_i T_i) \quad (6.9)$$

A steady-state equilibrium is considered, removing the first term in Equation 6.8. Convective and expansion losses are also neglected. The primary diffusive process is assumed to be radial heat conduction and the source terms are assumed to be Ohmic power input and bremsstrahlung radiation. Conservation of energy becomes

$$\nabla \cdot \mathbf{q} = \eta_\perp j^2 - P_{\text{Brem}} \quad (6.10)$$

where η_\perp is cross-field Spitzer resistivity. Equations 6.9 and 6.10 represent a set of differential equations that must be solved to determine the temperature and magnetic field

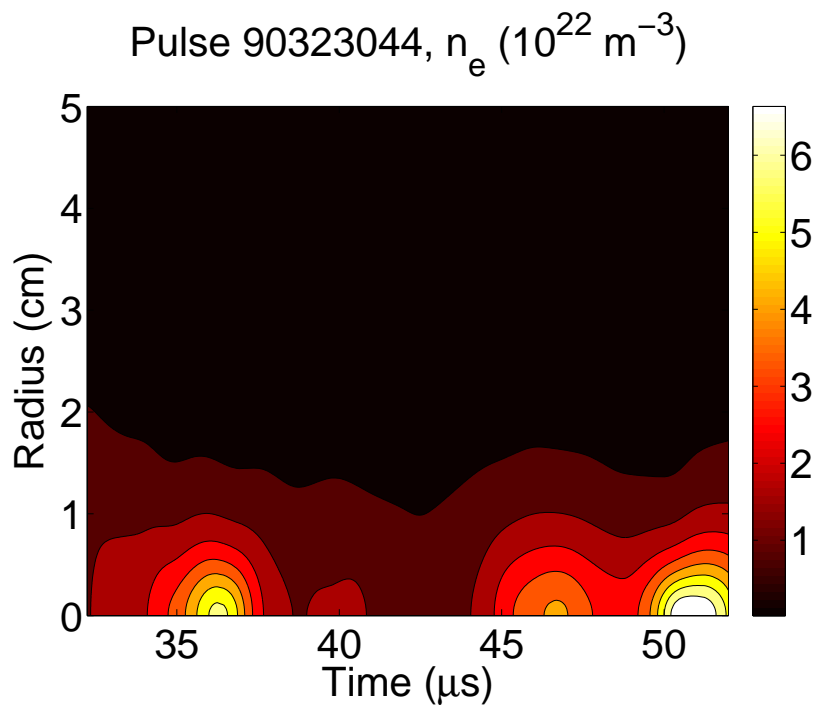


Figure 6.9: Contour plot of electron density for high peak field operating conditions. Electron density contours as a function of radius and time indicate the overall compression of the pinch and the irregular oscillations in the pinch radius. The peak density late in time is $7.5 \times 10^{22} \text{ m}^{-3}$.

profiles.

The radial force balance equation is treated first. Both sides of Equation 6.9 are multiplied by r^2 and the assumptions of $T = T_e = T_i$ and $n = n_e/Z_{\text{eff}} = n_i$ are made.

$$rB_\theta \frac{d}{dr}(rB_\theta) = -\mu_0 k_B (Z_{\text{eff}} + 1) r^2 \frac{d}{dr}(nT) \quad (6.11)$$

Using chain rule on both sides of the equation gives

$$\frac{d(rB_\theta)^2}{dr} = -2\mu_0 k_B (Z_{\text{eff}} + 1) r^2 \left(T \frac{dn}{dr} + n \frac{dT}{dr} \right) \quad (6.12)$$

$$\frac{d(rB_\theta)^2}{dr} = c_1 r^2 \left(T \frac{dn}{dr} + n \frac{dT}{dr} \right) \quad (6.13)$$

where $c_1 = -2\mu_0 k_B (Z_{\text{eff}} + 1)$. Equation 6.13 is the final form of the radial force balance equation.

The Ohmic power term is treated next. Cross-field Spitzer resistivity is [9]

$$\eta_\perp = 1.035 \times 10^{-4} Z_{\text{eff}} \ln \Lambda T_e^{-\frac{3}{2}} \quad (6.14)$$

From Ampere's Law,

$$\mathbf{j} = \frac{1}{\mu_0} \nabla \times \mathbf{B} \quad (6.15)$$

$$j^2 = \mathbf{j} \cdot \mathbf{j} = \frac{1}{\mu_0^2} (\nabla \times \mathbf{B}) \cdot (\nabla \times \mathbf{B}) \quad (6.16)$$

$$\eta_\perp j^2 = \frac{1.03 \times 10^{-4} Z_{\text{eff}} \ln \Lambda T_e^{-\frac{3}{2}}}{\mu_0^2} (\nabla \times \mathbf{B}) \cdot (\nabla \times \mathbf{B}) \quad (6.17)$$

$$(\nabla \times \mathbf{B}) \cdot (\nabla \times \mathbf{B}) = \frac{1}{r^2} \left(\frac{d(rB_\theta)}{dr} \right)^2 \quad (6.18)$$

From Equation 6.13

$$\left(\frac{d(rB_\theta)}{dr}\right)^2 = \frac{c_1^2 r^4}{4(rB_\theta)^2} \left(T \frac{dn}{dr} + n \frac{dT}{dr}\right)^2 \quad (6.19)$$

Defining $c_3 = \frac{1.035 \times 10^{-4} Z_{\text{eff}} \ln \Lambda}{\mu_0^2}$ gives

$$\eta_\perp j^2 = \frac{c_3 c_1^2 r^2}{4(rB_\theta)^2 T^{\frac{3}{2}}} \left[T^2 \left(\frac{dn}{dr}\right)^2 + 2nT \frac{dn}{dr} \frac{dT}{dr} + n^2 \left(\frac{dT}{dr}\right)^2 \right] \quad (6.20)$$

$$\eta_\perp j^2 = \frac{c_3 c_1^2}{4} \left[\frac{r^2 T^{\frac{1}{2}}}{(rB_\theta)^2} \left(\frac{dn}{dr}\right)^2 + \frac{2nr^2}{(rB_\theta)^2 T^{\frac{1}{2}}} \frac{dn}{dr} \frac{dT}{dr} + \frac{n^2 r^2}{(rB_\theta)^2 T^{\frac{3}{2}}} \left(\frac{dT}{dr}\right)^2 \right] \quad (6.21)$$

Equation 6.21 is the final form of the Ohmic power term.

The radial heat conduction term has the form

$$\nabla \cdot \mathbf{q} = -\frac{k_B}{r} \frac{d}{dr} \left[r \left(\kappa_{\perp e} \frac{dT_e}{dr} + \kappa_{\perp i} \frac{dT_i}{dr} \right) \right] \quad (6.22)$$

where the ion and electron thermal conductivities are

$$\kappa_{\perp i} = \frac{2n_i k_B T_i}{m_i \omega_{ci}^2 \tau_i} \quad (6.23)$$

$$\kappa_{\perp e} = \frac{4.66 n_e k_B T_e}{m_e \omega_{ce}^2 \tau_e} \quad (6.24)$$

the cyclotron frequencies are

$$\omega_{ci} = 9.58 \times 10^7 Z_{\text{eff}} B_\theta \quad (6.25)$$

$$\omega_{ce} = 1.76 \times 10^{11} B_\theta \quad (6.26)$$

and the self-collision times of the ions and electrons are

$$\tau_i = 2.09 \times 10^{13} \frac{T_i^{\frac{3}{2}}}{Z_{\text{eff}}^4 n_i \ln \Lambda} \quad (6.27)$$

$$\tau_e = 3.44 \times 10^{11} \frac{T_e^{\frac{3}{2}}}{Z_{\text{eff}}^2 n_i \ln \Lambda} \quad (6.28)$$

The thermal conductivities become

$$\kappa_{\perp e} = \frac{7.681 \times 10^{-23} n^2 Z_{\text{eff}}^3 \ln \Lambda}{B_\theta^2 T^{\frac{1}{2}}} \quad (6.29)$$

$$\kappa_{\perp i} = \frac{9.9898 \times 10^{-22} n^2 Z_{\text{eff}}^2 \ln \Lambda}{B_\theta^2 T^{\frac{1}{2}}} \quad (6.30)$$

and the radial heat conduction term becomes

$$\nabla \cdot \mathbf{q} = -\frac{k_B}{r} \frac{d}{dr} \left[r \frac{dT}{dr} \left(\frac{9.9898 \times 10^{-22} n^2 Z_{\text{eff}}^2 \ln \Lambda}{B_\theta^2 T^{\frac{1}{2}}} + \frac{7.681 \times 10^{-23} n^2 Z_{\text{eff}}^3 \ln \Lambda}{B_\theta^2 T^{\frac{1}{2}}} \right) \right] \quad (6.31)$$

$$\nabla \cdot \mathbf{q} = -\frac{c_2}{r} \frac{d}{dr} \left(r \frac{dT}{dr} \frac{n^2}{B_\theta^2 T^{\frac{1}{2}}} \right) \quad (6.32)$$

where $c_2 = k_B(9.9898 \times 10^{-22} Z_{\text{eff}}^2 \ln \Lambda + 7.681 \times 10^{-23} Z_{\text{eff}}^3 \ln \Lambda)$. Multiplying by r^2/r^2 inside the differential term in Equation 6.32 to produce an equation form that is more conducive to the analysis gives

$$\nabla \cdot \mathbf{q} = -\frac{c_2}{r} \frac{d}{dr} \left(\frac{dT}{dr} \frac{r^3 n^2}{(r B_\theta)^2 T^{\frac{1}{2}}} \right) \quad (6.33)$$

Expanding the differential term through the chain rule,

$$\frac{d}{dr} \left(\frac{dT}{dr} \frac{r^3 n^2}{(r B_\theta)^2 T^{\frac{1}{2}}} \right) = \frac{r^3 n^2}{(r B_\theta)^2 T^{\frac{1}{2}}} \frac{d^2 T}{dr^2} + \frac{dT}{dr} \frac{d}{dr} \left(\frac{r^3 n^2}{(r B_\theta)^2 T^{\frac{1}{2}}} \right) \quad (6.34)$$

$$\frac{d}{dr} \left(\frac{r^3 n^2}{(r B_\theta)^2 T^{\frac{1}{2}}} \right) = -\frac{r^3 n^2}{T^{\frac{1}{2}} (r B_\theta)^4} \frac{d(r B_\theta)^2}{dr} + \frac{1}{(r B_\theta)^2} \frac{d}{dr} \left(\frac{r^3 n^2}{T^{\frac{1}{2}}} \right) \quad (6.35)$$

$$\frac{d}{dr} \left(\frac{r^3 n^2}{T^{\frac{1}{2}}} \right) = \frac{3r^2 n^2}{T^{\frac{1}{2}}} + r^3 \frac{d}{dr} \left(\frac{n^2}{T^{\frac{1}{2}}} \right) \quad (6.36)$$

$$\frac{d}{dr} \left(\frac{n^2}{T^{\frac{1}{2}}} \right) = 2T^{\frac{1}{2}} n \frac{dn}{dr} - \frac{n^2}{2T^{\frac{3}{2}}} \frac{dT}{dr} \quad (6.37)$$

results in the following form of Equation 6.32

$$\begin{aligned} \nabla \cdot \mathbf{q} = & -\frac{c_2}{r} \left[\frac{r^3 n^2}{(rB_\theta)^2 T^{\frac{1}{2}}} \frac{d^2 T}{dr^2} + \frac{dT}{dr} \left(-\frac{r^3 n^2}{(rB_\theta)^4 T^{\frac{1}{2}}} \frac{d(rB_\theta)^2}{dr} \right. \right. \\ & \left. \left. + \frac{1}{(rB_\theta)^2} \left[\frac{3r^2 n^2}{T^{\frac{1}{2}}} + r^3 \left(2T^{\frac{1}{2}} n \frac{dn}{dr} - \frac{n^2}{2T^{\frac{3}{2}}} \frac{dT}{dr} \right) \right] \right) \right] \end{aligned} \quad (6.38)$$

replacing $\frac{d(rB_\theta)^2}{dr}$ with Equation 6.13, using the variable $u = (rB_\theta)^2$, multiplying through and grouping terms gives

$$\begin{aligned} \nabla \cdot \mathbf{q} = & -\frac{c_2 r^2 n^2}{u T^{\frac{1}{2}}} \frac{d^2 T}{dr^2} + \left(\frac{dT}{dr} \right)^2 \left(\frac{c_1 c_2 r^4 n^3}{T^{\frac{1}{2}} u^2} + \frac{c_2 r^2 n^2}{2u T^{\frac{3}{2}}} \right) + \\ & \frac{dT}{dr} \left(\frac{c_2 c_1 r^4 n^2 T^{\frac{1}{2}}}{u^2} \frac{dn}{dr} - \frac{3c_2 r n^2}{u T^{\frac{1}{2}}} - \frac{2c_2 r^2 n}{u T^{\frac{1}{2}}} \frac{dn}{dr} \right) \end{aligned} \quad (6.39)$$

Including the terms from Equation 6.21 the full equation for $\nabla \cdot \mathbf{q} = \eta j^2$ with grouped terms is

$$\begin{aligned} & -\frac{c_2 r^2 n^2}{u T^{\frac{1}{2}}} \frac{d^2 T}{dr^2} + \left(\frac{dT}{dr} \right)^2 \left(\frac{c_1 c_2 r^4 n^3}{T^{\frac{1}{2}} u^2} + \frac{c_2 r^2 n^2}{2u T^{\frac{3}{2}}} - \frac{c_1^2 c_3 n^2 r^2}{4u T^{\frac{3}{2}}} \right) + \\ & \frac{dT}{dr} \left(\frac{c_1 c_2 r^4 n^2 T^{\frac{1}{2}}}{u^2} \frac{dn}{dr} - \frac{3c_2 r n^2}{u T^{\frac{1}{2}}} - \frac{2c_2 r^2 n}{u T^{\frac{1}{2}}} \frac{dn}{dr} - \frac{c_1^2 c_3 r^2 n}{2u T^{\frac{1}{2}}} \frac{dn}{dr} \right) = \frac{c_1^2 c_3 r^2 T^{\frac{1}{2}}}{4u} \left(\frac{dn}{dr} \right)^2 \end{aligned} \quad (6.40)$$

The final result is two non-linear ordinary differential equations which are summarized below. From Equation 6.40,

$$\frac{d^2 T}{dr^2} + \beta_1 \left(\frac{dT}{dr} \right)^2 + \chi_1 \frac{dT}{dr} = \Gamma_1 \quad (6.41)$$

where the coefficient of $\frac{d^2 T}{dr^2}$ has been divided through the equation. The resulting values for β_1 , χ_1 and Γ_1 are

$$\beta_1 = \frac{c_1^2 c_3}{4c_2 T} - \frac{c_1 r^2 n}{u} - \frac{1}{2T} \quad (6.42)$$

$$\chi_1 = -\frac{c_1 r^2 T}{u} \frac{dn}{dr} + \frac{3}{r} + \frac{2}{n} \frac{dn}{dr} + \frac{c_1^2 c_3}{2c_2 n} \frac{dn}{dr} \quad (6.43)$$

$$\Gamma_1 = -\frac{c_1^2 c_3 T}{4c_2 n^2} \left(\frac{dn}{dr} \right)^2 + P_{\text{Brem}} \quad (6.44)$$

The bremsstrahlung term is

$$P_{\text{Brem}} = 1.69 \times 10^{-38} Z_{\text{eff}}^2 n^2 T^{\frac{1}{2}} \quad (6.45)$$

Alternately, the bremsstrahlung term can be replaced with a total radiation term, $I_f n^2 10^{P_z}$, where I_f is the impurity fraction and

$$\begin{aligned} \log(P_z) = & A_0 + A_1 \left[\log\left(\frac{T}{1000}\right) \right] + A_2 \left[\log\left(\frac{T}{1000}\right) \right]^2 + A_3 \left[\log\left(\frac{T}{1000}\right) \right]^3 + \\ & A_4 \left[\log\left(\frac{T}{1000}\right) \right]^4 + A_5 \left[\log\left(\frac{T}{1000}\right) \right]^5 \end{aligned} \quad (6.46)$$

where the coefficients A_i can be found in the report by Post [58] for multiple temperature ranges and an assumed primary impurity radiator. This model assumes coronal equilibrium and ignores time-dependent radiation effects. Given the impurity fraction, an average charge state of the impurities can also be determined from the same reference.

$$\begin{aligned} \langle Z_i \rangle = & B_0 + B_1 \left[\log\left(\frac{T}{1000}\right) \right] + B_2 \left[\log\left(\frac{T}{1000}\right) \right]^2 + B_3 \left[\log\left(\frac{T}{1000}\right) \right]^3 + \\ & B_4 \left[\log\left(\frac{T}{1000}\right) \right]^4 + B_5 \left[\log\left(\frac{T}{1000}\right) \right]^5 \end{aligned} \quad (6.47)$$

Z_{eff} for the plasma is calculated as a sum of average charge states of the ions across all ion species.

$$Z_{\text{eff}} = \frac{\sum_i n_i Z_i^2}{\sum_i n_i Z_i} \quad (6.48)$$

From the radial force balance equation, Equation 6.13,

$$\frac{du}{dr} - \chi_2 \frac{dT}{dr} = \Gamma_2 \quad (6.49)$$

where

$$\chi_2 = c_1 r^2 n \quad (6.50)$$

$$\Gamma_2 = c_1 r^2 T \frac{dn}{dr} \quad (6.51)$$

This system of two equations can be further reduced into a system of three nonlinear first-order ordinary differential equations.

$$\gamma = \frac{dT}{dr} \quad (6.52)$$

$$\gamma' = \Gamma_1 - \beta_1 \gamma^2 - \chi_1 \gamma \quad (6.53)$$

$$u' = \Gamma_2 + \chi_2 \gamma \quad (6.54)$$

The boundary conditions for this system of equations are

$$\gamma(r = 0) = 0 \quad (6.55)$$

$$u(r = 0) = 0 \quad (6.56)$$

$$u(r = r_w) = (r_w B_w)^2 \quad (6.57)$$

By inspection, the equation set would appear to have $1/r$ and $1/u$ singularities at the axis. These occur in Equations 6.43 and 6.42. These terms are multiplied by dT/dr , which is zero at the axis, resolving the singularity issues.

Numerical errors occur when $T \rightarrow 0$. To treat these issues, temperature is redefined in the equation set as a constant minimum temperature in addition to a changing values of temperature that is calculated as a logarithm.

$$T = T_{\min} + 10^\alpha \quad (6.58)$$

$$\gamma = \frac{1}{\ln(10) \left(T_{\min} + 10^\alpha \right)} \gamma' \quad (6.59)$$

where α is a fundamental solution variable.

The system of equations can be solved with a fourth-order Runge-Kutta shooting method. A value for the temperature at the axis is guessed and the equation set is integrated through the domain. The equations are functions of three unknown variables T , γ and u and two known variables n and $\frac{dn}{dr}$. Assume that $\alpha = f(r, n, \frac{dn}{dr}, T, \gamma, u)$, $\gamma' = g(r, n, \frac{dn}{dr}, T, \gamma, u)$, $u' = w(r, n, \frac{dn}{dr}, T, \gamma, u)$ and $h = \Delta r$. The following equations are used to increment the solution through the domain.

$$k_1^i = hf(r_i, n(r = r_i), \frac{dn}{dr}(r = r_i), T_i, \gamma_i, u_i) \quad (6.60)$$

$$l_1^i = hg(r_i, n(r = r_i), \frac{dn}{dr}(r = r_i), T_i, \gamma_i, u_i) \quad (6.61)$$

$$m_1^i = hw(r_i, n(r = r_i), \frac{dn}{dr}(r = r_i), T_i, \gamma_i, u_i) \quad (6.62)$$

$$k_2^i = hf(r_i + \frac{1}{2}h, n(r = r_i + \frac{1}{2}h), \frac{dn}{dr}(r = r_i + \frac{1}{2}h), T_i + \frac{1}{2}k_1^i, \gamma_i + \frac{1}{2}l_1^i, u_i + \frac{1}{2}m_1^i) \quad (6.63)$$

$$l_2^i = hg(r_i + \frac{1}{2}h, n(r = r_i + \frac{1}{2}h), \frac{dn}{dr}(r = r_i + \frac{1}{2}h), T_i + \frac{1}{2}k_1^i, \gamma_i + \frac{1}{2}l_1^i, u_i + \frac{1}{2}m_1^i) \quad (6.64)$$

$$m_2^i = hw(r_i + \frac{1}{2}h, n(r = r_i + \frac{1}{2}h), \frac{dn}{dr}(r = r_i + \frac{1}{2}h), T_i + \frac{1}{2}k_1^i, \gamma_i + \frac{1}{2}l_1^i, u_i + \frac{1}{2}m_1^i) \quad (6.65)$$

$$k_3^i = hf(r_i + \frac{1}{2}h, n(r = r_i + \frac{1}{2}h), \frac{dn}{dr}(r = r_i + \frac{1}{2}h), T_i + \frac{1}{2}k_2^i, \gamma_i + \frac{1}{2}l_2^i, u_i + \frac{1}{2}m_2^i) \quad (6.66)$$

$$l_3^i = hg(r_i + \frac{1}{2}h, n(r = r_i + \frac{1}{2}h), \frac{dn}{dr}(r = r_i + \frac{1}{2}h), T_i + \frac{1}{2}k_2^i, \gamma_i + \frac{1}{2}l_2^i, u_i + \frac{1}{2}m_2^i) \quad (6.67)$$

$$m_3^i = hw(r_i + \frac{1}{2}h, n(r = r_i + \frac{1}{2}h), \frac{dn}{dr}(r = r_i + \frac{1}{2}h), T_i + \frac{1}{2}k_2^i, \gamma_i + \frac{1}{2}l_2^i, u_i + \frac{1}{2}m_2^i) \quad (6.68)$$

$$k_4^i = hf(r_i + h, n(r = r_i + h), \frac{dn}{dr}(r = r_i + h), T_i + k_3^i, \gamma_i + l_3^i, u_i + m_3^i) \quad (6.69)$$

$$l_4^i = hg(r_i + h, n(r = r_i + h), \frac{dn}{dr}(r = r_i + h), T_i + k_3^i, \gamma_i + l_3^i, u_i + m_3^i) \quad (6.70)$$

$$m_4^i = hw(r_i + h, n(r = r_i + h), \frac{dn}{dr}(r = r_i + h), T_i + \frac{1}{2}k_3^i, \gamma_i + l_3^i, u_i + m_3^i) \quad (6.71)$$

$$T_{i+1} = T_i + \frac{1}{6}(k_1^i + 2k_2^i + 2k_3^i + k_4^i) \quad (6.72)$$

$$\gamma_{i+1} = \gamma_i + \frac{1}{6}(l_1^i + 2l_2^i + 2l_3^i + l_4^i) \quad (6.73)$$

$$u_{i+1} = u_i + \frac{1}{6}(m_1^i + 2m_2^i + 2m_3^i + m_4^i) \quad (6.74)$$

The nonlinear terms in the equation set result in a stiff system of equations that a simple shooting method is incapable of properly solving. A more advanced method called multiple shooting is used.

6.3 Multiple Shooting Method

Consider the system of equations to have the following form,

$$y' = f(r, y) \quad (6.75)$$

$$y = \begin{pmatrix} T \\ \gamma \\ u \end{pmatrix} \quad (6.76)$$

In the case of a simple shooting method, a vector of initial guesses, s , for the on-axis values of y is made. For this equation set, the guess is only for the values of T because γ and u have boundary conditions at the axis.

$$s^i = \begin{pmatrix} T^i \\ 0 \\ 0 \end{pmatrix} \quad (6.77)$$

The starting guess is then iterated by means of Newton's method:

$$s^{i+1} = s^i - \frac{F(s^i)}{F'(s^i)} \quad (6.78)$$

where

$$F(s) = y(r = r_{\text{wall}}; s) - y(r = r_{\text{wall}}) \quad (6.79)$$

The right side of this equation is interpreted as the difference between the calculated values of y at the boundary due to the shooting method and the prescribed boundary conditions at the wall. $F'(s^i)$ is the derivative of F with respect to s . This derivative can be approximated as a difference quotient $\Delta F(s^i)$,

$$\Delta F(s^i) = \frac{F(s^i + \Delta s^i) - F(s^i)}{\Delta s^i} \quad (6.80)$$

where Δs^i is chosen sufficiently small, in this case $\Delta s^i = \sqrt{\epsilon} s^i$, where $\epsilon \approx 10^{-16}$ is machine precision.

The simple shooting method (one integration across full domain of integration) can be problematic because even if the boundary-value problem is well-posed, the resulting initial-value problem that is being solved can be very sensitive to the initial conditions. A method of addressing these issues is to break the domain of integration into multiple sections and integrating each of the section independently with its own starting guess. This method is called multiple shooting and is described more completely elsewhere [59], but will be summarized below.

A diagram of the logic behind a multiple shooting method is shown in Figure 6.10. The domain is broken into $m - 1$ subdomains and each subdomain has its own individual set of initial guesses, s_k , for y determined by an initial guess of the radial profiles of y .

$$s_k^i = \begin{pmatrix} T_{g,k}^i \\ \gamma_{g,k}^i \\ u_{g,k}^i \end{pmatrix} \quad (6.81)$$

The equation set is then integrated within each domain using the fourth-order Runge-Kutta method. The calculated values of y at the right side of each domain are calculated and compared to the initial guess at the left side of the next domain.

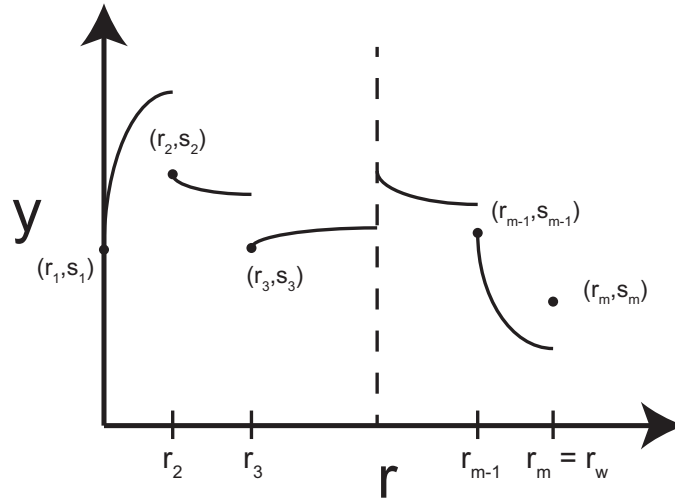


Figure 6.10: Diagram of the multiple shooting technique. The domain of integration is partitioned into subdomains. Within each subdomain, the integration is carried out independently with its own vector of initial guesses.

$$F(s_k^i) = \begin{pmatrix} T_{c,k+1}^i - T_{g,k+1}^i \\ \gamma_{c,k+1}^i - \gamma_{g,k+1}^i \\ u_{c,k+1}^i - u_{g,k+1}^i \end{pmatrix} \quad (6.82)$$

where the subscripts g and c indicate initial guesses and calculated values based on those guesses, respectively.

The difference quotients are calculated by solving the equation set three more times for each subdomain using $s' = s + \Delta s$.

$$\Delta F(s_k^i) = \begin{pmatrix} T_{T,k+1}^i & T_{\gamma,k+1}^i & T_{u,k+1}^i \\ \gamma_{T,k+1}^i & \gamma_{\gamma,k+1}^i & \gamma_{u,k+1}^i \\ u_{T,k+1}^i & u_{\gamma,k+1}^i & u_{u,k+1}^i \end{pmatrix} \quad (6.83)$$

where

$$T_{T,k+1}^i = \frac{T_{c,k+1}^i(T_{g,k}^i + \Delta T_{g,k}^i, \gamma_{g,k}^i, u_{g,k}^i) - T_{c,k+1}^i(T_{g,k}^i, \gamma_{g,k}^i, u_{g,k}^i)}{\Delta T_{g,k}^i} \quad (6.84)$$

$$T_{\gamma,k+1}^i = \frac{T_{c,k+1}^i(T_{g,k}^i, \gamma_{g,k}^i + \Delta \gamma_{g,k}^i, u_{g,k}^i) - T_{c,k+1}^i(T_{g,k}^i, \gamma_{g,k}^i, u_{g,k}^i)}{\Delta \gamma_{g,k}^i} \quad (6.85)$$

$$T_{u,k+1}^i = \frac{T_{c,k+1}^i(T_{g,k}^i, \gamma_{g,k}^i, u_{g,k}^i + \Delta u_{g,k}^i) - T_{c,k+1}^i(T_{g,k}^i, \gamma_{g,k}^i, u_{g,k}^i)}{\Delta u_{g,k}^i} \quad (6.86)$$

So, for multiple subdomains of integration the full difference quotient matrix

$$\Delta F(s^i) = \begin{pmatrix} G_1 & -I & 0 & \cdots & 0 \\ 0 & G_2 & -I & \ddots & 0 \\ \vdots & \ddots & \ddots & \ddots & \vdots \\ 0 & \ddots & \ddots & G_{m-1} & -I \\ A & 0 & \cdots & 0 & B \end{pmatrix} \quad (6.87)$$

where

$$G_k = \Delta F(s_k^i) \quad (6.88)$$

and A and B are matrices related to the global boundary conditions. The vector of initial guesses is

$$s^i = \begin{pmatrix} T_{g,1}^i \\ \gamma_{g,1}^i \\ u_{g,1}^i \\ T_{g,2}^i \\ \gamma_{g,2}^i \\ u_{g,2}^i \\ \vdots \\ T_{g,m-1}^i \\ \gamma_{g,m-1}^i \\ u_{g,m-1}^i \\ T_{g,m}^i \\ \gamma_{g,m}^i \\ u_{g,m}^i \end{pmatrix} \quad (6.89)$$

and the $F(s^i)$ vector is

$$F(s^i) = \begin{pmatrix} T_{c,2}^i - T_{g,2}^i \\ \gamma_{c,2}^i - \gamma_{g,2}^i \\ u_{c,2}^i - u_{g,2}^i \\ \vdots \\ T_{c,m}^i - T_{g,m}^i \\ \gamma_{c,m}^i - \gamma_{g,m}^i \\ u_{c,m}^i - u_{g,m}^i \\ \gamma_{g,1}^i - \gamma_{g,1}^i \\ u_{g,1}^i - u_{g,1}^i \\ u_{c,m}^i - r_w^2 B_w^2 \end{pmatrix} \quad (6.90)$$

In order to iterate the vector of guesses, s , the following system of equations is solved.

$$\Delta F(s^i) \Delta s = F(s^i) \quad (6.91)$$

where $\Delta s = s^{i+1} - s^i$. This process is continued until the solutions at all of the domain boundaries have converged. The values of ΔT and Δu must be constrained for reasons of physical reality and computational requirements due to the existence of square root terms. Relaxation factors are introduced into the Newton iteration that prevent T^{i+1} and u^{i+1} from being less than zero.

The initial profile guess for the multiple shooting method is a Bennett pressure profile calculated with the calculated density profile and total current in the pinch. These solutions are reached with the bremsstrahlung term as opposed to the total radiation term. This is chosen for purposes of consistency. If the calculated characteristic radius of the pinch is too large, the resulting total radiation term makes solution convergence difficult. The effect of the total radiation term is strongest at temperatures between 15 and 20 eV for an oxygen impurity. Figure 6.11 shows plots of the Runge-Kutta solution for the initial guess of the temperature for 22 subdomains and the final converged solution. Figure 6.12 shows the solutions for γ and Figure 6.13 shows the solutions for B_θ .

The initial profile guess overpredicts the temperature, dT/dr and the magnetic field profile as a function of radius. The conditions of matching the solutions at the subdomain boundaries is also clearly seen.

6.4 Generalized Thermal Conductivity

The previous sections use a form of the ion and electron thermal conductivity that assumes that the particles are magnetized throughout the domain (from the axis to the wall). A more accurate description takes into account the degree of magnetization of the particles, which is a comparison of the Larmor radius of the particles versus the mean free path of the particles. The generalized forms of the ion and electron thermal conductivities are,

$$\kappa_{\perp,i} = \frac{n_i k_B T_i \tau_i}{m_i} \left(\frac{2x_i^2 + 2.645}{x_i^4 + 2.7x_i^2 + 0.677} \right) \quad (6.92)$$

$$\kappa_{\perp,e} = \frac{n_e k_B T_e \tau_e}{m_e} \left(\frac{\gamma_1 x_e^2 + \gamma_0}{x_e^4 + \delta_1 x_e^2 + \delta_0} \right) \quad (6.93)$$

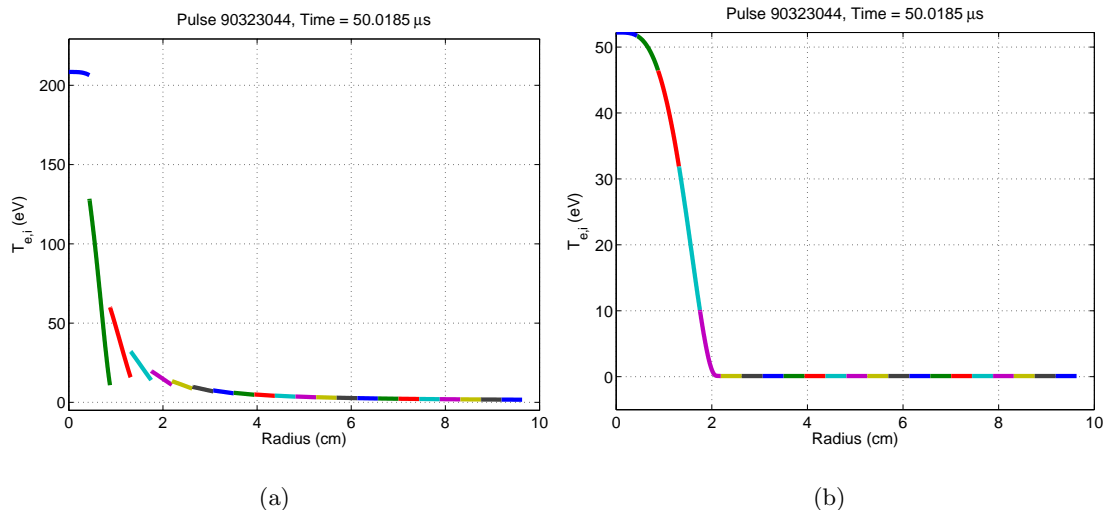


Figure 6.11: Multiple shooting method iterations for temperature. (a) First iteration of multiple shooting method with 22 subdomains originating from a Lorentzian temperature profile. (b) Converged solution with 22 subdomains results in a broader temperature profile than the initial guess with a lower peak temperature.

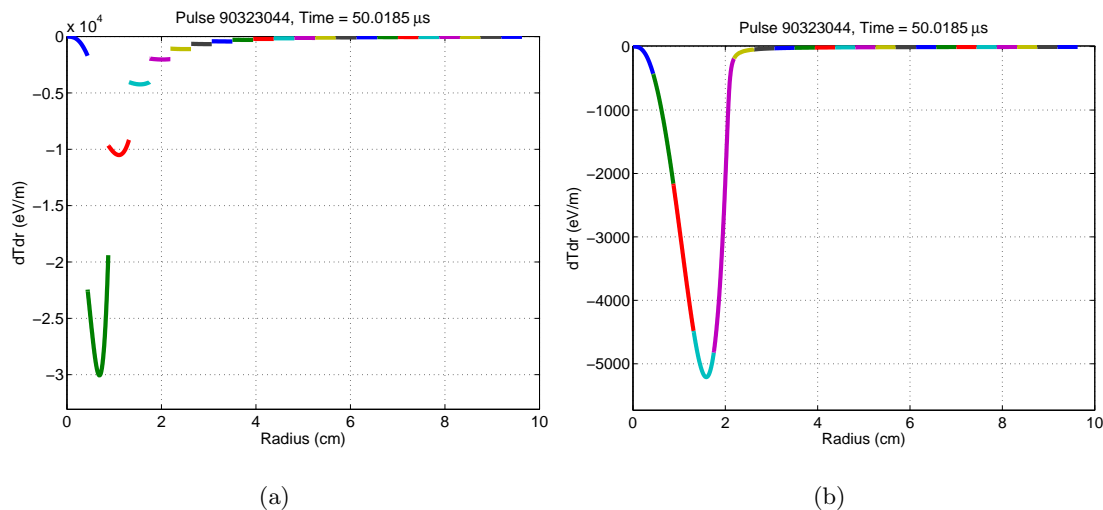


Figure 6.12: Multiple shooting method iterations for dT/dr . (a) First iteration of multiple shooting method with 22 subdomains for dT/dr . (b) Converged solution of the multiple shooting method for dT/dr results in a lower absolute magnitude of dT/dr .

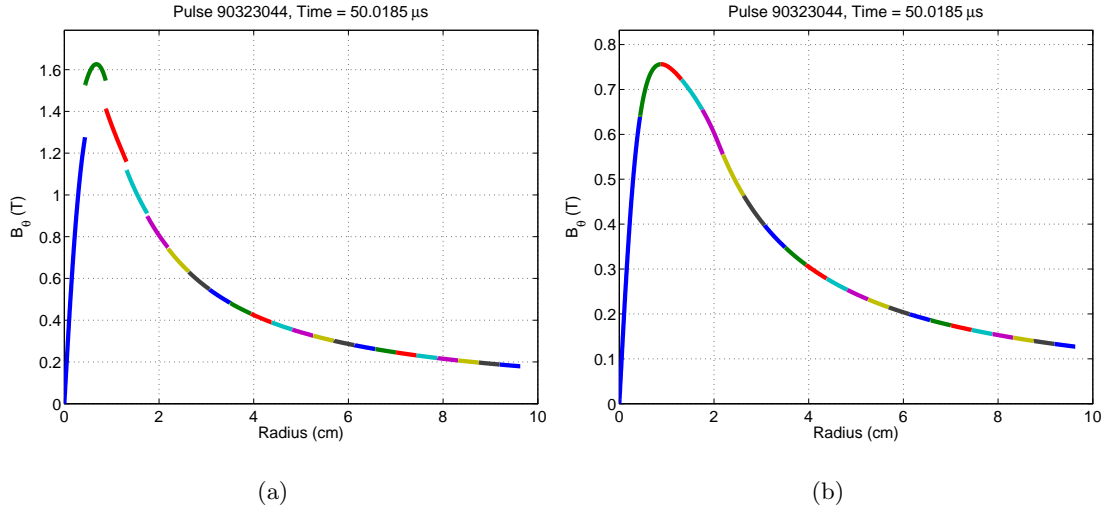


Figure 6.13: Multiple shooting method iterations for magnetic field. (a) First iteration of multiple shooting method for magnetic field. (b) Converged solution of multiple shooting method for magnetic field. Magnetic field profile is broader than the initial guess of a Bennett profile.

where

$$x_i = \omega_{ci}\tau_i \quad (6.94)$$

$$x_e = \omega_{ce}\tau_e \quad (6.95)$$

and the coefficients γ_1 , γ_0 , δ_1 and δ_0 are dependent on Z_{eff} [49]. This form of the thermal conductivities takes into account the unmagnetized behavior of the particles near the pinch axis where the magnetic field is zero as well as the magnetized behavior near the magnetic field peak.

A new form of the differential equation set is derived using this form of the thermal conductivity. The radial force balance equation is initially derived as previously.

$$\frac{du}{dr} = c_1 r^2 \left(T \frac{dn}{dr} + n \frac{dT}{dr} \right) \quad (6.96)$$

The radial heat conduction equation is treated differently than previously. Beginning with the initial form

$$\frac{1}{r} \frac{d}{dr}(rq) = \eta_{\perp} j^2 - P_{\text{Brem}} \quad (6.97)$$

Multiplying both sides by r gives

$$\frac{d}{dr}(rq) = r\eta_{\perp} j^2 - rP_{\text{Brem}} \quad (6.98)$$

recalling the definition of j from Equation 6.15 and 6.19, the equation for radial heat conduction becomes

$$\frac{d}{dr}(rq) = \frac{r^3 \eta_{\perp} c_1^2}{4\mu_0^2 u} \left(T \frac{dn}{dr} + n \frac{dT}{dr} \right)^2 - rP_{\text{Brem}} \quad (6.99)$$

From Fourier's Law of Cooling,

$$q = -k_B(\kappa_{\perp,i} + \kappa_{\perp,e}) \frac{dT}{dr} \quad (6.100)$$

Multiplying both sides by r and rearranging terms yields an equation for the temperature gradient.

$$\frac{dT}{dr} = -\frac{rq}{rk_B(\kappa_{\perp,i} + \kappa_{\perp,e})} \quad (6.101)$$

Substituting this equation into Equations 6.96 and 6.99 and substituting in the definition of the constant, c_3 , results in the following equations,

$$\frac{du}{dr} = c_1 r^2 \left(-\frac{n(rq)}{rk_B(\kappa_{\perp,i} + \kappa_{\perp,e})} + T \frac{dn}{dr} \right) \quad (6.102)$$

$$\frac{d}{dr}(rq) = \frac{c_1^2 r^3 c_3}{4uT^{\frac{3}{2}}} \left(-\frac{n(rq)}{rk_B(\kappa_{\perp,i} + \kappa_{\perp,e})} + T \frac{dn}{dr} \right)^2 - rP_{\text{Brem}} \quad (6.103)$$

Equations 6.101 - 6.103 represent the system of three equations that must be solved numerically. The equation set is solved with the multiple shooting method described earlier and

using the Matlab ODE solver, ode15s, which is effective for stiff systems. The boundary conditions are

$$rq(r = 0) = 0 \quad (6.104)$$

$$u(r = 0) = 0 \quad (6.105)$$

$$u(r = r_w) = (r_w B_w)^2 \quad (6.106)$$

Near the location of peak magnetic field, the thermal conductivity is such that the temperature is driven to zero very quickly. The ODE solver limits the maximum temperature gradient by imposing a minimum temperature scale length, $T/(\frac{dT}{dr})_{\max}$, which is specified by either the local Larmor radius or the local mean free path, whichever is shorter. The Larmor radius and mean free path for ions are defined as

$$r_{L,i} = \frac{v_{T,i}}{\omega_{ci}} \quad (6.107)$$

$$\lambda_{\text{mfp}} = v_{T,i} \tau_i \quad (6.108)$$

where

$$v_{T,i} = \sqrt{\frac{k_B T_i}{m_i}} \quad (6.109)$$

This drives the temperature to a specified minimum of $T_{\min} = 10^{-3}$ eV. Radial profiles beyond this point are determined by acknowledging that the temperature gradient will be zero, and therefore so will the gradient in rq (from Equation 6.100). The gradient in u has a finite change associated with the finite density gradient and the small finite temperature $T_{\min} \frac{dn}{dr}$.

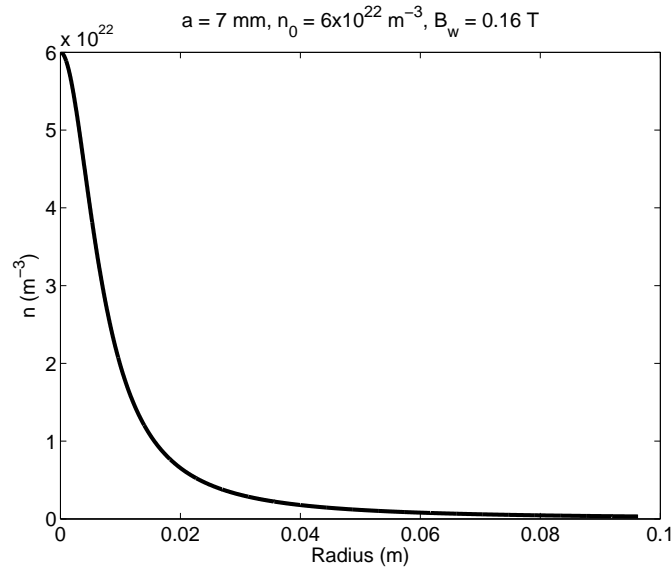


Figure 6.14: Synthetic density profile for comparing generalized and magnetized thermal conductivity. The synthetic density profile used for the comparison has a characteristic radius, $a = 7$ mm, and peak density, $n_0 = 6 \times 10^{22} \text{ m}^{-3}$. The same profile is used for both conductivity formulations.

Figure 6.14 shows a synthetic density profile which is used to compare the results of the generalized and magnetized thermal conductivity formulas. The characteristic radius is 7 mm and the peak density is $6 \times 10^{22} \text{ m}^{-3}$.

Figure 6.15 shows the magnetic field and temperature profiles for the above density profile with a wall magnetic field value of $B_w = 0.16$ T for both the generalized and magnetized formulas for thermal conductivity, magnetized in red and generalized in black. The data indicate that the generalized formula for thermal conductivity produces narrower temperature profiles with steeper temperature gradients, though they are in general very similar. Further, the temperature profiles near the axis for the magnetized formulation are flatter than for the generalized formulation. The peak temperature for the magnetized formulation is ≈ 51 eV and for the generalized formulation it is ≈ 57 eV, given this density profile with the associated magnetic field at the wall. The magnetic field profiles produce higher peak

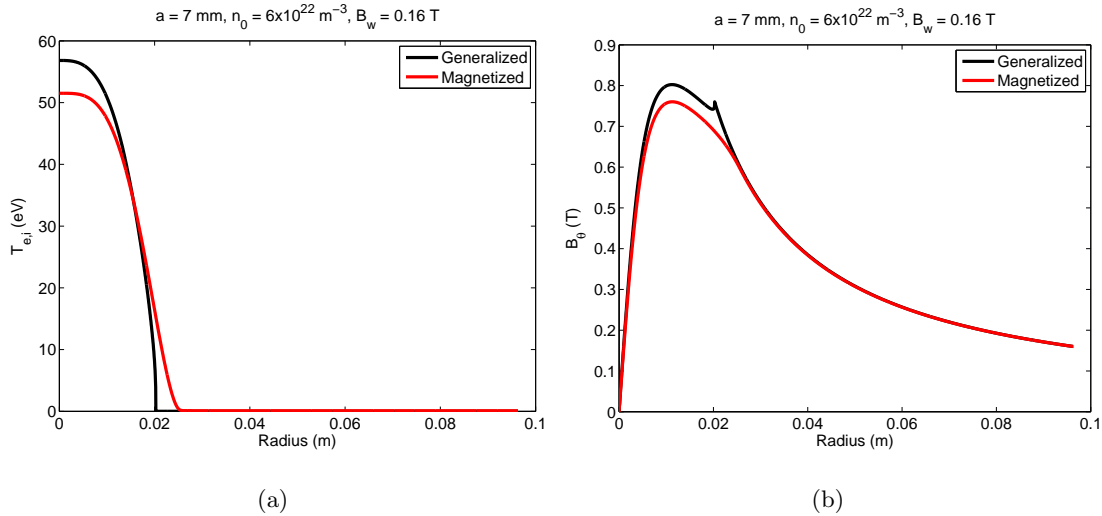


Figure 6.15: Temperature and magnetic field profiles comparing generalized and magnetized thermal conductivity. (a) Temperature profiles for the generalized formulation have a higher peak temperature with narrower profiles and steeper temperature gradients. (b) Magnetic field profiles for the generalized formulation produce a higher peak field and a noticeable increase in field at the region of largest temperature gradient. It is unknown whether this is due to a surface current or a consequence of the resolution of the ODE solver.

fields, 0.8 T compared to 0.75 T, for the generalized case with the existence of a sharp increase in field at the location where the temperature goes to its minimum value. This is indicative of a surface current near the edge of the pinch. This is shown in Figure 6.16 which shows the profile of current density for the generalized and magnetized formulations of the thermal conductivity. The calculated surface current is a consequence of the resolution of the ODE solver, not a real effect.

Figure 6.17 shows the ion thermal conductivity profiles, $\kappa_{\perp,i}$, and the profiles of the length scales of interest for the ions, Larmor radius and collisional mean free-path for both the generalized and magnetized thermal conductivity formulas, the solid lines are for the Larmor radii and the dashed lines are the collisional mean free-paths. These profiles provide the explanation for the differences in the profiles of temperature and magnetic field.

At the axis, the magnetized formulation produces thermal conductivities that approach

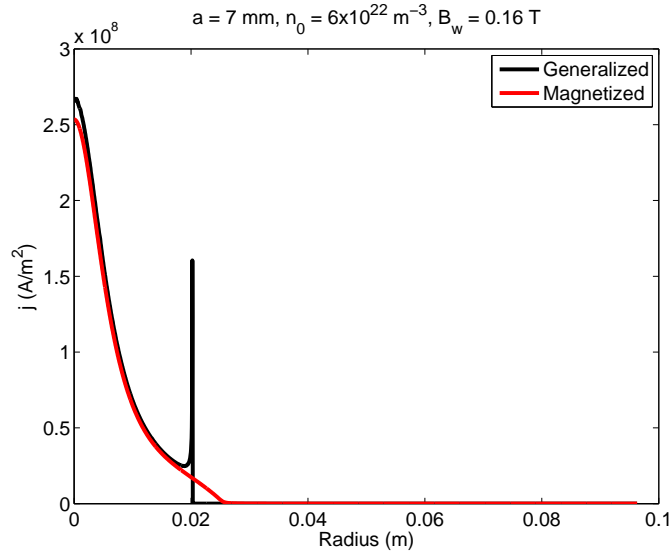


Figure 6.16: Current density profile for generalized and magnetized thermal conductivity. The current density indicates a peaked current profile with a large surface current at the location of largest temperature gradient for the generalized formulation. The magnetized formulation indicates a more gradual drop in the current.

ininity due to the $1/B^2$ dependence. In the generalized formulation, near the axis the dependence is based solely on the temperature, $\propto T^{\frac{5}{2}}$. The result is that the magnetized formulation produces a flatter temperature profile in this region. Similarly, at the edge the temperature profile for the magnetized formulation smoothly approaches the minimum temperature, generating a broader profile. This is due to the $1/\sqrt{T}$ dependence of the conductivity. The generalized formulation can, in some circumstances, be dominated by collisional aspects of the plasma which would result in the previously mentioned $T^{\frac{5}{2}}$ dependence at the edge which would produce a steep temperature gradient.

The plot of scale lengths further supports this interpretation. Near the axis, the collisional mean free-path is shorter than the Larmor radius indicating the transport is dominated by the collisions, meaning an effectively unmagnetized thermal conductivity should be used. At $r \approx 5$ mm, the Larmor radius becomes smaller than the mean free-path indicating that the transport is dominated by the Larmor orbits, meaning that a magnetized

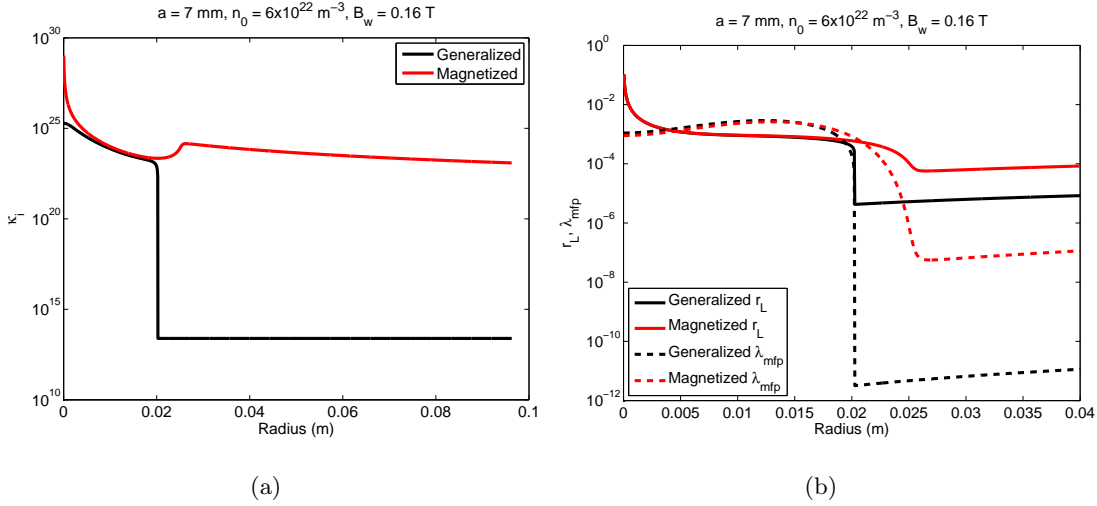


Figure 6.17: Thermal conductivity, Larmor radii and collisional mean free-path for ions. (a) The generalized thermal conductivity exhibits lower values near the axis because unmagnetized effects become dominant as the magnetic field approaches zero. The magnetized thermal conductivity approaches infinity because it is proportional to $1/B^2$. This is the explanation for the wider region of uniform temperature near the axis for the magnetized thermal conductivity case. Near the plasma edge, the magnetized thermal conductivity again increases due to the $1/\sqrt{T}$ proportionality. (b) The collisional mean free-path is shorter near the axis than the Larmor radius, indicating that transport is dominated by particle collisions. At $\approx 5 \text{ mm}$, the Larmor radius becomes smaller than the mean free-path, indicating that transport is dominated by the cyclotron orbits of the particles.

interpretation of thermal conductivity is necessary.

All temperature and magnetic field profiles presented for the remainder of this document are from the generalized formulation of thermal conductivity.

6.5 Solutions for Magnetic Field and Temperature Profiles

Figure 6.18 shows profiles of magnetic field and temperature for the previously considered pulse. The temperature profiles are characterized by a flat profile near the axis due to the high thermal conductivity. Away from the axis, the temperature profile becomes steep due to the magnetization of the plasma. This temperature profile, which is broader than the

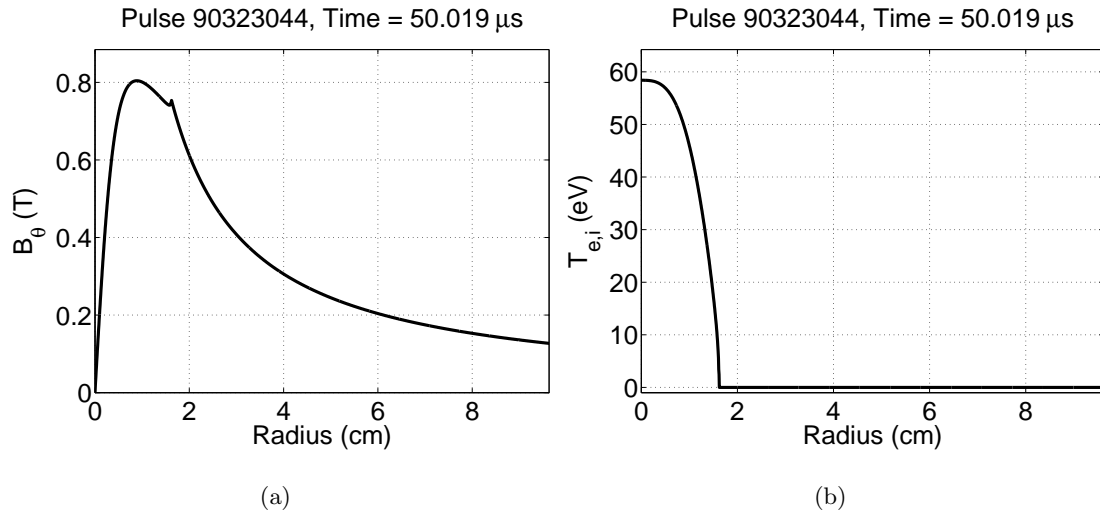


Figure 6.18: Magnetic field and temperature profiles for high peak magnetic field operating conditions. (a) Magnetic field profile peaks at 0.8 T and is noticeably broader than a Bennett profile. The profile transitions to $\approx 1/r$ behavior when the temperature profile reaches the minimum value. (b) Temperature profile peaks at 59 eV at this time during this pulse. The temperature profile is broader than the initial Lorentzian profile guess, which results in a broader pressure profile than a Kadomtsev profile, making it more stable to the $m = 0$ mode.

originally assumed Lorentzian profile, coupled with the calculated density profile produces a temperature profile which is broader than a Bennett pressure profile. This broader profile is more stable to the $m = 0$ mode than the Kadomtsev equilibrium which the Bennett profile is approximating. The magnetic field is also noticeably broader, but does transition to $\approx 1/r$ decay after the temperature reaches the minimum value, which is 10^{-3} eV.

Figure 6.19 shows the peak magnetic field and temperature as a function of time for this pulse. The data suffers from similar irregular oscillations as the characteristic pinch radius, but with clear overall trends highlighted by the linear trendlines. The magnetic field values are increasing as a function of time to a peak values near 0.9 T and the temperature is increasing at a similar rate with a peak values as a function of time of 61 eV for this pulse. These data combined with the characteristic radius and density data indicate that

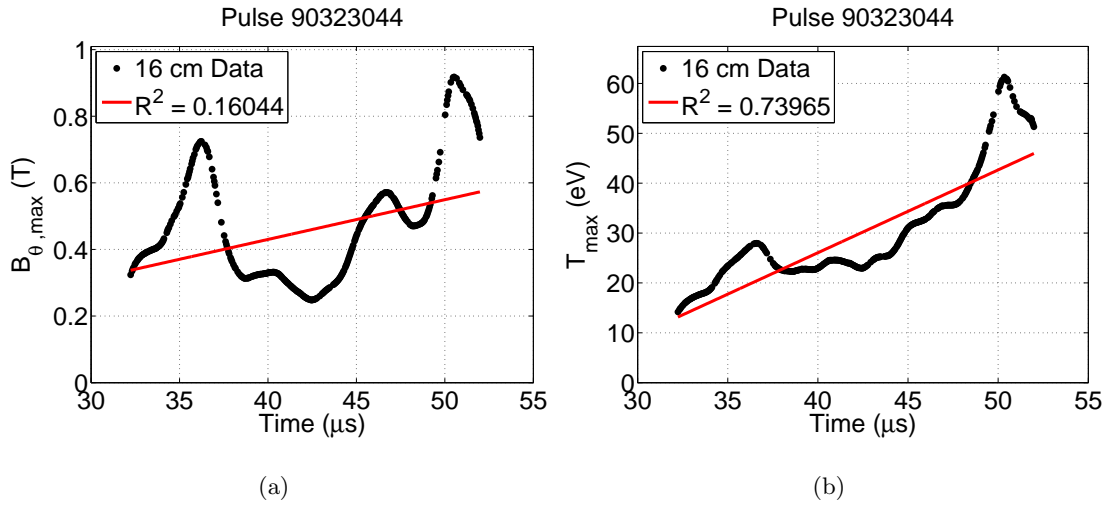


Figure 6.19: Peak magnetic field and temperature as a function of time for high peak magnetic field operating condition. (a) Peak magnetic field increases as a function of time by a factor of nearly 3 with an absolute peak of 0.9 T. These data agree with the interpretation of magnetic compression from the characteristic pinch radius and peak density plots. (b) Temperature increases as a function of time in a similar manner to the magnetic field. The magnetic compression is resulting in higher temperatures, peaking at 61 eV. The red lines are linear trendlines to the data.

the pinch is undergoing magnetic compression as the quiescent period progresses.

Figures 6.20 and 6.21 show contours of the temperature and magnetic field as a function of radius and time. These contours very clearly show the effects of magnetic compression: higher temperatures and peak magnetic fields.

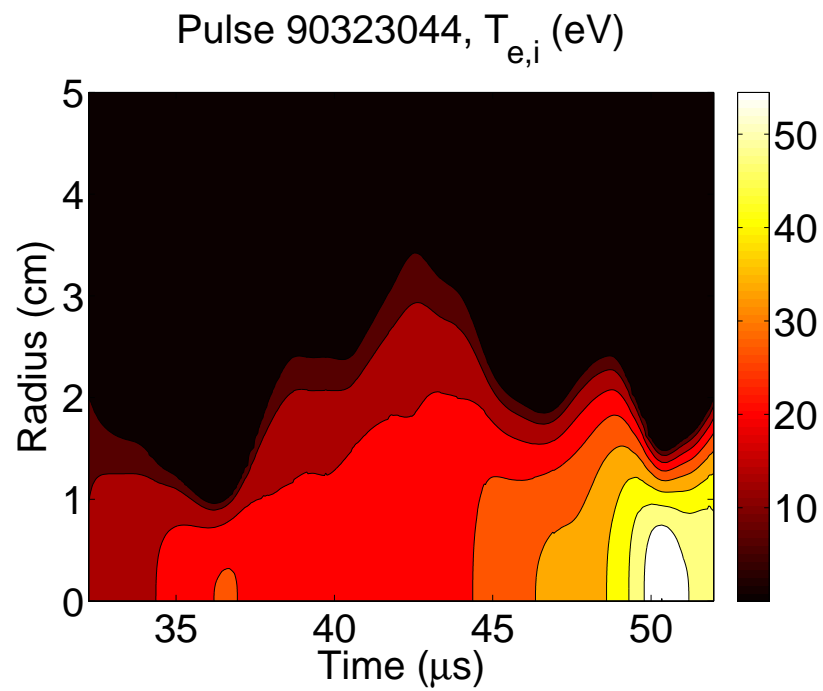


Figure 6.20: Temperature contours as a function of radius and time for high peak magnetic field operating condition. As time progresses, the compression and temperature increase of the pinch is observed.

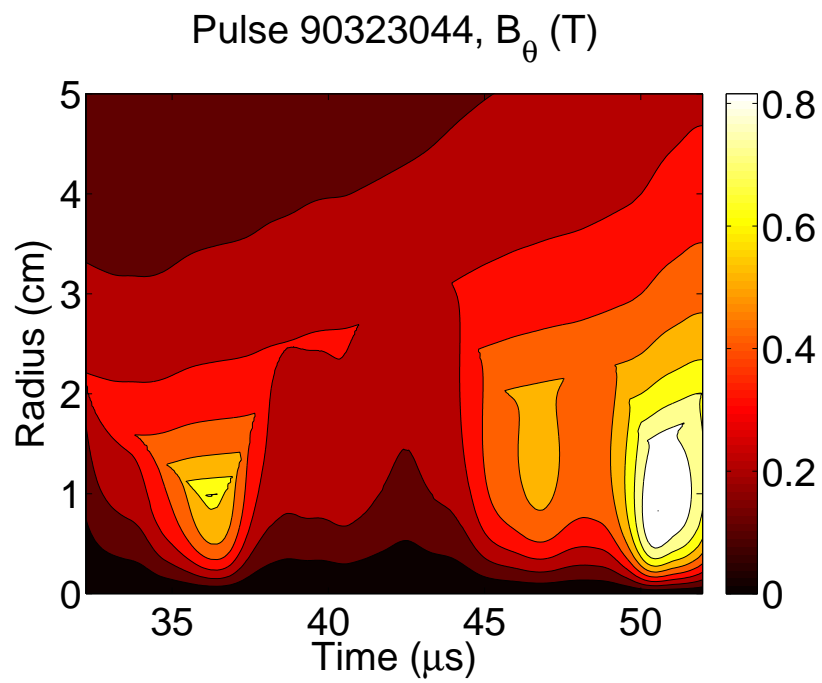


Figure 6.21: Magnetic field contours as a function of radius and time for high peak magnetic field operating condition. As time progresses the magnetic field increases causing the compression and temperature increase of the pinch.

Chapter 7

**COMPARISON OF EXPERIMENTAL PERFORMANCE FOR 10 CM
VS. 16 CM INNER ELECTRODES**

7.1 10 cm Inner Electrode and Comparison with Thomson Scattering and Doppler Spectroscopy Measurements

Figure 7.1 shows the magnetic mode data at $z = 0$ cm for a pulse with the 10 cm diameter inner electrode. The data indicates a long quiescent period with magnetic field values ranging from 0.1 to 0.18 T measured at the outer electrode. Figure 7.2 shows the chord-integrated densities measured by the four-chord interferometer and the y -location of the current centroid at $z = 0$ cm for this pulse. At the beginning and end of the quiescent period, oscillations are observed in the y -location of the centroid that prevent effective measurements of the density. In the middle of the quiescent period ($t = 40 - 60 \mu\text{s}$), fewer oscillations in the y -location give rise to an apparent gradient in the chord-integrated density. Figure 7.3 shows a zoomed view of this data.

Calculating the density evolution produces the evolution of the characteristic pinch radius and the on-axis density as a function of time, shown in Figure 7.4. The overall behavior for this pulse is a gradually increasing characteristic pinch radius and gradually decreasing peak density which is in reasonable agreement with the values of the total current and linear density shown in Figure 7.5 which indicates a generally constant value of linear density until after $55 \mu\text{s}$ and a decreasing value of the total current until after $55 \mu\text{s}$. The characteristic pinch radius also indicates irregular oscillations like the 16 cm diameter inner electrode, but with a lower magnitude of the oscillations. Note the occasional gaps in the data set. This is a consequence of either the density profile not being solved (i.e. not monotonically decreasing values of density with increasing impact parameter) or a failure of the multiple shooting code to produce a converged solution.

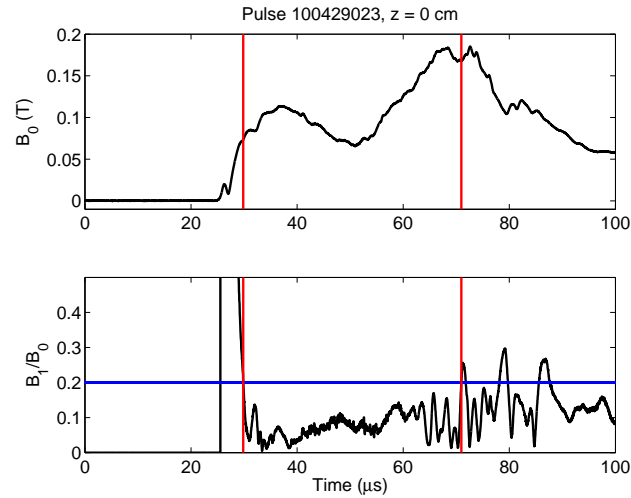


Figure 7.1: Magnetic mode data for 10 cm diameter inner electrode configuration. Pulses are characterized by a long quiescent period and a slowly varying magnetic field as a function of time. Vertical red lines indicate the beginning and end of the quiescent period.

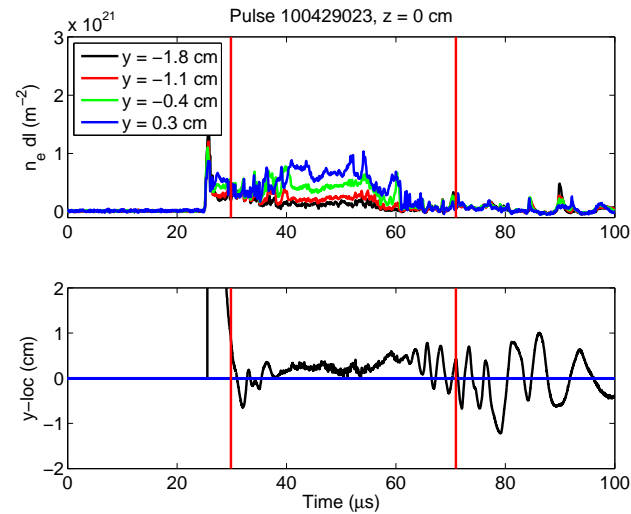


Figure 7.2: Four-chord interferometry data for 10 cm diameter inner electrode configuration. Bottom plot is the y -location of the current centroid. A gradient in chord-integrated density is observed in the middle of the quiescent period ($t = 40 - 60 \mu\text{s}$). At the beginning and end of the quiescent period, large oscillations in the y -location of the current centroid prevent effective density measurement. Vertical red lines indicate the beginning and end of the quiescent period.

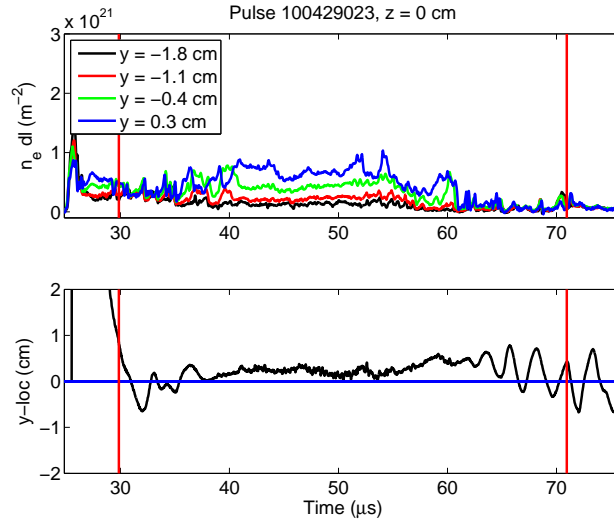


Figure 7.3: Inset view of interferometry data for 10 cm diameter inner electrode configuration. A well-defined pinch is observed in the middle of the quiescent period. Early and late in the quiescent period, large oscillations in the y -location prevent effective interferometry measurements. Vertical red lines indicate the beginning and end of the quiescent period.

Magnetic field and temperature values are calculated with the methods described in Section 6.2 and shown in Figure 7.6. The calculated data again track well with the measured value of the total current at that location. The overall trend of the peak magnetic field is dropping until after $55 \mu\text{s}$ at which point it sharply increases, coincident with characteristic radius compression and increasing temperatures. The temperature fluctuates between 35 and 60 eV for the majority of the quiescent period with an extended period between 35 and 40 eV.

Figure 7.7 shows experimentally-measured values of the electron and ion temperature measured with Thomson scattering and Doppler spectroscopy, respectively. The red symbols are the electron temperature from the two-point Thomson-scattering system and the black points are the ion temperature from the 20-chord imaging spectrometer. The data are not for the same pulse as shown in the previous figures, but operating conditions are similar. These data indicate three things that are in agreement with calculated values from the four-

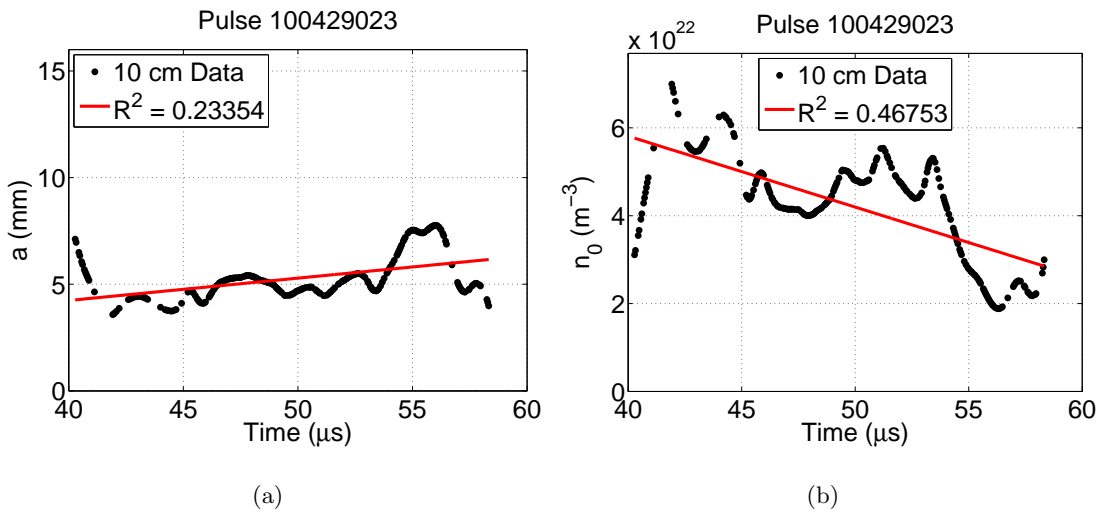


Figure 7.4: Characteristic pinch radius and peak density as a function of time for 10 cm diameter inner electrode. (a) Overall trend is an increase in the size of the pinch with increasing time. Irregular oscillations are smaller for the 10 cm diameter inner electrode. (b) On-axis density is anti-correlated with the pinch size, as expected. Overall trend is decreasing peak density. The pinch is expanding as a function of time. The red lines are linear trendlines to the data. Gaps in the data are a consequence of either the density profile not being solved (i.e. not monotonically decreasing values of density with increasing impact parameter) or a failure of the multiple shooting code to produce a converged solution.

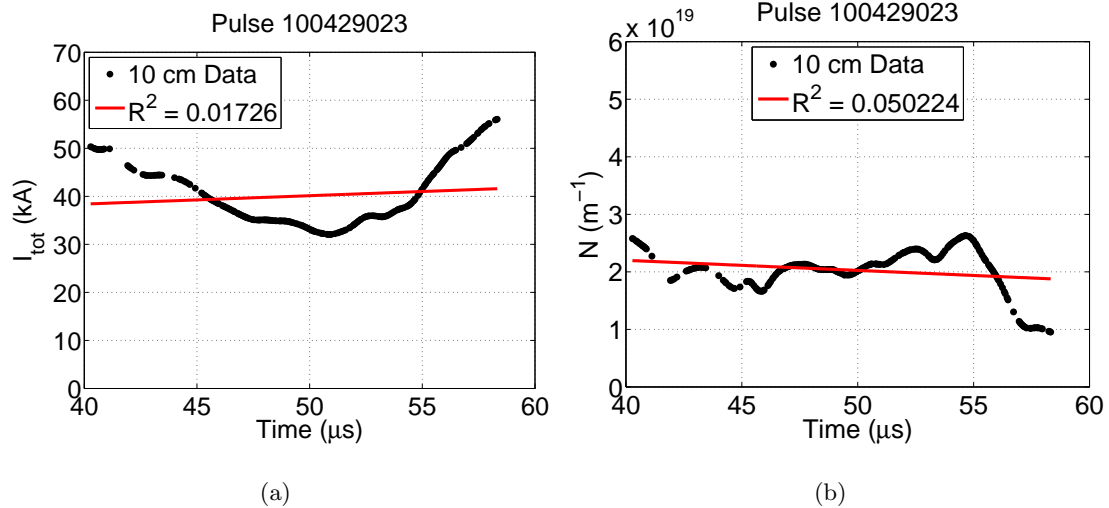


Figure 7.5: Total current and linear density as a function of time for the 10 cm diameter inner electrode. (a) Total current is decreasing until $t \approx 55 \mu\text{s}$ at which point it increases, consistent with increasing characteristic pinch radius. (b) The linear density is approximately constant as a function of time, resulting in a decrease in peak electron density due to expansion of the pinch. The red lines are linear trendlines.

chord interferometer. First, the measured values of the electron and ion temperatures range between 20 and 50 eV, similar to the calculated values from interferometry. Second, the profiles of temperature as a function of radius are flat to a radius of 1 cm which is consistent with the calculations of the temperature profiles from radial heat conduction. Third, the measured values of the electron and ion temperature are approximately the same. This is an assumption of the radial heat conduction analysis based on the short equipartition time of the particles. The measurements agree with this assumption.

7.2 Quiescent Period Behavior

The behavior of the pinch during the quiescent period is investigated for adiabatic or non-adiabatic behavior by analysing the evolution of the volume-averaged adiabat, $\langle \frac{p}{\rho\gamma} \rangle$. Adiabatic evolution of the pinch manifests as a constant value of the volume-averaged adiabatic function. An increasing value of the volume-averaged adiabatic function indicates that the

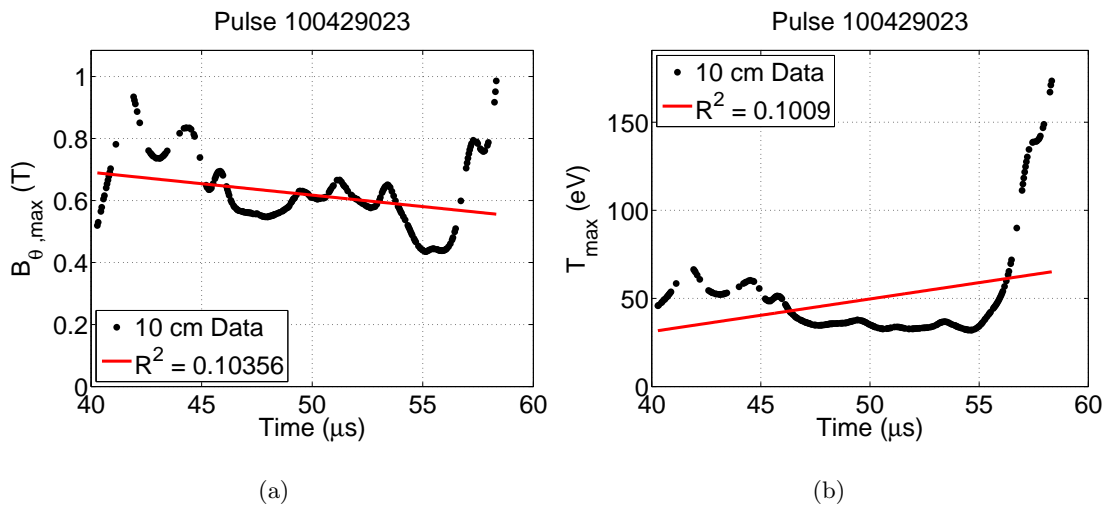


Figure 7.6: Peak magnetic field and peak temperature as a function of time for the 10 cm diameter inner electrode. (a) Magnetic field exhibits similar oscillations to characteristic pinch radius and has similar behavior to the total current. Peak field is 0.9 T. (b) The temperature fluctuates between 35 and 60 eV for most of the quiescent period. At $t > 55 \mu\text{s}$ the temperature increases significantly coincident with an increase in magnetic field and decrease in linear density.

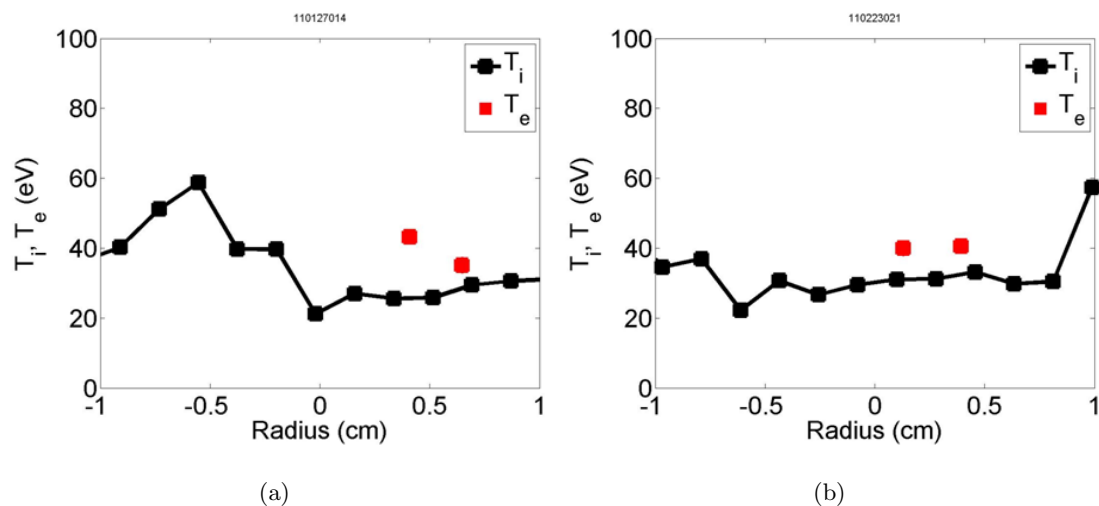


Figure 7.7: Electron and ion temperature data for a 10 cm diameter inner electrode pulse. The data for the Thomson scattering and Doppler spectroscopy diagnostics are collected at the same time during a pulse. The error bars on the data are smaller than the symbol size. The data indicate that $T_e \approx T_i \approx 40$ eV which is consistent with the calculated equipartition time. The data also show a flat temperature profile which is consistent with radial heat conduction analysis.

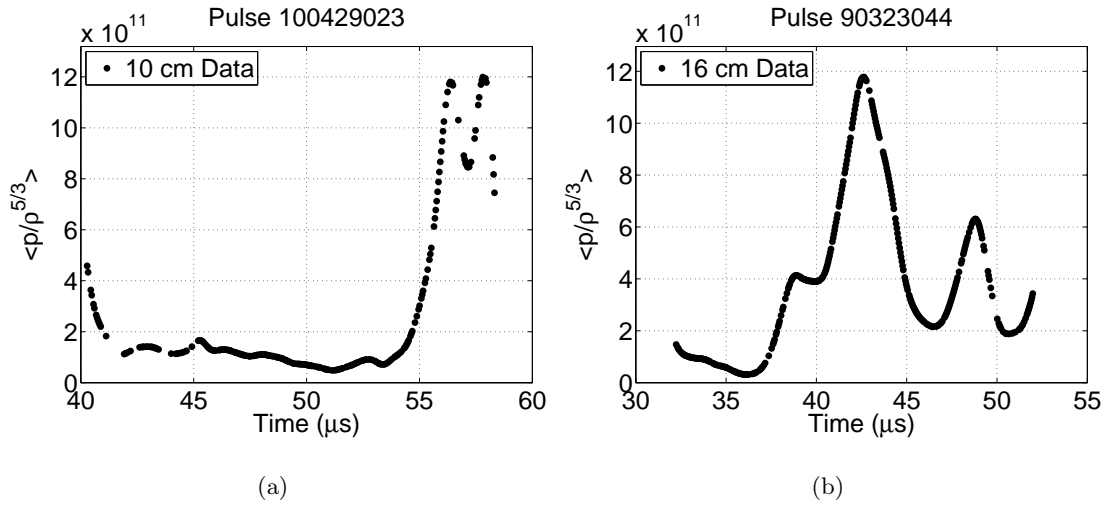


Figure 7.8: Volume-averaged adiabatic function as a function of time for 10 cm and 16 cm diameter electrode configurations. (a) 10 cm diameter inner electrode configuration evolves adiabatically for the majority of the quiescent period. (b) The 16 cm diameter inner electrode configuration evolves non-adiabatically throughout the quiescent period.

energy density of the pinch is increasing and a decreasing value indicates a reduction in the energy density of the pinch. Figure 7.8 shows the time evolution of the volume-averaged adiabatic function for the 10 cm diameter inner electrode (a) and the 16 cm diameter inner electrode (b). The 10 cm diameter inner electrode exhibits behavior during the majority of the quiescent period that suggests that the pinch evolution is occurring in a nearly adiabatic manner. The 16 cm diameter inner electrode configuration exhibits behavior that is non-adiabatic throughout the quiescent period.

Figure 7.9 shows the characteristic pinch radius for the 10 cm diameter inner electrode and the 16 cm diameter inner electrode. Both configurations exhibit irregular oscillations of the pinch radius. These oscillations are larger for the 16 cm diameter inner electrode configuration and it is observed that the characteristic pinch radius and the volume-averaged adiabatic function from Figure 7.8 are correlated with one another. This suggests that the pinch radius oscillations are related to non-adiabatic processes.

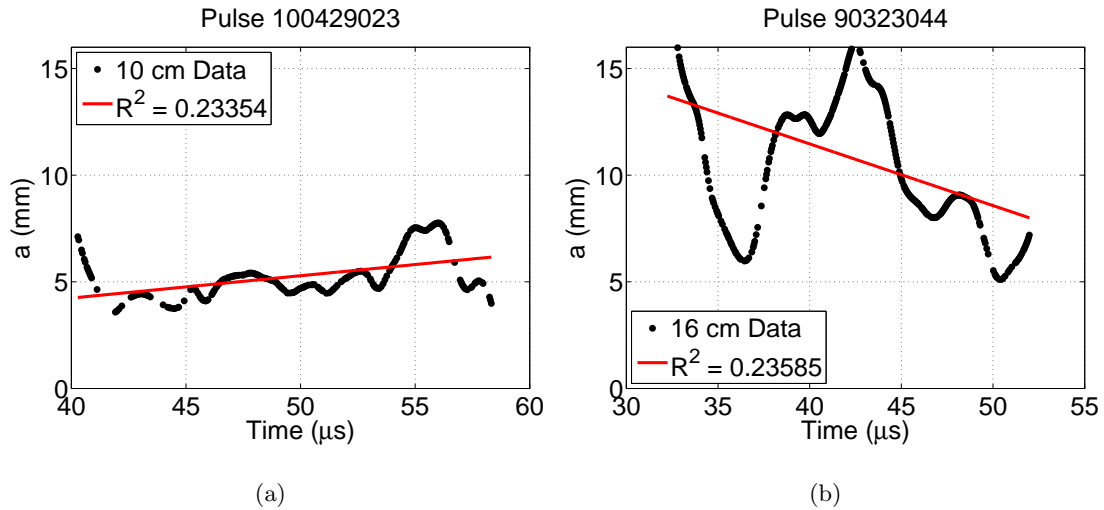


Figure 7.9: Characteristic pinch radius as a function of time for the 10 cm and 16 cm diameter inner electrode configurations. (a) 10 cm diameter electrode configuration results in smaller pinch radius oscillations that do not significantly affect the adiabatic behavior. (b) 16 cm diameter electrode configuration results in large pinch oscillations that are correlated with the variations in the volume-averaged adiabatic function.

Figure 7.10 shows the comparison of the volume-averaged calculated Ohmic power, $\langle \eta_{\perp} j^2 \rangle$, as a function of time and the characteristic pinch radius as a function of time for the 10 cm diameter and 16 cm diameter inner electrodes. For the following plots of $\langle \eta_{\perp} j^2 \rangle$, the equation for the thermal conductivity is the magnetized formulation. The anomalous skin current from the generalized formulation results in aberrant data, therefore the magnetized formulation is used. Furthermore, since the resulting profiles from the magnetized and generalized conductivity formulations are similar, the following analysis is valid for both cases.

The data indicate that these values are anti-correlated. A decrease in the size of the pinch results in an increase in the volume-averaged Ohmic power. This is a result of the j^2 dependence of the Ohmic power. For similar values of total current, I , the current is distributed through a smaller area. The current is approximately dependent on $\frac{1}{a^2}$. The resistivity is proportional to $T^{-\frac{3}{2}}$ and the temperature is dependent on changes in

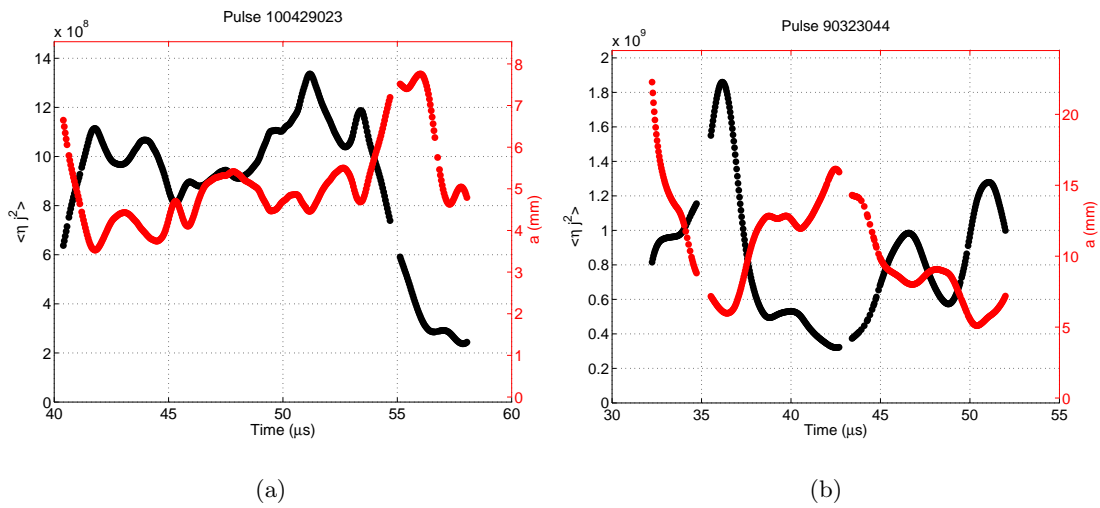


Figure 7.10: Volume-averaged Ohmic dissipation vs. characteristic pinch radius for 10 cm and 16 cm diameter inner electrode configurations. (a) Volume-averaged Ohmic dissipation is anti-correlated with characteristic pinch radius. The Ohmic dissipation term is in black and the characteristic pinch radius is in red. (b) Volume-averaged Ohmic dissipation is anti-correlated with characteristic pinch radius with a correlation in the magnitudes of the changes.

characteristic pinch radius, $T \propto \frac{1}{a^{\frac{4}{3}}}$. Therefore, the Ohmic power deposition is $\propto \frac{1}{a^2}$. Similarly, as the characteristic pinch radius increases, the volume-averaged Ohmic power decreases. The dependence is shown in Figure 7.11. Trendlines for a $\frac{1}{a^2}$ dependence are shown on the graphs. This dependence is approximately observed for the 16 cm diameter inner electrode. The 10 cm diameter inner electrode does not present in this manner. Two potential regions are fit with a $\frac{1}{a^2}$ dependence, but present in a manner closer to $\propto -a$. The likely reason for this is that the ohmic power is also dependent on I and N , $\langle \eta_{\perp} j^2 \rangle \propto \frac{I^2}{Na^2}$. For the 16 cm inner electrode, the dominant variations amongst these values is in the characteristic pinch radius, N and I are changing much more slowly, so the dependence on $\frac{1}{a^2}$ is more pronounced. For the 10 cm inner electrode the degree of change of the variables is comparable, so the relationship with the characteristic radius is more difficult to determine. Figure 7.12 shows the relationship between the volume-averaged adiabatic function and the volume-averaged Ohmic power deposition with a $\frac{1}{\langle p/\rho^{\gamma} \rangle}$ trendline. The data indicates that as the volume-averaged adiabatic function increases (increasing characteristic pinch radius), the Ohmic power deposition decreases. Based on the equations this is an unexpected result as $\langle \frac{p}{\rho^{\gamma}} \rangle \propto \frac{a^2 I^2}{N^{\frac{5}{3}}}$ and $\langle \eta_{\perp} j^2 \rangle \propto \frac{I^2}{Na^2}$. The behavior as it relates to the characteristic radius is inversely proportional, but the behavior related to I and N is not consistent with an inverse relationship. The experimental relationship suggests a possible explanation for the irregular pinch oscillations.

The proposed mechanism for the oscillating characteristic pinch radius is the balance of energy between Ohmic deposition and impurity radiation. Smaller pinch radii result in increased values of the Ohmic power deposition, dominating over radiation losses. The result of this overall input of energy to the system is the expansion of the pinch. The inertia of the expanding pinch causes an overexpansion, driving the Ohmic deposition down to a lower magnitude than the radiated power. The dominant radiation loss results in a contraction of the pinch. This process repeats until the end of the quiescent period. Impurity radiation is not used in the radial heat conduction analysis for numerical reasons. Potential values of the radiated power can be estimated ex post facto from the calculated

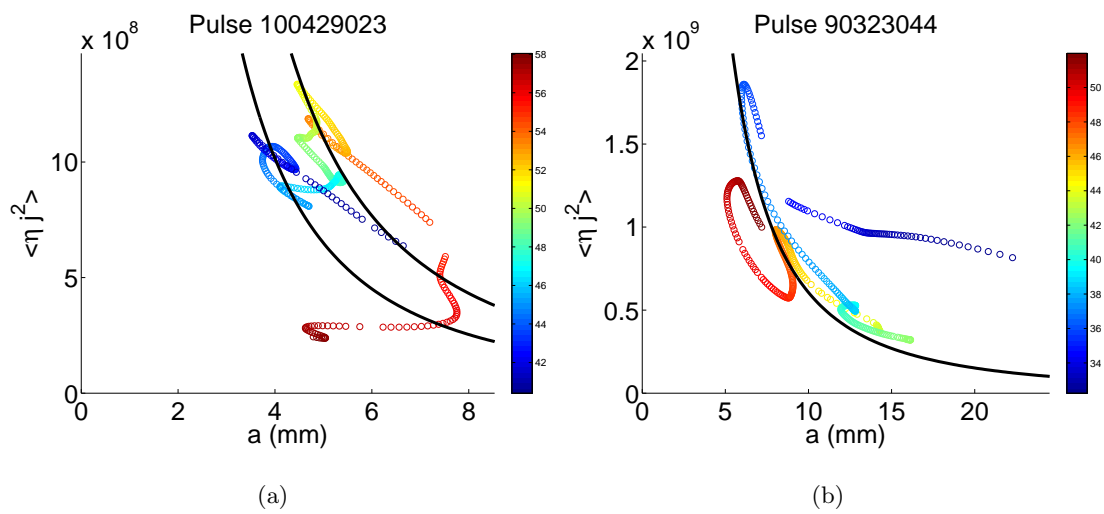


Figure 7.11: Volume-averaged Ohmic dissipation vs. characteristic pinch radius for 10 cm and 16 cm diameter inner electrode configurations. (a) The Ohmic dissipation increases with decreasing pinch radius. The colors of the symbols signify the time during the quiescent period. (b) Similarly with the 16 cm inner electrode, increased Ohmic dissipation is related to decreased characteristic pinch radius. The black trendlines indicate the $\frac{1}{a^2}$ dependence of the Ohmic dissipation.

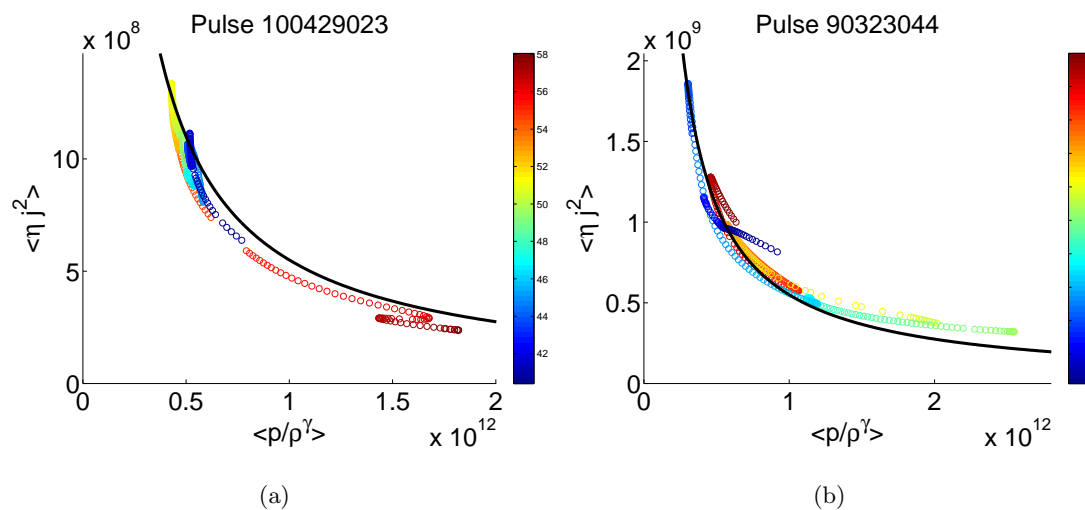


Figure 7.12: Volume-averaged Ohmic dissipation vs. volume-averaged adiabatic function for 10 cm and 16 cm diameter inner electrode configurations. For both electrode configurations the relationship between the volume-averaged adiabatic function and the volume-averaged Ohmic dissipation indicates that for lower values of the adiabatic function (reduced pinch radius) the Ohmic power dissipation is increased. The black trendlines indicate the $\frac{1}{\langle p/\rho^\gamma \rangle}$ dependence of the Ohmic dissipation.

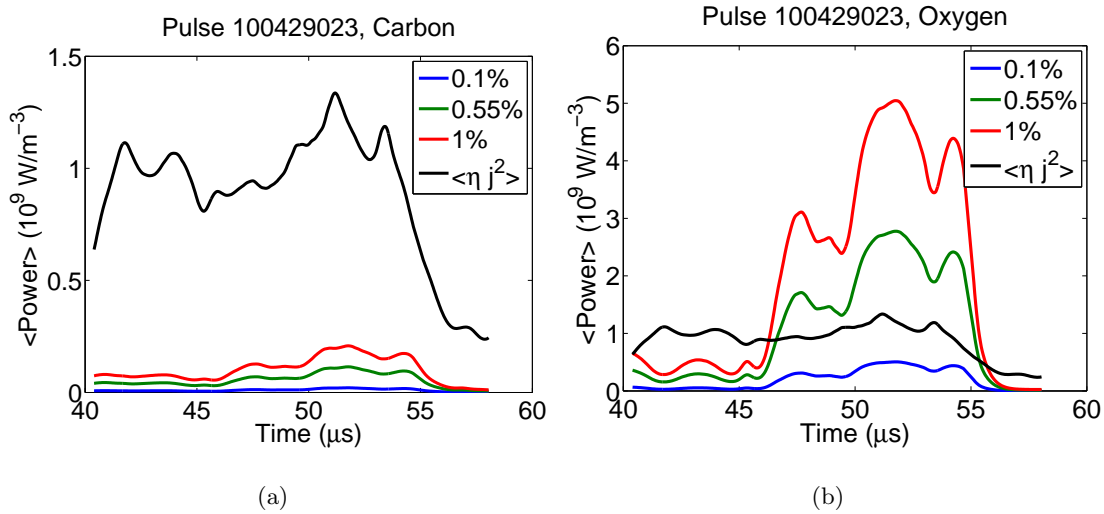


Figure 7.13: Volume-averaged radiation as a function of time for multiple impurity contents. (a) Carbon as the primary impurity radiator produces low levels of radiation at multiple impurity fractions, considerably less than the Ohmic power dissipation. (b) Oxygen as the primary impurity radiator produces higher levels of radiation. In multiple cases, radiation is the dominant term over the Ohmic power dissipation.

temperature and density profiles. Assumptions are required to produce volume-averaged radiation losses. The Z_{eff} of the plasma is unknown due to the lack of knowledge of the primary impurity radiators. Further, the proposed model assumes coronal equilibrium, therefore time-dependent radiation terms are not used. Estimates of the volume-averaged radiation are shown for primary impurity radiators of carbon and oxygen with impurity fractions of 0.1%, 0.55% and 1% in Figure 7.13 for the 10 cm diameter inner electrode. These values are compared with the volume-averaged Ohmic deposition. It is observed that oxygen is a stronger radiator than carbon. However, with a variety of oxygen impurity-dominant configurations, the radiation terms can dominate the Ohmic power deposition. This suggests that the proposed mechanism for the pinch oscillations is reasonable.

7.3 Comparison of 10 cm and 16 cm Inner Electrode Configuration Performance

The measurements of the equilibrium profiles in ZaP with the 10 cm and 16 cm inner electrode configurations are compared to each other. The calculated profiles are also compared to the predictions from the pinch formation analysis in Section 5.3. The assumed value for the pre-compression temperature is $T_a = 10$ eV, the width of the current sheet is assumed to be $L_a = 3$ cm and the length of the pinch is assumed to be $L_p = 1$ meter. Figure 7.14 shows the calculated values of the characteristic pinch radius (black) and the predicted values from the adiabatic compression analysis (red) for the 10 cm and 16 cm diameter inner electrodes. The 10 cm electrode exhibits behavior that matches the predictions of adiabatic compression reasonably accurately for the assumed values of T_a and L_a . The departures from the adiabatic predictions, particularly towards the beginning and end of the quiescent period, are likely related to the static nature of the T_a and L_a assumptions. For all of the observed times, these values are constant. This is not a likely scenario in the experiment as the conditions in the acceleration region are evolving.

The 16 cm electrode indicates a much larger divergence from the characteristic radii predicted from adiabatic analysis. The calculated values of characteristic radius are notably larger than predictions, though the overall trend of a decreasing pinch size does agree between measurements and predictions. This larger calculated pinch radius suggests that non-adiabatic processes are a substantial factor in the pinch formation. Further, it is also noted that the calculated characteristic radius for the 16 cm inner electrode is notably larger, by more than a factor of 2, than the 10 cm inner electrode. This is contrary to the goals of the 16 cm inner electrode which was proposed to produce a smaller characteristic radius due to the increased compression ratio.

Figure 7.15 shows the calculated and predicted peak electron density as a function of time for the 10 cm and 16 cm diameter inner electrodes. The trends observed are similar to the characteristic radius. The peak electron density calculated for the 10 cm electrode is similar to the predicted values from adiabatic compression. The divergence from adiabatic

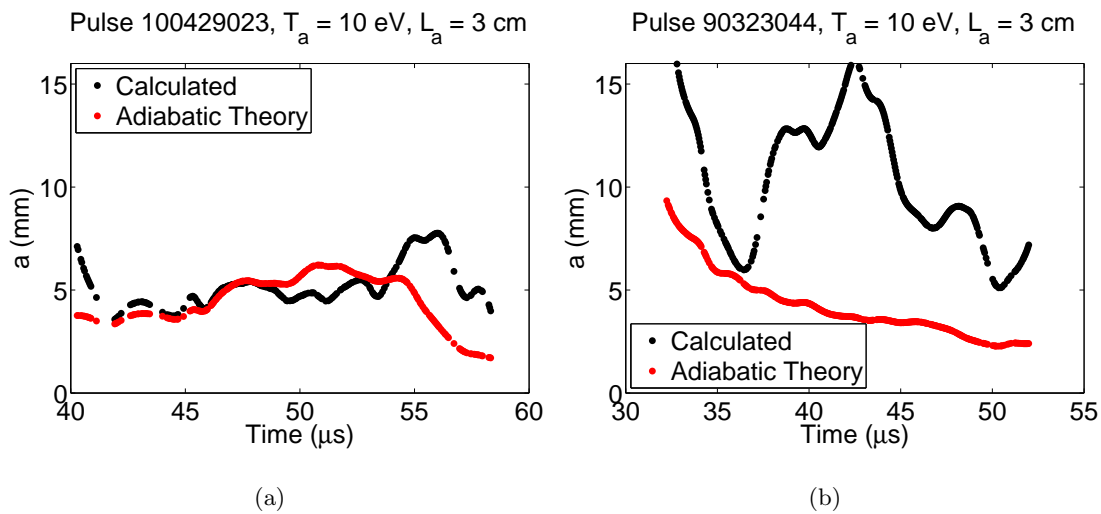


Figure 7.14: Calculated and predicted characteristic pinch radius for 10 cm and 16 cm diameter inner electrode configurations. (a) Calculated radii for the 10 cm electrode are very close to the predicted values from adiabatic compression for the assumed values of T_a and L_p . (b) Calculated values of the characteristic pinch radius for the 16 cm inner electrode are considerably higher than the predicted values and larger than the 10 cm inner electrode measurements.

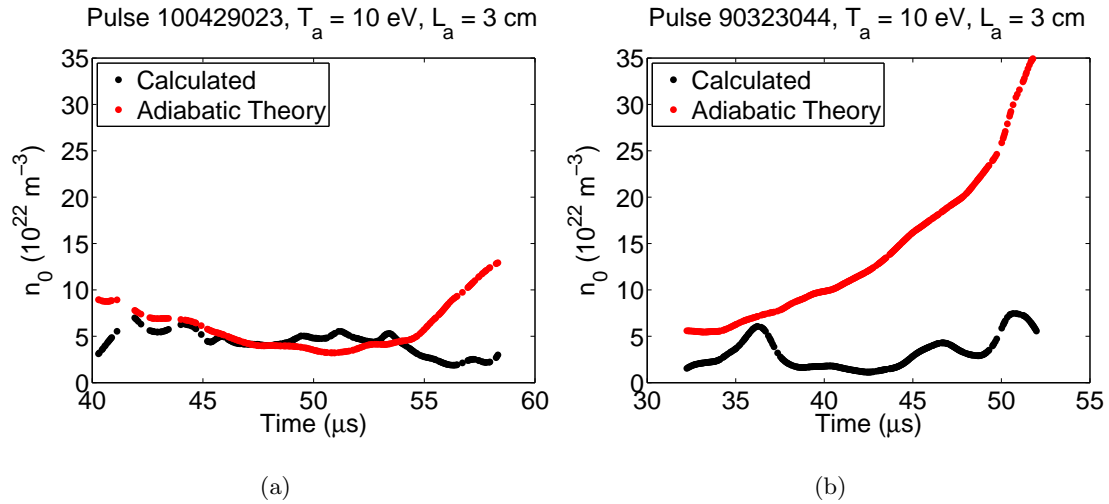


Figure 7.15: Calculated and predicted peak electron density for the 10 cm and 16 cm diameter inner electrode configurations. (a) Calculated peak values of electron density are similar to the values predicted from adiabatic compression for the 10 cm inner electrode. (b) Calculated values of peak electron density are much lower than predicted by adiabatic compression analysis for the 16 cm inner electrode.

predictions for the 16 cm electrode is significant and increases with increasing time in the quiescent period suggesting the influence of non-adiabatic processes. The peak density for the 16 cm diameter inner electrode is notably lower than the 10 cm electrode which, again, is contrary to the goals of the adiabatic compression experiment.

Figures 7.16 and 7.17 show the predicted and calculated values of the peak temperature and peak magnetic field as a function of time for the 10 cm and 16 cm diameter inner electrodes. The differences between the predicted and calculated peak temperature and magnetic field for the 10 cm inner electrode are substantially different from the expected relationships based on the previously-mentioned similarities between the characteristic pinch radius and the peak electron density (the expectation of similar temperature and magnetic field values). The primary reason for this difference is the assumption from the adiabatic compression analysis of a Lorentzian temperature profile and a magnetic field profile predicated on a Bennett pressure profile. These profiles have higher peak values than

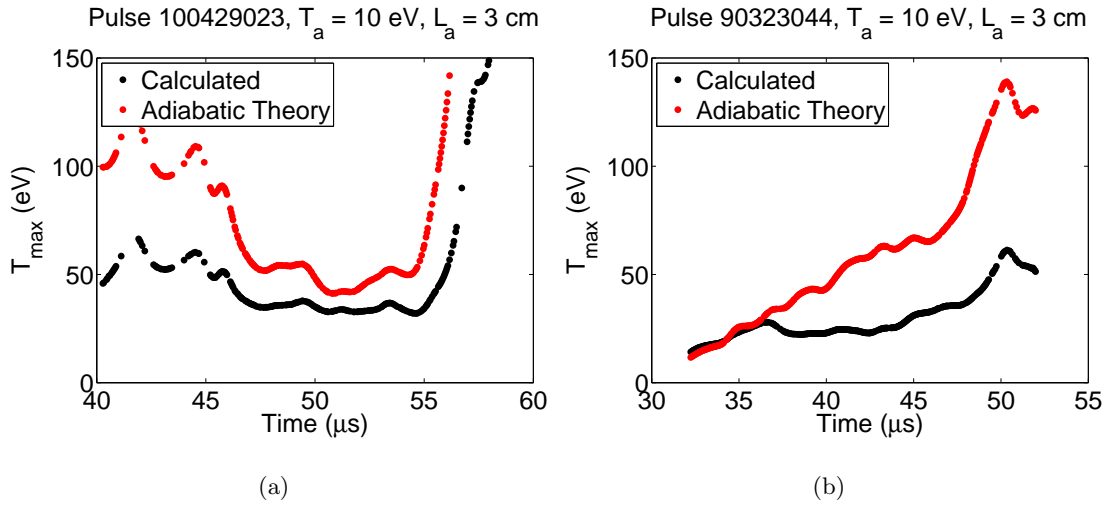


Figure 7.16: Calculated and predicted peak temperature as a function of time for 10 cm and 16 cm diameter inner electrode configurations. (a) Predicted peak temperature for the 10 cm electrode is approximately twice the calculated value. This is explained by the assumption in the adiabatic compression calculation of a Lorentzian temperature profile. The calculated value is broader with a lower peak temperature. (b) Predicted peak temperature for the 16 cm electrode is significantly larger than the calculated value. The calculated values for the 16 cm inner electrode is also much lower than for the 10 cm inner electrode.

the calculated profiles produced by radial heat conduction analysis due to the high thermal conductivity at the pinch axis. The result is broader calculated profiles with lower peaks.

The calculated temperature and magnetic field for the 16 cm inner electrode are lower than the calculated values for the 10 cm inner electrode. This is due to the increased characteristic radius for the 16 cm electrode. Non-adiabatic processes are the likely reason for these differences.

A possible explanation of the non-adiabatic processes is the existence of strong shocks during the formation process. Using the calculated values of the characteristic radius and the shock-modified compression analysis equations found in Section 5.3, values of the Mach number of a shock during formation can be estimated that would produce the resulting differences from adiabatic theory. These Mach numbers are shown in Figure 7.18 for the

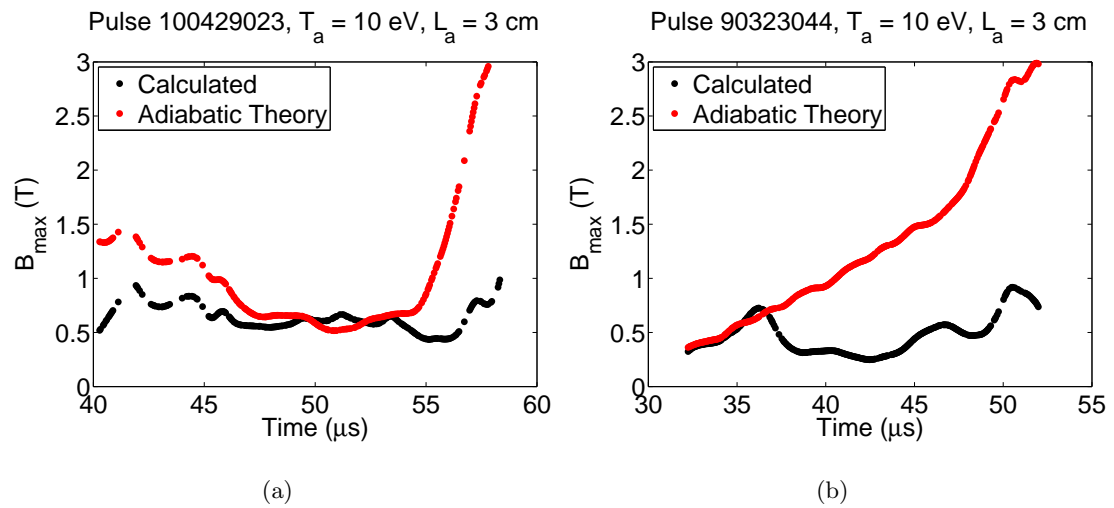


Figure 7.17: Calculated and predicted peak magnetic field as a function of time for 10 cm and 16 cm diameter inner electrode configurations. (a) Predicted peak magnetic field is higher than the calculated value. This is due to the Bennett equilibrium assumption of the adiabatic calculation. (b) Predicted peak magnetic field is considerably higher for the 16 cm inner electrode than the calculated value. These calculated values are lower than the 10 cm inner electrode values.

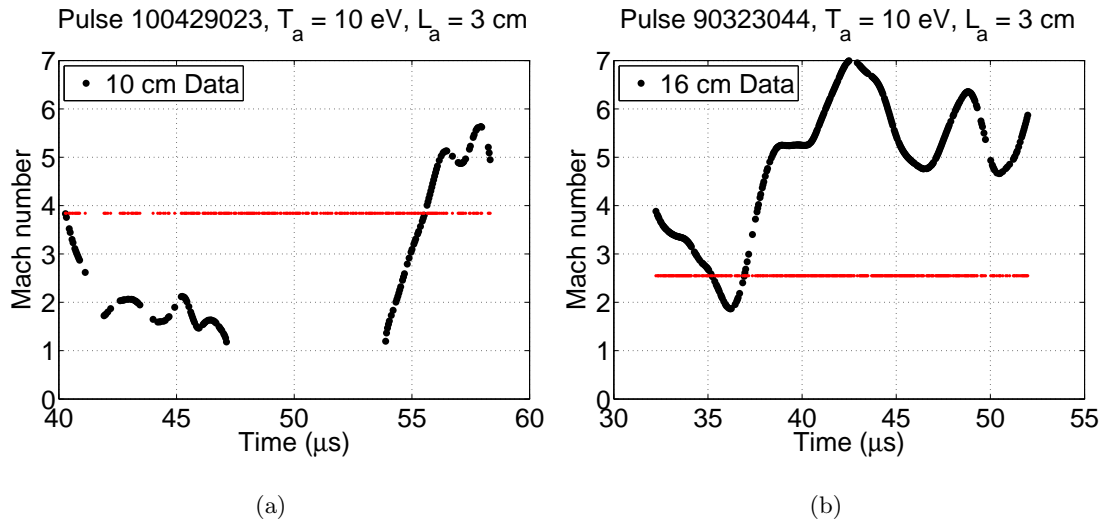


Figure 7.18: Predicted shock Mach number to account for difference in calculated and predicted equilibrium for 10 cm and 16 cm diameter inner electrode configurations. (a) The predicted Mach number to account for the discrepancies in the adiabatic predictions are less than $M = 3$ for the 10 cm electrode. (b) The predicted Mach number for the 16 cm electrode configuration is notably higher than the 10 cm electrode, $M > 6$. This strong shock may explain the large calculated values of the characteristic pinch radius.

10 cm and 16 cm diameter inner electrodes. The resulting Mach numbers for the 10 cm electrode tend to be weaker shocks, $M < 2$, that would explain the divergence of the calculated values from adiabatic predictions. For the 16 cm diameter electrode, strong shocks, $M > 5$, are required to explain the larger differences from adiabatic theory. The resulting compression speeds required to produce these Mach numbers just prior to the formation shock are shown in Figure 7.19. The velocities are on the order of $10^4 - 10^5$ m/s, which are reasonable velocities when compared with the measured axial flow velocity of the pinch, $\approx 10^5$ m/s, as well as the bulk plasma velocity measured at the end of the acceleration region in the experiment, indicated by the red horizontal lines.

Figure 7.20 shows magnetic field data at $z = -25$ cm and $z = -10$ cm (near the exit of the acceleration region) that allow an estimation of the bulk plasma velocity as it exits the acceleration region. Measuring the time difference between when each of the signals

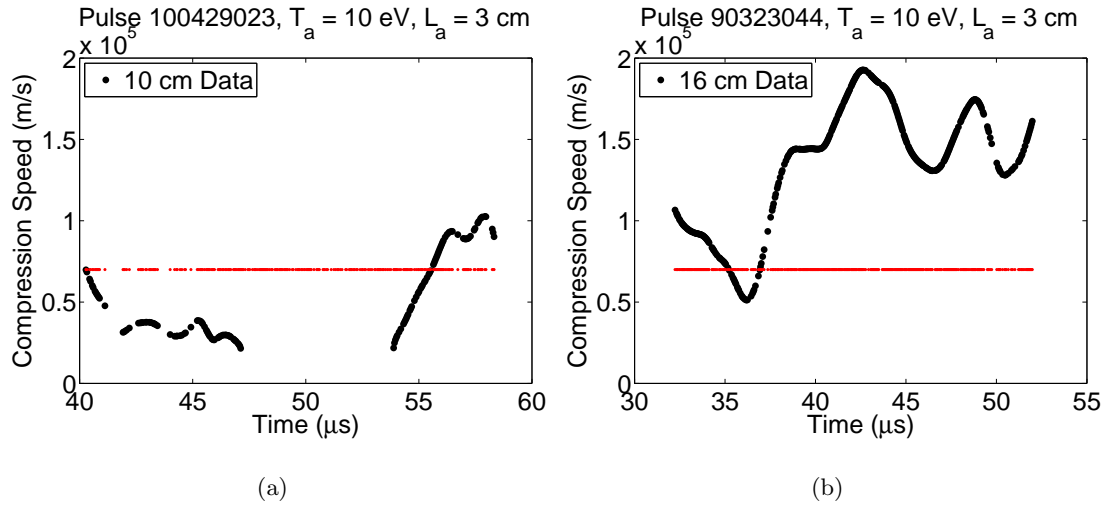


Figure 7.19: Predicted compression speed during formation process for 10 cm and 16 cm diameter inner electrode configurations. The predicted compression speeds to account for the potential shocks that would result in the divergence from adiabatic theory are reasonable in comparison to the plasma velocity in the acceleration region (horizontal red line).

begins to increase and dividing that by the length between the probes, an estimate of the velocity is made. For each of these pulses that velocity is $v_z \approx 7 \text{ cm}/\mu\text{s}$. The figure also suggests a possible explanation for the existence of stronger shocks in the 16 cm diameter inner electrode configuration. The magnetic field at $z = -25 \text{ cm}$ for the 16 cm electrode is higher than the 10 cm electrode configuration by a factor of 25 – 30%. This means a larger current in the acceleration region. A large current, coupled with the larger magnetic field results in a larger radial compression force which could produce higher compression velocities dependent on the mass being accelerated. Further, the nosecone of the 10 cm diameter inner electrode has a more gradual slope (30 degrees) than the 16 cm diameter inner electrode (45 degrees). This produces a greater radial force in the 16 cm diameter inner electrode than the 10 cm diameter inner electrode which could further contribute to shock formation.

The formation of stronger shocks in the 16 cm electrode configuration would produce

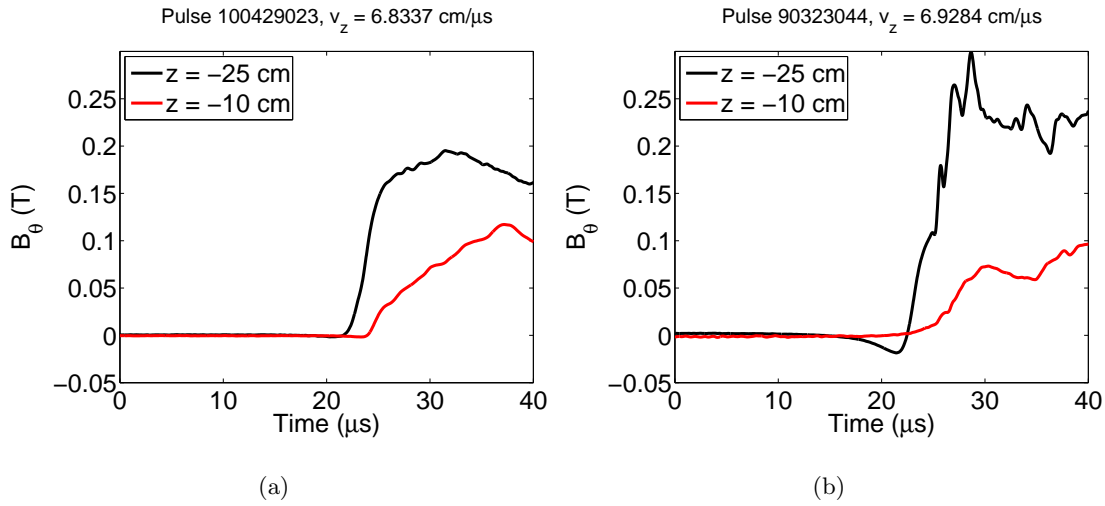


Figure 7.20: Plasma arrival in the acceleration region for 10 cm and 16 cm diameter inner electrode configurations. Arrival of the plasma at the exit of the ZaP acceleration region ($z = -25$ cm) and at $z = -10$ cm is separated by $\approx 2 \mu\text{s}$. This gives a velocity of $\approx 7 \text{ cm}/\mu\text{s}$.

greater initial overcompression of the pinch. The resulting effect on the characteristic pinch radius oscillations would be an increase in the magnitude of the oscillations and a probable decrease in their frequency (due to inertia of the plasma). These differences are observed between the two electrode configurations.

The overall goal of the 16 cm diameter inner electrode is to increase the density and temperature of the pinch through an increased compression ratio. The proposed operating conditions consisted of equal currents in both the 10 cm and 16 cm diameter electrode and an equal linear density in the pinch. Adiabatic theory predicted a 2x increase in the temperature and 3x increase in density with a corresponding decrease in the pinch radius. It has been observed that the temperatures and densities for the 16 cm electrode configuration are actually lower than the 10 cm electrode configuration. This is partially due to the proposed non-adiabatic mechanisms of shocks and the balance of Ohmic power and radiation. A more fundamental reason for the lack of success increasing the pinch temperature is shown in Figure 7.21, the linear density of the pinch as a function of time for the 10 cm and 16 cm

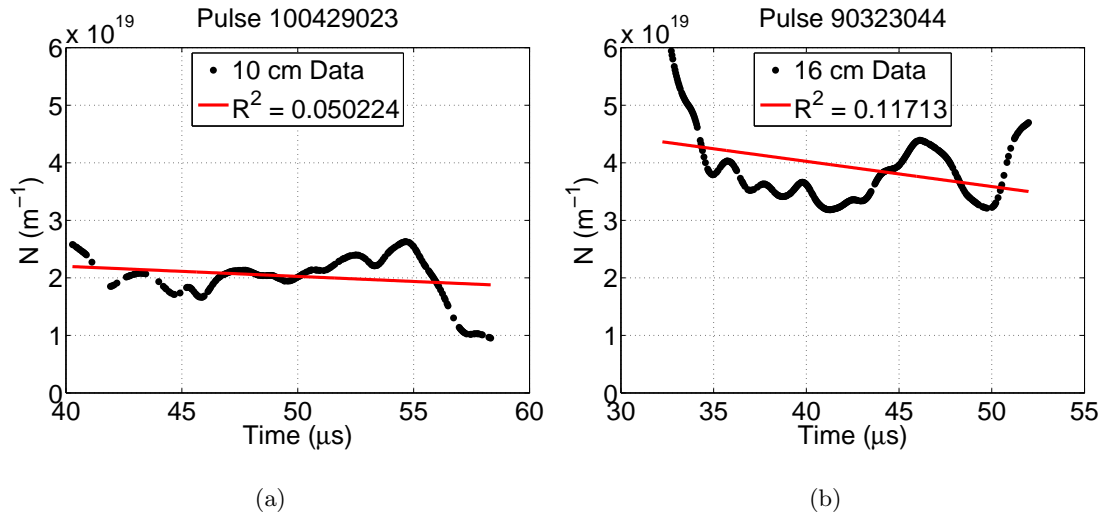


Figure 7.21: Calculated linear density as a function of time for 10 cm and 16 cm inner electrode configurations. (a) Calculated linear density for the 10 cm inner electrode is relatively constant with small oscillations during the quiescent period. (b) Linear density for the 16 cm inner electrode is a factor of 1.5 to 2 larger than for the 10 cm electrode. Oscillations have similar magnitude to the 10 cm electrode linear density.

electrode configurations. The calculated linear density in the pinch is higher for the 16 cm inner electrode by a factor of 2. Coupled with the similar values of total current shown in Figure 7.22, it is expected that temperatures would not increase as expected. The likely non-adiabatic effects made the failure more pronounced. The operating condition shown for the 16 cm diameter inner electrode was the optimum operating condition for low gas injection operations. Further reducing the injected gas resulted in poor performance pinches with short quiescent periods for which effective measurements are difficult.

Proposed methods of improving the 16 cm diameter electrode configuration design and operation include producing a new nosecone with a more gradual slope to potentially reduce shock strength during formation and producing a gas injection scheme that results in a smaller amount of particles for the initial pinch formation and a sufficient reservoir of gas to extend the length of the quiescent period.

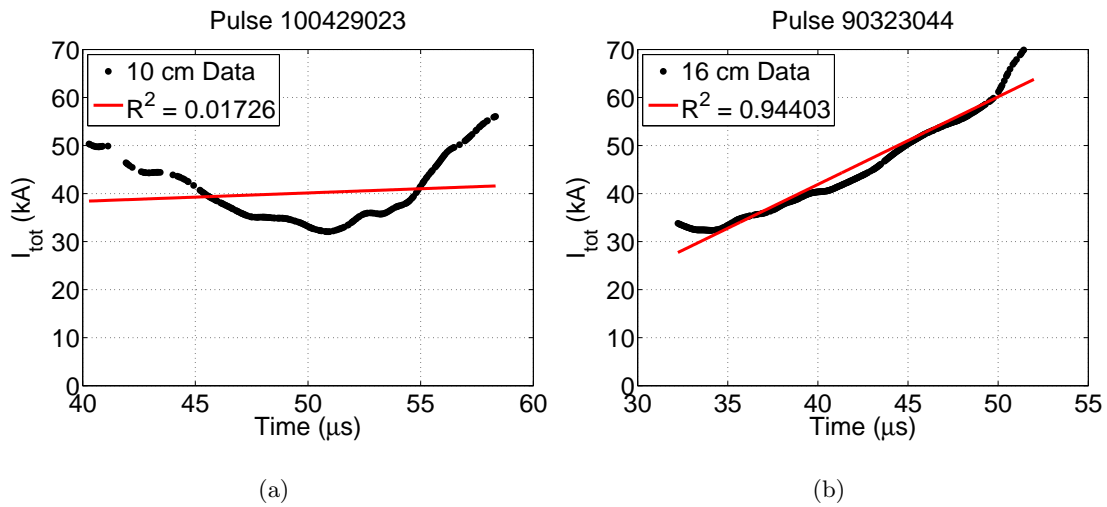


Figure 7.22: Total current as a function of time for 10 cm and 16 cm diameter inner electrode configurations. (a) Total current for the 10 cm inner electrode also exhibits oscillations as a function of time. (b) Total current for the 16 cm inner electrode is a similar magnitude to the 10 cm electrode with smaller magnitude oscillations.

Chapter 8

CONCLUSIONS

The ZaP Flow Z-Pinch is a basic plasma physics experiment which investigates the effect of a sheared axial velocity profile on the stability of a Z-pinch plasma. The 10 cm diameter inner electrode of ZaP is replaced with a 16 cm diameter inner electrode and the effects are measured. Two optimum operating conditions are identified for the 16 cm inner electrode: a soft-stop operating condition that consists of an extended quiescent period that is limited by the current pulse; a high peak magnetic field operating condition that consists of a magnetic field plateau preceding a magnetic field peak. The magnetic field peak precedes the end of the quiescent period in this operating condition.

A perforated outer electrode section is installed in ZaP to examine the effects of the conducting wall on the stability of the pinch. Experimental evidence with and without the perforated electrode section indicates that the conducting wall of the outer electrode has no effect on the stability of the pinch. An axially-coherent pinch structure is observed with and without the perforated electrode section with an extended period of stability. Numerical simulations using the HiFi code agree with experimental evidence.

The effect of installing the 16 cm inner electrode is expected to be an increase in temperature and density due to an increased compression ratio from the plasma acceleration region to the pinch. The increased compression ratio is predicted to increase the temperature by a factor of 2, increase density by a factor of 3 with a corresponding decrease in the characteristic pinch radius. The effects of potential non-adiabatic processes such as shocks and Ohmic heating are also investigated. These non-adiabatic processes would result in a larger characteristic pinch radius than the purely adiabatic case for given values of the linear density, N , and total current, I .

The equilibrium evolution for the 10 cm and 16 cm diameter inner electrode operating

conditions is calculated with a four-chord HeNe interferometer. The chord-integrated data are fit to a Lorentzian density profile. These density profiles are used with the measured current and the equations of radial force balance and radial heat conduction to calculate profiles of the temperature and magnetic field. The system of equations is solved using a multiple shooting method with appropriate boundary conditions. The multiple shooting method is effective in accurately solving the nonlinear system of equations that includes an Ohmic power source term and a bremsstrahlung radiation sink term. The system of equations does not address the effects of line radiation from the plasma due to issues with solution convergence. Impurity radiation in coronal equilibrium was used, ignoring time-dependent radiation effects, with an arbitrary impurity fraction. A more accurate model of radiation from the plasma should be employed in the future.

Both electrode configurations exhibit behavior that indicates magnetic compression is a dominant mechanism during the quiescent period. Both electrode configurations also display irregular oscillations in the characteristic radius of the pinch. These oscillations are more pronounced in the 16 cm inner electrode configuration. The oscillations appear to be related to the balancing of Ohmic power dissipation and radiation losses. As the characteristic pinch radius decreases, the Ohmic power dissipation dominates over the radiation losses causing an increase in the pinch radius. This results in the radiation losses dominating the Ohmic power dissipation causing the pinch to shrink. This process continues until the end of the quiescent period.

Neither electrode configuration is perfectly correlated with the predictions from adiabatic compression, but the 10 cm inner electrode configuration is more consistent than the 16 cm inner electrode configuration. The 16 cm inner electrode configuration exhibits shock behavior during the formation process that result in a much larger characteristic radius than predicted by adiabatic compression and also results in larger pinch radius oscillations as a result of the initial overcompression of the pinch due to the shock. These stronger shocks are likely a result of a blunter nosecone for the 16 cm diameter inner electrode and the larger current in the plasma acceleration region, increasing the compression force.

The primary aim of the 16 cm diameter inner electrode was to increase the temperature and density in the pinch for an equal value of the plasma current. The result of this investigation is that the 16 cm diameter inner electrode could not produce higher temperatures and densities because the reduction in the total particle inventory injected into the experiment could not be reduced sufficiently. Further reduction of injected gas into the experiment result in sub-optimum experimental operations that preclude measurements in the pinch.

Chapter 9

FUTURE WORK

Two primary issues prevented the desired increase in temperature and density for the 16 cm inner electrode: inability to reduce the particle inventory while maintaining a sufficiently stable pinch; and the likely existence of strong shocks, increasing the characteristic pinch radius. Experimental changes to address the shock issues are to manufacture a new nosecone for the 16 cm diameter inner electrode that has a more gradual convergence to the axis than the 45 degree nosecone that is presently available. The particle inventory can be addressed by determining a gas-injection method that creates an initial pinch formation with a reduced particle inventory, but maintains sufficient residual gas in the accelerator to produce a longer quiescent period. An experimental modification is presently being conducted that may address the particle inventory issues. The insulating region between the inner and outer electrodes is being extended axially to limit the upstream motion of the ionization front which can rapidly deplete the acceleration region.

Computational advancements are possible and should be addressed for the radial heat conduction analysis using a multiple shooting method. A more accurate model for radiation in the plasma is necessary which includes a more accurate assessment of Z_{eff} in the plasma.

Appendix A

ADDITIONAL PULSE DATA

This appendix includes the results of analysis on additional plasma pulses for both the 10 cm and 16 cm diameter inner electrodes. The data agrees with the data from the primary text which indicates that stronger shocks are evident for the 16 cm diameter inner electrode than the 10 cm diameter inner electrode. Due to time constraints, not all of the pulses shown in the appendix utilize the generalized formulation of thermal conductivity. As mentioned previously, the profiles for the magnetized and generalized thermal conductivity formulations are very similar, therefore the data is included. The formulation of thermal conductivity utilized for each pulse is specified.

A.1 10 cm Pulse Data

Figures A.1 - A.6 show additional pulse data for the 10 cm diameter inner electrode. The experimental conditions are 6 kV capacitor bank voltage on eight, 180 μF capacitors. The gas-injection pressure is 5000 Torr. This pulse utilizes the generalized formulation of thermal conductivity.

An extended quiescent period with a noticeable density gradient is observed with the interferometer chords from $\approx 35 - 75 \mu\text{s}$. The measured values of characteristic radius and peak electron density agree well with the predictions of adiabatic theory. Further, the oscillations in the characteristic pinch radius are small. This is in agreement with the data shown previously for the 10 cm diameter inner electrode. Densities are $\approx 4 \times 10^{22} \text{ m}^{-3}$ and pinch radii are $\approx 6 \text{ mm}$. The data indicate an adiabatic compression process for this pulse.

The total current at $z = 0 \text{ cm}$ decays initially before growing towards the end of the quiescent period. The linear density stays relatively constant during the quiescent period at $2 - 3 \times 10^{19} \text{ m}^{-1}$. Peak magnetic field values are $\approx 0.5 \text{ T}$ with temperatures of $40 - 60 \text{ eV}$.

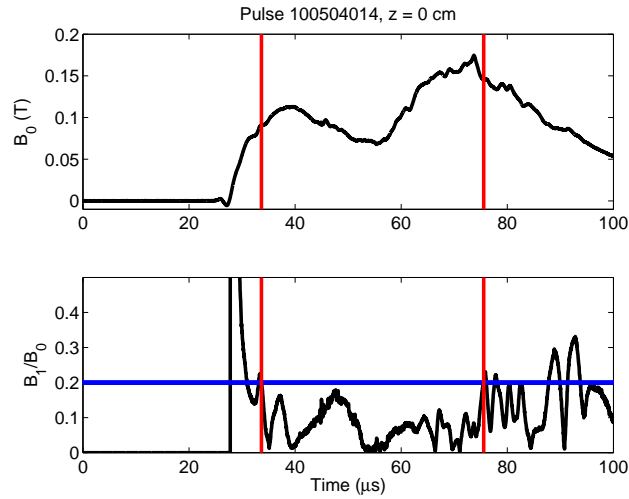


Figure A.1: Magnetic mode data for 10 cm diameter inner electrode configuration, Pulse 100504014. The capacitor bank voltage is 6 kV and the neutral-gas injection pressure is 5000 Torr. The pulse is characterized by a varying magnetic field with a peak magnetic field at the wall of ≈ 0.2 T. The quiescent period is ≈ 40 μs .

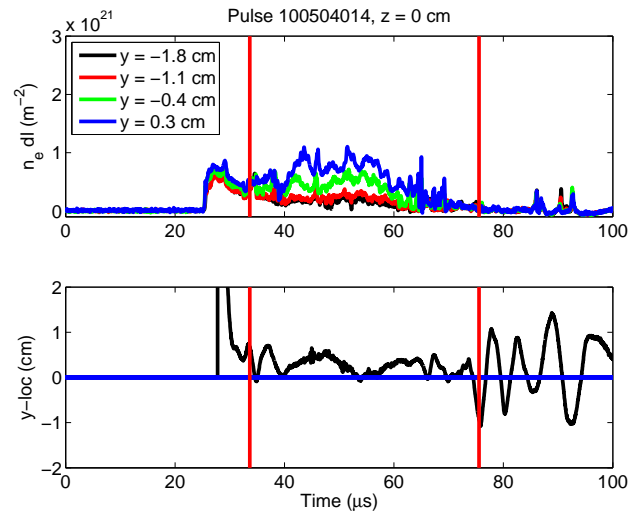


Figure A.2: Four-chord interferometry data for 10 cm diameter inner electrode configuration, Pulse 100504014. During the quiescent period the current centroid is located within 5 mm of the machine axis and the chord-integrated density data indicates a noticeable density gradient.

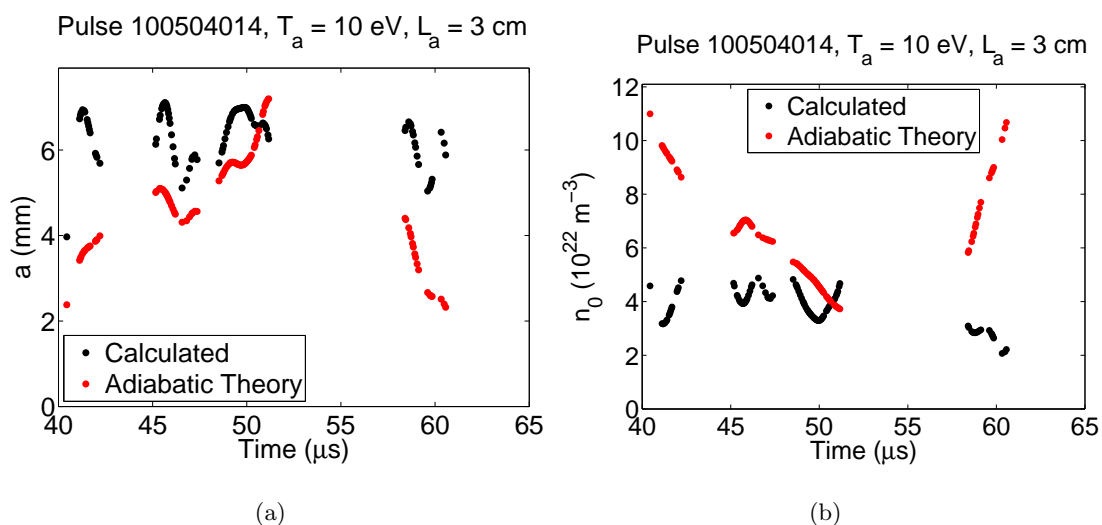


Figure A.3: Characteristic pinch radius and peak density as a function of time for 10 cm diameter inner electrode, Pulse 100504014. (a) Overall trend is a constant mean pinch radius as a function of time of ≈ 6 mm. Small-scale oscillations in the pinch size are observed. Predictions from adiabatic theory are in reasonable agreement with measured data. (b) The on-axis density also has a relatively constant mean value as a function of time, $\approx 4 \times 10^{22} \text{ m}^{-3}$, and agrees well with the predictions of adiabatic theory.

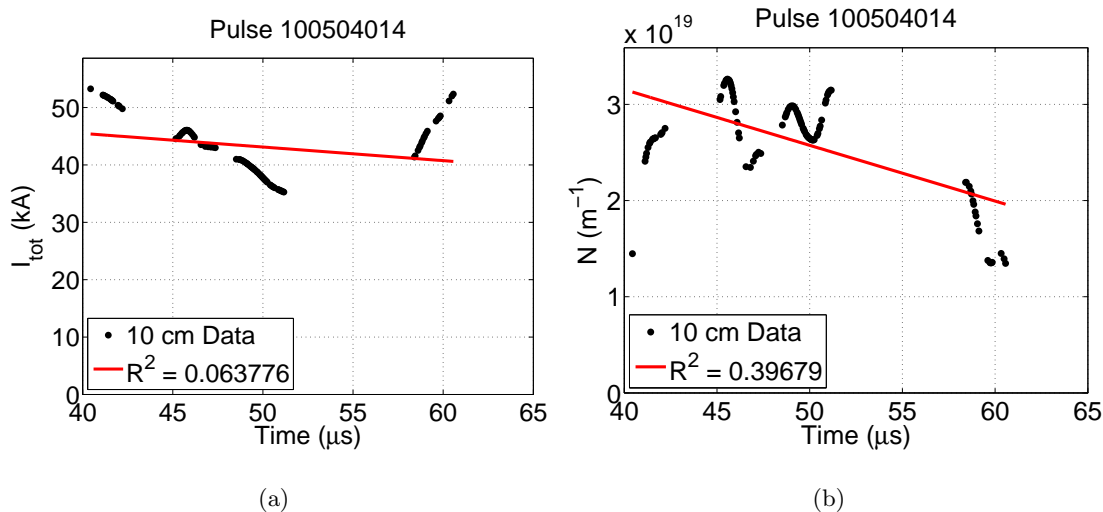


Figure A.4: Total current and linear density as a function of time for the 10 cm diameter inner electrode, Pulse 100504014. (a) Total current is decreasing until $t \approx 55 \mu\text{s}$ at which point it increases. (b) Linear density is approximately constant $2 - 3 \times 10^{19} \text{ m}^{-1}$, as a function of time until late in the quiescent period when it decreases. The red lines are linear trendlines to the data.

Predicted compression speeds and Mach numbers indicate that if there are shocks present during the formation process, they are fairly weak, $M < 3$, and the compression speeds are in line with the speeds measured at the exist of the plasma accelerator.

Figures A.7 - A.12 show additional pulse data for the 10 cm diameter inner electrode. The experimental conditions are 6 kV capacitor bank voltage on eight, $180 \mu\text{F}$ capacitors. The gas-injection pressure is 4500 Torr. This pulse utilizes the generalized formulation of thermal conductivity.

The behavior for this pulse is similar to the previous pulse. An extended quiescent period is observed with a noticeable density gradient. Low pinch radius oscillations about the mean radius of $\approx 5 \text{ mm}$ are observed with corresponding low oscillations in the peak density. The values of a and n_0 predicted from adiabatic theory match well with the experimentally-observed values, indicating that the compression process is adiabatic for this pulse.

Total current at $z = 0 \text{ cm}$ displays an initial decay before it increases towards the end of

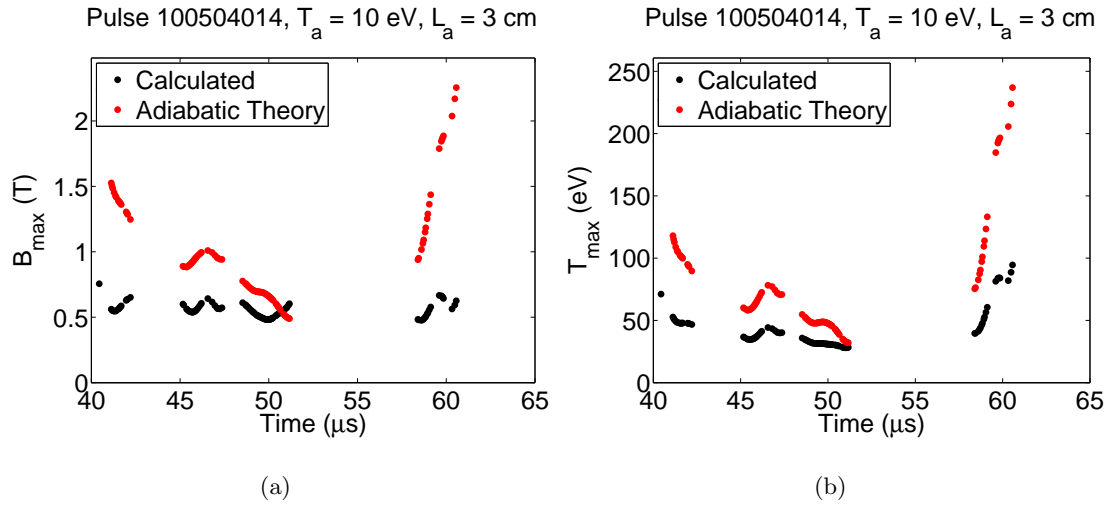


Figure A.5: Peak magnetic field and peak temperature as a function of time for the 10 cm diameter inner electrode, Pulse 100504014. (a) Calculated magnetic field values are in reasonable agreement with the predictions of adiabatic theory in the middle of the quiescent period. Peak magnetic field values are ≈ 0.5 T. (b) Temperature values are relatively constant as a function of time at 40 - 60 eV.

the quiescent period. The measured linear density is approximately constant as a function of time. The calculated peak magnetic field values are ≈ 0.5 T with peak temperatures of ≈ 40 eV.

Predicted shock strength indicates that shocks may not exist at all for this pulse a relatively small number of points during the measurement period exceeding the predictions of adiabatic theory.

Figures A.13 - A.18 show additional pulse data for the 10 cm diameter inner electrode. The experimental conditions are 5 kV capacitor bank voltage on eight, 180 μF capacitors. The neutral-gas line pressure is 3500 Torr. This pulse utilizes the generalized formulation of thermal conductivity.

The pulse exhibits an extended quiescent period with a noticeable density gradient. However, the pulse is the only one of the effectively measured 10 cm diameter inner electrode pulses that indicated non-adiabatic compression processes. The measured characteristic

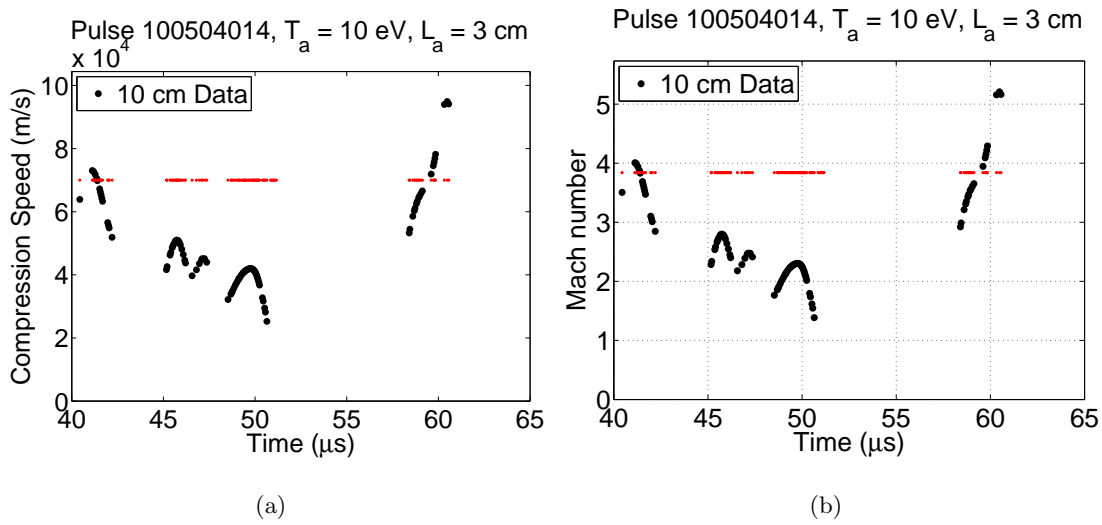


Figure A.6: Predicted formation compression speed and Mach number for the 10 cm diameter inner electrode, Pulse 100504014. (a) The predicted compression speed from the advanced adiabatic analysis is similar in magnitude to the measured velocity at the exit of the accelerator (horizontal red line). (b) The predicted shock strength for this pulse is weak ($M < 3$) and agrees well with the measured and calculated data and its comparison to adiabatic analysis, which suggests an approximately adiabatic formation process.

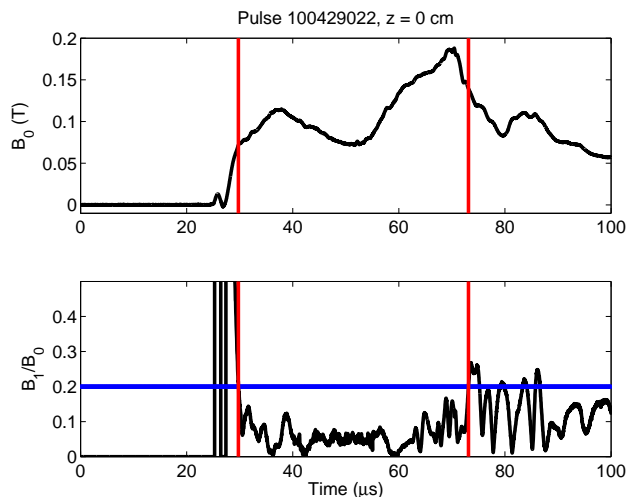


Figure A.7: Magnetic mode data for 10 cm diameter inner electrode configuration, Pulse 100429022. The pulse is for a 6 kV capacitor bank voltage and a 4500 Torr neutral-gas line pressure. A long quiescent period exists, $> 40 \mu\text{s}$, with magnetic field values measured at the wall fluctuating between 0.1 and 0.17 T.

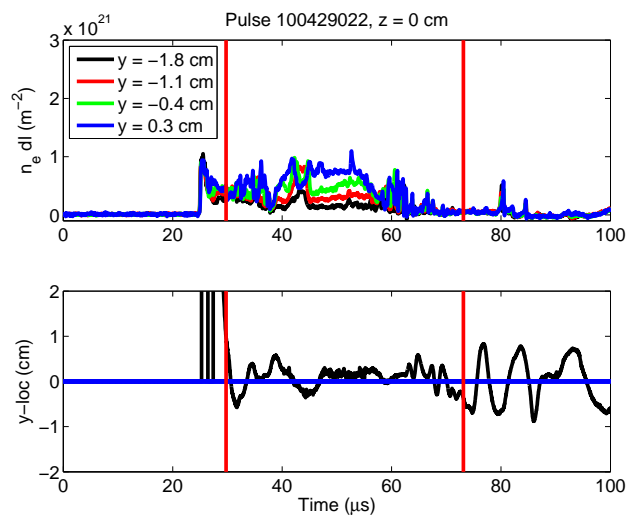


Figure A.8: Four-chord interferometry data for 10 cm diameter inner electrode configuration, Pulse 100429022. Magnetic mode data indicates a current centroid located within 5 mm of the machine axis during the quiescent period. A noticeable density gradient is also observed during the quiescent period.

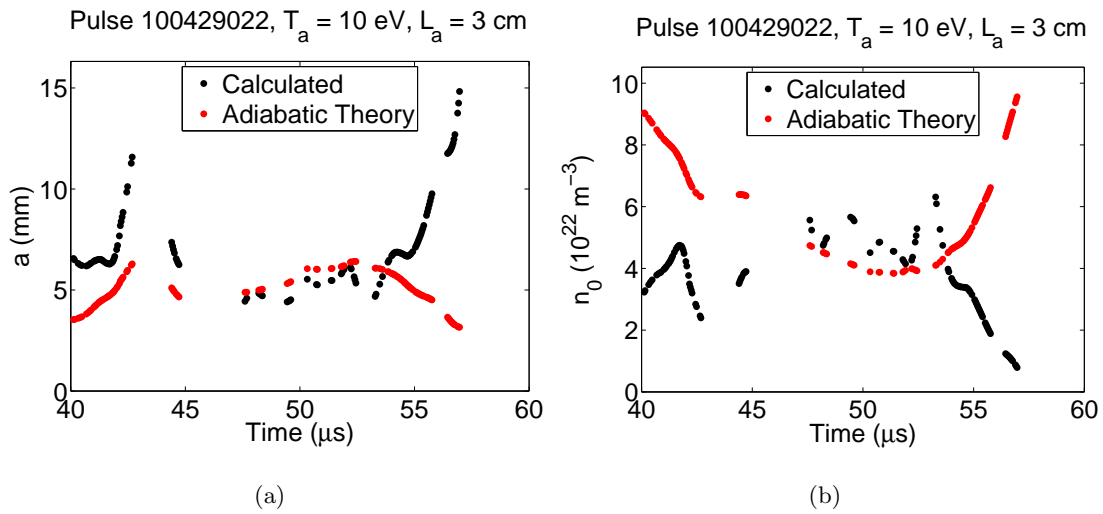


Figure A.9: Characteristic pinch radius and peak density as a function of time for 10 cm diameter inner electrode, Pulse 100429022. (a) From 45 – 55 μs , the characteristic radius fluctuates around 5 mm, consistent with the predictions of adiabatic compression. Towards the end of the measurement region, the size begins to increase. (b) The peak electron density fluctuates around $5 \times 10^{22} \text{ m}^{-3}$ during the quiescent period. This is also in agreement with the predictions of adiabatic compression.

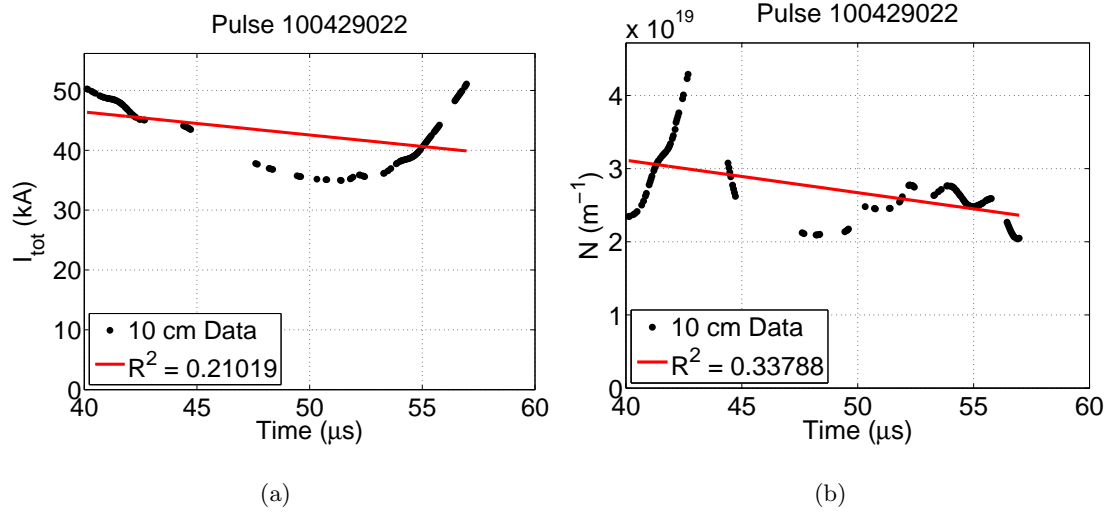


Figure A.10: Total current and linear density as a function of time for the 10 cm diameter inner electrode, Pulse 100429022. (a) Total current varies during the quiescent period between 35 and 50 kA. (b) Linear density remains relatively constant during the period between 45 and 55 μs at $2 - 3 \times 10^{19} \text{ m}^{-1}$. The red lines are linear trendlines to the data.

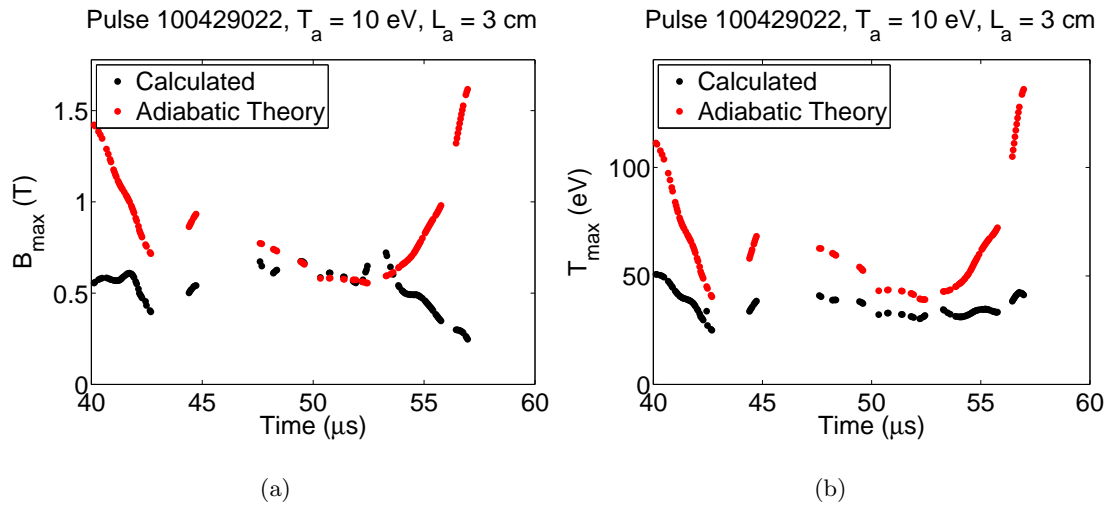


Figure A.11: Peak magnetic field and peak temperature as a function of time for the 10 cm diameter inner electrode, Pulse 100429022. (a) Peak magnetic field is relatively constant during the quiescent periods with small fluctuations about 0.5 T. The calculated values are similar to the predictions of adiabatic theory. (b) Temperature ranges between 35 and 50 eV during the measurement period.

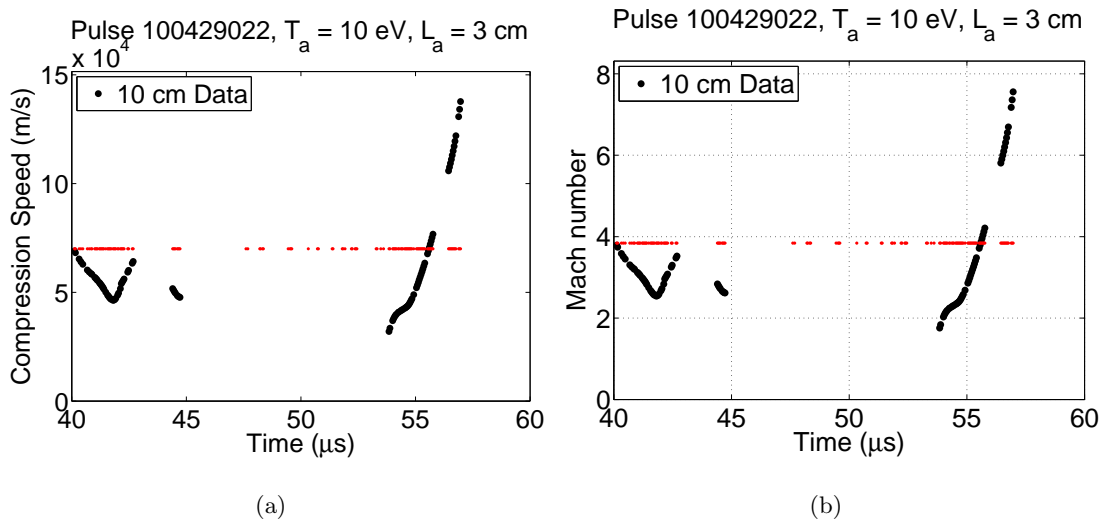


Figure A.12: Predicted formation compression speed and Mach number for the 10 cm diameter inner electrode, Pulse 100429022. (a) The predicted compression speed from the advanced adiabatic analysis is similar in magnitude to the measured velocity at the exit of the accelerator (horizontal red line). (b) The predicted shock strength for this pulse is weak (typically $M < 1$) and agrees well with the measured and calculated data and its comparison to adiabatic analysis which suggests an approximately adiabatic formation process.

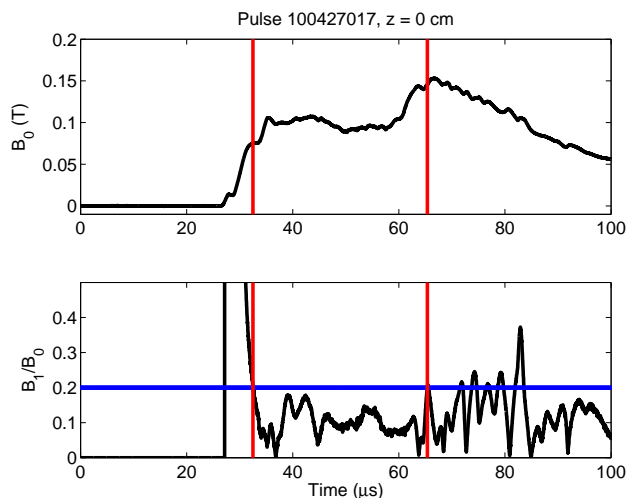


Figure A.13: Magnetic mode data for 10 cm diameter inner electrode configuration, Pulse 100427017. The pulse uses a 5 kV capacitor bank voltage and a 3500 Torr neutral-gas line pressure. The quiescent period length is $\approx 30 \mu\text{s}$ and the magnetic field measured at the wall ranges between 0.1 and 0.15 T during that time.

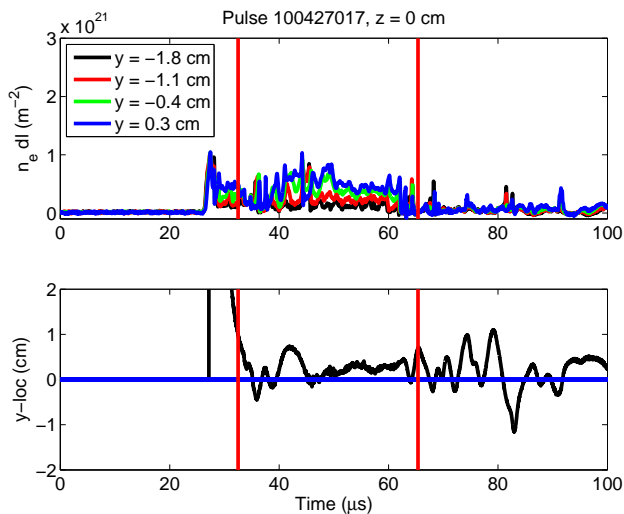


Figure A.14: Four-chord interferometry data for 10 cm diameter inner electrode configuration, Pulse 100427017. The centroid of the current is within 5 mm of the machine axis during the quiescent period and a noticeable density gradient is observed.

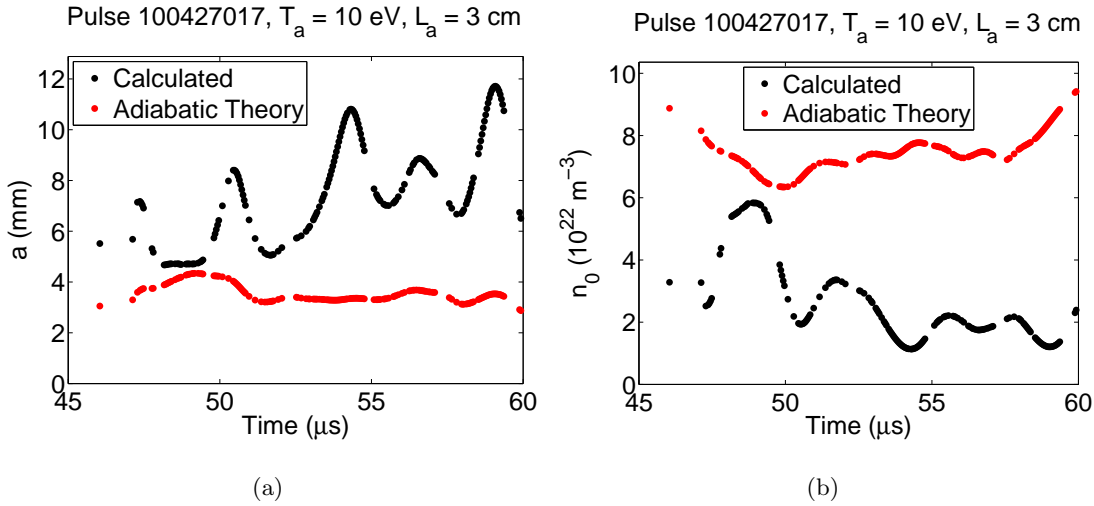


Figure A.15: Characteristic pinch radius and peak density as a function of time for 10 cm diameter inner electrode, Pulse 100427017. (a) The overall trend of the characteristic radius is to increase with increasing time. The characteristic radius also exhibits significant oscillations which are possible evidence of shocks during the formation process. The measured characteristic radius is also much larger than that predicted by adiabatic analysis. (b) Similarly, the peak electron density is much lower than predicted by adiabatic analysis with noticeable oscillations.

radius is noticeably larger than that predicted by adiabatic theory and also exhibits large oscillations, both indications of shocks during the pinch formation process. The peak electron density is similarly lower than predicted by adiabatic theory.

The pulse exhibits a constant current as a function of time removing the possibility of magnetic compression and expansion explaining the pinch size oscillations. The linear density is also constant as a function of time and lower than the previous pulses by $\approx 40\%$. This may explain the potential shock formation. Reducing the mass of the plasma slug that initially forms the pinch, would result in a greater final velocity during the formation process, possibly leading to shock formation.

Peak magnetic field values are well below the prediction of adiabatic theory at ≈ 0.5 T with peak temperatures of ≈ 50 eV. The approximately constant peak temperature as a

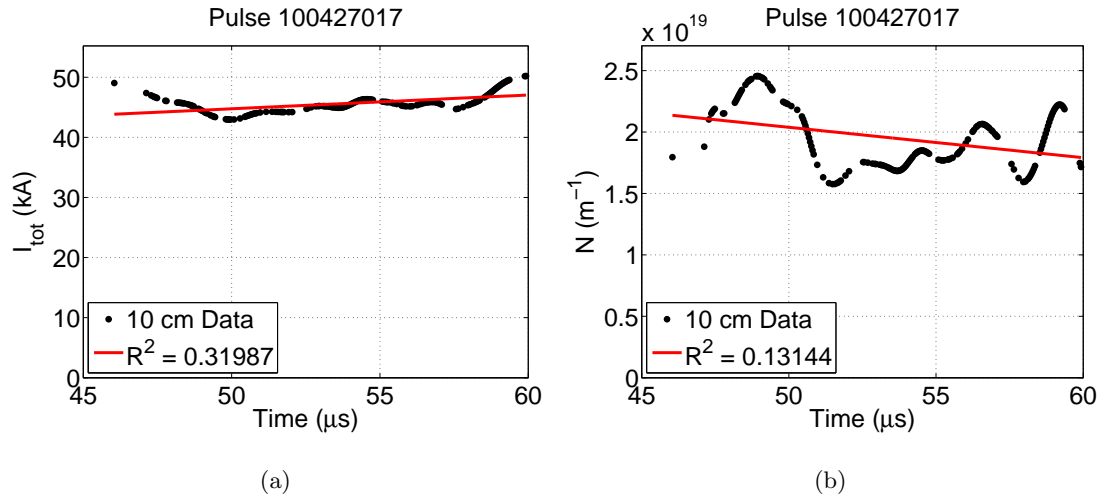


Figure A.16: Total current and linear density as a function of time for the 10 cm diameter inner electrode, Pulse 100427017. (a) Total current is nearly constant during the measurement period at 45 kA. This suggests that magnetic compression and expansion are not the source of the pinch radius oscillations. (b) Linear density is also relatively constant at $2 \times 10^{19} \text{ m}^{-1}$ during the measurement period. The red lines are linear trendlines.

function of time is consistent with the constant values of the measured current and the constant linear density.

The pulse indicates much stronger shocks than the previous pulses, $M = 3 - 6$, which agrees well with the large pinch size oscillations observed, as well as the lower temperatures, densities and magnetic fields compared to the predictions of adiabatic theory. The predicted compression speeds are within reasonable levels of the speed at the exit of the accelerator.

A.2 16 cm Pulse Data

Figures A.19 - A.24 show additional pulse data for the high peak magnetic field operating conditions for the 16 cm diameter inner electrode. The experimental conditions are 9 kV capacitor bank voltage on eight, $180 \mu\text{F}$ capacitors. The gas-injection pressure is 1500 Torr. This pulse utilizes the generalized formulation of thermal conductivity.

The magnetic field measured at the wall indicates a low-field plateau early in the quies-

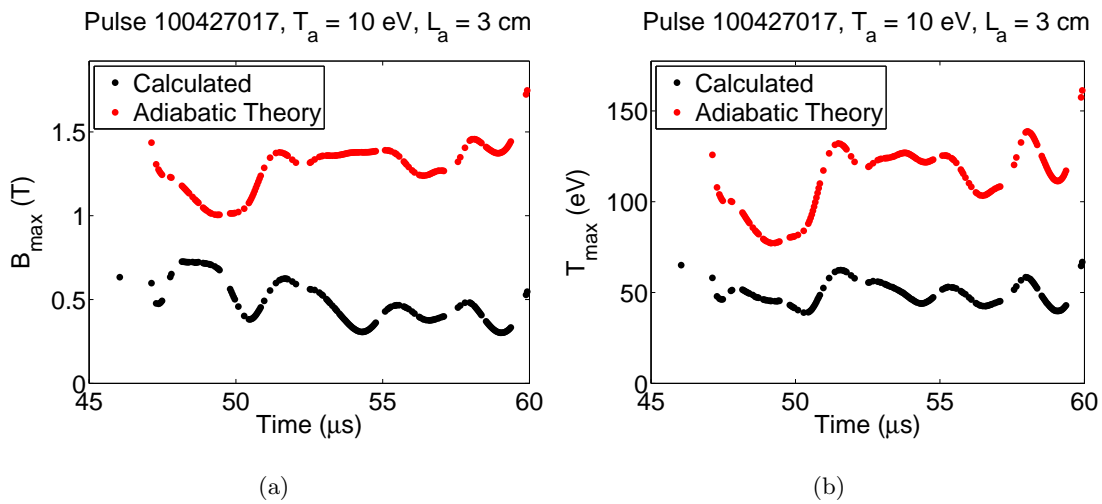


Figure A.17: Peak magnetic field and peak temperature as a function of time for the 10 cm diameter inner electrode, Pulse 100427017. (a) Peak magnetic field values are subject to oscillations and gradually decline with increasing time. The predicted values of the peak magnetic field are considerably higher than the calculated values, further evidence for shocks during the formation process. (b) Peak temperature oscillates about a value of ≈ 50 eV which is more than a factor of two less than the predictions from adiabatic theory.

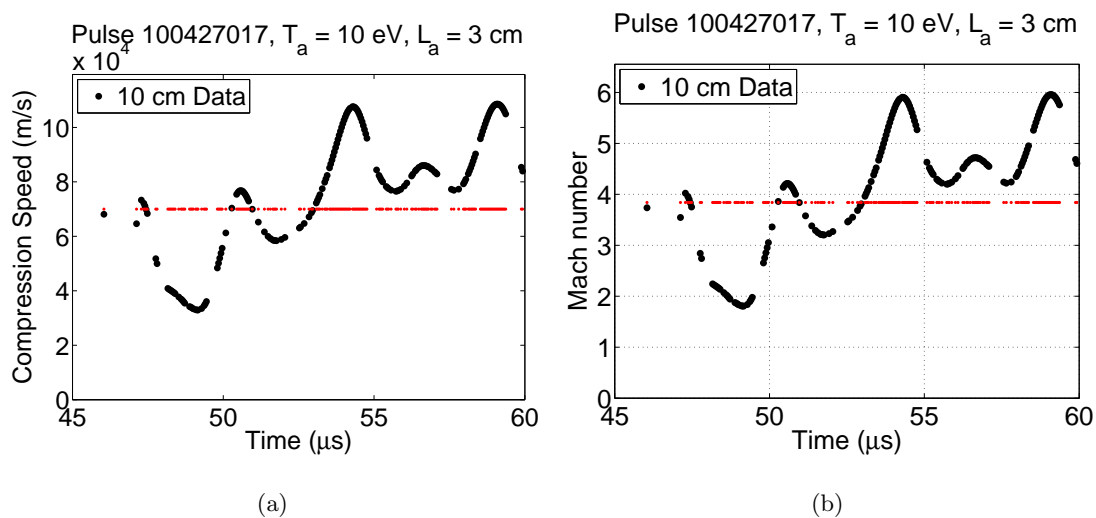


Figure A.18: Predicted formation compression speed and Mach number for the 10 cm diameter inner electrode, Pulse 100427017. (a) The predicted compression speed from the advanced adiabatic analysis is similar in magnitude to the measured velocity at the exit of the accelerator (horizontal red line). (b) The predicted shock strength for this pulse is strong ($M > 3$) and reinforces the measured and calculated data which suggests that shocks occur during the formation process, resulting in a larger pinch with increased size oscillations.

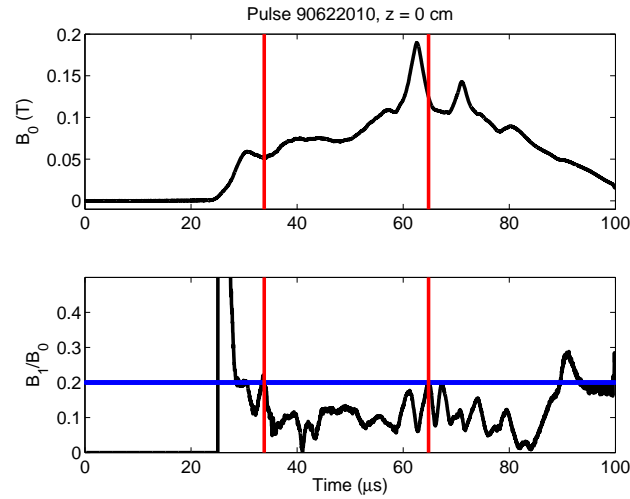


Figure A.19: Magnetic mode data for 16 cm diameter inner electrode configuration, Pulse 90622010. The pulse utilizes a 9 kV capacitor bank voltage and a 1500 Torr neutral-gas line pressure. The quiescent period is greater than $30 \mu\text{s}$ terminating after the magnetic field peak, as observed in the previous 16 cm diameter electrode data.

cent period, $\approx 0.1 \text{ T}$, which increases to a magnetic field peak that is nearly 0.2 T . This field peak precedes the end of the quiescent period. The length of the quiescent period for this pulse is greater than $30 \mu\text{s}$. Chord-integrated density measurements during the quiescent period indicate a noticeable density gradient and the location of the current centroid within a few mm of the machine axis.

The measured values of the characteristic radius are approximately 10 mm with large oscillations as a function of time. The peak density is $3 - 5 \times 10^{22} \text{ m}^{-3}$. The values of the characteristic radius are larger than those predicted by adiabatic theory. Similarly, the values of the peak electron density are considerably lower. This is indicative of shocks during the formation process.

The total current at $z = 0 \text{ cm}$ for this pulse increases during the quiescent period from 35 kA up to 70 kA. The linear density fluctuates about $3 - 5 \times 10^{19} \text{ m}^{-1}$. The peak magnetic field as a function of time is less than 0.6 T during the quiescent period and the temperature is increasing as a function of time, consistent with an increasing total current, from 30 up

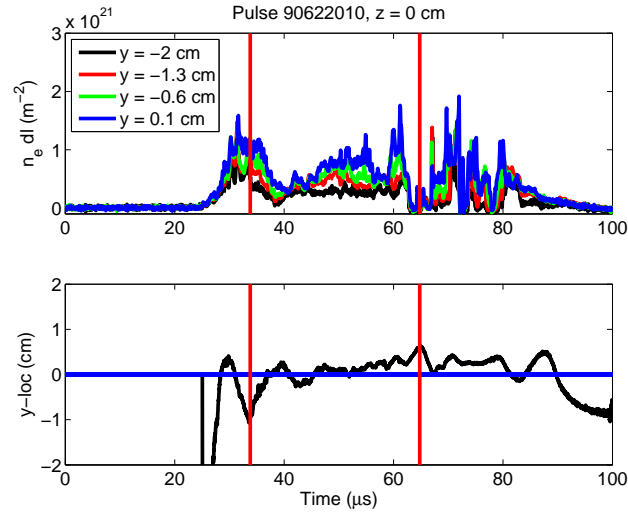


Figure A.20: Four-chord interferometry data for 16 cm diameter inner electrode configuration, Pulse 90622010. During the quiescent period, the centroid of the current is within 2 mm of the machine axis and a noticeable density gradient is observed for an extended period of time.

to 50 eV.

The 16 cm inner electrode pulse exhibits a strong predicted shock, $M \geq 4$, which is in agreement with other 16 cm electrode pulses and with the large oscillations measured in the characteristic radius. The differences in the measured values of the characteristic radius and the peak electron density and the calculated values of the temperature and magnetic field compared to the predictions of adiabatic compression can be attributed to these strong shocks during the formation process.

Figures A.25 - A.30 show additional pulse data for the high peak magnetic field operating conditions for the 16 cm diameter inner electrode. The experimental conditions are 9 kV capacitor bank voltage on eight, 180 μF capacitors. The gas-injection pressure is 1500 Torr. This pulse utilizes the magnetized formulation of thermal conductivity.

The magnetic field measured at the wall during the quiescent period increases from 0.05 T up to 0.2 T at the magnetic field peak. The end of the quiescent period lasts beyond the

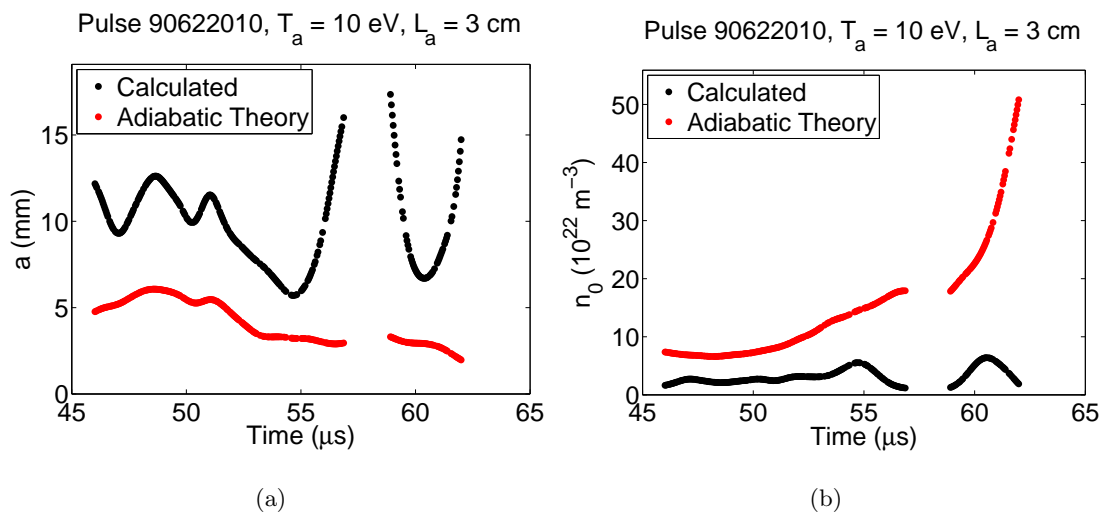


Figure A.21: Characteristic pinch radius and peak density as a function of time for 16 cm diameter inner electrode, Pulse 90622010. (a) Measured values for the characteristic radius are at some times greater than 1 cm and fluctuating substantially. Adiabatic theory predicts pinch radii that are less than 5 mm and decreasing as a function of time. (b) Peak electron density is also substantially less than predicted by adiabatic theory by more than a factor of two. The predicted density increases with increasing time, but the measured peak density decreases.

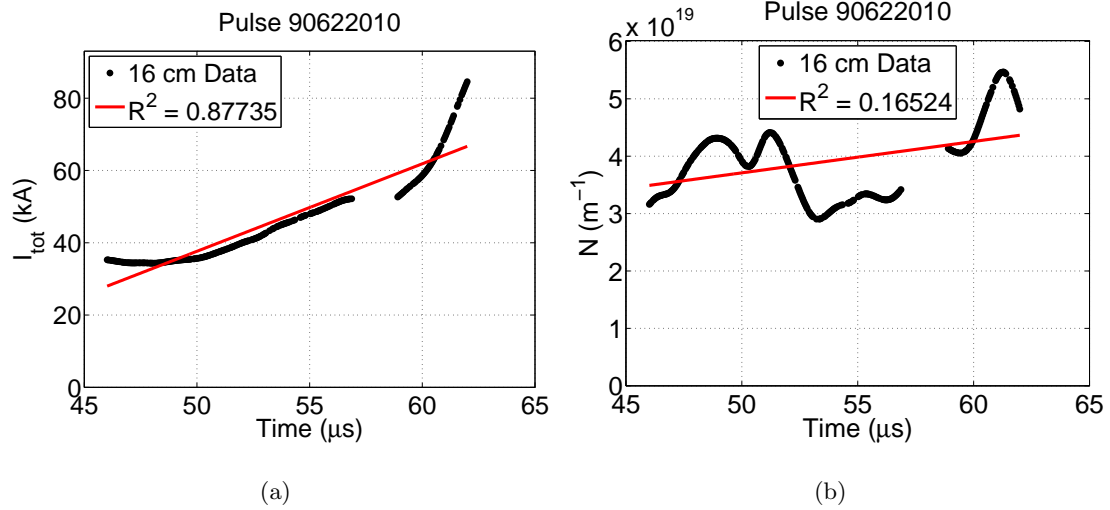


Figure A.22: Total current and linear density as a function of time for the 16 cm diameter inner electrode, Pulse 90622010. (a) Total current increases during the quiescent period from 35 to 70 kA. (b) Linear density has a slight increasing trend but magnitudes remain from $3 - 5 \times 10^{19} \text{ m}^{-1}$. The red lines are linear trendlines.

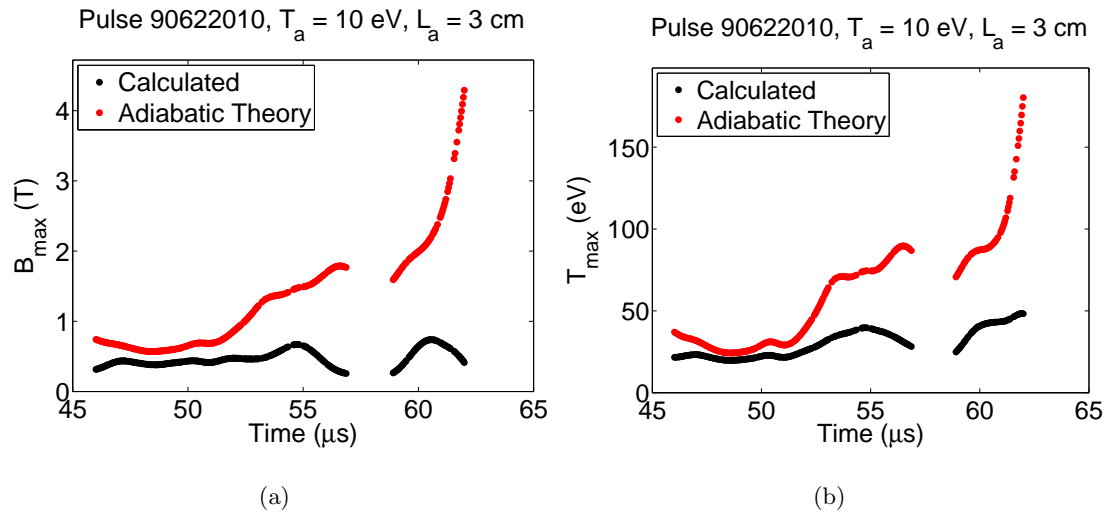


Figure A.23: Peak magnetic field and peak temperature as a function of time for the 16 cm diameter inner electrode, Pulse 90622010. (a) Calculated peak magnetic field values are a more than a factor of two less than the predictions of adiabatic theory with values below 0.6 T during the measurement period. (b) Similarly, peak temperature is well below the predictions of adiabatic theory with values from 20 - 50 eV.

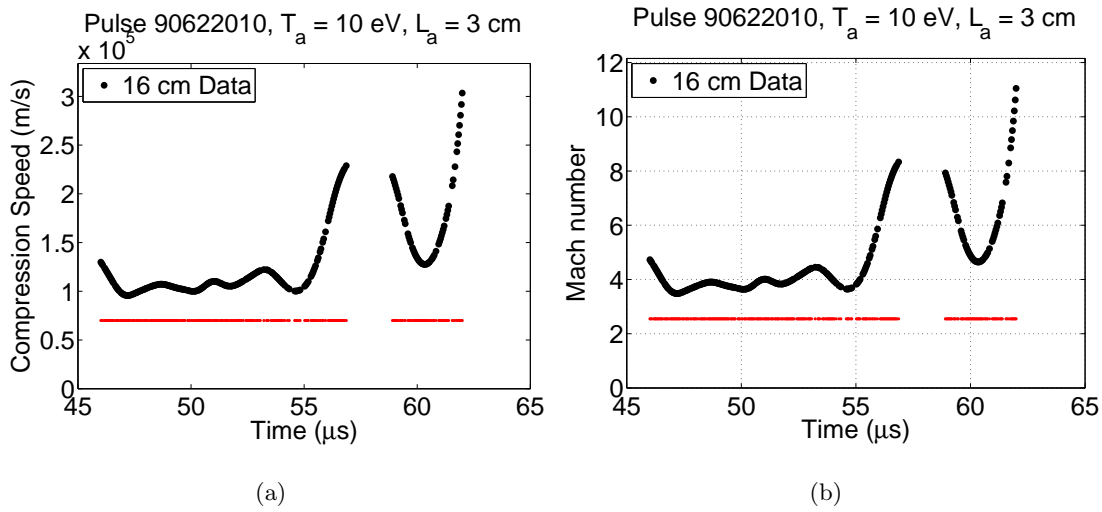


Figure A.24: Predicted formation compression speed and Mach number for the 16 cm diameter inner electrode, Pulse 90622010. (a) The predicted compression speed from the advanced adiabatic analysis is larger than the measured velocity at the exit of the accelerator (horizontal red line), but within the values of axial velocity measured in the experiment, ($v_z = 1-2 \times 10^5$ m/s). (b) The predicted shock strength for this pulse is strong ($M \geq 4$) and reinforces the measured and calculated data which suggests that shocks occur during the formation process, resulting in a larger pinch with increased size oscillations.

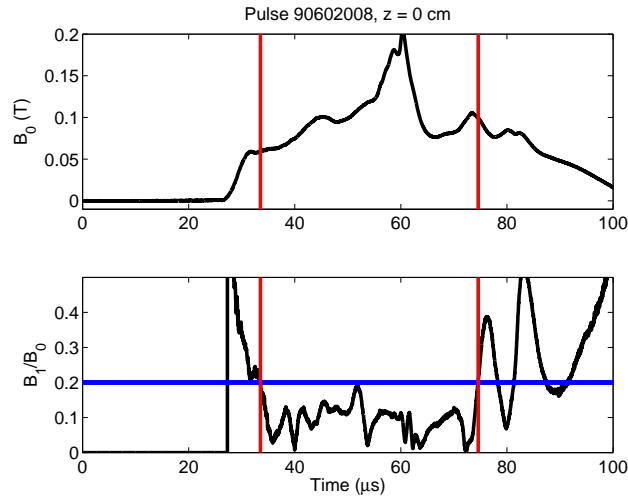


Figure A.25: Magnetic mode data for 16 cm diameter inner electrode configuration, Pulse 90602008. The maximum magnetic field measured at the wall is ≈ 0.2 T. The quiescent period extends well beyond the field peak in this case with a quiescent period length exceeding $40 \mu\text{s}$.

magnetic field peak for this particular pulse, resulting in a quiescent period length exceeding $40 \mu\text{s}$. The centroid of the current during the quiescent period is within $2 - 3$ mm of the machine axis and the chord-integrated data indicates a noticeable density gradient prior to the magnetic field peak, at which point the densities all crash simultaneously.

The measured values of the characteristic radius for this pulse are approximately 5 mm with small magnitude oscillations during the period of measurement. The peak values of the electron density are $4 - 10 \times 10^{22} \text{ m}^{-3}$. The predictions of adiabatic theory suggest smaller characteristic radii with high peak electron densities. This indicates that shocks during the formation process may be occurring.

Total current for this pulse increases from 30 to 70 kA during the measurement period. Linear density ranges from 1.5 to $3.5 \times 10^{19} \text{ m}^{-1}$. The values of peak magnetic field increase from 0.5 to 1.25 T during the measurement period and temperatures increasing from 20 to 110 eV, consistent with increasing total current.

The pulse exhibits behavior associated with strong shocks during the formation process

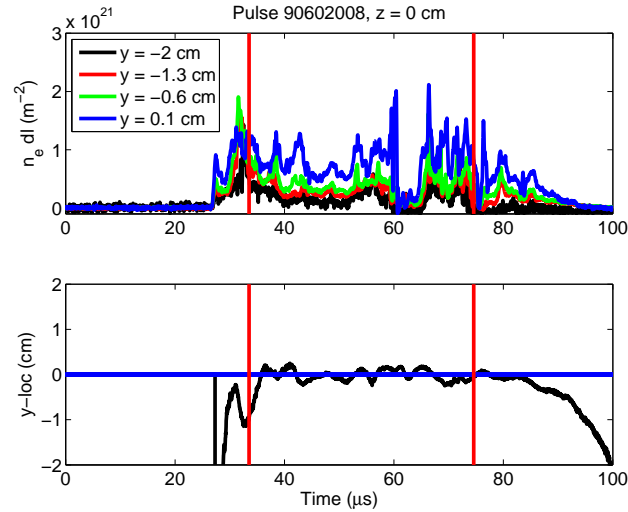


Figure A.26: Four-chord interferometry data for 16 cm diameter inner electrode configuration, Pulse 90602008. The chord-integrated density measurements exhibit the density crash near the field peak that is observed in other 16 cm diameter electrode pulses. Prior to this an extended period of time with a noticeable density gradient is observed. This period coincides with a well-centered current centroid.

with predicted shock strength in excess of $M = 3$. These data agrees with the oscillations in the characteristic pinch radius as well as the differences in the measured and calculated parameters when compared with adiabatic theory.

Figures A.31 - A.36 show additional pulse data for the high peak magnetic field operating conditions for the 16 cm diameter inner electrode. The experimental conditions are 9 kV capacitor bank voltage on eight, 180 μF capacitors. The gas-injection pressure is 1500 Torr. This pulse utilizes the magnetized formulation of thermal conductivity.

The pulse exhibits increasing values of magnetic field measured at the wall during the quiescent period from 0.1 T to 0.21 T. The quiescent period ends immediately after the magnetic field peak, a 30 μs quiescent period length. The current centroid is within 5 mm of the machine axis during this period and the interferometry chords indicate a noticeable density gradient.

The measured values of characteristic radius indicate a large pinch that compresses as

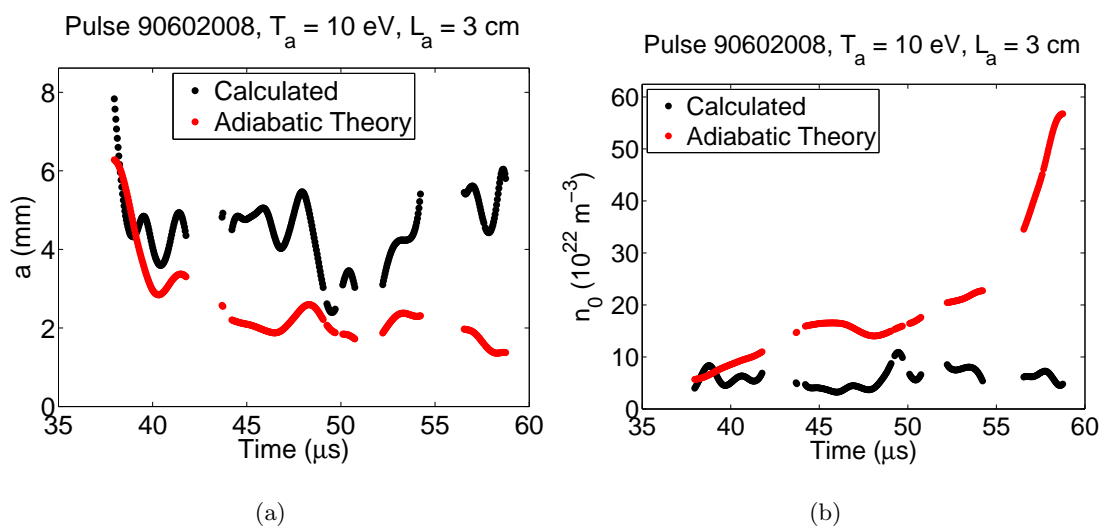


Figure A.27: Characteristic pinch radius and peak density as a function of time for 16 cm diameter inner electrode, Pulse 90602008. (a) Characteristic pinch radius oscillates around a mean value of ≈ 5 mm. The measured values are larger than predicted by adiabatic analysis, though not as substantial a difference as other 16 cm diameter pulses. (b) The peak density oscillates about $5 \times 10^{22} \text{ m}^{-3}$. This density is at least a factor of two lower than the predictions of adiabatic theory with this factor increasing with increasing time.

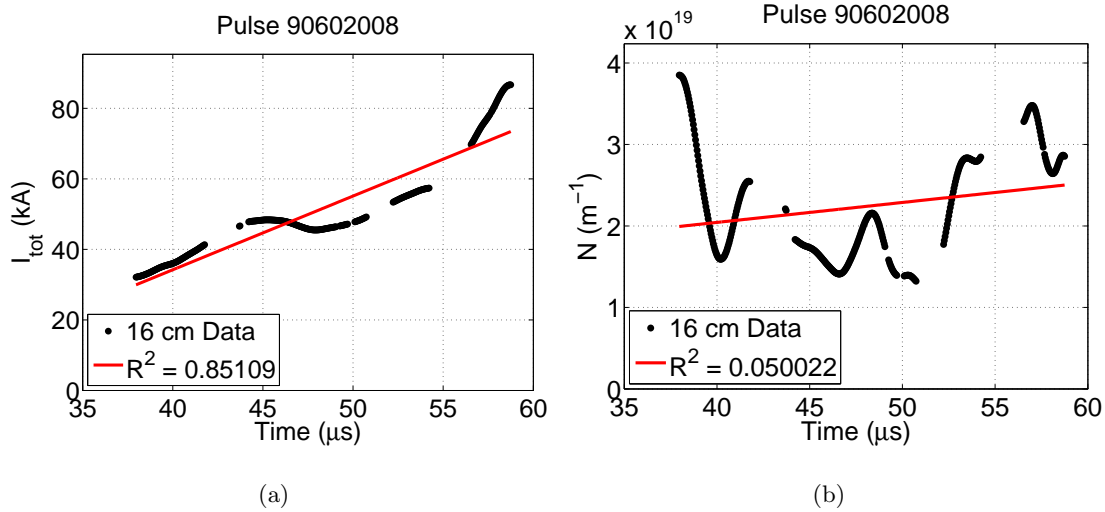


Figure A.28: Total current and linear density as a function of time for the 16 cm diameter inner electrode, Pulse 90602008. (a) Total current increases during the quiescent period from 30 to 60 kA. This does not correspond with an overall trend in the characteristic radius. (b) The linear density oscillates more than in any other pulse with a range from $1.5 - 3.5 \times 10^{19} \text{ m}^{-1}$. The red lines are linear trendlines.

the quiescent period progresses, with radii ranging from 14 mm to 5 mm at the end of the measurement period. Similarly, the peak electron density for this pulse increases from 3 to $9 \times 10^{22} \text{ m}^{-3}$. These values are significantly different from the predictions of adiabatic theory which suggests that, for an adiabatic formation process, the expected radii would be 2 – 3 mm with peak electron densities in excess of $3 \times 10^{23} \text{ m}^{-3}$. This indicates that strong non-adiabatic effects occur during this pulse.

The total current is slowly increasing during the period of measurement from 60 to 70 kA, but the linear density is decreasing from 4.5 to $3 \times 10^{19} \text{ m}^{-1}$. This is the reason for the increasing temperature during the measurement period which increases from 40 to 80 eV. The peak magnetic field also increases 0.4 to 1.1 T due to the compression of the pinch. These values are still a factor 4 - 6 less than predicted by adiabatic theory.

This pulse exhibits behavior that indicates exceptionally strong shocks during the formation process. The predicted shock strengths are $M > 6$ with compression speeds ap-

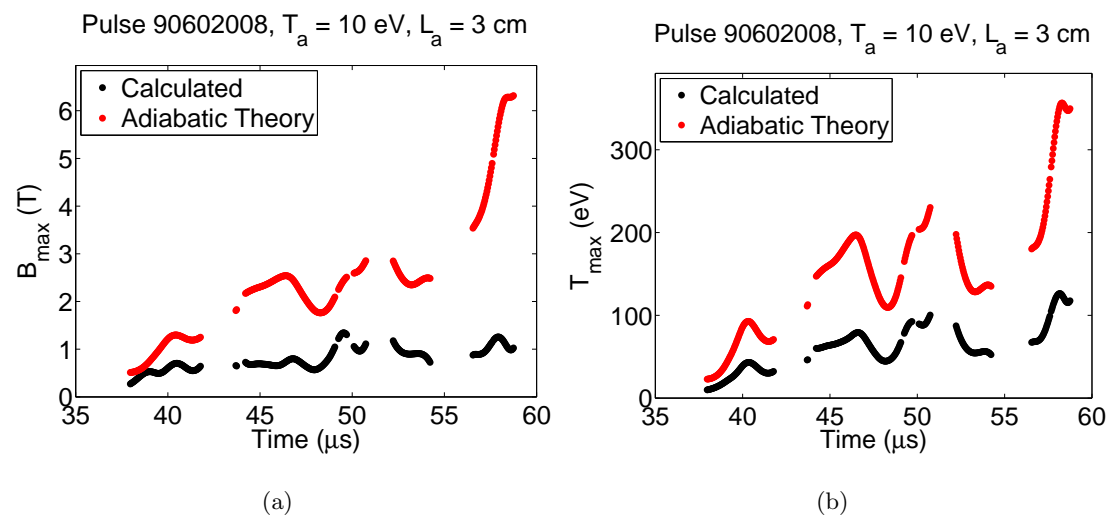


Figure A.29: Peak magnetic field and peak temperature as a function of time for the 16 cm diameter inner electrode, Pulse 90602008. (a) Peak magnetic field exhibits large oscillations, but with an overall trend of increasing field, which is in agreement with the total current. The predicted values from adiabatic theory are substantially larger than the calculated values. (b) The peak temperature also increases with the total current resulting in peak temperatures exceeding 100 eV near the end of the quiescent period. These values are a factor of two less than the predictions of adiabatic theory.

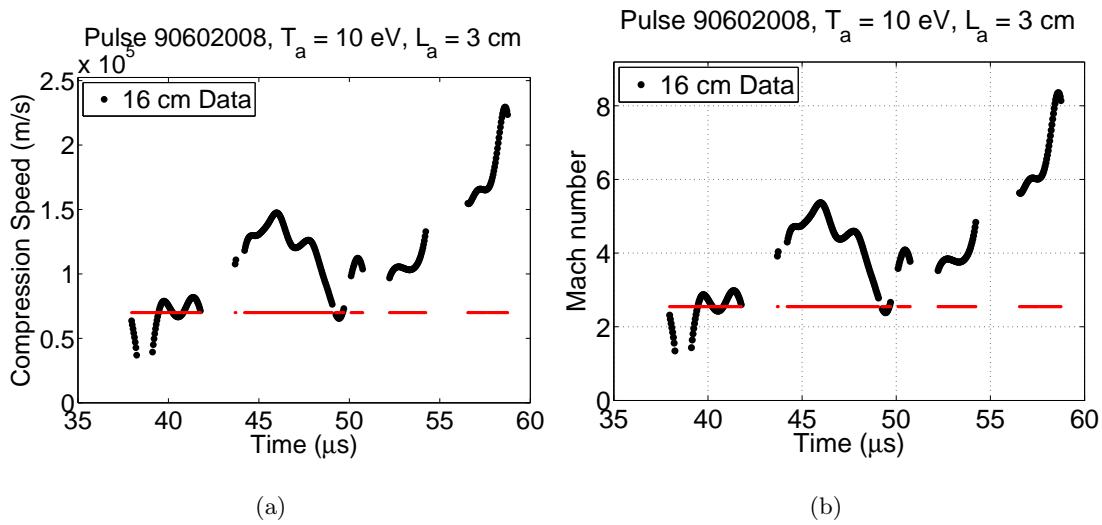


Figure A.30: Predicted formation compression speed and Mach number for the 16 cm diameter inner electrode, Pulse 90602008. (a) The predicted compression speed from the advanced adiabatic analysis is larger than the measured velocity at the exit of the accelerator (horizontal red line), but within the values of axial velocity measured in the experiment, ($v_z = 1 - 2 \times 10^5$ m/s). (b) The predicted shock strength for this pulse is strong ($M > 3$) and reinforces the measured and calculated data which suggests that shocks occur during the formation process, resulting in a larger pinch with increased size oscillations.

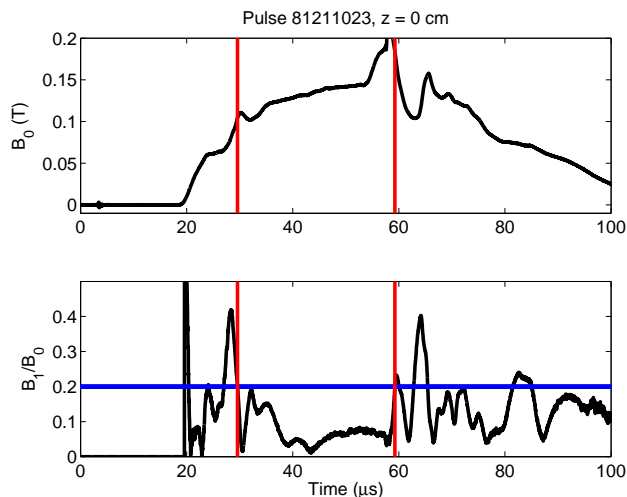


Figure A.31: Magnetic mode data for 16 cm diameter inner electrode configuration, Pulse 81211023. Magnetic field values at the wall range from 0.1 to 0.225 T during the quiescent period. The quiescent period ends immediately after the magnetic field peak for a quiescent period length of 30 μs .

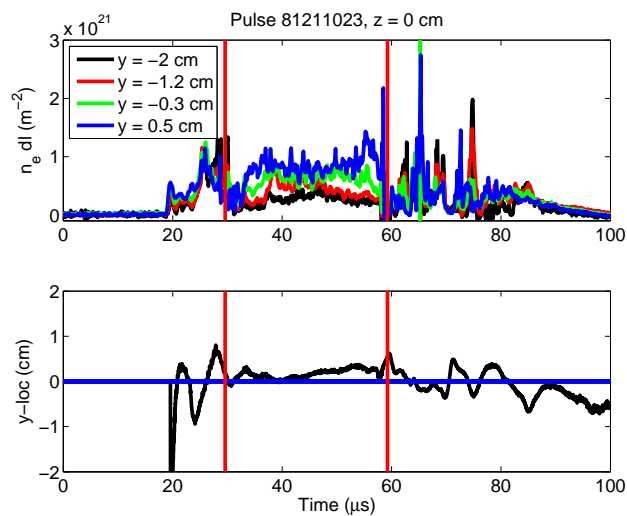


Figure A.32: Four-chord interferometry data for 16 cm diameter inner electrode configuration, Pulse 81211023. The centroid of the current is within 3 mm of the machine axis during the quiescent period. A noticeable density gradient is observed from the interferometry chords during this time.

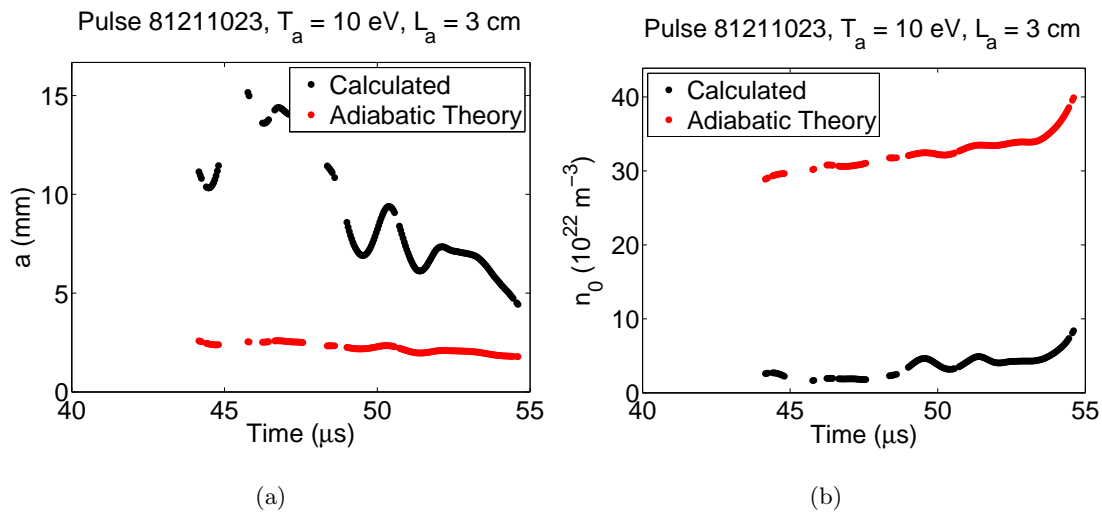


Figure A.33: Characteristic pinch radius and peak density as a function of time for 16 cm diameter inner electrode, Pulse 81211023. (a) The measured characteristic radius ranges from 7 to 15 mm with a trend of compression as the quiescent period progresses. The measured values are considerably larger than the predictions of adiabatic theory. Large oscillations in the pinch size are observed. (b) Peak electron density increases from 3 to $9 \times 10^{22} \text{ m}^{-3}$. These values are a factor of 3 to 10 less than the predictions of adiabatic theory.

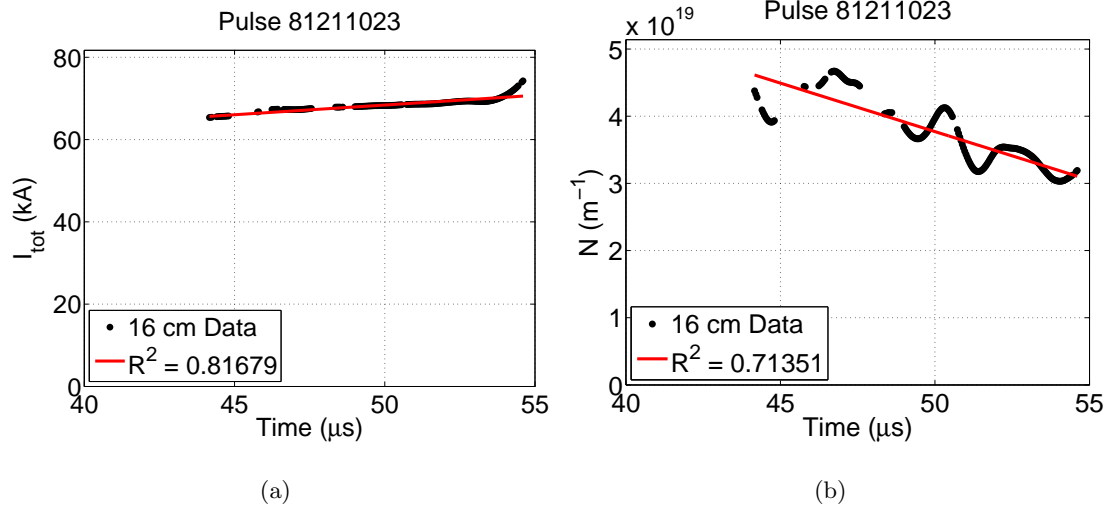


Figure A.34: Total current and linear density as a function of time for the 16 cm diameter inner electrode, Pulse 81211023. (a) Total current increases slowly during the measurement period from 60 to 70 kA. (b) The linear density is decreasing from a value of $5 \times 10^{19} \text{ m}^{-1}$ to $3 \times 10^{19} \text{ m}^{-1}$.

proaching the highest values of axial velocity observed in ZaP, $v_z \approx 2 \times 10^5 \text{ m/s}$. These data agrees with the large pinch size oscillations, as well as the large deviations away from the predictions of adiabatic theory in the values of pinch radius, electron density, magnetic field and temperature.

Figures A.37 - A.42 show additional pulse data for the high peak magnetic field operating conditions for the 16 cm diameter inner electrode. The experimental conditions are 9 kV capacitor bank voltage on eight, $180 \mu\text{F}$ capacitors. The gas-injection pressure is 1500 Torr. This pulse utilizes the magnetized formulation of thermal conductivity.

The magnetic field measured at the wall for this pulse increases from 0.075 to 0.175 T during the quiescent period. The quiescent period ends $\approx 5 \mu\text{s}$ after the magnetic field peak for a quiescent period length of $\approx 30 \mu\text{s}$. The location of the current centroid moves up to 5 mm from the machine axis, but in the middle of the quiescent period it is within 1 mm of the axis and a noticeable density gradient is observed on the interferometry chords.

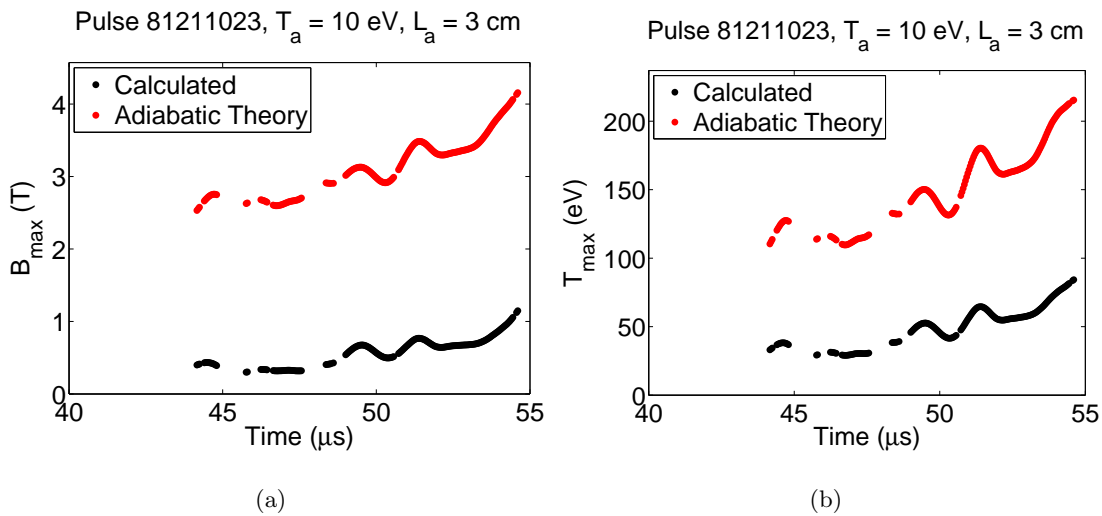


Figure A.35: Peak magnetic field and peak temperature as a function of time for the 16 cm diameter inner electrode, Pulse 81211023. (a) Peak magnetic field values increase as time progresses from 0.4 T to 1.1 T. This is in agreement with the compression of the pinch observed previously. (b) The peak temperature also increases with the decreasing radius, decreasing linear density and the increasing current from 40 eV to 80 eV. The values are a factor of 4 – 6 less than adiabatic theory predicts.

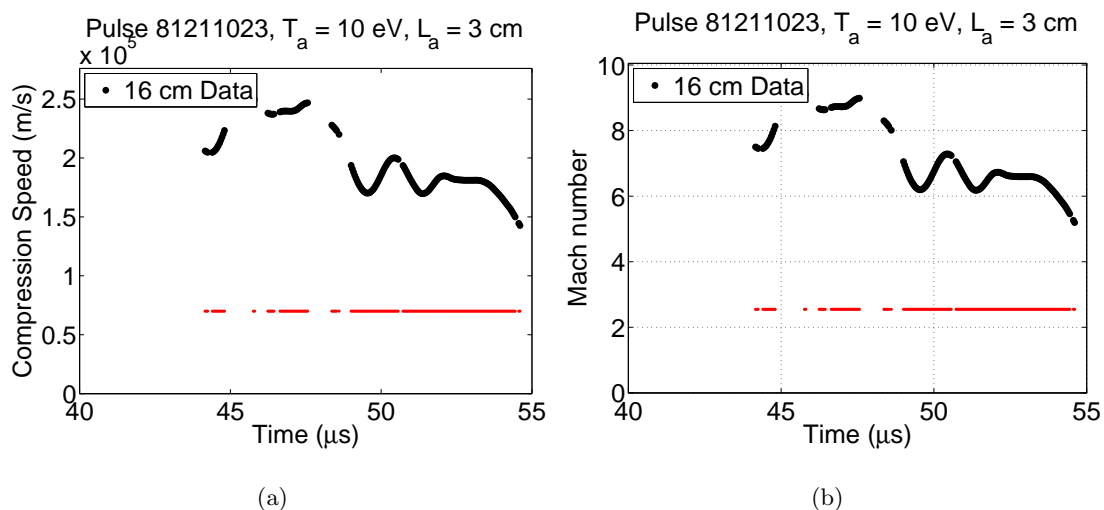


Figure A.36: Predicted formation compression speed and Mach number for the 16 cm diameter inner electrode, Pulse 81211023. (a) The predicted compression speed from the advanced adiabatic analysis is considerably larger than the measured velocity at the exit of the accelerator (horizontal red line), and larger than the values of axial velocity measured in the experiment, ($v_z = 1 - 2 \times 10^5$ m/s). (b) The predicted shock strength for this pulse is very strong ($M > 6$) and agrees with the measured and calculated data which suggests that strong shocks occur during the formation process, resulting in a larger pinch with increased size oscillations.

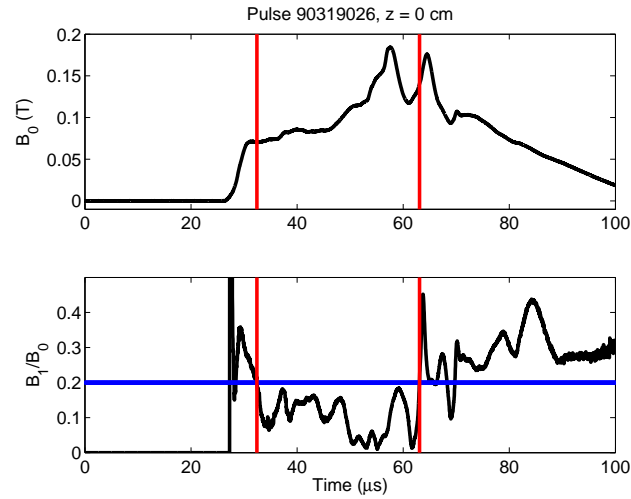


Figure A.37: Magnetic mode data for 16 cm diameter inner electrode configuration, Pulse 90319026. Magnetic field values at the wall during the quiescent period range from 0.075 to 0.175 T. The quiescent period ends soon after the magnetic field peak. The quiescent period length is $\approx 30 \mu\text{s}$.

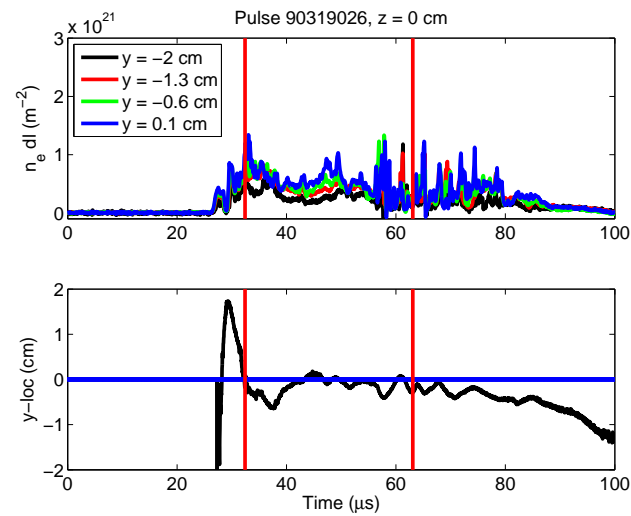


Figure A.38: Four-chord interferometry data for 16 cm diameter inner electrode configuration, Pulse 90319026. Centroid of the current is located within a few mm of the machine axis during the quiescent period. A noticeable density gradient is observed from the interferometry chords during this time.

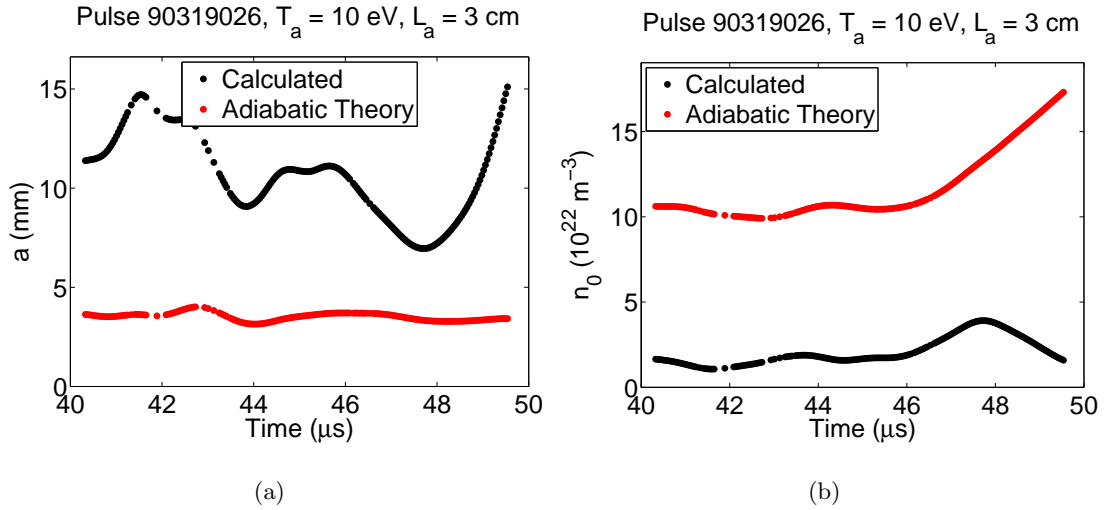


Figure A.39: Characteristic pinch radius and peak density as a function of time for 16 cm diameter inner electrode, Pulse 90319026. (a) The measured characteristic radius ranges between 7 and 15 mm with large oscillations during the measurement period. The measured values are much greater than the predictions of adiabatic compression. (b) Values of peak electron density range from $2 - 5 \times 10^{22}$ m $^{-3}$, which is a factor of 3 – 5 less than the predictions of adiabatic theory.

The measured characteristic radius of the pinch during the measurement period ranges from 7 to 15 mm with large oscillations observed. These values are a factor of 3–4 larger than the predictions of adiabatic theory. The measured peak electron density is $2 - 5 \times 10^{22}$ m $^{-3}$ which is a factor of 3 – 5 times less than the predictions of adiabatic theory.

The total current during the measurement period increases slightly from 40 to 50 kA and the linear density increases slightly from 3 to 4×10^{19} m $^{-1}$. These modest changes in current and linear density result in relatively flat profiles of peak magnetic field and peak temperature as a function of time. The values of peak magnetic field is consistently less than 0.5 T and temperatures are 20 – 25 eV.

This pulse exhibits behavior associated with strong shocks during the formation process including large pinch size oscillations, as well as large deviations between measured values of pinch size and electron density and calculated values of temperature and magnetic field

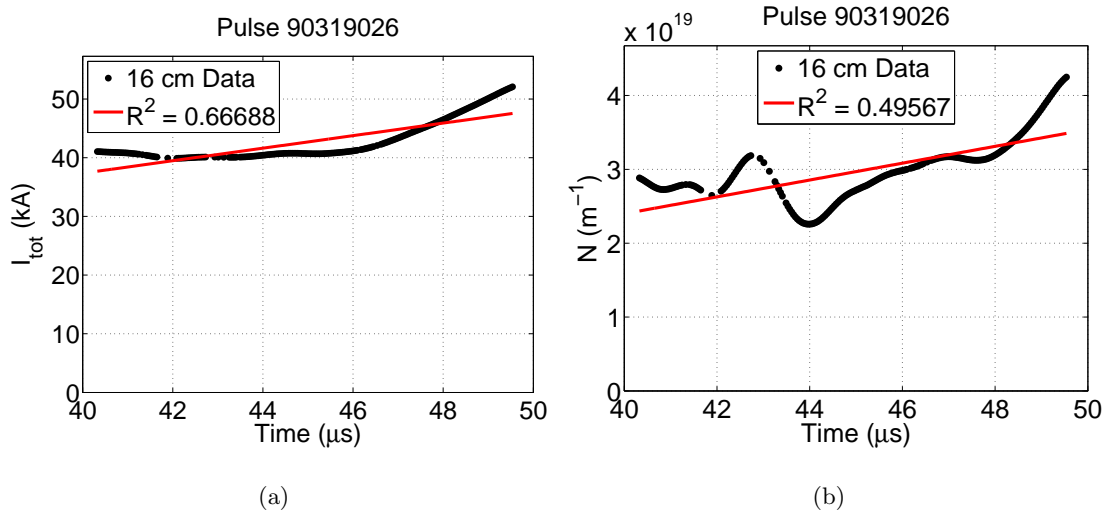


Figure A.40: Total current and linear density as a function of time for the 16 cm diameter inner electrode, Pulse 90319026. (a) Total current increases gradually over time from 40 to 50 kA during the measurement period. (b) The linear density is slightly increasing from 3 to $4 \times 10^{19} \text{ m}^{-1}$. The red lines are linear trendlines.

compared to the predictions of adiabatic theory. The predicted shock strength for this pulse is $M > 4$ and compression speeds of $\approx 1.5 \times 10^5 \text{ m/s}$.

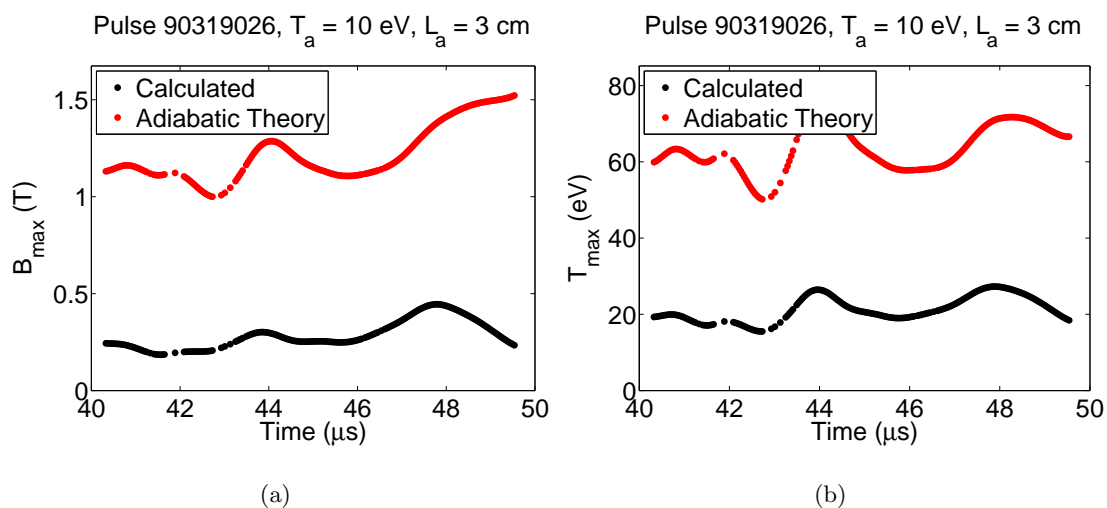


Figure A.41: Peak magnetic field and peak temperature as a function of time for the 16 cm diameter inner electrode, Pulse 90319026. (a) Peak magnetic field values are less than 0.5 T during the measurement period. This is more than a factor of 2 less than the predictions of adiabatic theory. (b) The temperature fluctuates between 20 and 30 eV during the measurement period. This is similarly more than a factor of 2 below the predictions of adiabatic theory.

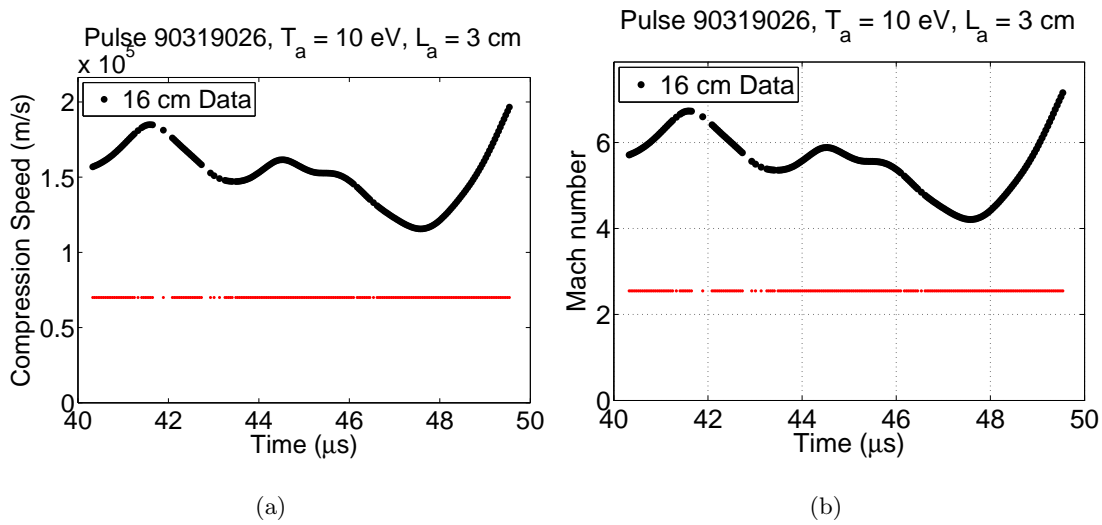


Figure A.42: Predicted formation compression speed and Mach number for the 16 cm diameter inner electrode, Pulse 90319026. (a) The predicted compression speed from the advanced adiabatic analysis is larger than the measured velocity at the exit of the accelerator (horizontal red line), but within the values of axial velocity measured in the experiment, ($v_z = 1 - 2 \times 10^5$ m/s). (b) The predicted shock strength for this pulse is strong ($M > 4$) and reinforces the measured and calculated data which suggests that shocks occur during the formation process, resulting in a larger pinch with increased size oscillations.

Appendix B

COMPUTER CODES

B.1 Four Chord Equilibrium Calculations

```
clear all
close all
clc

warning off all

% mdsconnect('landau.hit ');
shot = 100504014; % 10 cm electrode Complete 5000 Torr, 6 kV DONE

line_frac = 0;
brem_frac = 1;
theta = 1;
Zeff = 1;
alter_Z = 0;

for i = 1:length(shot)
    ohmic_sum_plot = [];
    dTdr_max_plot_temp = [];
    dTdr_plot_temp = [];
    I_plot = [];
    brem_sum_plot = [];
    line_sum_plot = [];
    loglam = 10;
    b_max_plot = [];
    b_max_plot_temp = [];
    temp_max_plot = [];
```

```
b_max_plot_nominal_temp = [];  
ne_ratio = [];  
n0_trouble = [];  
chord_dist = [];  
temp_max_plot_temp = [];  
temp_max_plot_nominal_temp = [];  
time_max_plot = [];  
density_max_plot = [];  
density_max_plot_temp = [];  
density_max_plot_nominal = [];  
density_max_plot_nominal_temp = [];  
I2_plot = [];  
density_mean_plot = [];  
Abel_density_plot = [];  
Abel_density_plot_temp = [];  
Abel_density_plot_nominal = [];  
Abel_density_plot_nominal_temp = [];  
lineal_plot = [];  
lineal_plot_temp = [];  
lineal_plot_nominal = [];  
lineal_plot_nominal_temp = [];  
Temp_plot = [];  
Temp_plot_temp = [];  
Temp_plot_nominal_temp = [];  
rad_plot = [];  
B_plot = [];  
B_plot_temp = [];  
B_plot_nominal_temp = [];  
radius_plot = [];  
radius_plot_temp = [];  
radius_plot_nominal = [];  
radius_plot_nominal_temp = [];  
e_radius = [];  
JxB_plot = [];  
gradp_plot = [];
```

```

ne_dl_plot = [];
radii_dl_plot = [];
radii_dl_plot_nominal = [];
time_dl_plot = [];
chord1_uncertain = [];
chord2_uncertain = [];
chord3_uncertain = [];
chord4_uncertain = [];
chord1_uncertain_temp = [];
chord2_uncertain_temp = [];
chord3_uncertain_temp = [];
chord4_uncertain_temp = [];
chord1_uncertain_temp1 = [];
chord2_uncertain_temp1 = [];
chord3_uncertain_temp1 = [];
chord4_uncertain_temp1 = [];
% mdsopen('zapmain', shot(i));
% y_4 = mdsvalue('\ne-4:y_loc')/100;
% y_3 = mdsvalue('\ne-3:y_loc')/100;
% y_2 = mdsvalue('\ne-2:y_loc')/100;
% y_1 = mdsvalue('\ne-1:y_loc')/100;
% y_4 = 0.003;
% y_3 = -0.004;
% y_2 = -0.011;
% y_1 = -0.018;
% rwall = mdsvalue('\r_wall');
% % rwall = 0.0968
% bad_probe = [];
% h = 0.2;
% kb = 1.38e-23;
% Zeff = 4;
%
time_max_plot_Bennett = [];
time_max_plot_Lorentz = [];

```

```
time_max_plot_Bennett_end = [];  
time_max_plot_Lorentz_end = [];  
  
density_max_plot_Bennett = [];  
density_max_plot_Lorentz = [];  
  
density_max_plot_Bennett_end = [];  
density_max_plot_Lorentz_end = [];  
  
lineal_plot_Bennett = [];  
lineal_plot_Lorentz = [];  
  
lineal_plot_Bennett_end = [];  
lineal_plot_Lorentz_end = [];  
  
lineal_plot_Bennett_end_34 = [];  
lineal_plot_Lorentz_end_34 = [];  
  
T_max_plot_Bennett = [];  
T_max_plot_Lorentz = [];  
  
T_max_plot_Bennett_end = [];  
T_max_plot_Lorentz_end = [];  
  
B_max_plot_Bennett = [];  
B_max_plot_Lorentz = [];  
  
B_max_plot_Bennett_end = [];  
B_max_plot_Lorentz_end = [];  
  
size_plot_Bennett = [];  
size_plot_Lorentz = [];  
  
size_plot_Bennett_end = [];  
size_plot_Lorentz_end = [];
```

```

I2_plot_Bennett = [];
I2_plot_Lorentz = [];

I2_plot_Bennett_end = [];
I2_plot_Lorentz_end = [];

I32_plot_Bennett_end = [];
I32_plot_Lorentz_end = [];

Temp_plot_temp_Lorentz_end = [];
B_plot_temp_Lorentz_end = [];
dense_plot_temp_Lorentz_end = [];

T_temp_sum_plot = [];
%
%      [m0p0 m1_norm t0p0 x_pos y_pos qp-s qp-e qp-l] = ...
%Fourier_Mode-Decomposition(shot(i), 'p0', [], [], 0.2);
%      h = h;
%      xpos = x_pos/100;
%      ypos = y_pos/100;
%      [min_t0p0 delta_t0p0 max_t0p0] = time_bounds(t0p0);
%
%      [tp ip] = mdsdata('\i_p', shot(i), 'landau.hit', 'zapmain', 1e6);
%      [min_tp delta_tp max_tp] = time_bounds(tp);
%
%      [te1 ne1] = mdsdata('\ne_1', shot(i), 'landau.hit', 'zapmain', 1e6);
%      [min_1 delta_1 max_1] = time_bounds(te1);
%
%      [te2 ne2] = mdsdata('\ne_2', shot(i), 'landau.hit', 'zapmain', 1e6);
%      [min_2 delta_2 max_2] = time_bounds(te2);
%
%      [te3 ne3] = mdsdata('\ne_3', shot(i), 'landau.hit', 'zapmain', 1e6);
%      [min_3 delta_3 max_3] = time_bounds(te3);
%

```

```

% [te4 ne4] = mdsdata('\ne_4', shot(i), 'landau.hit', 'zapmain', 1e6);
% [min_4 delta_4 max_4] = time_bounds(te4);
%
% [tgap vgap] = mdsdata('\v_gap', shot(i), 'landau.hit', 'zapmain', 1e6);
% [min_v delta_v max_v] = time_bounds(tgap);
%
% ne1 = IF_Fix_Baseline_no_filter(te1, ne1);
% ne2 = IF_Fix_Baseline_no_filter(te2, ne2);
% ne3 = IF_Fix_Baseline_no_filter(te3, ne3);
% ne4 = IF_Fix_Baseline_no_filter(te4, ne4);
%
% min_times = [min_t0p0, min_tp, min_1, min_2, min_3, min_4, min_v];
% max_times = [max_t0p0, max_tp, max_1, max_2, max_3, max_4, max_v];
% deltas = [delta_t0p0, delta_tp, delta_1, delta_2, delta_3, delta_4, delta_v];
%
% time = [max(min_times):max(deltas):min(max_times)];
%
% m0_p0 = fix_timebase(t0p0, m0p0, time);
% m1norm = fix_timebase(t0p0, m1norm, time);
% i_p = fix_timebase(tp, ip, time);
% ne_1 = fix_timebase(te1, ne1, time);
% ne_2 = fix_timebase(te2, ne2, time);
% ne_3 = fix_timebase(te3, ne3, time);
% ne_4 = fix_timebase(te4, ne4, time);
% x_pos = fix_timebase(t0p0, xpos, time);
% y_pos = fix_timebase(t0p0, ypos, time);
% v_gap = fix_timebase(tgap, vgap, time);
%
% clear ne1 ne2 ne3 ne4
%
% m0_p0 = dsmooth(m0_p0, 5, 7);
% m1norm = dsmooth(m1norm, 5, 7);
% i_p = dsmooth(i_p, 5, 7);
% x_pos = dsmooth(x_pos, 5, 7);
% y_pos = dsmooth(y_pos, 5, 7);

```

```

%      v_gap = dsmooth(v_gap,5,7);
%
%      t = 1:length(time);%t_base;%round(t_base/dtn);
%
% % the IMF's are calculated here
% % OPTIONS.COMPLEX_VERSION = 2;
% % OPTIONS.NDIRS = 4;
% % OPTIONS.FIX = 50;
% % OPTIONS.DISPLAY = 1;
% OPTIONS.MASK = .02*sin(2*pi*30000*time);
% OPTIONS.MAXITERATIONS = 10; % too many iterations causes more
% crosstalk between IMFs
% OPTIONS.MAXMODES = 10;
% % [imf,ort,nbits] = emd(x,OPTIONS);
% % [imf,ort,nbits] = emd_local(x);
% % figure(88);clf;plot(t_base, OPTIONS.MASK);hold on;plot(t_base, x, 'r');
%
% [imf,ort] = emd(ne_1, OPTIONS);
% [imf2,ort2] = emd(ne_2, OPTIONS);
% [imf3,ort3] = emd(ne_3, OPTIONS);
% [imf4,ort4] = emd(ne_4, OPTIONS);
%
% % imf = emd(x);
%
% % imf = transpose(imf1);
%
% %————— hilbert transform calculation, chord 1 —————%
% amp = zeros(size(imf));
% n_freq = zeros(size(imf));
% sm_amp = zeros(size(imf));
% sm_n_freq = zeros(size(imf));
% n_freq_cutoff = zeros(size(imf));
%
% n_smooth = 71;
% amp_cutoff = .3;

```

```

%
% reproduced_1_0 = zeros(1,max(size(imf(1,:)))));
% reproduced_1_1 = zeros(1,max(size(imf(1,:)))));
% reproduced_1_2 = zeros(1,max(size(imf(1,:)))));
% reproduced_1_3 = zeros(1,max(size(imf(1,:)))));
% reproduced_1_4 = zeros(1,max(size(imf(1,:)))));
% reproduced_1_5 = zeros(1,max(size(imf(1,:)))));
%
% for j = 1: length(imf(:,1))
%     [amp(j,2:end-1), n_freq(j,2:end-1), tt] = ...
%         hhspectrum(imf(j,:), t);
%     sm_amp(j,:) = FastCar(amp(j,:), n_smooth);
%     sm_n_freq(j,:) = FastCar(n_freq(j,:), n_smooth);
%     max_amp = max(amp(j,:));
%     n_freq_cutoff(j,:) = n_freq(j,:);
%     freq_lowamp = find(amp(j,:) < amp_cutoff*max_amp);
%     n_freq_cutoff(j,freq_lowamp) = NaN;
%
%     reproduced_1_0 = reproduced_1_0+imf(j,:);
%
%     if j <= 6
%         figure(3010)
%         subplot(6,1,j)
%         plot(time, imf(j,:))
%     end
%
%     if j == 1
%         continue
%     else
%         reproduced_1_1 = reproduced_1_1+imf(j,:);
%     end
%
%     if j == 1 | j == 2
%         continue
%     else

```

```

%         reproduced_1_2 = reproduced_1_2+imf(j ,:);
%     end
%
%     if j == 1 | j == 2 | j == 3
%         continue
%     else
%         reproduced_1_3 = reproduced_1_3+imf(j ,:);
%     end
%
%     if j == 1 | j == 2 | j == 3 | j == 4
%         continue
%     else
%         reproduced_1_4 = reproduced_1_4+imf(j ,:);
%     end
%
%     if j == 1 | j == 2 | j == 3 | j == 4 | j == 5
%         continue
%     else
%         reproduced_1_5 = reproduced_1_5+imf(j ,:);
%     end
% end
%
% % freq = n_freq*Sample_rate;
% % sm_freq = sm_n_freq*Sample_rate;
% % freq_cutoff = n_freq_cutoff*Sample_rate;
%
% %————— hilbert transform calculation , chord 2 —————%
% amp2 = zeros(size(imf2));
% n_freq2 = zeros(size(imf2));
% sm_amp2 = zeros(size(imf2));
% sm_n_freq2 = zeros(size(imf2));
% n_freq_cutoff2 = zeros(size(imf2));
%
% n_smooth2 = 71;
% amp_cutoff2 = .3;

```

```

%
% reproduced_2_0 = zeros(1,max(size(imf2(1,:))));
% reproduced_2_1 = zeros(1,max(size(imf2(1,:))));
% reproduced_2_2 = zeros(1,max(size(imf2(1,:))));
% reproduced_2_3 = zeros(1,max(size(imf2(1,:))));
% reproduced_2_4 = zeros(1,max(size(imf2(1,:))));
% reproduced_2_5 = zeros(1,max(size(imf2(1,:))));
%
% for j = 1: length(imf2(:,1))
%     [amp2(j,2:end-1), n_freq2(j,2:end-1), tt] = ...
%         hhspectrum(imf2(j,:), t);
%     sm_amp2(j,:) = FastCar(amp2(j,:), n_smooth2);
%     sm_n_freq2(j,:) = FastCar(n_freq2(j,:), n_smooth2);
%     max_amp2 = max(amp2(j,:));
%     n_freq_cutoff2(j,:) = n_freq2(j,:);
%     freq_lowamp2 = find(amp2(j,:) < amp_cutoff2*max_amp2);
%     n_freq_cutoff2(j,freq_lowamp2) = NaN;
%
%     reproduced_2_0 = reproduced_2_0+imf2(j,:);
%     if j == 1
%         continue
%     else
%         reproduced_2_1 = reproduced_2_1+imf2(j,:);
%     end
%
%     if j == 1 | j == 2
%         continue
%     else
%         reproduced_2_2 = reproduced_2_2+imf2(j,:);
%     end
%
%     if j == 1 | j == 2 | j == 3
%         continue
%     else
%         reproduced_2_3 = reproduced_2_3+imf2(j,:);

```

```

%     end
%
%     if j == 1 | j == 2 | j == 3 | j == 4
%         continue
%     else
%         reproduced_2-4 = reproduced_2-4+imf2(j, :);
%     end
%
%     if j == 1 | j == 2 | j == 3 | j == 4 | j == 5
%         continue
%     else
%         reproduced_2-5 = reproduced_2-5+imf2(j, :);
%     end
% end
%
% % freq2 = n_freq2*Sample_rate;
% % sm_freq2 = sm_n_freq2*Sample_rate;
% % freq_cutoff2 = n_freq_cutoff2*Sample_rate;
%
% %————— hilbert transform calculation , chord 3 —————%
% amp3 = zeros(size(imf3));
% n_freq3 = zeros(size(imf3));
% sm_amp3 = zeros(size(imf3));
% sm_n_freq3 = zeros(size(imf3));
% n_freq_cutoff3 = zeros(size(imf3));
%
% n_smooth3 = 71;
% amp_cutoff3 = .3;
%
% reproduced_3-0 = zeros(1,max(size(imf3(1, :))));
% reproduced_3-1 = zeros(1,max(size(imf3(1, :))));
% reproduced_3-2 = zeros(1,max(size(imf3(1, :))));
% reproduced_3-3 = zeros(1,max(size(imf3(1, :))));
% reproduced_3-4 = zeros(1,max(size(imf3(1, :))));
% reproduced_3-5 = zeros(1,max(size(imf3(1, :))));

```

```

%
% for j = 1: length(imf3(:,1))
%     [amp3(j,2:end-1), n_freq3(j,2:end-1), tt] = ...
%         hhspectrum(imf3(j,:), t);
%     sm_amp3(j,:) = FastCar(amp3(j,:), n_smooth3);
%     sm_n_freq3(j,:) = FastCar(n_freq3(j,:), n_smooth3);
%     max_amp3 = max(amp3(j,:));
%     n_freq_cutoff3(j,:) = n_freq3(j,:);
%     freq_lowamp3 = find(amp3(j,:) < amp_cutoff3*max_amp3);
%     n_freq_cutoff3(j, freq_lowamp3) = NaN;
%
%     reproduced_3_0 = reproduced_3_0+imf3(j,:);
%     if j == 1
%         continue
%     else
%         reproduced_3_1 = reproduced_3_1+imf3(j,:);
%     end
%
%     if j == 1 | j == 2
%         continue
%     else
%         reproduced_3_2 = reproduced_3_2+imf3(j,:);
%     end
%
%     if j == 1 | j == 2 | j == 3
%         continue
%     else
%         reproduced_3_3 = reproduced_3_3+imf3(j,:);
%     end
%
%     if j == 1 | j == 2 | j == 3 | j == 4
%         continue
%     else
%         reproduced_3_4 = reproduced_3_4+imf3(j,:);
%     end
%

```

```

%
%   if j == 1 | j == 2 | j == 3 | j == 4 | j == 5
%       continue
%   else
%       reproduced_3_5 = reproduced_3_5+imf3(j,:);
%   end
% end
%
% % freq3 = n_freq3*Sample_rate;
% % sm_freq3 = sm_n_freq3*Sample_rate;
% % freq_cutoff3 = n_freq_cutoff3*Sample_rate;
%
% %————— hilbert transform calculation , chord 4 —————%
% amp4 = zeros(size(imf4));
% n_freq4 = zeros(size(imf4));
% sm_amp4 = zeros(size(imf4));
% sm_n_freq4 = zeros(size(imf4));
% n_freq_cutoff4 = zeros(size(imf4));
%
% n_smooth4 = 71;
% amp_cutoff4 = .3;
%
% reproduced_4_0 = zeros(1,max(size(imf4(1,:))));
% reproduced_4_1 = zeros(1,max(size(imf4(1,:))));
% reproduced_4_2 = zeros(1,max(size(imf4(1,:))));
% reproduced_4_3 = zeros(1,max(size(imf4(1,:))));
% reproduced_4_4 = zeros(1,max(size(imf4(1,:))));
% reproduced_4_5 = zeros(1,max(size(imf4(1,:))));
%
% for j = 1: length(imf4(:,1))
%     [amp4(j,2:end-1), n_freq4(j,2:end-1), tt] = ...
%         hhspectrum(imf4(j,:), t);
%     sm_amp4(j,:) = FastCar(amp4(j,:), n_smooth4);
%     sm_n_freq4(j,:) = FastCar(n_freq4(j,:), n_smooth4);
%     max_amp4 = max(amp4(j,:));

```

```

%     n_freq_cutoff4(j,:) = n_freq4(j,:);
%     freq_lowamp4 = find(amp4(j,:) < amp_cutoff4*max_amp4);
%     n_freq_cutoff4(j,freq_lowamp) = NaN;
%
%     reproduced_4_0 = reproduced_4_0+imf4(j,:);
%     if j == 1
%         continue
%     else
%         reproduced_4_1 = reproduced_4_1+imf4(j,:);
%     end
%
%     if j == 1 | j == 2
%         continue
%     else
%         reproduced_4_2 = reproduced_4_2+imf4(j,:);
%     end
%
%     if j == 1 | j == 2 | j == 3
%         continue
%     else
%         reproduced_4_3 = reproduced_4_3+imf4(j,:);
%     end
%
%     if j == 1 | j == 2 | j == 3 | j == 4
%         continue
%     else
%         reproduced_4_4 = reproduced_4_4+imf4(j,:);
%     end
%
%     if j == 1 | j == 2 | j == 3 | j == 4 | j == 5
%         continue
%     else
%         reproduced_4_5 = reproduced_4_5+imf4(j,:);
%     end
% end

```

```

%
% % freq4 = n_freq4*Sample_rate;
% % sm_freq4 = sm_n_freq4*Sample_rate;
% % freq_cutoff4 = n_freq_cutoff4*Sample_rate;
%
    ne1 = [];
    ne2 = [];
    ne3 = [];
    ne4 = [];
    dense = [];
    time_fin = [];
    rad_fin = [];
    time_final = [];
    radii_final = [];
    densities_final = [];
    size_plot_1 = [];
    loc_max_b_plot_1 = [];
    final_time = [];

global check T_min extension unmag_param mag_param min_distance min_case

T_min = 1e-3;
rwall = 0.0963;
r_lim = rwall;
check = 1;
extension = 1e-3;
unmag_param = 1;
mag_param = 1;
% T_min = 0.001;
min_distance = 1e-6;
min_case = 1; % 0 is for a constant min_distance ,
% 1 is for the minimum of the mfp or larmor radius

data = dload([num2str(shot), '_Home_Data_2.txt ']);

```

```

time = data(:,1);
ne1 = data(:,2);
ne2 = data(:,3);
ne3 = data(:,4);
ne4 = data(:,5);
ip = data(:,6);
v_gap = data(:,7);
y_pos = data(:,8);
m0_p0 = data(:,9);
chord_locs = data(1:4,10);
y_1 = chord_locs(1);
y_2 = chord_locs(2);
y_3 = chord_locs(3);
y_4 = chord_locs(4);

width = 0.001;
na = 3;
change = linspace(-width, width, na);
change = 0;
%   change_1 = 0;

if shot(i) == 100504032
    time_values = find([time > 27 & time <= 47]);
elseif shot(i) == 90622071
    time_values = find([time > 32 & time < 53.2]);
elseif shot(i) == 90622017
    time_values = find([time > 38.5 & time < 63.5]);
elseif shot(i) == 90622010
    time_values = find([time > 46 & time < 62]);
elseif shot(i) == 90519041
    time_values = find([time > 33 & time < 54]);
elseif shot(i) == 100427017
    time_values = find([time > 39 & time < 62]);
elseif shot(i) == 100504027
    time_values = find([time > 28 & time < 41]);

```

```
elseif shot(i) == 100504014
    time_values = find([time > 40 & time < 62.5]);
elseif shot(i) == 100429023
    time_values = find([time > 40 & time < 61]);
elseif shot(i) == 100429022
    time_values = find([time > 40 & time < 57]);
elseif shot(i) == 90602008
    time_values = find([time > 33 & time < 61]);
elseif shot(i) == 90323044
    time_values = find([time > 31 & time < 52]);
elseif shot(i) == 90319026
    time_values = find([time > 40 & time < 51]);
elseif shot(i) == 90303033
    time_values = find([time > 27 & time < 55]);
elseif shot(i) == 90226009
    time_values = find([time > 31 & time < 56]);
elseif shot(i) == 90224033
    time_values = find([time > 26 & time < 51.2]);
elseif shot(i) == 81211034
    time_values = find([time > 32.5 & time < 58]);
elseif shot(i) == 90602011
    time_values = find([time > 33 & time < 61]);
elseif shot(i) == 81211023
    time_values = find([time > 33.5 & time < 58.5]);
elseif shot(i) == 90622010
    time_values = find([time > 34 & time < 62]);
elseif shot(i) == 90608032
    time_values = find([time > 54 & time < 78]);
elseif shot(i) == 90609028
    time_values = find([time > 60 & time < 79]);
elseif shot(i) == 90609034
    time_values = find([time > 67.5 & time < 82]);
elseif shot(i) == 90609039
    time_values = find([time > 67.5 & time < 79]);
elseif shot(i) == 90609052
```

```

        time_values = find ([time > 64 & time < 83.5]);
elseif shot(i) == 90610017
        time_values = find ([time > 41 & time < 58.5]);
elseif shot(i) == 90610033
        time_values = find ([time > 46 & time < 74]);
elseif shot(i) == 90612038
        time_values = find ([time > 50 & time < 65]); % forme
end

prev_T = [];
prev_u = [];
prev_dTdr = [];
prev_a = [];
prev_n0 = [];
prev_bwall = [];

failed = 0;
for j = time_values(1):time_values(length(time_values))

    radii_vector = [];
    density_vector = [];
    chord4_err = [];
    chord3_err = [];
    chord2_err = [];
    chord1_err = [];

    if isnan(y_pos(j)) == 1
        continue
    end

    for qq = 1:length(change)
        y1 = y_1+change(qq);
        for rr = 1:length(change)
            y2 = y_2+change(rr);
            for mm = 1:length(change)

```

```

y3 = y_3+change(mm);
for nn = 1:length(change)
    y4 = y_4+change(nn);

    ne_1(j) = ne1(j);
    ne_2(j) = ne2(j);
    ne_3(j) = ne3(j);
    ne_4(j) = ne4(j);

    center(j) = y_pos(j);
    dist_1(j) = abs(center(j) - y1);
    dist_2(j) = abs(center(j) - y2);
    dist_3(j) = abs(center(j) - y3);
    dist_4(j) = abs(center(j) - y4);

    rad_1(j) = (center(j) - y1);
    rad_2(j) = (center(j) - y2);
    rad_3(j) = (center(j) - y3);
    rad_4(j) = (center(j) - y4);
    rad_1_mirror(j) = -rad_1(j);
    rad_2_mirror(j) = -rad_2(j);
    rad_3_mirror(j) = -rad_3(j);
    rad_4_mirror(j) = -rad_4(j);

    if ne_4(j) >= ne_1(j) & ne_4(j) >= ne_2(j) & ...
        ne_4(j) >= ne_3(j) & ...
        (dist_4(j)) <= (dist_1(j)) & (dist_4(j)) ...
        <= (dist_2(j)) & (dist_4(j)) <= (dist_3(j)) & ...
        (dist_4(j)) <= ((y4-y3)/2) & ne_3(j) >= ...
        ne_2(j) & ne_3(j) >= ne_1(j) & ne_2(j) ...
        >= 0.9*ne_1(j) & ...
        ne_1(j) > 0 & ne_2(j) > 0 & ne_3(j) > 0 & ...
        ne_4(j) > 0

    elseif ne_3(j) > ne_4(j) & ne_3(j) > ne_2(j)...

```

```

& ne_3(j) > ne_1(j) & ...
ne_4(j) > ne_2(j) & ne_4(j) > ne_1(j)...
& ne_2(j) > 0.9*ne_1(j) & ...
ne_4(j) > 0 & ne_3(j) > 0 & ne_2(j)...
> 0 & ne_1(j) > 0 & ...
dist_3(j) < dist_4(j) & dist_3(j) < ...
dist_2(j) & dist_3(j) < dist_1(j) & ...
dist_4(j) < dist_2(j) & dist_4(j) <...
dist_1(j) & dist_2(j) < dist_1(j)

```

```

elseif ne_3(j) > ne_4(j) & ne_3(j) > ne_2(j)...
& ne_3(j) > ne_1(j) & ...
ne_2(j) > ne_4(j) & ne_2(j) > ne_1(j)...
& ne_4(j) > 0.9*ne_1(j) & ...
ne_4(j) > 0 & ne_3(j) > 0 & ne_2(j) ...
> 0 & ne_1(j) > 0 & ...
dist_3(j) < dist_4(j) & dist_3(j) <...
dist_2(j) & dist_3(j) < dist_1(j) & ...
dist_2(j) < dist_4(j) & dist_2(j) <...
dist_1(j) & dist_4(j) < dist_1(j)

```

```

elseif ne_2(j) > ne_4(j) & ne_2(j) > ne_3(j)...
& ne_2(j) > ne_1(j) & ...
ne_3(j) > ne_4(j) & ne_3(j) > ne_1(j)...
& ne_1(j) > 0.9*ne_4(j) & ...
ne_4(j) > 0 & ne_3(j) > 0 & ne_2(j) ...
> 0 & ne_1(j) > 0 & ...
dist_2(j) < dist_4(j) & dist_2(j) <...
dist_3(j) & dist_2(j) < dist_1(j) & ...
dist_3(j) < dist_4(j) & dist_3(j) <...
dist_1(j) & dist_1(j) < dist_4(j)

```

```

elseif ne_2(j) > ne_4(j) & ne_2(j) > ne_3(j)...
& ne_2(j) > ne_1(j) & ...
ne_3(j) > 0.9*ne_4(j) & ne_1(j) > ...

```

```

    ne_3(j) & ne_1(j) > ne_4(j) & ...
    ne_4(j) > 0 & ne_3(j) > 0 & ne_2(j)...
    > 0 & ne_1(j) > 0 & ...
    dist_2(j) < dist_4(j) & dist_2(j) <...
    dist_3(j) & dist_2(j) < dist_1(j) & ...
    dist_3(j) < dist_4(j) & dist_1(j) <...
    dist_3(j) & dist_1(j) < dist_4(j)

elseif ne_1(j) > ne_4(j) & ne_1(j) > ne_3(j) ...
    & ne_1(j) > ne_2(j) & ...
    ne_2(j) > ne_4(j) & ne_2(j) > ne_3(j)...
    & ne_3(j) > 0.9*ne_4(j) & ...
    ne_4(j) > 0 & ne_3(j) > 0 & ne_2(j) ...
    > 0 & ne_1(j) > 0 & ...
    dist_1(j) < dist_4(j) & dist_1(j) < ...
    dist_3(j) & dist_1(j) < dist_2(j) & ...
    dist_2(j) < dist_4(j) & dist_2(j) < ...
    dist_3(j) & dist_3(j) < dist_4(j)

else
    continue
end

ne1_mirror(j) = ne_1(j);
ne2_mirror(j) = ne_2(j);
ne3_mirror(j) = ne_3(j);
ne4_mirror(j) = ne_4(j);

rad_right = [rad_4(j); rad_3(j); rad_2(j); rad_1(j)];
rad_left = [rad_1_mirror(j); rad_2_mirror(j);...
    rad_3_mirror(j); rad_4_mirror(j)];

ne_right = [ne_4(j); ne_3(j); ne_2(j); ne_1(j)];
ne_left = [ne1_mirror(j); ne2_mirror(j);...
    ne3_mirror(j); ne4_mirror(j)];

```

```

rad_dim = vertcat(rad_left , rad_right);
ne_dim = vertcat(ne_left , ne_right);

chord_dense_setup = horzcat(rad_dim , ne_dim);
chord_dense_final = sortrows(chord_dense_setup);

radii = chord_dense_final(:,1);
densities = chord_dense_final(:,2);

radii_vector = vertcat(radii_vector , ...
    transpose(radii(5:8)));
density_vector = vertcat(density_vector , ...
    transpose(densities(5:8)));

chord4_err = vertcat(chord4_err , change(nn));
chord3_err = vertcat(chord3_err , change(mm));
chord2_err = vertcat(chord2_err , change(rr));
chord1_err = vertcat(chord1_err , change(qq));

clear rad_right rad_left ne_right ne_left rad_dim ...
    ne_dim chord_dense_setup chord_dense_final ...
    radii densities
end
end
end
end

if isempty(radii_vector) == 1
    continue
end

% break
for qq = 1:length(radii_vector(:,1))
    if (radii_vector(qq,2) - radii_vector(qq,1)) > 0.0013

```

```

    [a_temp(qq), n0_temp(qq), res_temp(qq)] = ...
        Bennett_nlinlsq_w_Temp(transpose(...
            density_vector(qq,:), transpose(radii_vector(qq,:)), rwall));
else
    [a_temp(qq), n0_temp(qq), res_temp(qq)] = ...
        Bennett_nlinlsq_w_Temp_close_shell(...
            transpose(density_vector(qq,:)), ...
            transpose(radii_vector(qq,:)), rwall);
end

end

plot_point_temp(j) = find(res_temp == min(res_temp));
if isempty(find(chord1_err == 0 & chord2_err == 0 & ...
    chord3_err == 0 & chord4_err == 0)) == 1
    nominal_point(j) = plot_point_temp(j);
else
    nominal_point(j) = find(chord1_err == 0 & chord2_err == 0 & ...
        chord3_err == 0 & chord4_err == 0);
end

if a_temp(plot_point_temp(j)) > 0.04 || ...
    a_temp(plot_point_temp(j)) < 0.0005 || ...
    n0_temp(plot_point_temp(j)) > 5e23
    continue
end

y_fin = linspace(0, rwall, 1501);
r2 = rwall;
x_fin = sqrt(r2^2 - y_fin.^2);

b_edge(j) = m0_p0(j)*rwall/y_fin(length(y_fin));

mu0 = 4*pi*1e-7;
I_total(j) = m0_p0(j)*2*pi*rwall/mu0;

```

```

Pin(j) = -v_gap(j)*(2*pi*rwall*m0_p0(j)/mu0);

n_values_temp(j) = n0_temp(plot_point_temp(j));
a_values_temp(j) = a_temp(plot_point_temp(j));
res_values_temp(j) = res_temp(plot_point_temp(j));
time_values_temp(j) = time(j);

final_temp = 2*n_values_temp(j)*a_values_temp(j)^2*...
    (atan(x_fin./sqrt(y_fin.^2+a_values_temp(j)^2))./sqrt(...
    y_fin.^2+a_values_temp(j)^2));

bennett_density_temp = n_values_temp(j)*a_values_temp(j)^2./...
    (y_fin.^2+a_values_temp(j)^2);
lineal_bennett_temp(j) = pi*n_values_temp(j)*a_values_temp(j)^2*...
    log(rwall^2+a_values_temp(j)^2)-...
    pi*n_values_temp(j)*a_values_temp(j)^2*log(a_values_temp(j)^2);

j_values_temp_prior(j) = j;

[T_temp, u_temp, dTdr_temp] = Newton_Iteration_Log_Solver_General...
    (y_fin, bennett_density_temp, a_values_temp(j), n_values_temp(j), ...
    b_edge(j), prev_a, prev_n0, prev_bwall, prev_T, prev_dTdr, prev_u, ...
    T_min, rwall, r_lim, j, shot(i), line_frac, brem_frac, theta, Zeff, ...
    alter_Z, time(j));
% [T_temp, u_temp, dTdr_temp] = Newton_Iteration_Log_Solver...
%(y_fin, bennett_density_temp, a_values_temp(j), n_values_temp(j), b_edge(j), ...
%prev_a, prev_n0, prev_bwall, prev_T, prev_dTdr, prev_u, T_min, rwall, r_lim, j, ...
%shot(i), line_frac, brem_frac, theta, Zeff, alter_Z, time(j));
if isempty(T_temp) == 1
    failed = failed+1;
    a_values_temp(j) = 0;
    n_values_temp(j) = 0;
    res_values_temp(j) = 0;
    b_edge(j) = 0;
    time_values_temp(j) = 0;

```

```

    figure(10000)
    plot([-1 1],[0 0])
    title([num2str(failed), '_Failed'])
    continue
end

j_values_temp(j) = j;

prev_T = T_temp;
prev_u = u_temp;
prev_dTdr = dTdr_temp;
prev_a = a_values_temp(j);
prev_n0 = n_values_temp(j);
prev_bwall = b_edge(j);

B_temp = sqrt(u_temp)./transpose(y_fin);
B_temp(1) = 0;

density_max_plot_temp = vertcat(density_max_plot_temp,...
    max(bennett_density_temp));
temp_max_plot_temp = vertcat(temp_max_plot_temp,max(T_temp));
radius_plot_temp = vertcat(radius_plot_temp,a_values_temp(j));
b_max_plot_temp = vertcat(b_max_plot_temp,max(B_temp));
dTdr_max_plot_temp = vertcat(dTdr_max_plot_temp,max(dTdr_temp));
I_plot = vertcat(I_plot,I_total(j));

time_max_plot = vertcat(time_max_plot,time(j));
Abel_density_plot_temp = horzcat(Abel_density_plot_temp,...
    transpose(bennett_density_temp));
Temp_plot_temp = horzcat(Temp_plot_temp,(T_temp));
B_plot_temp = horzcat(B_plot_temp,(B_temp));
dTdr_plot_temp = horzcat(dTdr_plot_temp,(dTdr_temp));
rad_plot = horzcat(rad_plot,transpose(y_fin));
lineal_plot_temp = vertcat(lineal_plot_temp,lineal_bennett_temp(j));
radii_dl_plot = vertcat(radii_dl_plot,radii_vector(plot_point_temp(j),:));

```

```

time_dl_plot = vertcat(time_dl_plot,[time(j),time(j),time(j),time(j)]);
ne_dl_plot = vertcat(ne_dl_plot,density_vector(plot_point_temp(j),:));

for kk = 1:length(time_max_plot)
    time_plot(1:length(y_fin),kk) = time_max_plot(kk);
end
clear rad_dense_matrix bennett_density B T final y_fin r x_fin ...
    radii_vector density_vector
end
% break
a_values_temp(find(a_values_temp == 0)) = [];
n_values_temp(find(n_values_temp == 0)) = [];
time_values_temp(find(time_values_temp == 0)) = [];
res_values_temp(find(res_values_temp == 0)) = [];
b_edge(find(b_edge==0)) = [];
j_values_temp_prior(find(j_values_temp_prior==0))= [];
j_values_temp(find(j_values_temp==0))= [];
a_values_temp = transpose(a_values_temp);
n_values_temp = transpose(n_values_temp);
b_edge = transpose(b_edge);
time_values_temp = transpose(time_values_temp);
data_matrix = horzcat(time_values_temp,a_values_temp,n_values_temp,...
    b_edge,transpose(res_values_temp));
csvwrite([num2str(shot(i)), '_DataPoints-General.txt'],data_matrix)

csvwrite([num2str(shot(i)), '_Radii-dl-General.txt'],radii_dl_plot);
csvwrite([num2str(shot(i)), '_ne-dl-General.txt'],ne_dl_plot);
csvwrite([num2str(shot(i)), '_time-dl-General.txt'],time_dl_plot);
csvwrite([num2str(shot(i)), '_total-current-General.txt'],I_plot);

    csvwrite([num2str(shot(i)), '_time-points-for-plotting-General.txt']...
        ,transpose(time_plot));
    csvwrite([num2str(shot(i)), '_radius-points-for-plotting-General.txt']...
        ,transpose(rad_plot));
    csvwrite([num2str(shot(i)), '_density-points-for-plotting-General.txt']...

```

```

        ,transpose( Abel_density_plot_temp ));
    csvwrite ([ num2str(shot(i)), '_temp_points_for_plotting-General.txt' ] ...
        ,transpose( Temp_plot_temp ));
    csvwrite ([ num2str(shot(i)), '_dTdr_points_for_plotting-General.txt' ] ...
        ,transpose( dTdr_plot_temp ));
    csvwrite ([ num2str(shot(i)), '_mag_field_points_for_plotting-General.txt' ] ...
        ,transpose( B_plot_temp ));

nn = 10;
v = linspace(0,max(max( Abel_density_plot_temp)),nn);
% [time,rad] = meshgrid(time_max_plot,rad_plot*100);
figure(7)
contourf(time_plot,rad_plot*100,Abel_density_plot_temp,v)
colormap hot
colorbar
xlabel('Time_(\mus)', 'FontSize',25)
ylabel('Radius_(cm)', 'FontSize',25)
ylim([0 rwall*100])
title(['Electron_Density_(m^{-3})'], 'FontSize',25)
set(gca, 'FontSize',25)
hold on
plot(time_dl_plot, radii_dl_plot*100, '+w', 'MarkerSize',10)
hold off
% print -depsc 100504032_Density-Contour-IMF
% saveas(gcf,['Uncertain10-Limits-Density-Contour-IMF'],'jpeg')

v2 = linspace(0,max(max( Temp_plot_temp)),nn);
figure(8)
contourf(time_plot,rad_plot*100,Temp_plot_temp,v2)
colormap hot
colorbar
ylim([0 rwall*100])
xlabel('Time_(\mus)', 'FontSize',25)
ylabel('Radius_(cm)', 'FontSize',25)
title(['Total_Temperature_(eV)'], 'FontSize',25)

```

```

set(gca, 'FontSize', 25)
%      print -depsc 100504032_Temp_Contour-IMF
%      saveas(gcf, ['Uncertain10-Limits_Temp_Contour-IMF'], 'jpeg')

v3 = linspace(0, max(max(B_plot_temp)), nn);
figure(9)
contourf(time_plot, rad_plot*100, B_plot_temp, v3)
colormap hot
colorbar
ylim([0 rwall*100])
xlabel('Time_(\mus)', 'FontSize', 25)
ylabel('Radius_(cm)', 'FontSize', 25)
title(['B_(T)'], 'FontSize', 25)
set(gca, 'FontSize', 25)
%      print -depsc 100504032_B_Contour-IMF
%      saveas(gcf, ['Uncertain10-Limits_B_Contour-IMF'], 'jpeg')
end

```

B.2 Multiple Shooting Solver

```

function [temp, mag_field, dTdr] = Newton_Iteration_Log_Solver_General(...
    radius, density1, a, n0, bwall, a_prev, n0_prev, bwall_prev, T_old, ...
    dTdr_old, u_old, T_min, rwall, r_lim, jj, shot, line_frac, brem_frac, ...
    theta, Zeff1, alter_Z, time)

```

```

warning off all

```

```

global check T_min extension unmag_param mag_param min_distance min_case

```

```

r = radius;
loglam = 10;
mu0 = 4*pi*1e-7;
kb = 1.38e-23;
k = 1.6e-19;
mi = 1.67e-27;
me = 9.11e-31;

```

```

dense = n0*a^2./(r.^2+a^2);
dndr = -2*n0*a^2*r./(r.^2+a^2).^2;

c1 = -2*mu0*k*(1+Zeff1);
c2 = 1.035e-4*Zeff1*loglam*(1+Zeff1)^2*k^2;
c3 = 1.69e-38*Zeff1^2;
c5 = 3.44e11*k/Zeff1/loglam/me;
c6 = 2.09e13*k/Zeff1^4/loglam/mi;
c7 = (1.76e11*3.44e11)^2;
c8 = (9.58e7*2.09e13)^2;
if Zeff1 == 1
    delta_0 = 3.7703;
    delta_1 = 14.79;
    gamma_1 = 4.664;
    gamma_0 = 11.92;
elseif Zeff1 == 2
    delta_0 = 1.0465;
    delta_1 = 10.8;
    gamma_1 = 3.957;
    gamma_0 = 5.118;
elseif Zeff1 == 3
    delta_0 = 0.5814;
    delta_1 = 9.618;
    gamma_1 = 3.721;
    gamma_0 = 3.525;
elseif Zeff1 == 4
    delta_0 = 0.4106;
    delta_1 = 9.055;
    gamma_1 = 3.604;
    gamma_0 = 2.841;
elseif Zeff1 > 4
    delta_0 = 0.0961;
    delta_1 = 7.482;
    gamma_1 = 3.25;
    gamma_0 = 1.20;

```

end

$I = 2 * \pi * r_{wall} * b_{wall} / \mu_0;$

$B_{field} = \text{sqrt}(1 + Z_{eff1}) * I * \mu_0 / (2 * \pi) * r ./ (r.^2 + a.^2);$

$press = (1 + Z_{eff1}) * \mu_0 * I^2 / (8 * \pi^2) * a.^2 ./ (r.^2 + a.^2).^2;$

$temp = press ./ (dense * kb) / 11604 / (1 + Z_{eff1});$

$curr_{dense} = I / \pi * \text{sqrt}(1 + Z_{eff1}) * a.^2 ./ (r.^2 + a.^2);$

$calc_{temp} = temp(1) * a.^2 ./ (r.^2 + a.^2) + 1;$

$u_{field} = (B_{field} .* r).^2;$

$u_{final} = (r_{wall} * b_{wall})^2;$

$\delta_{mult} = \text{sqrt}(\epsilon_{ps});$

$Pohmic = 1e7 / (\pi * (r_{wall}^2));$

$xe2 = c7 * u_{field} * calc_{temp}.^3 ./ (r.^2 * Z_{eff1}^4 * dense.^2 * \loglam.^2);$

$xe2(1) = 0;$

$xi2 = c8 * u_{field} * calc_{temp}.^3 ./ (r.^2 * Z_{eff1}^4 * dense.^2 * \loglam.^2);$

$xi2(1) = 0;$

$nume = \gamma_1 * xe2 + \gamma_0;$

$numi = 2 * xi2 + 2.645;$

$dene = xe2.^2 + \delta_1 * xe2 + \delta_0;$

$deni = xi2.^2 + 2.7 * xi2 + 0.677;$

$k_{perp_e} = c5 * calc_{temp}.^{2.5} * nume ./ dene;$

$k_{perp_i} = c6 * calc_{temp}.^{2.5} * numi ./ deni;$

$k_{perp} = k_{perp_e} + k_{perp_i};$

$calc_{dTdr} = -2 * temp(1) * a.^2 * r ./ (r.^2 + a.^2).^2;$

if isempty(a_prev)

$a_{percent} = 100;$

$n0_{percent} = 100;$

```

        b_percent = 100;
    else
        a_percent = abs(a-a_prev)/a_prev*100;
        n0_percent = abs(n0-n0_prev)/n0_prev*100;
        b_percent = abs(bwall-bwall_prev)/bwall_prev*100;
    end

    if line_frac == 0
        im_frac = 0.0001;
    else
        im_frac = linspace(0.0001,0.001,10);
    end

    percent_limit = 50;

    final_T = calc_temp;
    final_dTdr = -r.*k_perp.*calc_dTdr*k;
    final_u = u_field;
    k_start = 1;

    for kkk = k_start:length(im_frac)

        T_0_complex_multi = [];
        dTdr_0_complex_multi = [];
        u_0_complex_multi = [];
        vector_length = 101;
        impurity_frac = im_frac(kkk);
        impurity_ion = ['O'];
        alpha_prime = 0.99;
        i_length = (length(r)-1)/(vector_length-1);
        num_eqns = 3;

        percent_change_nominal = 0.99;
        if kkk == 1
            percent_change_nominal_dTdr = 5;

```

```

else
    percent_change_nominal_dTdr = 5;
end
percent_change_close_T = 0.75;
percent_change_close_dTdr = 3;
percent_change_close_u = 0.75;

T_0_complex_multi(1) = final_T(1);
dTdr_0_complex_multi(1) = 0;
u_0_complex_multi(1) = final_u(1);

u_lim = (rwall*bwall)^2;
delta_mult = sqrt(eps);

s_vector = vertcat(final_T(1),0,final_u(1));

for i = 1:i_length
    T_0_complex_multi = vertcat(T_0_complex_multi,final_T(i*vector_length-(i-1)));
    dTdr_0_complex_multi = vertcat(dTdr_0_complex_multi,...
        final_dTdr(i*vector_length-(i-1)));
    u_0_complex_multi = vertcat(u_0_complex_multi,final_u(i*vector_length-(i-1)));
    s_vector = vertcat(s_vector,final_T(i*vector_length-(i-1)),...
        final_dTdr(i*vector_length-(i-1)),final_u(i*vector_length-(i-1)));
end

T_0_complex_multi_track = [T_0_complex_multi];
dTdr_0_complex_multi_track = [dTdr_0_complex_multi];
u_0_complex_multi_track = [u_0_complex_multi];

for j = 1:500
    if isnan(T_0_complex_multi) == 1
        disp('NaN_error')
        break
    end
end

```

```

B_final_vector = [];
T_final_vector = [];
rad_final_vector = [];
dense_final_vector = [];
dTdr_final_vector = [];
u_final_vector = [];

A = zeros(num_eqns*(i_length+1));
b = [];
rad_vector = [];
T_vector = [];
u_vector = [];
dTdr_vector = [];
final_T = [];
final_u = [];
final_dTdr = [];
final_r = [];

for i = 1:i_length
    rad = r(((i-1)*vector_length-(i-2)):(i*vector_length-(i-1)));
    density = dense(((i-1)*vector_length-(i-2)):(i*vector_length-(i-1)));
    delta_T = T_0_complex_multi(i)*delta_mult;
    if dTdr_0_complex_multi(i) == 0
        delta_dTdr = delta_mult;
        delta_u = delta_mult;
    else
        delta_dTdr = dTdr_0_complex_multi(i)*delta_mult;
    end
    delta_u = u_0_complex_multi(i)*delta_mult;

options = odeset('RelTol',1e-3,'AbsTol',1e-6,'Events',...
    @eventsheatconduction);
Xo = [log10(T_0_complex_multi(i)-T_min);dTdr_0_complex_multi(i);...
    u_0_complex_multi(i)];

```

```

Xo_base = [log10(T_0_complex_multi(i));dTdr_0_complex_multi(i);...
           u_0_complex_multi(i)];
XodelT = [log10((T_0_complex_multi(i)+delta_T-T_min));...
          dTdr_0_complex_multi(i);u_0_complex_multi(i)];
XodelT_base = [log10((T_0_complex_multi(i)+delta_T));...
              dTdr_0_complex_multi(i);u_0_complex_multi(i)];
XodeldTdr = [log10(T_0_complex_multi(i)-T_min);...
             dTdr_0_complex_multi(i)+delta_dTdr;u_0_complex_multi(i)];
XodeldTdr_base = [log10(T_0_complex_multi(i));...
                  dTdr_0_complex_multi(i)+delta_dTdr;u_0_complex_multi(i)];
Xodelu = [log10(T_0_complex_multi(i)-T_min);dTdr_0_complex_multi(i);...
          u_0_complex_multi(i)+delta_u];
Xodelu_base = [log10(T_0_complex_multi(i));dTdr_0_complex_multi(i);...
              u_0_complex_multi(i)+delta_u];
rspan = [rad];

if rspan(1) == 0
    check = 1;
else check = 0;
end

if T_0_complex_multi(i) > T_min
    [radius,X] = ode15s(@HeatConduction,rspan,Xo,options,n0,a,...
                      T_min,brem_frac,line_frac,impurity_frac,impurity_ion,...
                      alter_Z,Zeff1,rwall);
    if isempty(X(:,1)) == 1
        temp = [];
        mag_field = [];
        dTdr = [];
        return
    end
    T_calc = T_min+10.^(X(:,1));
    dTdr_calc = X(:,2);
    u_calc = X(:,3);

```

```

else

    [radius ,X] = ode15s(@HeatConductionBaseline ,rspan ,Xo_base ,...
        [],n0,a,T_min,brem_frac ,line_frac ,impurity_frac ,...
        impurity_ion ,alter_Z ,Zeff1 ,rwall);
    if isempty(X(:,1)) == 1
        temp = [];
        mag_field = [];
        dTdr = [];
        return
    end
    T_calc = 10.^(X(:,1));
    dTdr_calc = X(:,2);
    u_calc = X(:,3);
end

if length(radius) < length(rad)

    n = n0*a^2/((radius(end))^2+a^2);
    dndr = -2*n0*a^2*(radius(end))/((radius(end))^2+a^2)^2;

    xe2 = c7*(u_calc(end))*(T_calc(end))^3/((radius(end))^2*...
        Zeff1^4*n^2*loglam^2)*mag_param;
    xi2 = c8*(u_calc(end))*(T_calc(end))^3/((radius(end))^2*...
        Zeff1^6*n^2*loglam^2)*mag_param;
    nume = gamma_1*xe2+gamma_0*unmag_param;
    numi = 2*xi2+2.645*unmag_param;
    dene = xe2^2+delta_1*unmag_param*xe2+delta_0*unmag_param;
    deni = xi2^2+2.7*unmag_param*xi2+0.677*unmag_param;
    k_perp_e1 = c5*(T_calc(end))^2.5*nume/dene;
    k_perp_i1 = c6*(T_calc(end))^2.5*numi/deni;
    k_perp = k_perp_e1+k_perp_i1;

    gyro = 1.02e2*Zeff1*sqrt(T_calc(end))/(sqrt(u_calc(end)))/...
        radius(end)*1e4)/100;

```

```

mfp = 2.04e13*T_calc(end)^2/(Zeff1*n/1e6*loglam)/100;

if isnan(min([gyro,mfp])) == 1
    temp = [];
    mag_field = [];
    dTdr = [];
    return
end

if min_case == 1
    if rad(end)-radius(end) < min([gyro,mfp])
        if length(radius) < vector_length-1
            radius_add = linspace(radius(end),rad(end),...
                vector_length+1-length(radius));
            T_end = T_calc(end);
            if length(T_calc) == 1
                T_end.1 = T_calc(end);
            else
                T_end.1 = T_calc(end-1);
            end
            T_calc = vertcat(T_calc,T_end+(T_min-T_end)/...
                min([gyro,mfp]).*(transpose(radius_add(2:end))...
                -radius(end)));
        else
            T_calc = vertcat(T_calc,T_calc(end)+(T_min-...
                T_calc(end))/min([gyro,mfp]).*(rad(end)-radius(end)));
        end
    else
        final_deltar = min([gyro,mfp]);
        T_calc = vertcat(T_calc,T_calc(end)+(T_min-T_calc(end)));
    end
end
else
    T_calc = vertcat(T_calc,T_calc(end)+(T_min-T_calc(end)));
end
end

```

```

if min_case == 1
    if rad(end)-radius(end) < min([gyro , mfp])
        if length(radius) < vector_length-1
            n_u = n0*a^2./((radius_add(2:end)).^2+a^2);
            dndr_u = -2*n0*a^2*(radius_add(2:end))./...
                ((radius_add(2:end)).^2+a^2).^2;

            u_calc = vertcat(u_calc , u_calc(end)+(c1*transpose(...
                radius_add(2:end)).^2.*((T_min-T_end_1)/(min([gyro...
                , mfp, (rad(end)-radius(end)])))*transpose(n_u)+...
                T_end_1.*transpose(dndr_u)).*(transpose(radius_add...
                (2:end))-radius(end)));
        else
            u_calc = vertcat(u_calc , u_calc(end)+(c1*radius(end)^2*...
                ((T_min-T_calc(end-1))/(min([gyro , mfp, (rad(end)-...
                radius(end)])))*n+T_calc(end-1)*dndr))*(rad(end)-...
                radius(end)));
        end
    else
        u_calc = vertcat(u_calc , u_calc(end)+(c1*radius(end)^2*...
            ((T_min-T_calc(end-1))/(min([gyro , mfp, (rad(end)-radius...
            (end)])))*n+T_calc(end-1)*dndr))*(min([gyro , mfp, (rad...
            (end)-radius(end)]))));
        end
    else
        u_calc = vertcat(u_calc , u_calc(end)+(c1*radius(end)^2*(...
            (T_min-T_calc(end-1))/(min_distance)*n+T_calc(end-1)*...
            dndr))*(min_distance));
    end

if min_case == 1
    if rad(end)-radius(end) < min([gyro , mfp])
        if length(radius) < vector_length-1
            n_rq = n0*a^2./((radius_add(2:end)).^2+a^2);
            dndr_rq = -2*n0*a^2*(radius_add(2:end))./((radius_add...

```

```

        (2:end)).^2+a^2).^2;

xe2_rq = c7*(u_calc(length(radius)+1:end)).*(T_calc...
    (length(radius)+1:end)).^3./(transpose(radius_add...
    (2:end)).^2*Zeff1^4.*transpose(n_rq).^2*loglam^2)*mag_param;
xi2_rq = c8*(u_calc(length(radius)+1:end)).*(T_calc...
    (length(radius)+1:end)).^3./(transpose(radius_add...
    (2:end)).^2*Zeff1^6.*transpose(n_rq).^2*loglam^2)*mag_param;
nume_rq = gamma_1*xe2_rq+gamma_0*unmag_param;
numi_rq = 2*xi2_rq+2.645*unmag_param;
dene_rq = xe2_rq.^2+delta_1*unmag_param*xe2_rq+...
    delta_0*unmag_param;
deni_rq = xi2_rq.^2+2.7*unmag_param*xi2_rq+0.677*unmag_param;
k_perp_el_rq = c5*(T_calc(length(radius)+1:end)).^...
    2.5.*nume_rq./dene_rq;
k_perp_il_rq = c6*(T_calc(length(radius)+1:end)).^...
    2.5.*numi_rq./deni_rq;
k_perp_rq = k_perp_el_rq+k_perp_il_rq;
dTdr_end = dTdr_calc(end);
dTdr_calc = vertcat(dTdr_calc,dTdr_end+(-transpose...
    (radius_add(2:end)).*k_perp_rq*k*(T_min-T_end)/...
    min([gyro,mfp]).*transpose(radius_add(2:end))));

    else
        dTdr_calc = vertcat(dTdr_calc,-rad(end)*k_perp*...
            (T_min-T_calc(end))/min([gyro,mfp]));
    end
end
else
    dTdr_calc = vertcat(dTdr_calc,0);
end
end
else
    dTdr_calc = vertcat(dTdr_calc,0);
end
end

if min_case == 1

```

```

if rad(end)-radius(end) < min([gyro , mfp])
    if length(radius) < vector_length-1
        radius = vertcat(radius , transpose(radius_add(2:end)));
    else
        radius = vertcat(radius , radius(end)+(rad(end)-radius(end)));
    end
else
    radius = vertcat(radius , radius(end)+min([gyro , mfp , ...
        (rad(end)-radius(end))]);
    end
else
    radius = vertcat(radius , radius(end)+min_distance);
end

if length(radius) == vector_length

else

    Xo_base = [log10(T_calc(end));dTdr_calc(end);u_calc(end)];
    rspan_base = linspace(radius(end),rspan(end),vector_length-...
        length(radius)+1);
    [radius_base , X_base] = ode15s(@HeatConductionBaseline , ...
        rspan_base , Xo_base , options , n0 , a , T_min , brem_frac , line_frac , ...
        impurity_frac , impurity_ion , alter_Z , Zeff1 , rwall);
    T_calc_base = 10.^(X_base(:,1));
    dTdr_calc_base = X_base(:,2);
    u_calc_base = X_base(:,3);
    if length(rspan_base) == 2

        T_calc = vertcat(T_calc , T_calc_base(end));
        dTdr_calc = vertcat(dTdr_calc , dTdr_calc_base(end));
        u_calc = vertcat(u_calc , u_calc_base(end));
        radius = vertcat(radius , transpose(rspan_base(end)));
    else

```

```

T_calc = vertcat(T_calc, T_calc_base(2:end));
dTdr_calc = vertcat(dTdr_calc, dTdr_calc_base...
    (2:length(dTdr_calc_base)));
u_calc = vertcat(u_calc, u_calc_base(2:end));
radius = vertcat(radius, transpose(rspan_base(2:end)));

if radius_base(end) < rwall && length(T_calc) < ...
    vector_length && i == i_length
    T_calc = vertcat(T_calc, T_calc(end));
    dTdr_calc = vertcat(dTdr_calc, dTdr_calc(end));
    u_calc = vertcat(u_calc, u_calc(end));
    radius = vertcat(radius, transpose(rspan_base(end)));
end

end

end

end

if rspan(1) == 0
    check = 1;
else check = 0;
end

if T_0_complex_multi(i) > T_min
    [radius_delT, X_delT] = ode15s(@HeatConduction, rspan, XdelT, ...
        options, n0, a, T_min, brem_frac, line_frac, impurity_frac, ...
        impurity_ion, alter_Z, Zeff1, rwall);
    if isempty(X_delT(:,1)) == 1
        temp = [];
        mag_field = [];
        dTdr = [];
        return
    end
    T_delT = T_min + 10.^(X_delT(:,1));
    dTdr_delT = X_delT(:,2);

```

```

    u_delT = X_delT(:,3);
else
    [radius_delT, X_delT] = ode15s(@HeatConductionBaseline, rspan, ...
        XodelT_base, [], n0, a, T_min, brem_frac, line_frac, impurity_frac, ...
        impurity_ion, alter_Z, Zeff1, rwall);
    if isempty(X_delT(:,1)) == 1
        temp = [];
        mag_field = [];
        dTdr = [];
        return
    end
    T_delT = 10.^(X_delT(:,1));
    dTdr_delT = X_delT(:,2);
    u_delT = X_delT(:,3);
end

if length(radius_delT) < length(rad)

    n = n0*a^2/((radius_delT(end))^2+a^2);
    dndr = -2*n0*a^2*(radius_delT(end))/((radius_delT(end))^2+a^2)^2;

    xe2 = c7*(u_delT(end))*(T_delT(end))^3/((radius_delT(end))^2*...
        Zeff1^4*n^2*loglam^2)*mag_param;
    xi2 = c8*(u_delT(end))*(T_delT(end))^3/((radius_delT(end))^2*...
        Zeff1^6*n^2*loglam^2)*mag_param;
    nume = gamma_1*xe2+gamma_0*unmag_param;
    numi = 2*xi2+2.645*unmag_param;
    dene = xe2^2+delta_1*unmag_param*xe2+delta_0*unmag_param;
    deni = xi2^2+2.7*unmag_param*xi2+0.677*unmag_param;
    k_perp_e1 = c5*(T_delT(end))^2.5*nume/dene;
    k_perp_i1 = c6*(T_delT(end))^2.5*numi/deni;
    k_perp = k_perp_e1+k_perp_i1;

    gyro = 1.02e2*Zeff1*sqrt(T_delT(end))/(sqrt(u_delT(end)))/...

```

```

        radius_delT(end)*1e4)/100;
mfp = 2.04e13*T_delT(end)^2/(Zeff1*n/1e6*loglam)/100;

if isnan(min([gyro,mfp])) == 1
    temp = [];
    mag_field = [];
    dTdr = [];
    return
end

if min_case == 1
    if rad(end)-radius_delT(end) < min([gyro,mfp])
        if length(radius_delT) < vector_length-1
            radius_add_delT = linspace(radius_delT(end),rad(end),...
                vector_length+1-length(radius_delT));
            T_end = T_delT(end);
            if length(T_delT) == 1
                T_end_1 = T_delT(end);
            else
                T_end_1 = T_delT(end-1);
            end
            T_delT = vertcat(T_delT,T_end+(T_min-T_end)/...
                min([gyro,mfp]).*(transpose(radius_add_delT...
                (2:end))-radius_delT(end)));
        else
            T_delT = vertcat(T_delT,T_delT(end)+(T_min-...
                T_delT(end))/min([gyro,mfp]).*(rad(end)-...
                radius_delT(end)));
        end
    else
        T_delT = vertcat(T_delT,T_delT(end)+(T_min-T_delT(end)));
    end
end
else
    T_delT = vertcat(T_delT,T_delT(end)+(T_min-T_delT(end)));
end
end

```

```

if min_case == 1
    if rad(end)-radius_delT(end) < min([gyro, mfp])
        if length(radius_delT) < vector_length-1
            n_u_delT = n0*a^2./((radius_add_delT(2:end)).^2+a^2);
            dndr_u_delT = -2*n0*a^2*(radius_add_delT(2:end))./...
                ((radius_add_delT(2:end)).^2+a^2).^2;

            u_delT = vertcat(u_delT, u_delT(end)+(c1*transpose(...
                radius_add_delT(2:end)).^2.*((T_min-T_end_1)/...
                (min([gyro, mfp, (rad(end)-radius_delT(end))]))).*...
                transpose(n_u_delT)+T_end_1.*transpose(...
                \dndr_u_delT))).*(transpose(radius_add_delT(2:end)...
                )-radius_delT(end)));
        else
            u_delT = vertcat(u_delT, u_delT(end)+(c1*radius_delT(...
                end)^2*((T_min-T_delT(end-1))/(min([gyro, mfp, (rad(...
                end)-radius_delT(end))]))*n+T_delT(end-1)*dndr))*...
                (rad(end)-radius_delT(end)));
        end
    else
        u_delT = vertcat(u_delT, u_delT(end)+(c1*radius_delT(end)^2*...
            ((T_min-T_delT(end-1))/(min([gyro, mfp, (rad(end)-...
            radius_delT(end))]))*n+T_delT(end-1)*dndr))*(min([...
            gyro, mfp, (rad(end)-radius_delT(end))])));
        end
    else
        u_delT = vertcat(u_delT, u_delT(end)+(c1*radius_delT(end)^2*...
            ((T_min-T_delT(end-1))/(min_distance)*n+T_delT(end-1)*...
            dndr))*(min_distance));
        end
end

if min_case == 1
    if rad(end)-radius_delT(end) < min([gyro, mfp])
        if length(radius_delT) < vector_length-1

```

```

n_rq_delT = n0*a^2./((radius_add_delT(2:end)).^2+a^2);
dndr_rq_delT = -2*n0*a^2*(radius_add_delT(2:end))./...
    ((radius_add_delT(2:end)).^2+a^2).^2;

xe2_rq_delT = c7*(u_delT(length(radius_delT)+...
    1:end)).*(T_delT(length(radius_delT)+1:end)...
    ).^3./(transpose(radius_add_delT(2:end)).^2*...
    Zeff1^4.*transpose(n_rq_delT).^2*loglam^2)*mag_param;
xi2_rq_delT = c8*(u_delT(length(radius_delT)+...
    1:end)).*(T_delT(length(radius_delT)+1:end)...
    ).^3./(transpose(radius_add_delT(2:end)).^2*...
    Zeff1^6.*transpose(n_rq_delT).^2*loglam^2)*mag_param;
nume_rq_delT = gamma_1*xe2_rq_delT+gamma_0*unmag_param;
numi_rq_delT = 2*xi2_rq_delT+2.645*unmag_param;
dene_rq_delT = xe2_rq_delT.^2+delta_1*unmag_param*...
    xe2_rq_delT+delta_0*unmag_param;
deni_rq_delT = xi2_rq_delT.^2+2.7*unmag_param*...
    xi2_rq_delT+0.677*unmag_param;
k_perp_e1_rq_delT = c5*(T_delT(length(radius_delT)+...
    1:end)).^2.5.*nume_rq_delT./dene_rq_delT;
k_perp_i1_rq_delT = c6*(T_delT(length(radius_delT)+...
    1:end)).^2.5.*numi_rq_delT./deni_rq_delT;
k_perp_rq_delT = k_perp_e1_rq_delT+k_perp_i1_rq_delT;
dTdr_end = dTdr_delT(end);
dTdr_delT = vertcat(dTdr_delT, dTdr_end+(-transpose(...
    radius_add_delT(2:end)).*k_perp_rq_delT*k*(T_min-...
    T_end)/min([gyro, mfp]).*transpose(radius_add_delT...
    (2:end))));

else
    dTdr_delT = vertcat(dTdr_delT, (T_min-T_delT(end))./...
        min([gyro, mfp]));
end
else
dTdr_delT = vertcat(dTdr_delT, 0);

```

```

    end
else
    dTdr_delT = vertcat(dTdr_delT,0);
end

if min_case == 1
    if rad(end)-radius_delT(end) < min([gyro, mfp])
        if length(radius_delT) < vector_length-1
            radius_delT = vertcat(radius_delT, transpose(...
                radius_add_delT(2:end)));
        else
            radius_delT = vertcat(radius_delT, radius_delT(end)...
                +(rad(end)-radius_delT(end)));
        end
    else
        radius_delT = vertcat(radius_delT, radius_delT(end)+...
            min([gyro, mfp, (rad(end)-radius_delT(end))]));
    end
else
    radius_delT = vertcat(radius_delT, radius_delT(end)+min_distance);
end

if length(radius_delT) == vector_length

else

    Xo_base_delT = [log10(T_delT(end)); dTdr_delT(end); u_delT(end)];
    rspan_base_delT = linspace(radius_delT(end), rspan(end), ...
        vector_length-length(radius_delT)+1);
    [radius_base_delT, X_base_delT] = ode15s(@HeatConductionBaseline, ...
        rspan_base_delT, Xo_base_delT, options, n0, a, T_min, brem_frac, ...
        line_frac, impurity_frac, impurity_ion, alter_Z, Zeff1, rwall);
    T_calc_base_delT = 10.^(X_base_delT(:,1));
    dTdr_calc_base_delT = X_base_delT(:,2);
    u_calc_base_delT = X_base_delT(:,3);

```

```

if length(rspan_base_delT) == 2
    T_delT = vertcat(T_delT, T_calc_base_delT(end));
    dTdr_delT = vertcat(dTdr_delT, dTdr_calc_base_delT(end));
    u_delT = vertcat(u_delT, u_calc_base_delT(end));
else
    T_delT = vertcat(T_delT, T_calc_base_delT(2:end));
    dTdr_delT = vertcat(dTdr_delT, dTdr_calc_base_delT(2:end));
    u_delT = vertcat(u_delT, u_calc_base_delT(2:end));

    if radius_delT(end) < rwall && length(T_delT) < ...
        vector_length && i == i.length
            T_delT = vertcat(T_delT, T_delT(end));
            dTdr_delT = vertcat(dTdr_delT, dTdr_delT(end));
            u_delT = vertcat(u_delT, u_delT(end));
        end
    end
end
end

if rspan(1) == 0
    check = 1;
else check = 0;
end

if T_0_complex_multi(i) > T_min
    [radius_deldTdr, X_deldTdr] = ode15s(@HeatConduction, rspan, ...
        XodeldTdr, options, n0, a, T_min, brem_frac, line_frac, ...
        impurity_frac, impurity_ion, alter_Z, Zeff1, rwall);
    if isempty(X_deldTdr(:,1)) == 1
        temp = [];
        mag_field = [];
        dTdr = [];
        return
    end
    T_deldTdr = T_min + 10.^(X_deldTdr(:,1));

```

```

dTdr_deldTdr = X_deldTdr(:,2);
u_deldTdr = X_deldTdr(:,3);
else

[radius_deldTdr, X_deldTdr] = ode15s(@HeatConductionBaseline, ...
    rspan, XodeldTdr_base, [], n0, a, T_min, brem_frac, line_frac, ...
    impurity_frac, impurity_ion, alter_Z, Zeff1, rwall);
if isempty(X_deldTdr(:,1)) == 1
    temp = [];
    mag_field = [];
    dTdr = [];
    return
end
T_deldTdr = 10.^(X_deldTdr(:,1));
dTdr_deldTdr = X_deldTdr(:,2);
u_deldTdr = X_deldTdr(:,3);
end

if length(radius_deldTdr) < length(rad)

n = n0*a^2/((radius_deldTdr(end))^2+a^2);
dn dr = -2*n0*a^2*(radius_deldTdr(end))/((radius_deldTdr(end))^2+a^2)^2;

xe2 = c7*(u_deldTdr(end))*(T_deldTdr(end))^3/((radius_deldTdr ...
    (end))^2*Zeff1^4*n^2*loglam^2)*mag_param;
xi2 = c8*(u_deldTdr(end))*(T_deldTdr(end))^3/((radius_deldTdr ...
    (end))^2*Zeff1^6*n^2*loglam^2)*mag_param;
nume = gamma_1*xe2+gamma_0*unmag_param;
numi = 2*xi2+2.645*unmag_param;
dene = xe2^2+delta_1*unmag_param*xe2+delta_0*unmag_param;
deni = xi2^2+2.7*unmag_param*xi2+0.677*unmag_param;
k_perp_e1 = c5*(T_deldTdr(end))^2.5*nume/dene;
k_perp_i1 = c6*(T_deldTdr(end))^2.5*numi/deni;
k_perp = k_perp_e1+k_perp_i1;

```

```

gyro = 1.02e2*Zeff1*sqrt(T_deldTdr(end))/(sqrt(u_deldTdr(end))/...
    radius_deldTdr(end)*1e4)/100;
mfp = 2.04e13*T_deldTdr(end)^2/(Zeff1*n/1e6*loglam)/100;

if isnan(min([gyro,mfp])) == 1
    temp = [];
    mag-field = [];
    dTdr = [];
    return
end

if min_case == 1
    if rad(end)-radius_deldTdr(end) < min([gyro,mfp])
        if length(radius_deldTdr) < vector_length-1
            radius_add_deldTdr = linspace(radius_deldTdr(end),...
                rad(end),vector_length+1-length(radius_deldTdr));
            T_end = T_deldTdr(end);
            if length(T_deldTdr) == 1
                T_end_1 = T_deldTdr(end);
            else
                T_end_1 = T_deldTdr(end-1);
            end
            T_deldTdr = vertcat(T_deldTdr,T_end+(T_min-T_end)/...
                min([gyro,mfp]).*(transpose(radius_add_deldTdr...
                (2:end))-radius_deldTdr(end)));
        else
            T_deldTdr = vertcat(T_deldTdr,T_deldTdr(end)+...
                (T_min-T_deldTdr(end))/min([gyro,mfp])*...
                (rad(end)-radius_deldTdr(end)));
        end
    else
        T_deldTdr = vertcat(T_deldTdr,T_deldTdr(end)+...
            (T_min-T_deldTdr(end)));
    end
end

```

```

    T_deldTdr = vertcat(T_deldTdr, T_deldTdr(end)+(T_min-T_deldTdr(end)));
end

if min_case == 1
    if rad(end)-radius_deldTdr(end) < min([gyro, mfp])
        if length(radius_deldTdr) < vector_length-1
            n_u_deldTdr = n0*a^2./((radius_add_deldTdr(2:end)).^2+a^2);
            dndr_u_deldTdr = -2*n0*a^2*(radius_add_deldTdr...
                (2:end))./((radius_add_deldTdr(2:end)).^2+a^2).^2;

            u_deldTdr = vertcat(u_deldTdr, u_deldTdr(end)+(c1*...
                transpose(radius_add_deldTdr(2:end)).^2*((T_min...
                    -T_end_1)/(min([gyro, mfp, (rad(end)-radius_deldTdr...
                        (end)])))*transpose(n_u_deldTdr)+T_end_1.*...
                    transpose(dndr_u_deldTdr)))*(transpose(...
                        radius_add_deldTdr(2:end))-radius_deldTdr(end)));
        else
            u_deldTdr = vertcat(u_deldTdr, u_deldTdr(end)+(c1*...
                radius_deldTdr(end)^2*((T_min-T_deldTdr(end-1))/...
                    (min([gyro, mfp, (rad(end)-radius_deldTdr(end)])))*n...
                    +T_deldTdr(end-1)*dndr))*(rad(end)-radius_deldTdr(end)));
        end
    else
        u_deldTdr = vertcat(u_deldTdr, u_deldTdr(end)+(c1*...
            radius_deldTdr(end)^2*((T_min-T_deldTdr(end-1))/...
                (min([gyro, mfp, (rad(end)-radius_deldTdr(end)])))*n...
                +T_deldTdr(end-1)*dndr))*(min([gyro, mfp, (rad(end)-...
                    radius_deldTdr(end)]))));
    end
else
    u_deldTdr = vertcat(u_deldTdr, u_deldTdr(end)+(c1*...
        radius_deldTdr(end)^2*((T_min-T_deldTdr(end-1))/...
            (min_distance)*n+T_deldTdr(end-1)*dndr))*(min_distance));
end
end

```

```

if min_case == 1
    if rad(end)-radius_deldTdr(end) < min([gyro, mfp])
        if length(radius_deldTdr) < vector_length-1
            n_rq_deldTdr = n0*a^2./((radius_add_deldTdr(2:end)).^2+a^2);
            dndr_rq_deldTdr = -2*n0*a^2*(radius_add_deldTdr...
                (2:end))./((radius_add_deldTdr(2:end)).^2+a^2).^2;

            xe2_rq_deldTdr = c7*(u_deldTdr(length(radius_deldTdr)...
                +1:end)).*(T_deldTdr(length(radius_deldTdr)+1:end)...
                ).^3./((transpose(radius_add_deldTdr(2:end)).^2*...
                Zeff1^4.*transpose(n_rq_deldTdr).^2*loglam^2)*mag_param);
            xi2_rq_deldTdr = c8*(u_deldTdr(length(radius_deldTdr)...
                +1:end)).*(T_deldTdr(length(radius_deldTdr)+1:end)...
                ).^3./((transpose(radius_add_deldTdr(2:end)).^2*...
                Zeff1^6.*transpose(n_rq_deldTdr).^2*loglam^2)*mag_param);
            nume_rq_deldTdr = gamma_1*xe2_rq_deldTdr+gamma_0*unmag_param;
            numi_rq_deldTdr = 2*xi2_rq_deldTdr+2.645*unmag_param;
            dene_rq_deldTdr = xe2_rq_deldTdr.^2+delta_1*unmag_param*...
                xe2_rq_deldTdr+delta_0*unmag_param;
            deni_rq_deldTdr = xi2_rq_deldTdr.^2+2.7*unmag_param*...
                xi2_rq_deldTdr+0.677*unmag_param;
            k_perp_e1_rq_deldTdr = c5*(T_deldTdr(length(...
                radius_deldTdr)+1:end)).^2.5.*nume_rq_deldTdr./...
                dene_rq_deldTdr;
            k_perp_i1_rq_deldTdr = c6*(T_deldTdr(length(...
                radius_deldTdr)+1:end)).^2.5.*numi_rq_deldTdr./...
                deni_rq_deldTdr;
            k_perp_rq_deldTdr = k_perp_e1_rq_deldTdr+...
                k_perp_i1_rq_deldTdr;
            dTdr_end = dTdr_deldTdr(end);
            dTdr_deldTdr = vertcat(dTdr_deldTdr, dTdr_end+...
                (-transpose(radius_add_deldTdr(2:end)).*...
                k_perp_rq_deldTdr*k*(T_min-T_end)/min([gyro, mfp])).*...
                transpose(radius_add_deldTdr(2:end)));

```

```

        else
            dTdr_deldTdr = vertcat(dTdr_deldTdr ,...
                (T_min-T_deldTdr(end))/min([gyro , mfp]));
        end
    else
        dTdr_deldTdr = vertcat(dTdr_deldTdr , 0);
    end
end
else
    dTdr_deldTdr = vertcat(dTdr_deldTdr , 0);
end

if min_case == 1
    if rad(end)-radius_deldTdr(end) < min([gyro , mfp])
        if length(radius_deldTdr) < vector_length-1
            radius_deldTdr = vertcat(radius_deldTdr ,...
                transpose(radius_add_deldTdr(2:end)));
        else
            radius_deldTdr = vertcat(radius_deldTdr ,...
                radius_deldTdr(end)+(rad(end)-radius_deldTdr(end)));
        end
    else
        radius_deldTdr = vertcat(radius_deldTdr , radius_deldTdr(end)...
            +min([gyro , mfp , (rad(end)-radius_deldTdr(end))]);
    end
end
else
    radius_deldTdr = vertcat(radius_deldTdr ,...
        radius_deldTdr(end)+min_distance);
end

if length(radius_deldTdr) == vector_length

else

    Xo_base_deldTdr = [log10(T_deldTdr(end)); dTdr_deldTdr(end);...
        u_deldTdr(end)];

```

```

rspan_base_deldTdr = linspace(radius_deldTdr(end), ...
    rspan(end), vector_length-length(radius_deldTdr)+1);
[radius_base_deldTdr, X_base_deldTdr] = ode15s(...
    @HeatConductionBaseline, rspan_base_deldTdr, ...
    Xo_base_deldTdr, options, n0, a, T_min, brem_frac, ...
    line_frac, impurity_frac, impurity_ion, alter_Z, Zeff1, rwall);
T_calc_base_deldTdr = 10.^(X_base_deldTdr(:,1));
dTdr_calc_base_deldTdr = X_base_deldTdr(:,2);
u_calc_base_deldTdr = X_base_deldTdr(:,3);
if length(rspan_base_deldTdr) == 2
    T_deldTdr = vertcat(T_deldTdr, T_calc_base_deldTdr(end));
    dTdr_deldTdr = vertcat(dTdr_deldTdr, ...
        dTdr_calc_base_deldTdr(end));
    u_deldTdr = vertcat(u_deldTdr, u_calc_base_deldTdr(end));
else
    T_deldTdr = vertcat(T_deldTdr, T_calc_base_deldTdr(2:end));
    dTdr_deldTdr = vertcat(dTdr_deldTdr, ...
        dTdr_calc_base_deldTdr(2:end));
    u_deldTdr = vertcat(u_deldTdr, u_calc_base_deldTdr(2:end));

    if radius_deldTdr(end) < rwall && length(T_deldTdr) < ...
        vector_length && i == i.length
        T_deldTdr = vertcat(T_deldTdr, T_deldTdr(end));
        dTdr_deldTdr = vertcat(dTdr_deldTdr, dTdr_deldTdr(end));
        u_deldTdr = vertcat(u_deldTdr, u_deldTdr(end));
    end
end
end
end

if rspan(1) == 0
    check = 1;
else check = 0;
end
if T_0_complex_multi(i) > T_min

```

```

[ radius_delu , X_delu ] = ode15s (@HeatConduction , rspan , Xodelu , ...
    options , n0 , a , T_min , brem_frac , line_frac , impurity_frac , ...
    impurity_ion , alter_Z , Zeff1 , rwall );
if isempty( X_delu (: , 1) ) == 1
    temp = [];
    mag_field = [];
    dTdr = [];
    return
end
T_delu = T_min + 10.^( X_delu (: , 1) );
dTdr_delu = X_delu (: , 2);
u_delu = X_delu (: , 3);
else

[ radius_delu , X_delu ] = ode15s (@HeatConductionBaseline , rspan , ...
    Xodelu_base , [] , n0 , a , T_min , brem_frac , line_frac , impurity_frac , ...
    impurity_ion , alter_Z , Zeff1 , rwall );
if isempty( X_delu (: , 1) ) == 1
    temp = [];
    mag_field = [];
    dTdr = [];
    return
end
T_delu = 10.^( X_delu (: , 1) );
dTdr_delu = X_delu (: , 2);
u_delu = X_delu (: , 3);
end

if length( radius_delu ) < length( rad )

n = n0 * a ^ 2 / (( radius_delu ( end ) ) ^ 2 + a ^ 2 );
ndnr = -2 * n0 * a ^ 2 * ( radius_delu ( end ) ) / (( radius_delu ( end ) ) ^ 2 + a ^ 2 ) ^ 2;

xe2 = c7 * ( u_delu ( end ) ) * ( T_delu ( end ) ) ^ 3 / (( radius_delu ( end ) ) ^ 2 * ...
    Zeff1 ^ 4 * n ^ 2 * loglam ^ 2 ) * mag_param ;

```

```

xi2 = c8*(u_delu(end))*(T_delu(end))^3/((radius_delu(end))^2*...
      Zeff1^6*n^2*loglam^2)*mag_param;
nume = gamma_1*xe2+gamma_0*unmag_param;
numi = 2*xi2+2.645*unmag_param;
dene = xe2^2+delta_1*unmag_param*xe2+delta_0*unmag_param;
deni = xi2^2+2.7*unmag_param*xi2+0.677*unmag_param;
k_perp_e1 = c5*(T_delu(end))^2.5*nume/dene;
k_perp_i1 = c6*(T_delu(end))^2.5*numi/deni;
k_perp = k_perp_e1+k_perp_i1;

gyro = 1.02e2*Zeff1*sqrt(T_delu(end))/(sqrt(u_delu(end))/...
      radius_delu(end)*1e4)/100;
mfp = 2.04e13*T_delu(end)^2/(Zeff1*n/1e6*loglam)/100;

if isnan(min([gyro,mfp])) == 1
    temp = [];
    mag_field = [];
    dTdr = [];
    return
end

if min_case == 1
    if rad(end)-radius_delu(end) < min([gyro,mfp])
        if length(radius_delu) < vector_length-1
            radius_add_delu = linspace(radius_delu(end),...
                rad(end),vector_length+1-length(radius_delu));
            T_end = T_delu(end);
            if length(T_delu) == 1
                T_end_1 = T_delu(end);
            else
                T_end_1 = T_delu(end-1);
            end
            T_delu = vertcat(T_delu,T_end+(T_min-T_end)/...
                min([gyro,mfp]).*(transpose(radius_add_delu...
                (2:end))-radius_delu(end)));

```

```

else
    T_delu = vertcat(T_delu, T_delu(end)+(T_min...
        -T_delu(end))/min([gyro, mfp])*(rad(end)...
        -radius_delu(end)));
end
else
    T_delu = vertcat(T_delu, T_delu(end)+(T_min-T_delu(end)));
end
else
    T_delu = vertcat(T_delu, T_delu(end)+(T_min-T_delu(end)));
end

if min_case == 1
    if rad(end)-radius_delu(end) < min([gyro, mfp])
        if length(radius_delu) < vector_length-1
            n_u_delu = n0*a^2./((radius_add_delu(2:end)).^2+a^2);
            dndr_u_delu = -2*n0*a^2*(radius_add_delu(2:end))./...
                ((radius_add_delu(2:end)).^2+a^2).^2;

            u_delu = vertcat(u_delu, u_delu(end)+(c1*transpose(...
                radius_add_delu(2:end)).^2*((T_min-T_end_1)/...
                (min([gyro, mfp, (rad(end)-radius_delu(end)])))*n...
                transpose(n_u_delu)+T_end_1.*transpose(...
                dndr_u_delu))).*(transpose(radius_add_delu(2:end))...
                -radius_delu(end)));
        else
            u_delu = vertcat(u_delu, u_delu(end)+(c1*...
                radius_delu(end)^2*((T_min-T_delu(end-1))/...
                (min([gyro, mfp, (rad(end)-radius_delu(end)])))*n...
                +T_delu(end-1)*dndr))*(rad(end)-radius_delu(end)));
        end
    else
        u_delu = vertcat(u_delu, u_delu(end)+(c1*...
            radius_delu(end)^2*((T_min-T_delu(end-1))/...
            (min([gyro, mfp, (rad(end)-radius_delu(end)])))*n...
            +T_delu(end-1)*dndr))*(rad(end)-radius_delu(end)));
    end
end

```

```

        +T_delu(end-1)*dndr))*(min([gyro, mfp, (rad(end) - ...
        radius_delu(end))])));
    end
else
    u_delu = vertcat(u_delu, u_delu(end)+(c1*radius_delu(end)^2*...
        ((T_min-T_delu(end-1))/(min_distance)*n+T_delu(end-1)*...
        dndr))*(min_distance));
end

if min_case == 1
    if rad(end)-radius_delu(end) < min([gyro, mfp])
        if length(radius_delu) < vector_length-1
            n_rq_delu = n0*a^2./((radius_add_delu(2:end)).^2+a^2);
            dndr_rq_delu = -2*n0*a^2*(radius_add_delu(2:end))./...
                ((radius_add_delu(2:end)).^2+a^2).^2;

            xe2_rq_delu = c7*(u_delu(length(radius_delu)+1:end)).*...
                (T_delu(length(radius_delu)+1:end)).^3./(transpose(...
                radius_add_delu(2:end)).^2*Zeff1^4.*transpose(...
                n_rq_delu).^2*loglam^2)*mag_param;
            xi2_rq_delu = c8*(u_delu(length(radius_delu)...
                +1:end)).*(T_delu(length(radius_delu)+1:end)).^3./...
                (transpose(radius_add_delu(2:end)).^2*Zeff1^6.*...
                transpose(n_rq_delu).^2*loglam^2)*mag_param;
            nume_rq_delu = gamma_1*xe2_rq_delu+...
                gamma_0*unmag_param;
            numi_rq_delu = 2*xi2_rq_delu+2.645*unmag_param;
            dene_rq_delu = xe2_rq_delu.^2+...
                delta_1*unmag_param*xe2_rq_delu+...
                delta_0*unmag_param;
            deni_rq_delu = xi2_rq_delu.^2+...
                2.7*unmag_param*xi2_rq_delu+0.677*unmag_param;
            k_perp_e1_rq_delu = c5*(T_delu(length(radius_delu)+...
                1:end)).^2.5.*nume_rq_delu./dene_rq_delu;
            k_perp_i1_rq_delu = c6*(T_delu(length(radius_delu)+...

```

```

1:end)).^2.5.*numi_rq_delu./deni_rq_delu;
k_perp_rq_delu = k_perp_e1_rq_delu+k_perp_i1_rq_delu;
dTdr_end = dTdr_delu(end);
dTdr_delu = vertcat(dTdr_delu,dTdr_end+(-transpose(...
    radius_add_delu(2:end)).*k_perp_rq_delu*k*(T_min-...
    T_end)/min([gyro,mfp]).*transpose(radius_add_delu(...
    2:end))));

else
    dTdr_delu = vertcat(dTdr_delu,(T_min-T_delu(end))/...
        min([gyro,mfp]));
end
else
    dTdr_delu = vertcat(dTdr_delu,0);
end
else
    dTdr_delu = vertcat(dTdr_delu,0);
end

if min_case == 1
    if rad(end)-radius_delu(end) < min([gyro,mfp])
        if length(radius_delu) < vector_length-1
            radius_delu = vertcat(radius_delu,transpose(...
                radius_add_delu(2:end)));
        else
            radius_delu = vertcat(radius_delu,radius_delu(end)...
                +(rad(end)-radius_delu(end)));
        end
    else
        radius_delu = vertcat(radius_delu,radius_delu(end)+...
            min([gyro,mfp,(rad(end)-radius_delu(end))]));
    end
else
    radius_delu = vertcat(radius_delu,radius_delu(end)+...
        min_distance);
end

```

```

end

if length(radius_delu) == vector_length

else

    Xo_base_delu = [log10(T_delu(end)); dTdr_delu(end); u_delu(end)];
    rspan_base_delu = linspace(radius_delu(end), rspan(end), ...
        vector_length - length(radius_delu) + 1);
    [radius_base_delu, X_base_delu] = ode15s(...
        @HeatConductionBaseline, rspan_base_delu, Xo_base_delu ...
        , options, n0, a, T_min, brem_frac, line_frac, impurity_frac, ...
        impurity_ion, alter_Z, Zeff1, rwall);
    T_calc_base_delu = 10.^(X_base_delu(:, 1));
    dTdr_calc_base_delu = X_base_delu(:, 2);
    u_calc_base_delu = X_base_delu(:, 3);
    if length(rspan_base_delu) == 2
        T_delu = vertcat(T_delu, T_calc_base_delu(end));
        dTdr_delu = vertcat(dTdr_delu, dTdr_calc_base_delu(end));
        u_delu = vertcat(u_delu, u_calc_base_delu(end));
    else
        T_delu = vertcat(T_delu, T_calc_base_delu(2:end));
        dTdr_delu = vertcat(dTdr_delu, dTdr_calc_base_delu(2:end));
        u_delu = vertcat(u_delu, u_calc_base_delu(2:end));

        if radius_delu(end) < rwall && length(T_delu) < ...
            vector_length && i == i_length
            T_delu = vertcat(T_delu, T_delu(end));
            dTdr_delu = vertcat(dTdr_delu, dTdr_delu(end));
            u_delu = vertcat(u_delu, u_delu(end));
        end
    end
end
end
end
end

```

```

% Build F(s) vector

u_final_vector = horzcat(u_final_vector ,(u_calc));
T_final_vector = horzcat(T_final_vector ,(T_calc));
dTdr_final_vector = horzcat(dTdr_final_vector ,(dTdr_calc));
rad_final_vector = horzcat(rad_final_vector ,radius);

Fsu = real(u_calc(length(u_calc)))-real(u_0_complex_multi(i+1));
FsT = real(T_calc(length(T_calc)))-real(T_0_complex_multi(i+1));
FsdTdr = real(dTdr_calc(length(dTdr_calc)))-real(...
    dTdr_0_complex_multi(i+1));

del_FsuT = real(u_delT(length(u_delT)))-real(...
    u_0_complex_multi(i+1));
del_FsudTdr = real(u_deldTdr(length(u_deldTdr)))-real(...
    u_0_complex_multi(i+1));
del_Fsuu = real(u_delu(length(u_delu)))-real(...
    u_0_complex_multi(i+1));

del_FsTT = real(T_delT(length(T_delT)))-real(...
    T_0_complex_multi(i+1));
del_FsTdTdr = real(T_deldTdr(length(T_deldTdr)))-real(...
    T_0_complex_multi(i+1));
del_FsTu = real(T_delu(length(T_delu)))-real(...
    T_0_complex_multi(i+1));

del_FsdTdrT = real(dTdr_delT(length(dTdr_delT)))-real(...
    dTdr_0_complex_multi(i+1));
del_FsdTdrdTdr = real(dTdr_deldTdr(length(dTdr_deldTdr)))-real(...
    dTdr_0_complex_multi(i+1));
del_FsdTdru = real(dTdr_delu(length(dTdr_delu)))-real(...
    dTdr_0_complex_multi(i+1));

dFsuT = (del_FsuT-Fsu)/delta_T;
if i == 1

```

```

    dFsuu = 0;
    dFsudTdr = 0;
else
    dFsuu = (del_Fsuu-Fsu)/delta_u;
    dFsudTdr = (del_FsudTdr-Fsu)/delta_dTdr;
end

dFsTT = (del_FsTT-FsT)/delta_T;
if i == 1
    dFsTdTdr = 0;
    dFsTu = 0;
else
    dFsTdTdr = (del_FsTdTdr-FsT)/delta_dTdr;
    dFsTu = (del_FsTu-FsT)/delta_u;
end

dFsdTdrT = (del_FsdTdrT-FsdTdr)/delta_T;
if i == 1
    dFsdTdrdTdr = 0;
    dFsdTdrdru = 0;
else
    dFsdTdrdTdr = (del_FsdTdrdTdr-FsdTdr)/delta_dTdr;
    dFsdTdrdru = (del_FsdTdrdru-FsdTdr)-delta_u;
end

A((num_eqns*i-2),(num_eqns*i-2)) = dFsTT;
A((num_eqns*i-2),(num_eqns*i-1)) = dFsTdTdr;
A((num_eqns*i-2),(num_eqns*i)) = dFsTu;
A((num_eqns*i-1),(num_eqns*i-2)) = dFsdTdrT;
A((num_eqns*i-1),(num_eqns*i-1)) = dFsdTdrdTdr;
A((num_eqns*i-1),(num_eqns*i)) = dFsdTdrdru;
A((num_eqns*i),(num_eqns*i-2)) = dFsuT;
A((num_eqns*i),(num_eqns*i-1)) = dFsudTdr;
A((num_eqns*i),(num_eqns*i)) = dFsuu;
A((num_eqns*i-2),(num_eqns*i+1)) = -1;

```

```

A((num_eqns*i-1),(num_eqns*i+2)) = -1;
A((num_eqns*i),(num_eqns*i+3)) = -1;

b = vertcat(b,FsT,FsdTdr,Fsu);

    if i == i_length
        fin_u = u_calc(length(u_calc));
    end
end
b = vertcat(b,0,0,fin_u-u_lim);
A(max(size(A))-(num_eqns-1),2) = 1;
A(max(size(A))-(num_eqns-2),3) = 1;
A(max(size(A)),max(size(A))) = 1;

iteration = A\b;

T_mod = iteration(1:num_eqns:length(iteration)-(num_eqns-1));
dTdr_mod = iteration(2:num_eqns:length(iteration)-(num_eqns-2));
u_mod = iteration(3:num_eqns:length(iteration));

close_value = abs(T_final_vector(length(T_final_vector(:,1)),:))...
    -transpose(T_0_complex_multi(2:length(T_0_complex_multi))));

if max(close_value)>1
    percent_change_T = percent_change_nominal;
    percent_change_dTdr = percent_change_nominal_dTdr;
    percent_change_u = percent_change_nominal;

elseif max(close_value) >= 0.1 && max(close_value)<=1
    percent_change_T = percent_change_close_T;
    percent_change_dTdr = percent_change_close_dTdr;
    percent_change_u = percent_change_close_u;
else
    percent_change_T = 0.5;
    percent_change_dTdr = percent_change_close_dTdr;

```

```

    percent_change_u = percent_change_close_u;
end

T_mod_check = T_0_complex_multi-T_mod;
dTdr_mod_check = dTdr_0_complex_multi-dTdr_mod;
u_mod_check = u_0_complex_multi-u_mod;

T_negs = find(T_mod_check(1:length(T_mod_check))<=0);
dTdr_pos = find(dTdr_mod_check(1:length(dTdr_mod_check))<0);
u_negs = find(u_mod_check(1:length(u_mod_check))<0);

alpha_T_1 = min(percent_change_T*abs(T_0_complex_multi)./abs(T_mod));
alpha_dTdr_1 = min(percent_change_dTdr*abs(...
    dTdr_0_complex_multi)./abs(dTdr_mod));
alpha_u_1 = min(percent_change_u*abs(u_0_complex_multi)./abs(u_mod));

if isempty(T_negs) == 1
    alpha_T_2 = alpha_prime;
else
    alpha_T_2 = alpha_prime;
    T_mod(T_negs) = (T_0_complex_multi(T_negs)-(0))/2;
end

if isempty(dTdr_pos) == 1
    alpha_dTdr_2 = alpha_prime;
else
    alpha_dTdr_2 = alpha_prime;
    dTdr_mod(dTdr_pos) = dTdr_0_complex_multi(dTdr_pos)/2;
end

if isempty(u_negs) == 1
    alpha_u_2 = alpha_prime;
else
    alpha_u_2 = alpha_prime;
    u_mod(u_negs) = u_0_complex_multi(u_negs)/2;
end

```

```

end

alpha_T = min(alpha_T_1 , alpha_T_2);
alpha_dTdr = min(alpha_dTdr_1 , alpha_dTdr_2);
alpha_u = min(alpha_u_1 , alpha_u_2);

alpha_T_count(j) = alpha_T;
alpha_dTdr_count(j) = alpha_dTdr;
alpha_u_count(j) = alpha_u;

T_mod = alpha_T*T_mod;
dTdr_mod = alpha_dTdr*dTdr_mod;
u_mod = alpha_u*u_mod;

for i = 1:i_length
    if i == 1
        final_T = vertcat(final_T , T_final_vector(:, i));
        final_dTdr = vertcat(final_dTdr , dTdr_final_vector(:, i));
        final_u = vertcat(final_u , u_final_vector(:, i));
        final_r = vertcat(final_r , rad_final_vector(:, i));
    else
        final_T = vertcat(final_T , T_final_vector(2:length(...
            T_final_vector(:, i)), i));
        final_dTdr = vertcat(final_dTdr , dTdr_final_vector(...
            2:length(dTdr_final_vector(:, i)), i));
        final_u = vertcat(final_u , u_final_vector(2:length(...
            u_final_vector(:, i)), i));
        final_r = vertcat(final_r , rad_final_vector(2:end, i));
    end
end

end

final_B = sqrt(final_u)./transpose(r);
final_B(1) = 0;

T_final_vector_end_points = T_final_vector(length(T_final_vector), :);

```

```

T_match_points = abs(T_final_vector_end_points(1:length(...
    T_final_vector_end_points)-1)-transpose(T_0_complex_multi(...
    2:length(T_0_complex_multi)-1)));
dTdr_final_vector_end_points = dTdr_final_vector(length(...
    dTdr_final_vector),:);
dTdr_match_points = abs(dTdr_final_vector_end_points(...
    1:length(dTdr_final_vector_end_points)-1)-transpose(...
    dTdr_0_complex_multi(2:length(dTdr_0_complex_multi)-1)));
u_final_vector_end_points = u_final_vector(length(u_final_vector),:);
u_match_points = abs(u_final_vector_end_points(...
    1:length(u_final_vector_end_points)-1)-transpose(...
    u_0_complex_multi(2:length(u_0_complex_multi)-1)));

T_0_complex_multi = T_0_complex_multi-T_mod;
dTdr_0_complex_multi = dTdr_0_complex_multi-dTdr_mod;
u_0_complex_multi = u_0_complex_multi-u_mod;
%     end

s_vector = [];
for i = 1:i_length+1
    s_vector = vertcat(s_vector, T_0_complex_multi(i), ...
        dTdr_0_complex_multi(i), u_0_complex_multi(i));
end

T_0_complex_multi_track = horzcat(T_0_complex_multi_track, ...
    T_0_complex_multi);
dTdr_0_complex_multi_track = horzcat(dTdr_0_complex_multi_track, ...
    dTdr_0_complex_multi);
u_0_complex_multi_track = horzcat(u_0_complex_multi_track, ...
    u_0_complex_multi);

dTdr_0_convergence = dTdr_0_complex_multi;
T_0_convergence = T_0_complex_multi;
u_0_convergence = u_0_complex_multi;

```

```

dTdr_0_convergence(find(dTdr_0_convergence<=eps)) = 0;

convergence_T = abs(T_mod./T_0_convergence);
convergence_T(find(T_0_convergence<1.1*T_min)) = ...
    T_mod(find(T_0_convergence<1.1*T_min));
convergence_dT = abs(dTdr_mod./dTdr_0_convergence);
convergence_dT(find(T_0_convergence<1.1*T_min)) = ...
    dTdr_mod(find(T_0_convergence<1.1*T_min));
convergence_dT(find(isnan(convergence_dT)==1 | ...
    isinf(convergence_dT)==1)) = ...
    abs(dTdr_mod(find(isnan(convergence_dT)==1 | ...
    isinf(convergence_dT)==1)));
convergence_u = abs(u_mod./u_0_convergence);
convergence_u(find(isnan(convergence_u)==1 | isinf(convergence_u)==1))...
    = abs(u_mod(find(isnan(convergence_u)==1 | isinf(convergence_u)==1)));

convergence_limit = 1e-4;
convergence_limit_dT = 1e-4;

max_convergence_T(j) = sqrt(dot(convergence_T,convergence_T));
max_convergence_dT(j) = sqrt(dot(convergence_dT,convergence_dT));
max_convergence_u(j) = sqrt(dot(convergence_u,convergence_u));

figure(1)
subplot(3,1,1)
semilogy([1:1:j],max_convergence_T, '-k', 'LineWidth',1)
title('T_convergence')

subplot(3,1,2)
semilogy([1:1:j],max_convergence_dT, '-k', 'LineWidth',1)
title('dT_convergence')

subplot(3,1,3)
semilogy([1:1:j],max_convergence_u, '-k', 'LineWidth',1)
title('u_convergence')

```

figure (4)

```

    plot(rad_final_vector*100,T_final_vector,'LineWidth',4)
    xlabel('Radius(cm)','FontSize',15)
    ylabel('T_{e,i}(eV)','FontSize',15)
    ylim([-5 1.1*max(max(T_final_vector))])
    title(['Pulse_',num2str(shot),'_',Time='_',num2str(time),...
          '\mus'],'FontSize',15)
    set(gca,'FontSize',15)
    grid on

    if max_convergence_T(j) < convergence_limit && max_convergence_dT(j) <...
        convergence_limit_dT && max_convergence_u(j) < convergence_limit

        break
    end

    if j == 250
        temp = [];
        mag_field = [];
        dTdr = [];
        return
    end

end

end

end

if final_dTdr(length(final_dTdr))>0
    temp = [];
    mag_field = [];
    dTdr = [];
else
    temp = final_T;
    mag_field = final_u;
    dTdr = final_dTdr;

```

end

B.3 ode15s Heat Conduction Equations

```

function ds_dt = HeatConduction(r,s,n0,a,T_min,brem_frac,line_frac,...
    impurity_frac,impurity_ion,alter_Z,Zeff1,rwall)

global check T_min extension unmag_param mag_param min_distance min_case

loglam = 10;
k = 1.6e-19;
mi = 1.67e-27;
me = 9.11e-31;
mu0 = 4*pi*1e-7;
c1 = -2*mu0*k*(1+Zeff1);
c2 = 1.035e-4*Zeff1*loglam*(1+Zeff1)^2*k^2;
c3 = 1.69e-38*Zeff1^2;
c5 = 3.44e11*k/Zeff1/loglam/me;
c6 = 2.09e13*k/Zeff1^4/loglam/mi;
c7 = (1.76e11*3.44e11)^2;
c8 = (9.58e7*2.09e13)^2;

if Zeff1 == 1
    delta_0 = 3.7703;
    delta_1 = 14.79;
    gamma_1 = 4.664;
    gamma_0 = 11.92;
elseif Zeff1 == 2
    delta_0 = 1.0465;
    delta_1 = 10.8;
    gamma_1 = 3.957;
    gamma_0 = 5.118;
elseif Zeff1 == 3
    delta_0 = 0.5814;
    delta_1 = 9.618;
    gamma_1 = 3.721;

```

```

    gamma_0 = 3.525;
elseif Zeff1 == 4
    delta_0 = 0.4106;
    delta_1 = 9.055;
    gamma_1 = 3.604;
    gamma_0 = 2.841;
elseif Zeff1 > 4
    delta_0 = 0.0961;
    delta_1 = 7.482;
    gamma_1 = 3.25;
    gamma_0 = 1.20;
end

n = n0*a^2/((r)^2+a^2);
dndr = -2*n0*a^2*(r)/((r)^2+a^2)^2;

xe2 = c7*(s(3))*(T_min+10^(s(1)))^3/((r)^2*Zeff1^4*n^2*loglam^2)*mag_param;
xi2 = c8*(s(3))*(T_min+10^(s(1)))^3/((r)^2*Zeff1^6*n^2*loglam^2)*mag_param;
nume = gamma_1*xe2+gamma_0*unmag_param;
numi = 2*xi2+2.645*unmag_param;
dene = xe2^2+delta_1*unmag_param*xe2+delta_0*unmag_param;
deni = xi2^2+2.7*unmag_param*xi2+0.677*unmag_param;
k_perp_e1 = c5*(T_min+10^(s(1)))^2.5*nume/dene;
k_perp_i1 = c6*(T_min+10^(s(1)))^2.5*numi/deni;
k_perp = k_perp_e1+k_perp_i1;
brem = c3*(r)*n^2*sqrt(T_min+10^(s(1)));
eta_term1 = c2/(T_min+10^(s(1)))^1.5;

if r == 0
    ds_dt(1) = 0;
    ds_dt(2) = 0;
    ds_dt(3) = 0;
elseif [r~=0 && check == 1] || r<1e-6
    ds_dt(1) = -s(2)/(r*k_perp*k*log(10)*(T_min+10^(s(1))));
    ds_dt(2) = 0;

```

```

    ds_dt(3) = (c1*(r)^2*(T_min+10^(s(1)))*dndr);
    check = 0;
else
ds_dt(1) = -s(2)/(r*k_perp*k*log(10)*(T_min+10^(s(1))));
ds_dt(2) = eta_term1*r^3/s(3)*((T_min+10^(s(1)))*dndr-n*s(2)/...
    (r*k_perp*k))^2-r*brem;
ds_dt(3) = c1*r^2*((T_min+10^(s(1)))*dndr-n*s(2)/(r*k_perp*k));
end
ds_dt = ds_dt';

```

B.4 ode15s Heat Conduction Baseline Equations

```

function ds_dt = HeatConductionBaseline(r,s,n0,a,T_min,brem_frac,...
    line_frac,impurity_frac,impurity_ion,alter_Z,Zeff1,rwall)

global check T_min extension unmag_param mag_param min_distance min_case

loglam = 10;
k = 1.6e-19;
mi = 1.67e-27;
me = 9.11e-31;
mu0 = 4*pi*1e-7;
c1 = -2*mu0*k*(1+Zeff1);
c2 = 1.035e-4*Zeff1*loglam*(1+Zeff1)^2*k^2;
c3 = 1.69e-38*Zeff1^2;
c5 = 3.44e11*k/Zeff1/loglam/me;
c6 = 2.09e13*k/Zeff1^4/loglam/mi;
c7 = (1.76e11*3.44e11)^2;
c8 = (9.58e7*2.09e13)^2;

if Zeff1 == 1
    delta_0 = 3.7703;
    delta_1 = 14.79;
    gamma_1 = 4.664;
    gamma_0 = 11.92;
elseif Zeff1 == 2

```

```

    delta_0 = 1.0465;
    delta_1 = 10.8;
    gamma_1 = 3.957;
    gamma_0 = 5.118;
elseif Zeff1 == 3
    delta_0 = 0.5814;
    delta_1 = 9.618;
    gamma_1 = 3.721;
    gamma_0 = 3.525;
elseif Zeff1 == 4
    delta_0 = 0.4106;
    delta_1 = 9.055;
    gamma_1 = 3.604;
    gamma_0 = 2.841;
elseif Zeff1 > 4
    delta_0 = 0.0961;
    delta_1 = 7.482;
    gamma_1 = 3.25;
    gamma_0 = 1.20;
end

n = n0*a^2/((r)^2+a^2);
dndr = -2*n0*a^2*(r)/((r)^2+a^2)^2;

xe2 = c7*(s(3))*(10^(s(1)))^3/((r)^2*Zeff1^4*n^2*loglam^2)*mag_param;
xi2 = c8*(s(3))*(10^(s(1)))^3/((r)^2*Zeff1^6*n^2*loglam^2)*mag_param;
nume = gamma_1*xe2+gamma_0*unmag_param;
numi = 2*xi2+2.645*unmag_param;
dene = xe2^2+delta_1*unmag_param*xe2+delta_0*unmag_param;
deni = xi2^2+2.7*unmag_param*xi2+0.677*unmag_param;
k_perp_e1 = c5*(10^(s(1)))^2.5*nume/dene;
k_perp_i1 = c6*(10^(s(1)))^2.5*numi/deni;
k_perp = k_perp_e1+k_perp_i1;
brem = c3*(r)*n^2*sqrt(10^(s(1)));
eta_term1 = c2/(T_min+10^(s(1)))^1.5;

```

```

if r == 0
    ds_dt(1) = 0;
    ds_dt(2) = 0;
    ds_dt(3) = 0;

elseif [r~=0 && check == 1] || r < 1e-6
    ds_dt(1) = 0;
    ds_dt(2) = -r*brem;
    ds_dt(3) = (c1*(r)^2*((10^(s(1)))*dndr+n*(10^(s(1)))/...
        (r-rwall-extension));
    check = 0;
else

    ds_dt(1) = 0;
    ds_dt(2) = 0;
    ds_dt(3) = (c1*(r)^2*((10^(s(1)))*dndr));
end

ds_dt = ds_dt';

```

B.5 ode15s Heat Conduction Events Equations

```

function [values, isterminal, direction] = eventsheatconduction(r,s,n0,a,...
    T_min,brem_frac,line_frac,impurity_frac,impurity_ion,alter_Z,Zeff1,...
    rwall)

```

```

global check T_min extension unmag_param mag_param min_distance min_case

```

```

loglam = 10;
k = 1.6e-19;
mi = 1.67e-27;
me = 9.11e-31;
mu0 = 4*pi*1e-7;
c1 = -2*mu0*k*(1+Zeff1);
c2 = 1.035e-4*Zeff1*loglam*(1+Zeff1)^2*k^2;

```

```

c3 = 1.69e-38*Zeff1 ^2;
c5 = 3.44e11*k/Zeff1/loglam/me;
c6 = 2.09e13*k/Zeff1 ^4/loglam/mi;
c7 = (1.76e11*3.44e11) ^2;
c8 = (9.58e7*2.09e13) ^2;

if Zeff1 == 1
    delta_0 = 3.7703;
    delta_1 = 14.79;
    gamma_1 = 4.664;
    gamma_0 = 11.92;
elseif Zeff1 == 2
    delta_0 = 1.0465;
    delta_1 = 10.8;
    gamma_1 = 3.957;
    gamma_0 = 5.118;
elseif Zeff1 == 3
    delta_0 = 0.5814;
    delta_1 = 9.618;
    gamma_1 = 3.721;
    gamma_0 = 3.525;
elseif Zeff1 == 4
    delta_0 = 0.4106;
    delta_1 = 9.055;
    gamma_1 = 3.604;
    gamma_0 = 2.841;
elseif Zeff1 > 4
    delta_0 = 0.0961;
    delta_1 = 7.482;
    gamma_1 = 3.25;
    gamma_0 = 1.20;
end

n = n0*a ^2/((r)^2+a ^2);
dndr = -2*n0*a ^2*(r)/((r)^2+a ^2) ^2;

```

```

xe2 = c7*(s(3))*(T_min+10^(s(1)))^3/((r)^2*Zeff1^4*n^2*loglam^2)*mag_param;
xi2 = c8*(s(3))*(T_min+10^(s(1)))^3/((r)^2*Zeff1^6*n^2*loglam^2)*mag_param;
nume = gamma_1*xe2+gamma_0*unmag_param;
numi = 2*xi2+2.645*unmag_param;
dene = xe2^2+delta_1*unmag_param*xe2+delta_0*unmag_param;
deni = xi2^2+2.7*unmag_param*xi2+0.677*unmag_param;
k_perp_e1 = c5*(T_min+10^(s(1)))^2.5*nume/dene;
k_perp_i1 = c6*(T_min+10^(s(1)))^2.5*numi/deni;
k_perp = k_perp_e1+k_perp_i1;

gyro = 1.02e2*Zeff1*sqrt(T_min+10^(s(1)))/(sqrt(s(3))/r*1e4)/100;
mfp = 2.04e13*(T_min+10^(s(1)))^2/(Zeff1*n/1e6*loglam)/100;

if min_case == 1
values = [-s(2)/(r*k_perp*k)-(T_min-(T_min+10^(s(1))))/(min([gyro,mfp]))];
else
values = [-s(2)/(r*k_perp*k)-(T_min-(T_min+10^(s(1))))/(min_distance)];
end
isterminal = [1]; % Stop integration
direction = [-1]; % for a negative going zero crossing

```

BIBLIOGRAPHY

- [1] R. Aymar et al. The ITER Design. *Plasma Phys. Control. Fusion*, 44:519, 2002.
- [2] U. Shumlak and C. W. Hartman. Sheared flow stabilization of the $m = 1$ kink mode in Z-pinch. *Phys. Rev. Lett.*, 75(18):3285–3288, Oct 1995.
- [3] B.B. Kadomtsev. *Reviews of Plasma Physics*, volume 2, chapter Hydromagnetic stability of a plasma. Consultants Bureau, New York, 1966.
- [4] M. Kruskal and M. Schwarzschild. Some instabilities of a completely ionized plasma. In *Proc. R. Soc. London, Ser. A*, volume 223 of *A*, pages 348–360. The Royal Society, 1954.
- [5] J. Marshall. Performance of a hydromagnetic plasma gun. *Phys. Fluids*, 3(1):134–135, 1960.
- [6] D.Y. Cheng. Plasma deflagration and the properties of a coaxial plasma deflagration gun. *Nucl. Fusion*, 10:305, 1970.
- [7] I.H. Hutchinson. *Principles of Plasma Diagnostics*. Cambridge University Press, 2002.
- [8] N.E. Huang et al. The empirical mode decomposition and the Hilbert spectrum for nonlinear and non-stationary time series analysis. *Proc. R. Soc. Lond. A*, 454:903–995, 1998.
- [9] J.D. Huba. *NRL: Plasma Formulary*. Naval Research Laboratory Beam Physics Branch, 2011.
- [10] L. Spitzer Jr. *Physics of Fully Ionized Gases*. Dover Publications, Inc., 31 East 2nd Street, Mineola, NY 11501, second edition, 1962.
- [11] H. Maecker. Elektronendichte und temperatur in der saule des hochstromkohlebogens. *Zeitschrift fur Physik A Hadrons and Nuclei*, 136:119–136, 1953.
- [12] J. Shumaker. Arc source for high temperature gas studies. *Rev. Sci. Instrum.*, 32:65–67, 1961.

- [13] R. Jahn. *Physics of Electric Propulsion*. Dover Publications Inc., Mineola, NY, 1968.
- [14] R. John, S. Bennett, and J. Connors. Arcjet engine performance: experiment and theory. *AIAA*, 1, 1963.
- [15] L. Wallner and L. Czilos. NASA TN D-2868. Technical Report 2868, NASA, 1965.
- [16] V. Watson and E. Pegot. TN-D-4042. Technical report, NASA, 1967.
- [17] H. Stine, V. Watson, and C. Shepard. Effect of axial flow on the behavior of the wall-constricted arc. Technical report, NASA, 1964.
- [18] R. Graves and W. Wells. Preliminary studies of a wall-stabilized constricted arc. Technical Report NASA TM X-2700, NASA, 1973.
- [19] R. Preston. Spectroscopic studies of a plasma temperature and radiation standard based on wall-stabilized arc. *Journal of Quantitative Spectroscopy and Radiative Transfer*, 18:337–360, 1977.
- [20] K. Clark and R. Jahn. The magnetoplasmadynamic arcjet. *Astronautica Acta*, 13:315–325, 1967.
- [21] R. Kilb, H. Hurwitz Jr., and W. Westendorp. Wall stabilization effects in theta pinch configurations. *Phys. Fluids*, 5, 1962.
- [22] R. Kilb, H. Hurwitz Jr., and W. Westendorp. Wall stabilization effects in theta-pinch configurations. *Phys. Fluids*, 6:1332, 1963.
- [23] F. Haas and J. Wesson. Stability of the theta-pinch. *Phys. Fluids*, 9:2472, 1966.
- [24] F. Haas and J. Wesson. Stability of the theta-pinch II. *Phys. Fluids*, 10:2245, 1967.
- [25] F. Ribe. LASL controlled thermonuclear research program progress report for a 12-month period ending December 1972. Technical report, LANL, 1973.
- [26] J. Goedbloed, D. Pfirsch, and H. Tasso. Instability of a pinch surrounded by a resistive wall. *Nuc. Fusion*, 12:649, 1972.
- [27] E. Strait et al. Wall stabilization of high beta tokamak discharges in DIII-D. *Phys. Rev. Lett.*, 74:2483, 1995.
- [28] T. Jarboe. The spheromak confinement device. *Phys. of Plasmas*, 12:058103, 2005.

- [29] M. Rosenbluth and M. Bussac. MHD stability of spheromak. *Nuc. Fusion*, 19:489, 1979.
- [30] U. Shumlak, R.P. Golingo, B.A. Nelson, and D.J. Den Hartog. Evidence of stabilization in the Z-pinch. *Phys. Rev. Lett.*, 87(20):205005, 2001.
- [31] U. Shumlak, B.A. Nelson, R.P. Golingo, S.L. Jackson, E.A. Crawford, and D.J. Den Hartog. Sheared flow stabilization experiments in the ZaP flow Z-pinch. *Phys. Plasmas*, 10:1683, 2003.
- [32] V. Lukin, A. Glasser, W. Lowrie, and E. Meier. HiFi Adaptive, Implicit, High Order Finite Element Code for General Multi-Fluid Applications. In *AAS/Solar Physics Division Meeting*, 2009.
- [33] U. Shumlak, C. Adams, J. Blakely, B. Chan, R. Golingo, S. Knecht, B. Nelson, R. Oberto, M. Sybouts, and G. Vogman. Equilibrium, flow shear and stability measurements in the Z-pinch. *Nuc. Fusion*, 49:075039, 2009.
- [34] W. Lowrie. *Development and Application of a Multi-Block High Order Finite Element Modeling Code as an Engineering Design Tool*. Ph.D. Dissertation, University of Washington, Seattle, WA, 2012.
- [35] V.S. Lukin, A.H. Glasser, W. Lowrie, and E. Meier. HiFi-Adaptive, Implicit, High Order Finite Element Code for General Multi-Fluid Applications. In *AAS/Solar Physics Division Meeting*, volume 40, 2009.
- [36] H. P. Furth and S. Yoshikawa. Adiabatic compression of tokamak discharges. *Phys. Fluids*, 13(10):2593–2596, 1970.
- [37] K. Bol, R. A. Ellis, H. Eubank, H.P. Furth, R.A. Jacobsen, L.C. Johnson, E. Mazzucato, W. Stodiek, and E.L. Tolnas. Adiabatic compression of the tokamak discharge. *Phys. Rev. Lett.*, 29(22):1495–1498, Nov 1972.
- [38] V.E. Golant. The investigation of adiabatic compression in tokamaks. *Plasma Phys. and Control. Fusion*, 26:77, 1984.
- [39] M. Yamada et al. Experimental investigation of magnetic compression of a spheromak plasma. *Phys. Fluids B*, 2:3074, 1990.
- [40] R. L. Spencer, M. Tuszewski, and R. K. Linford. Adiabatic compression of elongated field-reversed configurations. *Phys. Fluids*, 26(6):1564–1568, 1983.

- [41] D.J. Rej et al. High-power magnetic-compression heating of field-reversed configurations. *Phys. Fluids B*, 4:1909, 1992.
- [42] G.A. Wurden et al. FRCHX magnetized target fusion HEDLP experiments. In *22nd IAEA Fusion Energy Conference*, 2008.
- [43] W. H. Bennett. Magnetically self-focussing streams. *Phys. Rev.*, 45(12):890–897, Jun 1934.
- [44] F. deHoffman and E. Teller. Magneto-hydrodynamic shocks. *Phys. Rev.*, 80:692, 1950.
- [45] E.A. McLean et al. Spectroscopic study of helium plasmas produced by magnetically driven shock waves. *Phys. of Fluids*, 3:843, 1960.
- [46] A.C. Kolb. Production of high-energy plasmas by magnetically driven shock waves. *Phys. Rev.*, 107:345, 1957.
- [47] D.C. Hagerman and J.W. Mather. Neutron production in a high-power pinch apparatus. *Nature*, 181:226, 1958.
- [48] K. Boyer et al. Studies of plasma heated in a fast-rising axial magnetic field (Scylla). *Phys. Rev.*, 119:831, 1960.
- [49] S.I. Braginskii. Transport processes in a plasma. *Reviews of Plasma Physics*, 1:205, 1965. (Consultants Bureau, New York, 1965).
- [50] Y. B. Zel'dovich and Y. P. Raizer. *Physics of Shock Waves and High-Temperature Hydrodynamic Phenomena*, volume 1. Academic, New York, 1966.
- [51] M.A. Liberman and A.L. Velikovich. *Physics of Shock Waves in Gases and Plasmas*. Springer, Heidelberg, 1986.
- [52] A. L. Velikovich, K. G. Whitney, and J. W. Thornhill. A role for electron viscosity in plasma shock heating. *Phys. Plasmas*, 8(10):4524–4533, 2001.
- [53] R.S. Pease. Equilibrium characteristics of a pinched gas discharge cooled by bremsstrahlung radiation. *Proc. Phys. Soc.*, B70:11, 1957.
- [54] S.I. Braginskii. *Sov. Phys. JETP*, 6:494, 1958.
- [55] M.G. Haines. An analytic model of radiative collapse in a Z-pinch. *Plasma Phys. and Cont. Fusion*, 31:759, 1989.

- [56] M.G. Haines. The Joule heating of a stable pinched plasma. *Proc. Phys. Society*, 76:250, 1960.
- [57] J. P. Freidberg. *Plasma Physics and Fusion Energy*. Cambridge University Press, 32 Avenue of the Americas, New York, NY 10013, USA, first edition, 2007.
- [58] D.E. Post, R.V. Jensen, C.B. Tarter, W.H. Grasberger, and W.A. Lokke. Steady-state radiative cooling rates for low-density high-temperature plasmas. *Atomic Data and Nuclear Data Tables*, 20:397, 1977.
- [59] J. Stoer and R. Bulirsch. *Introduction to Numerical Analysis*. Springer, 1980.